JOURNAL OF THE

# Electrochemical Society

ol. 114, No. 10 October 1967

# In the long run...

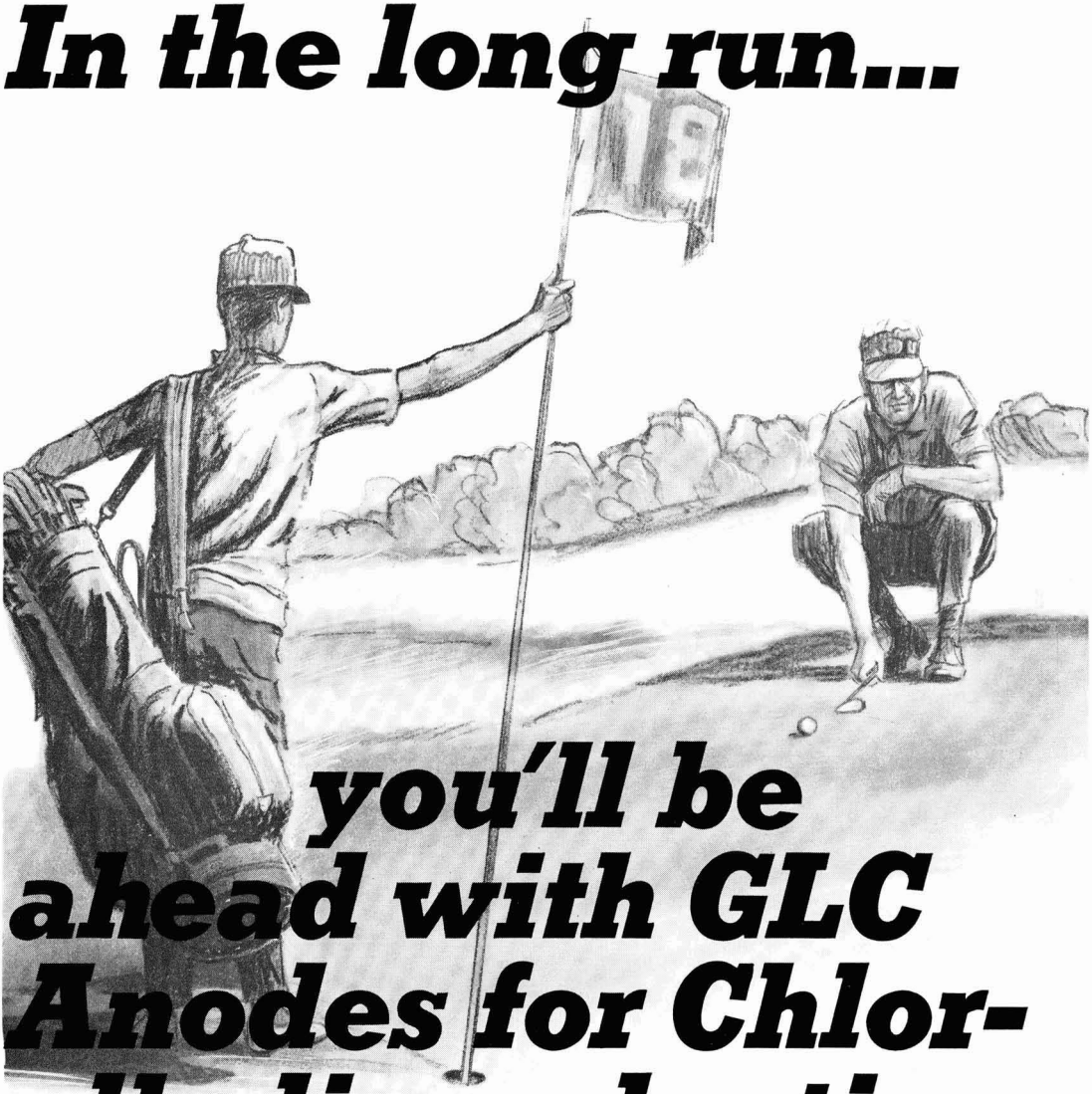

# you'll be ahead with GLC Anodes for Chlor-alkali production.

PRODUCTS YOU CAN TRUST ® GLC

GRAPHITE PRODUCTS DIVISION
**GREAT LAKES CARBON CORPORATION**
299 Park Avenue • New York, N. Y. 10017
OFFICES AND AGENTS FROM COAST-TO-COAST AND AROUND THE WORLD

*Great Lakes Carbon Corporation is one of the world's largest manufacturers of graphite for electrochemical and electro-thermic processes—and for aerospace, nuclear, metallurgical and other industrial uses.*

Vol. 114 • No. 10

# JOURNAL OF THE ELECTROCHEMICAL SOCIETY





Manuscripts submitted to the Journal should be sent, in triplicate, to the Editorial Office at 30 East 42 St., New York, N. Y., 10017. They should conform to the revised Instructions to Authors published on pp. 263C-264C of this issue. Manuscripts so submitted become the property of The Electrochemical Society and may not be published elsewhere, in whole or in part, unless permission is requested of and granted by the Editor.

The Electrochemical Society does not maintain a supply of reprints of papers appearing in its Journal. A photoprint copy of any particular paper, however, may be obtained by corresponding direct with the Engineering Societies Library, 345 E. 47 St., New York, N. Y., 10017.

Inquiries re positive microfilm copies of volumes should be addressed to University Microfilms, Inc., 300 N. Zeeb St., Ann Arbor, Mich.

Walter J. Johnson, Inc., 111 Fifth Ave., New York, N. Y., 10003, have reprint rights to out-of-print volumes of the Journal, and also have available for sale back volumes and single issues, with the exception of the current calendar year. Anyone interested in securing back copies should correspond direct with them.

Published monthly by **The Electrochemical Society, Inc.,** at 215 Canal St., Manchester, N. H.; **Executive Offices, Editorial Office and Circulation Dept.,** and **Advertising Office** at 30 East 42 St., New York, N. Y., 10017, combining the JOURNAL and TRANSACTIONS OF THE ELECTROCHEMICAL SOCIETY. Statements and opinions given in articles and papers in the JOURNAL OF THE ELECTROCHEMICAL SOCIETY are those of the contributors, and The Electrochemical Society assumes no responsibility for them.

Claims for missing numbers will not be allowed if received more than 60 days from date of mailing plus time normally required for postal delivery of JOURNAL and claim. No claims allowed because of failure to notify the Circulation Dept., The Electrochemical Society, 30 East 42 St., New York, N. Y., 10017, of a change of address, or because copy is "missing from files." Subscription to members as part of membership service; subscription to nonmembers $24.00 plus $1.50 for postage outside U.S and Canada Single copies $1.70 to members, $2.25 to nonmembers.  Entered as second-class matter at the Post Office at Manchester N. H., under the act of August 24, 1912. Postage paid at Manchester, N. H.

Report from

**BELL LABORATORIES**

# "Functional" Tantalum Integrated Circuits

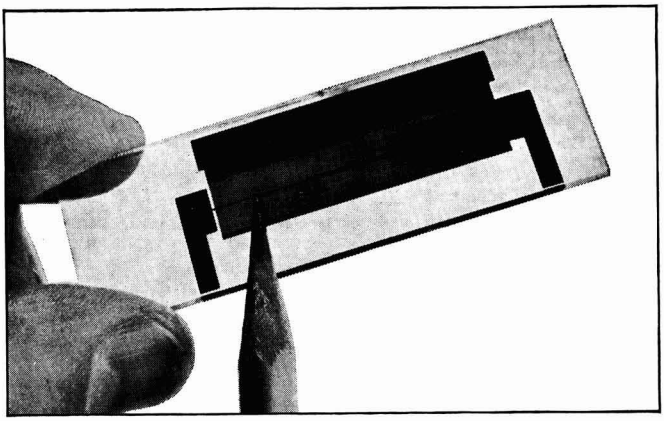

**The new "functional" thin-film circuit, shown in the above photo and in the drawing, right, is a two-terminal network consisting of thin films deposited on a glass substrate. For equivalent electrical performance, a conventional thin-film circuit would require at least three resistors and four capacitors (drawing, below).**

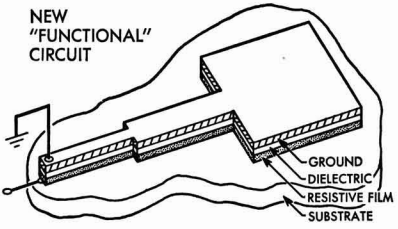


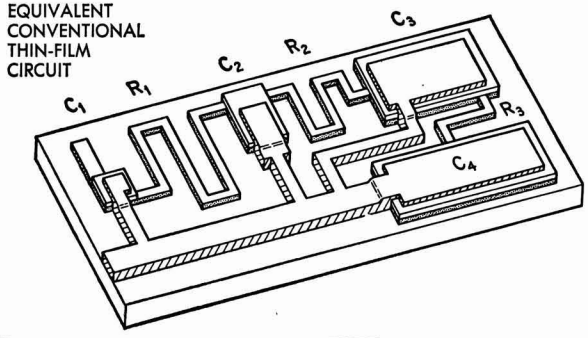


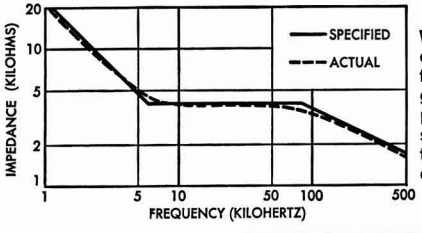


**Wyndrum formulated a class of equations which relate frequency response to the geometry of the thin-film pattern. The curves, left, show the specified and actual performance of such a circuit.**

As electronic systems have grown in size and complexity, tantalum integrated circuits have reduced costs while increasing reliability and performance. To obtain even further integration of circuit functions, however, engineers at Bell Telephone Laboratories have used tantalum technology to build single thin-film components equivalent to networks of thin-film resistors and capacitors.

This new single, "functional" component (left) is basically a film capacitor with one electrode of resistive tantalum and a second electrode of conductive gold, separated by a dielectric layer of tantalum pentoxide. The component is made by depositing a thin film of tantalum onto a glass substrate, converting a portion of this layer to the insulating oxide, and then depositing the conductive gold electrode onto the oxide. In this arrangement, resistance and capacitance are distributed throughout the structure rather than among discrete electrical components. In addition to providing reliability and economy, this approach also offers the advantages of simpler fabrication and fewer electrical parasitics.

As an important contribution to the design of such structures, Bell Laboratories engineer Ralph W. Wyndrum, Jr., showed that it was possible to convert circuit performance specifications directly to tantalum thin-film patterns. Furthermore, he showed how appropriate geometries and film compositions could yield a wide range of impedance and transfer functions.

Wyndrum developed this synthesis technique while doing graduate work at New York University. He has advanced this technique further at Bell Laboratories, where tantalum integrated circuits were first created some ten years ago.

**Bell Telephone Laboratories**
Research and Development Unit of the Bell System

# EDITORIAL

## Electronic Materials Here and in the USSR

The symposium on the "Chemical Bond in Semiconductors" held last June in Minsk, White Russia (BSSR), was another manifestation of the established interdisciplinary patterns in the science and technology of electronic materials. The spectrum covered was broad indeed, ranging from traditional inorganic chemical aspects to complex quantum mechanical theoretical treatments. Within these two extremes there were thermodynamic studies, experimental investigations on energy band structure, and reports on relationships between properties and empirical or semiquantitative bonding parameters. The symposium was sponsored by the Academy of Sciences of the USSR (the Department of Physico-chemical and Inorganic Material Technology, the Scientific Board of Physics and Chemistry of Semiconductors) and the Academy of BSSR (the Institute of Solids and Semiconductors).

Such a broad symposium is not uncommon in the Eastern countries but it is rare, even nonexistent, in this country and in Western Europe. Classical inorganic chemistry reports are simply not included in Western symposia where the physics (experimental and theoretical) of materials is discussed. And conversely, in the meetings covering the preparation, purity, crystalline perfection, compositional ranges or, in general, synthetic aspects of materials, theoretical studies are conspicuously absent.

I am pointing out these differences because I believe they reflect significant differences in attitude toward the basic chemical approach to electronic materials between this country and the USSR. Although I was aware of such differences they became perfectly clear at the Minsk symposium and during my visits to a number of Academy Institutes and other laboratories in Minsk, Leningrad, Moscow, and Kiev. Along with the USSR I should include the Eastern European countries, judging from my visit to several academy laboratories in Warsaw and from extensive discussions with scientists from Czechoslovakia, Rumania, and Bulgaria.

The classical inorganic chemistry tradition, which is fading in this country, has found in the USSR new fertile soil in electronic materials and particularly in semiconductor compounds. Unlike this country, in the USSR large institutes or research groups are devoted to the synthesis of semiconductor compounds, their purification, single crystal growth, stoichiometry, impurity distribution, phase diagrams and the like. Although this work may not involve refined electrical or optical measurements it stands on its own and ranks high along with modern mathematics, physics, and electrical engineering. Scientists and engineers doing the work are considered perfectly in tune with modern science and technology. The tedious complexities associated with the design and preparation of pure semiconductor materials are quite clearly appreciated in all segments of solid state science both in universities across the USSR and in research laboratories.

It is certainly most interesting to speculate on and discuss the reasons for the prevailing attitudes—and therefore the prevailing activities—regarding materials engineering in the solid state. But it is even more pertinent to examine the outcome of the materials engineering effort of recent years in the USSR on semiconductor compounds (apparently on the recommendation of the late Academician Ioffe) which is striking indeed. The availability of high purity single crystals of many semiconductor compounds (II-VI, III-V, IV-IV, and their alloys) is incomparably greater in the Eastern than in the Western countries. Here are two typical instances: single crystals of silicon carbide with an impurity concentration of $10^{15}$ to $10^{16}$ per cubic centimeter are readily available in the USSR. As a direct consequence, silicon carbide devices—electroluminescence diodes and monolithic digital display devices —are finding their way into electronic systems. Silicon carbide radiation detectors have been made to operate at 700°C where no other available material can perform. Silicon carbide devices of this type do not exist in this country. Another striking example, reflecting the results of concentrated effort on materials engineering (this time on elemental semiconductors) is the solid state radiation counter made of germanium compensated by gamma radiation. The advantages of such counters over the existing ones are apparently great. To my knowledge no radiation-compensated counter is operating in this country, yet they are readily available in the USSR.

The prevailing fashion and esteem in the Western countries, and particularly in this country, for certain facets of mathematics and physics has apparently caused much essential materials engineering in universities and research laboratories to be replaced with second-class science. And yet hardly anyone will disagree that first-class materials engineering must rank, in practice and in fashion, higher than second-class science. More specifically, first-class materials engineering in electronic materials is not just preferable to second-class physics, it is indispensible. For first-class fundamental solid state physics and solid state electronics can only be based on first-class electronic materials.

Harry C. Gatos, President
The Electrochemical Society, Inc.

# Go by the book-

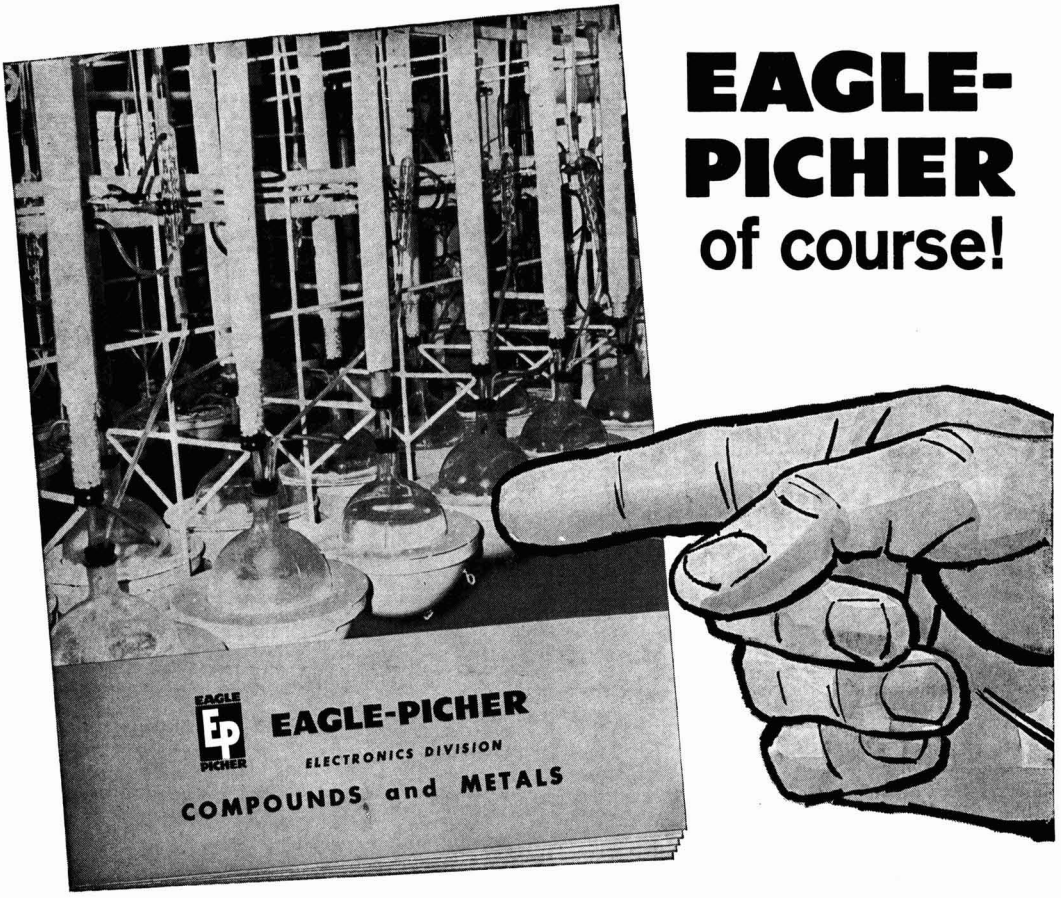


## EAGLE-PICHER of course!

Helpful! Informative! Free! Our currently most important Compounds and Metals are described fully with complete technical data. Write today for your free copy.

We hate to brag, so why not read the book? Eagle-Picher was first to perfect a process for recovering Germanium and first to perfect this metal's resistivity minimum to 40 ohm-cm. We continue to lead in the production of *ultra-high purity* semiconductor compounds and metals. There *are no higher standards of purity* than the standards of Eagle-Picher.

**BORON:** Ultra-high purity elemental Boron; Tribromide; Oxide

**CADMIUM:** Ultra-high purity Cadmium metal; Sulfide, powder, crystal chips, melt and vapor phase crystals; Cadmium Selenide and Cadmium Telluride powder

**GALLIUM:** Metal; Sesquioxide, Trichloride

**GERMANIUM:** First Reduction Metal; Intrinsic Metal; Single Crystals; Dioxide; Tetrachloride; Tetrabromide; Tetraiodide; Monoxide; Diiodide; Sodium Metagermanate; Sodium Heptagermanate

**ZINC:** Metal; Sulfide, powder, crystal chips, melt and vapor phase crystals; Zinc Selenide and Zinc Telluride powders

*Clip coupon and write for your copy today*

Eagle-Picher Industries, Inc., Electronics Division
Dept. JES-1067, Miami, Oklahoma 74354

Please send me a copy of the book,
"Eagle-Picher Compounds and Metals."

Name_____ Title_____

Firm_____

Address_____

EAGLE PICHER Since 1843

**EAGLE-PICHER INDUSTRIES, INC.**

General Office · Cincinnati, Ohio 45201

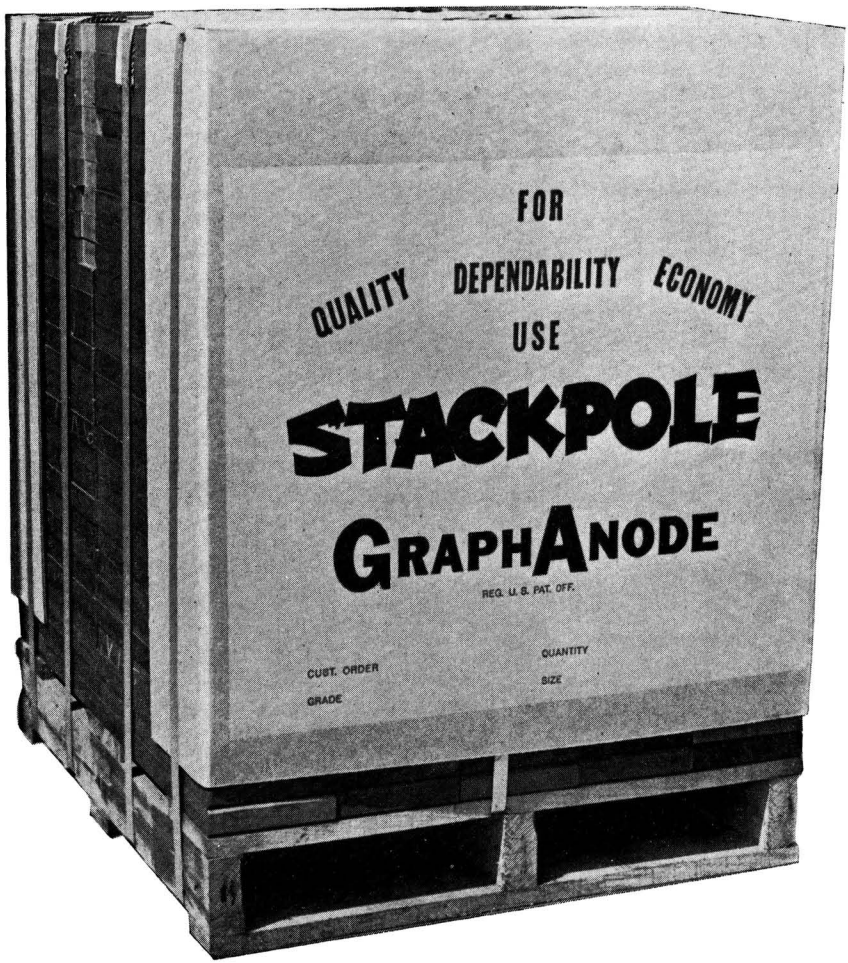


# GET A LOAD OF THIS

If you're looking for improved performance, greater productivity, and reduced operating costs, investigate the savings of Stackpole GraphAnodes®. Rigid manufacturing controls assure material uniformity and permit proper cell alignment that makes for even wear and longer life. Whatever your anode needs, Stackpole GraphAnodes® can help you cut costs. Try a load. Write or call: Stackpole Carbon Company, Carbon Division, St. Marys, Pennsylvania 15857. Phone: 814-781-8463. TWX: 510-693-4511.

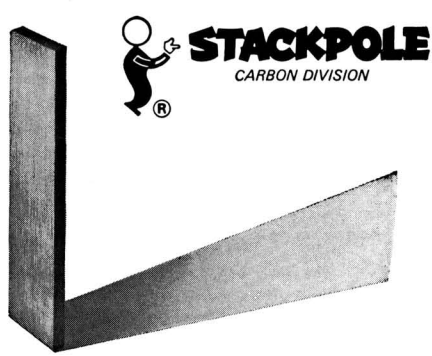

JOURNAL OF THE ELECTROCHEMICAL SOCIETY

# ELECTROCHEMICAL SCIENCE

OCTOBER 1967



*Journal of The Electrochemical Society* is the fundamental research journal serving the interdisciplinary interests of chemistry, physics, electronics, biology, medicine, and engineering as they pertain to electrochemistry and to electrochemical phenomena. Written for the research scientist in industry, government, the independent laboratory and the university, it publishes contributed Technical Papers, Technical Notes and Brief Communications describing current basic research of original character, and is edited in two sections: 1) ***Electrochemical Science*** including such areas as batteries, fuel cells, corrosion and corrosion mechanisms, electrothermics and metallurgy, electrodeposition, electroorganic reactions and phenomena, and allied work of theoretical electrochemical nature. 2) ***Solid State Science*** including such areas as dielectrics and insulation, electrothermics and metallurgy, semiconductors, luminescence and related solid state investigations.



## TECHNICAL PAPERS



## TECHNICAL NOTES



## BRIEF COMMUNICATION



## TECHNICAL PAPERS

September 1967



(The above papers appeared in the September 1967 issue of the Journal and were omitted on the contents page.)

# High Activity Platinum Electrocatalysts for the Direct Anodic Oxidation of Saturated Hydrocarbons

E. J. Cairns[1] and E. J. McInerney[2]

*General Electric Research and Development Center, Schenectady, New York*

ABSTRACT

The fact that hydrocarbon fuels can be directly oxidized at reasonable current densities using fuel cells with platinum anodes and acidic electrolytes has been demonstrated previously. The next logical step was to reduce the amount of platinum electrocatalyst required for a given current density. Two approaches have been taken toward this objective: the preparation of higher activity unsupported electrocatalysts, and the use of conducting support materials to permit more effective utilization of the platinum. Results are reported for the anodic oxidation of both gaseous and liquid normal saturated hydrocarbons using a number of unsupported and carbon-supported electrocatalysts. Indications are that power densities of about 35 mw/cm$^2$ (resistance-free) are possible with a propane-oxygen fuel cell using 36 m/o (mole per cent) hydrofluoric acid at 105°C as the electrolyte with an anode containing 10 mg Pt/cm$^2$ as a carbon-supported electrocatalyst.

There has been a concerted effort during the last few years to accomplish the direct anodic oxidation of saturated hydrocarbons in fuel cells. This has been achieved by several investigators, all using platinum as the electrocatalyst. The amount of platinum used has ranged from 45 to 180 mg/cm$^2$ and the electrolytes used have been cesium carbonate (1, 2), sulfuric acid (3), phosphoric acid (4-6), hydrofluoric acid (7, 8), and cesium fluoride-hydrofluoric acid mixtures (7-9). The temperatures used in these investigations have ranged from 100° to 200°C. The normal saturated hydrocarbons which yielded the highest current densities were ethane, propane, and butane (2, 3, 5, 7, 10); consequently, most of the work has been done with them.

Even though acceptable performances have been obtained with the systems mentioned above, it has not been economically interesting to attempt the construction of practical power sources, largely because of the high cost of the large amounts of platinum necessary to obtain reasonable power densities. The next logical step after proving operational feasibility was to attempt to improve the economics of the system by reducing the amount of platinum required. Several approaches can be taken toward this goal:

1. Make more effective use of the platinum by preparing higher area blacks.
2. Prepare very high-area platinum on a support which can act as a current collector and perhaps also as an enhancement to the platinum activity.
3. Alloy the platinum with other metals in such a way that more activity per unit weight of platinum is obtained.
4. Replace the platinum with a less costly, but effective, electrocatalyst.

The first method listed above has not previously met with a great deal of success because platinum black with a specific surface area significantly above 15 m$^2$/g sinters under conditions of electrode preparation and may sinter with use at the higher fuel cell operating temperatures, resulting in a fairly rapid loss of area. The fourth method is generally considered the most difficult due to the multiple requirements placed on any successful electrocatalyst, not the least of which is excellent corrosion resistance to hot acids. The present work is concerned with approaches 1 and 2 above.

[1] Present address: Argonne National Laboratory, Argonne, Illinois.

[2] Present address: General Electric Company Major Appliances Division, Louisville, Kentucky.

## Experimental

*Electrolyte.*—The electrolyte chosen for this work was the maximum-boiling HF-$H_2O$ azeotrope, containing approximately 36 m/o hydrofluoric acid which boils at approximately 112°C (7, 8, 11). This electrolyte has several advantages:

1. Because it is an azeotrope, its composition can be considered essentially uniform with time and position in the system.
2. It can support high current densities at a moderate temperature, allowing a wider range of current densities to be studied, thus simplifying the analysis of results.
3. It has provided for smooth, continuous operation with no cycling of the cell potential or current with any fuel under any of the test conditions.
4. It has fluid properties similar to those of water, so pumping and flow are not a problem.

The electrolyte was prepared from Baker and Adamson reagent grade 48 w/o (weight per cent) hydrofluoric acid having less than 20 ppm impurities, and from quartz-redistilled water. The temperature of operation was 105°C. This is near the maximum operational temperature attainable with this electrolyte at atmospheric pressure, and its selection is consistent with carbon deposition considerations (12, 13) and previously observed performance-temperature relationships (8). Under these conditions, the electrolyte has a resistivity of 1.8 ohm-cm (11).

*Apparatus.*—All portions of the apparatus which contacted the electrolyte were fabricated of Teflon in order to prevent any contamination of the electrolyte. The cell parts are shown in Fig. 1. The gas compartments were circular, 3 mm deep, and had an area

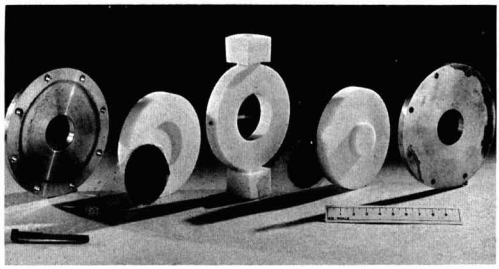

Fig. 1. Photograph of cell parts

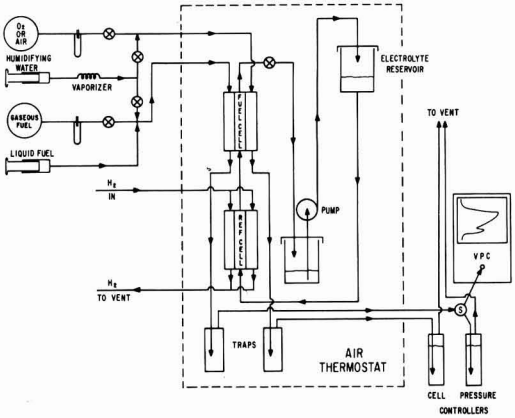


**Fig. 2. Schematic diagram of fuel cell apparatus**

of 11.38 cm². The electrolyte compartment had identical dimensions. The cell parts were assembled with electrodes as shown in Fig. 1. The assembly was held rigid by the Monel end plates and bolts.

A schematic diagram of the entire apparatus is shown in Fig. 2. This apparatus is similar to that discussed in ref. (2), (7), and (8). The fuel cell and an identical reference cell were operated in a forced-convection air thermostat maintained at 105°C. The reference cell contained two high-area reversible hydrogen reference electrodes of Teflon-bonded platinum black. Gaseous fuel and oxidant flows were controlled with needle valves and were monitored using capillary-tube flowmeters. The liquid fuel flow rate was set by use of a constant-speed (0.01%) syringe drive. The injection of humidifying water into either the fuel or oxidant stream was provided for, but this was not required with the azeotropic electrolyte. The exit gas streams from both cells passed through traps (which separated any liquid present) and then to water bubblers before venting. The exit fuel stream could be sampled and analyzed by a vapor-phase chromatograph as desired.

The electrolyte was circulated by gravity from an upper reservoir, passing upward through the reference cell and fuel cell at a flow rate of 2 or 3 cell volumes per minute. The effluent from the upper cell passed into a standpipe to eliminate any syphon action and was collected in a lower basin from which it was pumped to the upper reservoir by means of an all-Teflon microbellows pump. The electrolyte flow rate was controlled by varying the amount of head supplied by the upper reservoir.

*Electrodes.*—The electrodes were of the Teflon-bonded variety; 45 mesh platinum screen was used both for support and as a current collector. A porous Teflon wetproofing film was incorporated on the gas side of the electrodes. These electrodes were similar in structure to those originally reported by Niedrach and Alford (14), although the preparation techniques were sometimes different, as dictated by the physical properties and behavior of the electrocatalyst materials. When the platinum present in the electrode was in an oxidized rather than an elemental form, the removal of the aluminum foil used as a backing material during the fabrication was done electrochemically. The premature reduction of the catalyst to elemental platinum by the hydrogen generated during the chemical stripping processes was prevented by maintaining the electrode at a potential higher than that required for oxygen evolution. The hydrogen formed during the electrochemical reaction was evolved from a counter electrode sufficiently removed from the test electrode to prevent the hydrogen from diffusing back to the test electrode through the solution. The oxidized platinum present in the test electrode was subsequently reduced under carefully controlled conditions before testing in the fuel cell. This reduction was usually accomplished *in situ* by electrochemical and/or chemical methods.

*Electrocatalysts.*—Several electrocatalysts were tested, falling into two main categories: unsupported and supported.

The unsupported commercial electrocatalysts tested were platinum, palladium, iridium, and rhodium. The two remaining platinoid elements were not tested for the following reasons: ruthenium is corrosively attacked by the hot hydrofluoric acid electrolyte and osmium forms dangerous volatile oxides under the conditions of electrode preparation. All of the unsupported electrocatalysts were tested in the form of commercial blacks which were prepared by reduction from aqueous solution. The platinum black had a specific area of about 20 m²/g; the palladium, iridium, and rhodium blacks had lower specific areas. Platinum was also tested by subjecting Adams catalyst ($PtO_2 \cdot H_2O$) to the previously mentioned *in situ* reduction procedures which result in a high-area platinum black. Adams catalyst from two sources was tested: commercial Adams catalyst, and some freshly prepared by the authors and denoted as $PtO_2$-Preparation A. The Adams catalyst was prepared by the usual procedure involving the oxidation of a platinum salt in a fused sodium nitrate bath (15-21).

Carbon is one of the few inexpensive materials which show excellent resistance to hot acidic electrolytes and is electronically conducting. Many types of carbon power are available, covering a wide range of physical properties. Not all of these powders, however, are compatible with the techniques used in the preparation of Teflon-bonded electrodes. The selection of the candidate substrates is limited to those powders which can be fabricated into useful electrode structures. The carbon powders with low specific areas (10-50 m²/g) and particle sizes in the range 0.1-10$\mu$ have usually been employed with the most success. The one which most consistently yielded useful electrodes is a byproduct of the production of calcium cyanamid from calcium carbide. This carbon powder was obtained from the American Cyanamid Company and its properties are given in Table I (22).

Various carbon-supported electrocatalysts were prepared and evaluated. The carbon powder described in Table I was used as the substrate in every case. These electrocatalysts were prepared by various methods involving the deposition of a platinum salt from an aqueous solution onto the carbon surface. This deposition was followed either by room-temperature hydrogen reduction to elemental platinum (preparation 10) or by roasting in air to prepare an oxidized form of platinum on the carbon surface (preparations 20 and 21). When the oxidized form of platinum was present, the electrocatalyst was subjected to the previously mentioned *in situ* reduction process prior to testing.

Several commercially available carbon-supported electrocatalysts were also evaluated. Specific information concerning their preparation is proprietary and therefore was not available to the authors, but they were prepared by a variety of techniques involving the deposition of platinum black or a platinum salt on the surface of a carbon powder followed by reduction, as necessary.

**Table 1. Properties of carbon powder (22)**

| | |
|---|---|
| Purity | 99% |
| Impurities | $SiO_2$, CaO, $Fe_2O_3$, $Al_2O_3$ |
| Particle diameter | 0.25-2.0$\mu$ |
| Specific surface area | 11.4 m²/g |
| Resistivity @ 2000 psi | 0.02 ohm-cm |
| Bulk density @ 2000 psi | 1.28 g/cm³ |
| Porosity @ 2000 psi | 40% |
| Structure | graphite |

*Fuels and oxidant.*—Propane was chosen as the gaseous hydrocarbon fuel of primary interest and n-octane (bp = 125.7°C) was considered to be representative of the liquid hydrocarbon fuels. Matheson instrument-grade propane, 99.5 m/o minimum purity, and Philips research grade n-octane, 99.85 m/o minimum purity, were used. Other fuels tested were: Matheson ultra-high-purity methane, 99.95 m/o minimum purity; Matheson C.P. ethane, 99.0 m/o minimum purity; Matheson instrument grade n-butane, 99.5 m/o minimum purity; Phillips research grade n-pentane, 99.84 m/o minimum purity; Phillips research grade n-hexane, 99.85 m/o minimum purity; Phillips research grade n-decane, 99.49 m/o minimum purity.

The oxidant in every case reported was electrolytic grade oxygen, 99.6 m/o minimum purity.

*Electrical measurements.*—Electrical measurements were carried out using a 60 Hz modified Kordesch-Marko interrupter circuit (23, 24). The application of the 60 Hz interrupting frequency has been shown to have a limitation when rapid electrochemical reactions take place on electrodes containing only small amounts of active catalyst (25). The recovery of the cell potential during the period of interruption was checked using an oscilloscope to view the cell potential as a function of time during the operation of the interrupter. With an anode containing 8 mg Pt/cm² as a carbon-supported platinum electrocatalyst, the cell potential recovered about 5 mv at a current of 455 ma (40 ma/cm²) when propane was used as the fuel. A high-loading (52 mg Pt/cm²) platinum black cathode was used at all times, so this 5 mv recovery of the cell potential only reflected processes occurring at the low-loading anode used. This amounted to an error of less than 2%, within the limits of reproducibility of the results, so no correction was made.

The interrupter circuit yielded potential readings on a resistance-free basis and all results are reported on this basis unless otherwise specified. The potentials of the individual electrodes are reported with respect to a reversible hydrogen reference electrode in the same electrolyte at the same temperature. The current-potential data were taken at steady state (usually about 5 min after a change in current) and in the order of increasing current, starting at open circuit. No hysteresis effect was observed with decreasing current, except at low currents (less than 25 ma).

Resistance-included cell voltages ($E_{cell}$) can be estimated from the reported resistance-free ($E_{a\text{-}c}$) values using the expression

$$E_{cell} = E_{a\text{-}c} - i\rho l \qquad [1]$$

where $i$ is the current density; $\rho$ is the specific resistance of the electrolyte, 1.8 ohm-cm; and $l$ is the interelectrode distance, 0.3 cm. This is only an estimate since it does not consider the (small) resistance of the electrodes.

## Results and Discussion

*Unsupported electrocatalysts.*—The evaluation of commercially available platinoid element blacks was undertaken as a preliminary electrocatalyst survey. Emphasis was directed toward improving the specific activity of platinum when it became apparent that it was at least an order of magnitude better than the other three platinoid element blacks tested. This observation was not unexpected and is consistent with the results of other investigators (26, 27).

The sintering of high-area platinum black to a lower surface area under the conditions of electrode fabrication is one of the major problems obstructing the preparation of high-activity platinum electrodes. It was hoped that this problem could be avoided by starting with a more stable, highly oxidized form of platinum and reducing it to its elemental form after the electrode was prepared. Adams catalyst ($PtO_2 \cdot H_2O$) was selected as the starting material. An *in situ* reduction technique was then developed to accomplish the desired purpose. Initial successes prompted attempts to prepare a more optimal starting material and $PtO_2$-Preparation A was synthesized. A direct comparison of the propane performance in hydrofluoric acid at 105°C using the three most active unsupported electrocatalysts (Pt black, $PtO_2$-Commercial, and $PtO_2$-Preparation A) is shown in Fig. 3, where a loading of 25 mg Pt/cm² was used in each anode. It is evident that reduced $PtO_2$ is a much more active material than platinum black and the $PtO_2$-Preparation A electrode gave a cell performance (resistance-free) of about 150 ma/cm² at an anode *vs.* cathode potential of 0.4v. This was in contrast to 104 ma/cm² for commercial $PtO_2$ and 40 ma/cm² for platinum black. These anode *vs.* cathode potentials were calculated by determining the difference between the observed anode *vs.* reference potential and the cathode *vs.* reference potential obtained with a "standard" oxygen cathode (52 mg Pt black/cm²) at the same current density. This standard oxygen cathode performance was determined by averaging about 15 representative cathode current density-voltage curves; this allowed cell-performance comparisons on the basis of anode performance only. The anode *vs.* cathode potentials for all the cells reported here were determined in a similar manner.

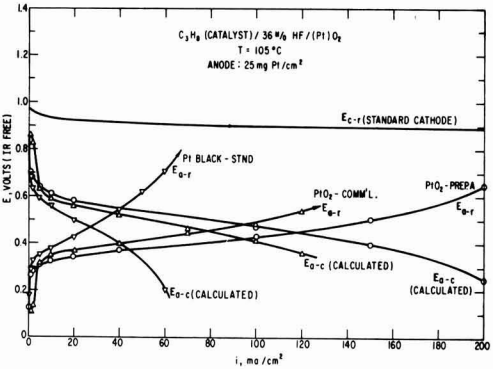


**Fig. 3. Comparison of propane performance on the three most active unsupported electrocatalysts.**

The propane performances with platinum black and reduced commercial Adams catalyst were determined at several levels of catalyst loading to evaluate the effect of catalyst loading on the specific performance (expressed as ma/mg Pt at an anode *vs.* reference potential of 0.5v). Figure 4 shows the results using

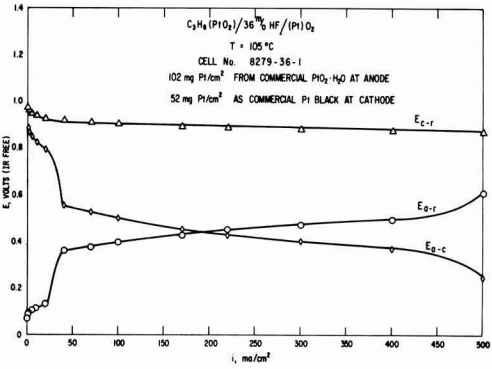


**Fig. 4. Propane anode performance on reduced commercial $PtO_2$**

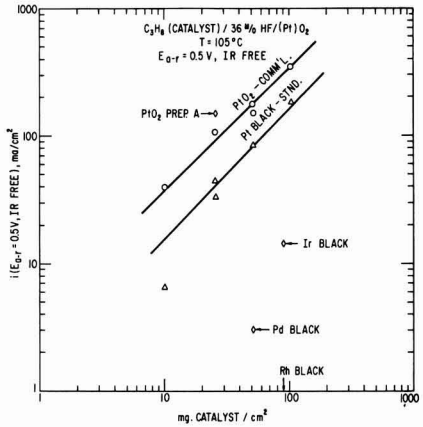


**Fig. 5. Summary of the performance of propane on various unsupported electrocatalysts as a function of catalyst loading.**

a high-loading anode containing 102 mg Pt/cm² reduced from commercial Adams catalyst. This cell had a limiting current density greater than 500 ma/cm², and a peak power point of about 140 mw/cm². The high platinum loading in this electrode is economically uninteresting, but the data do prove that very high levels of performance are possible with direct hydrocarbon fuel cells at 105°C using propane as the fuel.

All the results for the investigation of the unsupported electrocatalysts are presented in Fig. 5 in terms of the current density obtained with propane at an anode *vs.* reference potential of 0.5v as a function of platinoid element catalyst loading. Note that the data for commercial Adams catalyst and $PtO_2$-Preparation A fall above the data for commercial platinum black, indicating that these materials have higher specific activities than commercial platinum black, while the data for the other platinoid element blacks fall more than an order of magnitude below the platinum black data. It is also of interest that the data for commercial Adams catalyst and platinum black can be correlated with straight lines having a slope of nearly unity. Straight lines having a unit slope indicate that there is a direct proportionality between catalyst loading and current density. In other words, the specific activity of each of these electrocatalysts remained constant at loadings differing by an order of magnitude (10-100 mg Pt/cm²).

This invariance of the specific performance of an electrocatalyst allows all data to be related to a datum level of performance for ease of comparison. Commercial platinum black was chosen to represent this datum. A so-called "Effectiveness Ratio" was defined as the ratio of the specific performance observed with a given electrocatalyst to the specific performance observed with platinum black, both measured at the same anode *vs.* reference potential, that is

$$\text{Effectiveness Ratio} = \frac{\text{ma/mg catalyst}}{\text{ma/mg Pt black}}, \quad (E_{a\text{-}r} = \text{constant}) \qquad [2]$$

Table II presents this effectiveness ratio along with the data presented in Fig. 5, showing the comparison of propane performance using unsupported electrocatalysts at 105°C in hydrofluoric acid at an anode *vs.* reference potential of 0.5v (resistance-free). The value of the effectiveness ratio in Table II is an indication of the position (relative to platinum black) of a datum point on the current density scale of Fig. 5. As an example, a platinum electrode prepared by reducing $PtO_2$-Preparation A gave 3.5 times the current observed with a commercial platinum black electrode

**Table II. Comparison of unsupported electrocatalysts**

$C_3H_8$ (catalyst)/36 m/o HF/(Pt)$O_2$
T = 105°C
$E_{a-r}$ = 0.5v (IR free)

| Catalyst | Catalyst* loading, mg catalyst/cm² | Current density, ma/cm² | Specific current, ma/mg catalyst | Effectiveness ratio |
|---|---|---|---|---|
| Pt black | 52 | 83.0 | 1.602 | 1.00 |
| Pd black | 52 | 3.0 | 0.0579 | 0.036 |
| Ir black | 90 | 14.2 | 0.158 | 0.098 |
| Rh black | 90 | 0.34 | 0.00378 | 0.0024 |
| $PtO_2$ | 52 | 175.0 | 3.38 | 2.1 |
| $PtO_2$-Prep. A | 26 | 149.0 | 5.60 | 3.5 |

* This represents the catalyst content after reduction.

at the same loading. This is verified by Fig. 3, where performance data are presented for this particular case.

The effectiveness ratio allows the direct comparison of data obtained with considerably different catalyst loadings and becomes considerably more useful when the supported electrocatalysts are considered.

*Carbon-supported electrocatalysts.*—Supported electrocatalysts are of interest because the small crystallites which can be obtained by use of supports should make a higher percentage of the platinum available at the surface and thus allow a higher specific area electrocatalyst to be prepared. Supported electrocatalysts also should be less susceptible to sintering because the active crystallites can be widely dispersed on the support surface.

The success of the high-activity platinum black prepared from $PtO_2$ prompted attempts to combine the expected enhancement produced by supporting the platinum on a substrate with the avoidance of sintering during electrode fabrication by starting with a highly oxidized platinum compound. This thought led to the development of Pt/C-Preparations 20 and 21. The propane performances with Pt/C-Preparation 20 and two commercially prepared carbon-supported electrocatalysts are shown in Fig. 6. The catalyst loadings are comparable, but not equal (4.7-7.1 mg Pt/cm²). The improvement of performance obtained with Pt/C-Preparation 20 is appreciable.

The results from all the electrocatalysts tested are presented in Fig. 7 in terms of the current density obtained with propane at an anode *vs.* reference potential of 0.5v, as a function of the platinoid element catalyst loading. The data for unsupported electrocatalysts previously presented in Fig. 5 are included as closed points for purposes of comparison, while the carbon-supported platinum electrocatalysts are shown as open points. Electrocatalyst Preparations 20 and 21 and Commercial Catalyst 4 show consider-

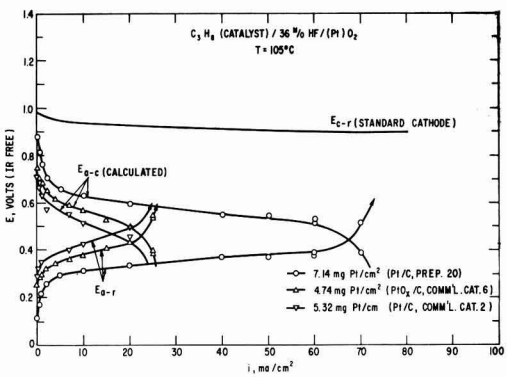


**Fig. 6. Comparison of propane performance on three representative carbon-supported electrocatalysts.**

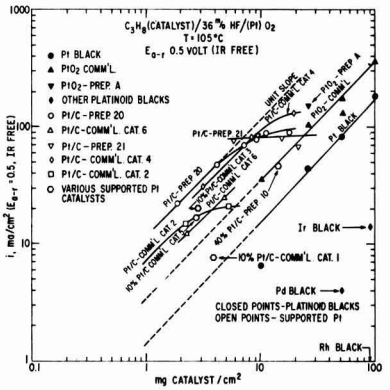


**Fig. 7. Summary of the performance of propane on all the electrocatalysts tested as a function of catalyst loading.**

ably higher specific activities than all the other electrocatalysts tested, but tend to deviate from a line of unit slope at the higher catalyst loadings, indicating a decrease in their specific activities. This loss of specific activity is also reflected by the reduction of the effectiveness ratios for propane performance with the carbon-supported platinum electrocatalysts at an anode *vs.* reference potential of 0.4v presented in Table III. This lower anode *vs.* reference potential is useful when comparing the carbon-supported platinum electrocatalysts because they operate at a higher voltage efficiency (28), and are approaching a maximum current condition at an anode *vs.* reference potential of 0.5v, as evidenced by the current density-voltage data presented in Fig. 6. The decrease in the specific activity of the carbon-supported electrocatalysts at high loadings should be alleviated by using substrates having higher specific surface areas. What should be noted is that effectiveness ratios near 10 have been obtained, indicating that a full order of magnitude improvement over the performance observed with commercial platinum black can be attained with these new carbon-supported platinum electrocatalysts. This means that a propane-oxygen fuel cell using 10 mg Pt/cm² at the anode as a carbon-supported electrocatalyst can deliver about 35 mw/cm²

**Table III. Comparison of supported electrocatalysts**

$C_3H_8$ (catalyst)/36 m/o HF/(Pt)$O_2$
$T$ = 105°C
$E_{a-r}$ = 0.4v (IR free)

| Catalyst | Catalyst Pt content, w/o | Catalyst loading, mg Pt/cm² | Current density, ma/cm² | Specific current, ma/mg Pt | Effectiveness* ratio |
|---|---|---|---|---|---|
| Pt/C—Prep. 10 | 40 | 14.0 | 18.6 | 1.31 | 1.6 |
| Pt/C—Prep. 20 | 7 | 1.9 | 9.70 | 5.14 | 6.3 |
| | 14 | 4.1 | 33.0 | 8.03 | 9.9 |
| | 21 | 7.1 | 65.5 | 8.26 | 10.0 |
| | 28 | 9.2 | 48.5 | 5.27 | 6.5 |
| | 35 | 11.0 | 60.5 | 5.48 | 6.7 |
| | 42 | 18.0 | 64.0 | 3.62 | 4.4 |
| Pt/C—Prep. 21 | 20 | 5.8 | 41.0 | 7.11 | 8.8 |
| | 30 | 9.4 | 43.0 | 4.58 | 5.6 |
| | 40 | 15.0 | 56.5 | 3.72 | 4.6 |
| | 50 | 22.0 | 38.5 | 1.96 | 2.4 |
| Pt/C—Comm'l Cat. 1 | 10 | 3.9 | 1.22 | 0.313 | 0.38 |
| Pt/C—Comm'l Cat. 2 | 5 | 1.1 | 4.20 | 3.79 | 4.7 |
| | 10 | 2.2 | 7.17 | 3.29 | 4.0 |
| | 20 | 5.3 | 7.05 | 1.33 | 1.6 |
| Pt/C—Comm'l Cat. 3 | 10 | 2.8 | 15.0 | 5.30 | 6.5 |
| Pt/C—Comm'l Cat 4 | 10 | 3.2 | 15.0 | 4.76 | 5.8 |
| | 25 | 8.4 | 55.0 | 6.56 | 8.1 |
| | 50 | 19.0 | 70.0 | 3.60 | 4.4 |
| Pt/C—Comm'l Cat. 5 | 10 | 2.8 | 6.25 | 2.24 | 2.8 |
| Pt/C—Comm'l Cat. 6 | 8 | 2.3 | 6.20 | 2.74 | 3.4 |
| | 16 | 4.7 | 14.7 | 3.10 | 3.8 |
| *Pt black | 100 | 52.0 | 42.0 | 0.814 | 1.00 |

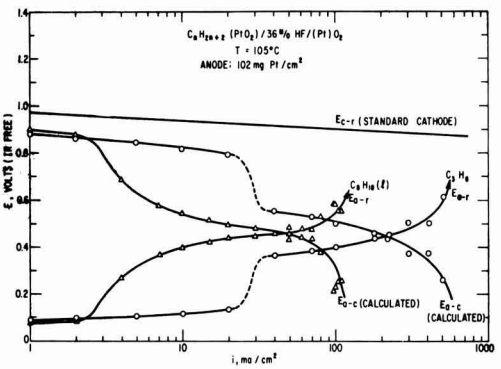


**Fig. 8. Propane and n-octane anode performance on reduced commercial $PtO_2$.**

(resistance-free) at 105°C using hydrofluoric acid as the electrolyte.

*Other fuels.*—A comparison of the performance of gaseous propane and liquid n-octane on reduced commercial $PtO_2$ is shown in Fig. 8. The propane data presented in this figure are the same as those presented in Fig. 4, and the anode catalyst loading is the same 102 mg Pt/cm². The maximum current density obtained with n-octane was about 120 ma/cm². The ratio of the performances for propane and n-octane shown in this figure is about the same as that reported earlier for platinum black (7). These data again demonstrate, as did Fig. 4, that high levels of performance can be obtained with direct hydrocarbon fuel cells at moderate temperatures, even when liquid hydrocarbons are used as the fuel.

The specific performances of several gaseous and liquid normal saturated hydrocarbon fuels (expressed as ma/mg Pt at an anode *vs.* reference potential of 0.5v, resistance-free) on commercial platinum black, reduced commercial $PtO_2$ and a commercial carbon-supported platinum are summarized in Fig. 9. The data presented for commercial platinum black in this

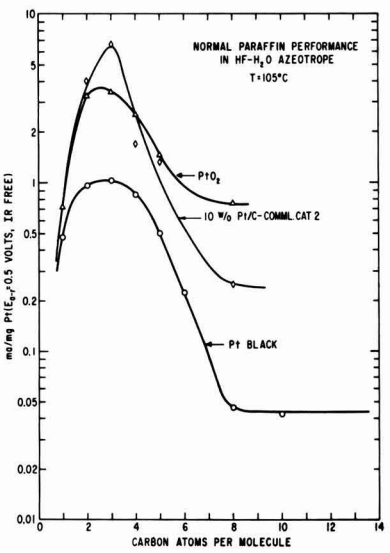


**Fig. 9. Effect of molecular weight of normal saturated hydrocarbon fuels on specific performance at the anode. Platinum loadings were 52 mg commercial platinum black/cm²; 102 mg platinum (reduced from commercial $PtO_2 \cdot H_2O$)/cm²; 2.2 mg platinum/cm² as 10 w/o Pt/C, commercial catalyst 2.**

figure are not the best performances observed at this catalyst loading (improvements in the electrode structure have allowed better performances to be achieved), but this was the only single electrode for which all the desired data were available. Ethane and propane give slightly higher current densities than butane, which gives higher current densities than the other hydrocarbons. Comparing the standard platinum black with the other two catalysts shows than an improved utilization of the platinum catalyst has been achieved with $PtO_2$ and Pt/C for all the hydrocarbon fuels tested.

In contrast to other strong-acid electrolytes (3, 29, 30) no cycling of the cell potential or current has been observed when using the hydrofluoric acid electrolyte with any fuel under any of the test conditions. This observation has previously been reported in connection with high-loading platinum black electrodes (7). The present work extends this observation to include other electrocatalysts, including low-loading carbon-supported platinum.

## Conclusions

1. Both the use of higher activity forms of unsupported platinum, particularly the one reduced from Adams catalyst, and the use of carbon-supported platinum electrocatalysts are effective in reducing the amount of platinum required for a given amount of power from a direct hydrocarbon fuel cell.

2. Carbon-supported platinum electrocatalysts are effective in reducing the amount of platinum required for a given propane performance by about a factor of 10. Further improvements are likely.

3. A propane-oxygen fuel cell using 10 mg $Pt/cm^2$ as carbon-supported platinum at the anode can deliver about 35 $mw/cm^2$ (resistance-free) using a 36 m/o hydrofluoric acid electrolyte at 105°C.

4. No cycling of the cell current or potential has been observed with any saturated hydrocarbon fuel under any conditions when using the hydrofluoric acid electrolyte.

## Acknowledgments

The authors wish to thank Dr. W. T. Grubb for information concerning deposition of platinum salts and Messrs. D. J. Surd and G. J. Holm for assistance in performing some of the experiments. Helpful discussions were provided by Dr. E. L. Simons and Dr. J. L. Holman. Mr. L. D. Sangermano, of the General Electric Company, Direct Energy Conversion Operation, supplied some of the Teflon binder used in these experiments.

This work is a part of the program under contracts DA-44-009-AMC-479(T) and DA-44-009-ENG-4909, ARPA Order No. 247 with the U. S. Army Engineer Research and Development Laboratories, Ft. Belvoir, Virginia, to develop a technology which will facilitate the design and fabrication of practical military fuel cell power plants for operation on ambient air and hydrocarbon fuels.

Manuscript received May 23, 1967.

Any discussion of this paper will appear in a Discussion Section to be published in the June 1968 JOURNAL.

## REFERENCES

1. E. D. Cairns and D. I. Macdonald, *Electrochem. Tech.*, **2**, 65 (1964).
2. E. J. Cairns and G. J. Holm, Paper presented at the Washington, D. C., Meeting of the Society, Oct. 1964, Abstract No. 30; see also Extended Abstracts, Battery Div., **9**, 75 (1964).
3. H. Binder, A. Köhling, H. Krupp, K. Richter, and G. Sandstede, *This Journal*, **112**, 355 (1965).
4. W. T. Grubb and L. W. Niedrach, *ibid.*, **110**, 1086 (1963).
5. R. Jasinski, J. Huff, S. Tomter, and L. Swette, *Ber.*, **68**, 400 (1964).
6. H. G. Oswin, A. J. Hartner, and F. Malaspina, *Nature*, **200**, 256 (1963).
7. E. J. Cairns, *This Journal*, **113**, 1200 (1966).
8. E. J. Cairns, Paper presented at the Atlantic City Meeting of the American Chemical Soc., Sept., 1965, Abstract No. 31L; see also "Hydrocarbon Fuel Cell Technology," B. S. Baker, Editor, Academic Press, New York (1965).
9. E. J. Cairns, *Nature*, **210**, 161 (1966).
10. W. T. Grubb and C. J. Michalske, Proc. 18th Ann. Power Sources Conf., Atlantic City (May 1964).
11. E. J. Cairns, *Electrochem. Tech.*, **5**, 4 (1967).
12. E. J. Cairns, A. D. Tevebaugh, and G. J. Holm, *This Journal*, **110**, 1025 (1963).
13. E. J. Cairns and A. D. Tevebaugh, *J. Chem. Eng. Data*, **9**, 453 (1964).
14. L. W. Niedrach and H. R. Alford, *This Journal*, **112**, 117 (165).
15. R. Adams, V. Voorhees, and R. L. Shriner, "Organic Synthesis," Col. Vol. I, John Wiley & Sons, Inc., New York (1932).
16. V. Voorhees and R. Adams, *J. Am. Chem. Soc.*, **44**, 1397 (1922).
17. R. Adams and R. S. Shriner, *ibid.*, **45**, 2171 (1923).
18. A. H. Cook and R. P. Linstead, *J. Chem. Soc.*, **1934**, 946
19. W. F. Bruce, *J. Am. Chem. Soc.*, **58**, 687 (1936).
20. V. L. Frampton, J. D. Edwards, and H. R. Henze, *ibid.*, **73** 4432 (1950).
21. C. W. Keenan, B. W. Gisemann, and H. A. Smith, *ibid.*, **76**, 229 (1953).
22. R. G. Haldeman, W. P. Colman, S. H. Langer, and W. A. Barber, in "Fuel Cell Systems," p.113, R. F. Gould, Editor, Adv. in Chem. Series No. 47, Amer. Chem. Soc., Washington, D. C. (1965).
23. K. Kordesch and A. Marko, *This Journal*, **107**, 480 (1960).
24. E. J. Cairns and A. D. Tevebaugh, Saturated Hydrocarbon Fuel Cell Program, Technical Summary Report No. 3, Part I, Task IV, Jan. 1-June 30, 1963, Contract No. DA-44-009-ENG-4909, ARPA Order No. 247, U.S.A.E.R.D.L.
25. L. W. Niedrach and M. Tochner, *Electrochem. Tech.*, **5**, 270 (1967).
26. W. T. Grubb, *Nature*, submitted.
27. J. O'M. Bockris and S. Srinivasan, Proc. 19th Ann. Power Sources Conf., Atlantic City (May, 1965).
28. E. J. Cairns and D. C. Bartosik, *Electrochem. Tech.*, **111**, 1205 (1964).
29. R. P. Hamlen and E. J. Szymalak, *ibid.*, **4**, 172 (1966).
30. E. R. White and H. J. R. Maget, Proc. 19th Ann. Power Sources Conf., Atlantic City (May, 1965).

# Complex Scale Formation on an Iron-18% Chromium Alloy

**D. P. Whittle and G. C. Wood**

*Corrosion Science Division, Department of Chemical Engineering, University of Manchester Institute of Science and Technology, Manchester, England*

ABSTRACT

The oxidation of a pure Fe-18.0% Cr alloy in oxygen at 1 atm pressure in the temperature range 800°-1200°C has been studied using thermogravimetry, metallography, and electron probe microanalysis. Chromium oxide, containing minor amounts of dissolved iron, is the only oxide formed at 800° and 1000°C. This oxide is also formed initially at 1200°C, but its subsequent mechanical failure permits rapid oxidation of the underlying chromium-depleted alloy. Three types of scale formation are found in this second oxidation stage on different regions of the specimen surface. Each of these types of scale contains alternate layers of chromium-rich and iron-rich oxides. Two of the scale types are eventually healed by formation of a basal $Cr_2O_3$-rich layer; the third, occurring at the edges of the specimens, grows unimpeded. The mechanism of formation of these stratified scales and, where relevant, their subsequent healing, is explained by a theory involving the variation of the mobilities of $Fe^{3+}$, $Fe^{2+}$, and $Cr^{3+}$ ions with composition in the spinel, $FeFe_{(2-x)}Cr_{(x)}O_4$, $(O \leq x \leq 2)$.

When chromium-rich iron-chromium alloys are oxidized in oxygen in the range 800°-1200°C, they form almost pure chromium oxide (1, 2) (subsequently designated $Cr_2O_3$ because it contains only minor quantities of dissolved iron). More dilute alloys containing 14-25% Cr also form this oxide under all but the severest conditions (1, 3, 4), when failure of the $Cr_2O_3$ scale allows thick stratified scale to develop. The mechanism of protective scale failure, proposed earlier (1-5), is substantiated here.

The nature of the stratified scales formed on the second class of alloys depends on the surface chromium content of the alloy when it is exposed by the protective scale failure. This critical dependence is exemplified in the present paper by the scales on Fe-18% Cr which vary according to their location around the specimen surface. Generally this type of variation (4) is expected where the bulk alloy chromium content is close to the border-line between protective and nonprotective behavior; in more dilute alloys the situation is not as critical (2, 3), and only one type of stratified scale is produced. Also, with the more dilute alloys, breakthrough and stratified scale growth are disastrous, and complete destruction of the specimen occurs, whereas with the 18% Cr alloy some self-healing of the scale is observed.

## Experimental

The Fe-18.0 w/o Cr alloy was made from a base of special Swedish iron and pure chromium by vacuum melting, and subsequent hot and cold rolling to strip 0.040 cm thick (1). The impurity content of a similar alloy of the same batch was: C 0.017, N 0.023, S 0.014, P 0.002, Mn 0.02, Si 0.08, O 0.023, Al 0.04, Ni 0.01, Sn <0.002, Nb <0.006, W <0.05, Ti <0.04, Cu <0.01, Mo <0.005, V <0.004, B <0.0015 w/o.

Specimens 2.5 x 0.5 x 0.040 cm were annealed *in vacuo* ($10^{-5}$ Torr) for 5 hr at 1000°C in order to remove any residual stresses in the alloy and to give a starting material of approximately constant grain size. Immediately prior to oxidation, specimens were individually electropolished for a total time of approximately 3 min in a mixture of glacial acetic acid and perchloric acid (sp gr 1.72) in the ratio 20 parts to 1 by volume. During polishing the current density was maintained in the range 0.4-0.8 amp $cm^{-2}$ and the electrolyte cooled to 15°C. Specimens were then given a minimum cathodic etch at 10 $\mu$a $cm^{-2}$ for 90 sec in 4*N* HCl producing a slightly etched but "clean" surface.

After a standard time of 30 min the prepared coupon was rapidly located in the hot zone of a previously heated silica spring thermobalance (sensitivity ± 0.05 mg $cm^{-2}$) containing slowly flowing dry oxygen ($O_2$ 99.5%, A 0.5%, $CO_2$ 5 ppm, $H_2$ 50 ppm, hydrocarbons 10 ppm, $N_2$ trace, CO nil, $H_2O$ < 0.15 $g^{-3}$). Loss of a volatile chromium oxide species [probably $CrO_3$ (6)] from the oxidizing sample was minimized by surrounding it with a $Cr_2O_3$-coated crucible. Weight gains were measured within several minutes of exposure and were continued for periods up to 50 hr. At the termination of the run the specimens were cooled to room temperature over a period of about 15 min.

The oxidized specimens were examined in plan by optical microscopy and also in cross section after standard metallographic preparation.

The prepared cross sections, made conducting by a thin carbon film, were also studied in a Cambridge Mark II "Microscan" microanalyzer at 29 kv. The results are presented as scanning x-ray images or as ultra slow-scanning line concentration profiles. The individual points on these traverses indicate where absorption and fluorescence corrections have been made, rather than the location of static probe measurements. The latter were occasionally used to check results. Distances marked on the abcissae scales are measured from the scale/atmosphere interface.

## Results and Interpretation

*Oxidation kinetics.*—The over-all oxidation behavior can be divided into three stages, as shown in Fig. 1 which gives the weight gain/time curves at 1200°C. These three stages are: (*a*) an initial protective stage, shown in detail in the inset of Fig. 1, (*b*) a period of very rapid, apparently linear, oxidation, and (c) a further period of slow protective oxidation.

(*a*) During this period at 1200°C there was generally good agreement between the weight gains of the various specimens and of the time taken to breakthrough, (typically 1 hr, although it varied between 45 min and 2 hr). The scale thickened at an approximately parabolic rate, the mean rate constant being 8 x $10^{-10}$ $g^2$ $cm^{-4}$ $sec^{-1}$. This is only slightly higher than that for alloys richer in chromium at this temperature (1, 2).

At 800° and 1000°C only this oxidation stage occurs, at least up to 50 hr. Growth occurs reproducibly with only a slight negative deviation from the parabolic law, as has been observed for alloys richer in chromium (1, 2). At 1000°C, the parabolic rate constant is 4.3 x $10^{-11}$ $g^2$ $cm^{-4}$ $sec^{-1}$ compared with 5.8 x $10^{-11}$ $g^2$ $cm^{-4}$ $sec^{-1}$ for an Fe-28% Cr alloy of similar purity (1, 2). Corresponding rate constants at 800°C are 1.0 x $10^{-12}$ and 4.7 x $10^{-12}$ $g^2$ $cm^{-4}$ $sec^{-1}$.

(*b*) The linear oxidation rate during the second

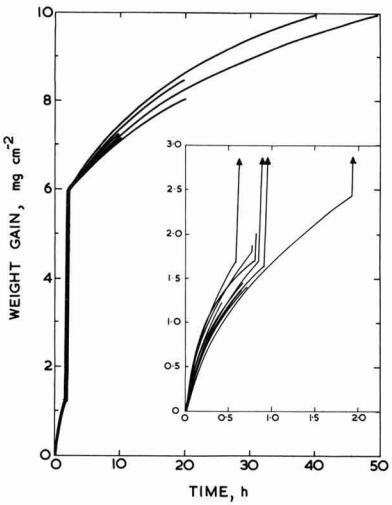


Fig. 1. Weight gain/time curves for the oxidation of Fe-18.0% Cr at 1200°C in oxygen.

stage was (5.1-6.5) x $10^{-6}$ g cm$^{-2}$ sec$^{-1}$, corresponding approximately to a rate of increase in scale thickness of 0.6 $\mu$m min$^{-1}$ which is considerably slower than the corresponding value for an Fe-14.0% Cr alloy (5 $\mu$m min$^{-1}$) (2). However, these rate constants carry very little meaning as they refer only to the very rapid localized nodular scale growth, as will be seen later. This stage of oxidation lasted in all cases until a weight gain of approximately 6.0 mg cm$^{-2}$ had been obtained, this probably being when the whole specimen surface had been subjected to rapid oxidation.

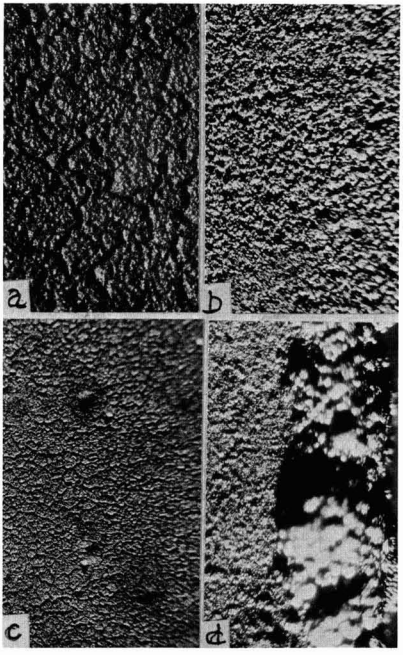


Fig. 2. Surface topography of scales formed on Fe-18.0% Cr; oblique illumination: a, 1 hr at 1000°C, magnification *ca.* 80X; b, 50 hr at 1000°C, magnification *ca.* 80X; c, 5 hr at 1200°C, magnification *ca.* 24X; d, 50 hr at 1200°C, magnification *ca.* 24X.

(*c*) During the final stage, the weight gain/time curves again apparently follow a parabolic law, with the parabolic rate constant slightly greater than that during the first stage. The absolute value of the rate constant is not important because the scale being formed shows marked differences around the specimen. However, metallographic examination shows later that a "healing" layer of $Cr_2O_3$ is growing over most of the surface, accounting for the similarity between the rate constant here and that during the first stage.

*Surface metallography.*—At 800° and 1000°C the superficial appearance of the scale was reasonably uniform except that the alloy grain boundaries were replicated in the scale, Fig. 2a. As oxidation proceeded, the scale surface became less angular in nature and the alloy grain boundaries were not observed, Fig. 2b; scales formed in the initial stages at 1200°C were similar. Occasionally, the scale formed at 1000°C showed nodular growths, Fig. 2c, approximately 50-80 $\mu$m in diameter and 10 $\mu$m high. This failure of the protective scale was always very localized and never showed any tendency to spread by disrupting adjacent areas of protective scale. Furthermore, nodular growth was always so slight at 1000°C as to be undetectable in the weight gain/time curves. At 1200°C, nodular growth was much more extensive and, once initiated, spread rapidly over the whole specimen. Generally, the scales at the edges of the specimen appeared much thicker than over the remainder of the surface and had a characteristic silvery appearance, Fig. 2d.

*Metallography in cross section and electron probe microanalysis.*—For ease of presentation this section is divided into three parts corresponding to the three stages noted in the oxidation kinetic curves at 1200°C.

*Initial protective oxidation stage.*—Only $Cr_2O_3$ was observed during this stage of the oxidation. However, the morphology of the scales formed at 800° and 1000°C was considerably different from that formed at 1200°C. At the lower temperatures, the $Cr_2O_3$ scale was a single layer and did not vary in thickness around the prepared cross section by more than about 30%. At 1200°C, the scale was highly irregular and contained many oxide balloons (Fig. 3). The extent to which the irregularities in the scale have been accentuated by the metallographic preparation and differential contraction between scale and alloy on cooling from the oxidation temperature is difficult to establish. The irregularity of the alloy/oxide interface is possibly indicative of scale lifting at temperature, but it is more likely to be due to plastic deformation of the alloy surface layers (7) by stresses in the specimen. In any event, the alloy/oxide interface was more rugged than that of other Fe-Cr alloys (27.4 and 59.5% Cr) when oxidized at this temperature (1, 2). Cracking at temperature of $Cr_2O_3$ scale lifted

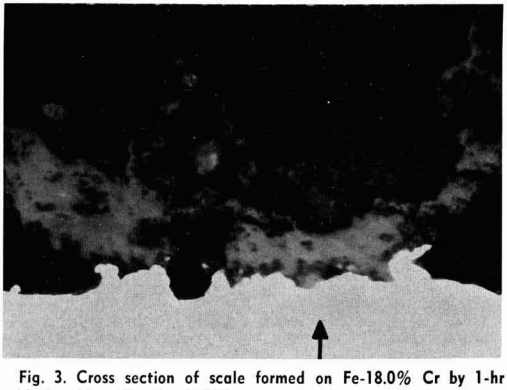

Fig. 3. Cross section of scale formed on Fe-18.0% Cr by 1-hr oxidation. Magnification 1000X.

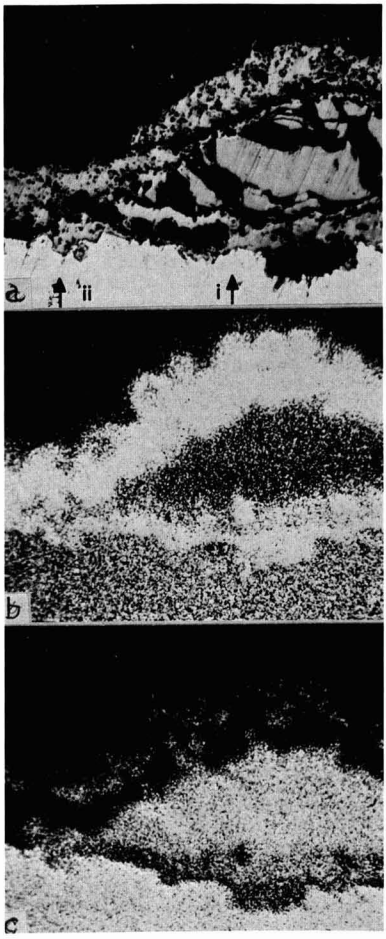


Fig. 4. Cross section of scale formed on Fe-18.0% Cr by 70-min oxidation at 1200°C: a, optical; b, KαCr image; c, KαFe image. Magnification *ca.* 400X.

from the alloy followed by re-formation of $Cr_2O_3$ is unlikely because the chromium concentration at the alloy/oxide interface is too low (5). Certainly the layered-type of $Cr_2O_3$ scales found on Fe-59.5% Cr oxidized at this temperature are absent (1, 2).

A typical electron probe microanalysis of a $Cr_2O_3$ scale formed after 50-hr oxidation at 1000°C gave 60.2% Cr and 1.5% Fe. These values can be normalized to a total metal content of 67.6% as most of the error is due to overlapping effects of the x-ray source in analyzing these thin films; normalized values are 65.9% Cr and 1.7% Fe. A similar analysis, 60.7% Cr and 1.1% Fe (normalized values 66.4% Cr and 1.2% Fe) was obtained for the scale formed for 1 hr at 1200°C.

The chromium concentration profile in the alloy, along the line shown in Fig. 3, indicates a relatively sharp decrease in chromium concentration near to the alloy/oxide interface down to a value of 9.5% Cr. Although not easily detectable in the microanalyzer the chromium-depleted zone should reach about 120 μm into the alloy because the alloy interdiffusion coefficient is relatively large (5).

*Linear oxidation stage.*—Generally, when the oxidation was terminated during this stage, there were areas of the specimen surface still covered by $Cr_2O_3$ and areas of fully developed stratified scale, described in the next section. As the linear oxidation stage proceeded, only the relative areas of the specimen surface covered by these two types of scale changed. The stratified scale must have grown extremely rapidly as it was very difficult to obtain examples of the scale at the start of its growth.

Figure 4a shows how the protective $Cr_2O_3$ separated away from the alloy surface and how stratified scale was formed beneath it. Other similar configurations of $Cr_2O_3$ and stratified scale are possible (1-4), but none shows the mechanism as clearly as Fig. 4a. The outer layer of $Cr_2O_3$ is visible over the whole field of view, Fig. 4b. At the left side of the micrograph, the $Cr_2O_3$ is adjacent to the alloy whereas over the remainder of the visible surface it is separated from the alloy by a mixed oxide nodule, Fig. 4b and 4c. The thickness of this outer $Cr_2O_3$ layer is independent of its position in the scale because it was formed during the first stage of oxidation. All the oxide layers are very porous, but this is largely connected with the poor metallographic preparation. The concentration profiles, Fig. 4d, across the line marked (i) in Fig. 4a confirm the general pattern of the elemental distribution shown in the x-ray images. The outer oxide is $Cr_2O_3$ as it contains 66.9% Cr and only 0.3% Fe. The remaining part of the scale is similar to the double layer scales observed on other alloys (1-3); an outer, almost pure iron oxide layer 30 μm thick, and inner, mixed layer containing undulating chromium and iron concentration profiles, also 30 μm thick. In order to identify these oxides completely, x-ray diffraction of the scales would be necessary. However, until a technique for microdiffraction becomes available, bulk analysis of scales stratified on such a fine scale is not very informative.

Traverses across lines such as (ii) in Fig. 4a show a simple $Cr_2O_3$ scale together with a chromium depletion in the underlying alloy.

*Third stage of oxidation.*—During this final stage, four general types of scale are found around the specimen cross sections: (i) over most of the specimen surface a stratified scale containing a chromium-rich layer at the alloy/oxide interface; (ii) a thicker stratified scale without the chromium-rich basal layer and usually confined to areas close to the specimen edges; (iii) a stratified scale intermediate between types (i) and (ii) also found near to specimen edges; and (iv) areas where the initial protective $Cr_2O_3$ scale still remained.

Figure 5a, together with its x-ray images 5b and c, shows a typical area where scales of type (i) and (iv) are adjacent. Clearly the thinner, protective oxide in these areas is $Cr_2O_3$ containing very little iron. The thicker, nodular oxide contains layers of chromium-rich and iron-rich oxides and is discussed more fully later.

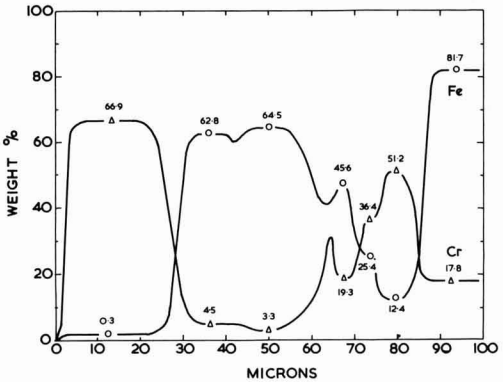


Fig. 4d. Concentration profiles along the line marked (i) in Fig. 4a.

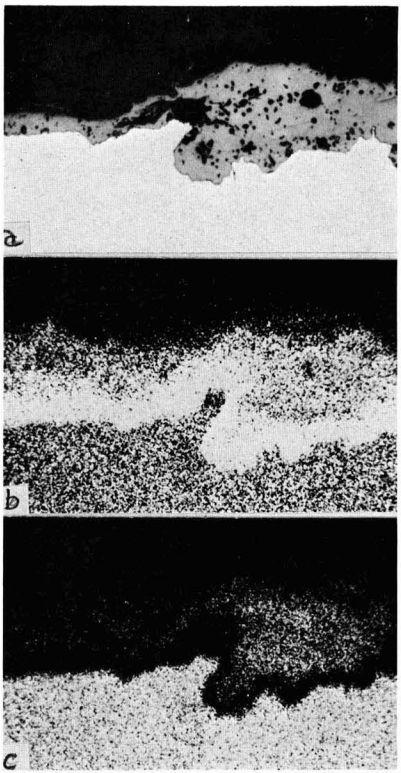


Fig. 5. Cross section of scale formed on Fe-18.0% Cr by 10-hr oxidation at 1200°C: a, optical, b, K$\alpha$Cr image; c, K$\alpha$Fe image. Magnification *ca.* 400X.

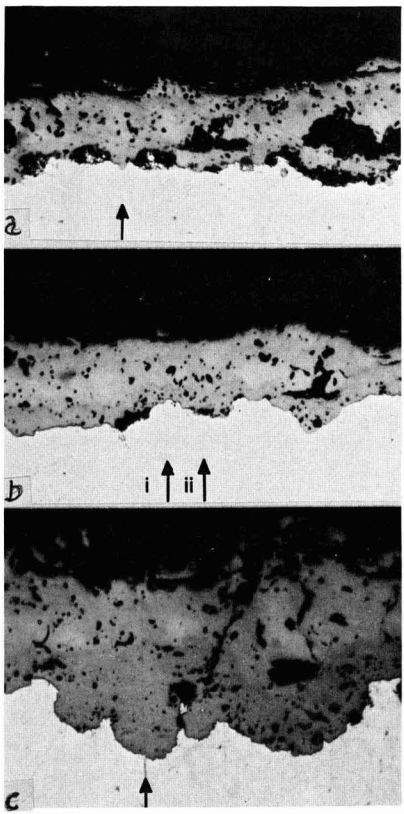


Fig. 6. Cross sections of scale formed on Fe-18.0% Cr by: a, 5-hr oxidation at 1200°C; b, 10-hr oxidation at 1200°C; c, 50-hr oxidation at 1200°C. Magnification *ca.* 400X.

Figure 6a, b, and c show the typical growth sequence of scales of type (i), these specimens having been oxidized for 5, 10, and 50 hr, respectively. The individual oxide layers are more easily distinguishable in the corresponding concentration profiles measured along the lines marked in Fig. 6a, b, and c and presented in Fig. 7a, b (i and ii) and c, respectively. Two traverses, (i) and (ii), are given in Fig. 7b corresponding to lines (i) and (ii) in Fig. 6b. In Fig. 7a two outer layers, not separable in the photomicrograph (Fig. 6a), are indicated, the outer one being richer in iron. Beneath these is an iron-rich, lighter-colored phase which does not form a continuous layer in the scale (Fig. 6a). The layer adjacent to the alloy/oxide interface is $Cr_2O_3$ and is approximately 3-4 $\mu$m thick. There is no internal oxide.

Scales of this type do not increase very greatly in thickness as oxidation proceeds. Figure 7b shows that all the increase in thickness after oxidation for 10 hr is associated with the thickening of the inner $Cr_2O_3$ layer, now 6-7 $\mu$m thick. The two traverses (i) and (ii) again show that the light-colored, iron-rich oxide does not form a continuous layer in the scale, being present in scan (i) but not in scan (ii). Furthermore, interdiffusion appears to have taken place between the two outer layers, although there is still an enrichment of iron at the scale/atmosphere interface.

After oxidation for 50 hr the inner $Cr_2O_3$ layer is about 30 $\mu$m thick (Fig. 6c). There is the expected distribution of iron and chromium across the scale (Fig. 7c) with interdiffusion between all the scale layers, except the innermost $Cr_2O_3$ layer, being well advanced. Again no internal oxide is present, although this is hardly surprising behind as stable an oxide as $Cr_2O_3$.

A typical scale of type (ii) which, as stated previously, occurs at the ends of the specimen cross sections, is presented in Fig. 8a. The darker colored oxide, typical of $Fe_3O_4$, is observed in these regions whereas it did not appear to be present in the other types of scales. Furthermore, this darker colored phase is surmounted by a lighter colored oxide, $Fe_2O_3$ while the inner scale is apparently porous. Reference to the x-ray images, Fig. 8b and c, indicates that there is no $Cr_2O_3$ layer at the base of this type of scale and as a result of this, the formation of internal oxide,

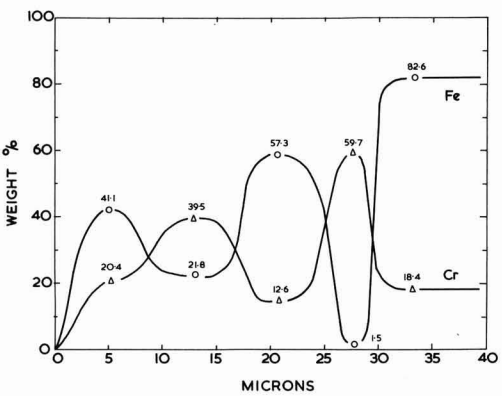


Fig. 7a. Concentration profile across scale and adjoining alloy for Fe-18.0% Cr oxidized 5 hr at 1200°C (line of traverse in Fig. 6a).

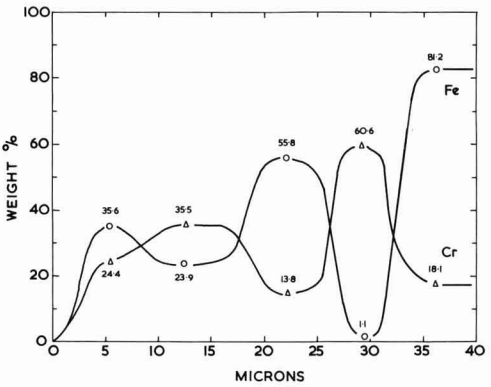


Fig. 7b (i). Concentration profile across scale and adjoining alloy for Fe-18.0% Cr oxidized 10 hr at 1200°C (line of traverse in Fig. 6b).

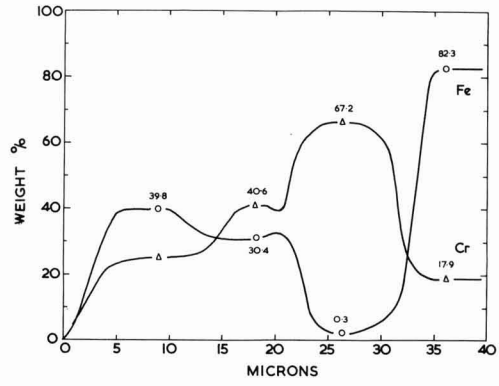


Fig. 7b (ii). Concentration profiles across scale and adjoining alloy for Fe-18.0% Cr oxidized 10 hr at 1200°C (line of traverse in Fig. 6b).

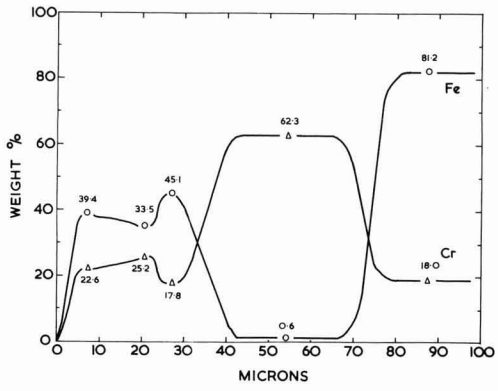


Fig. 7c. Concentration profile across scale and adjoining alloy for Fe-18.0% Cr oxidized 50 hr at 1200°C (line of traverse in Fig. 6c).

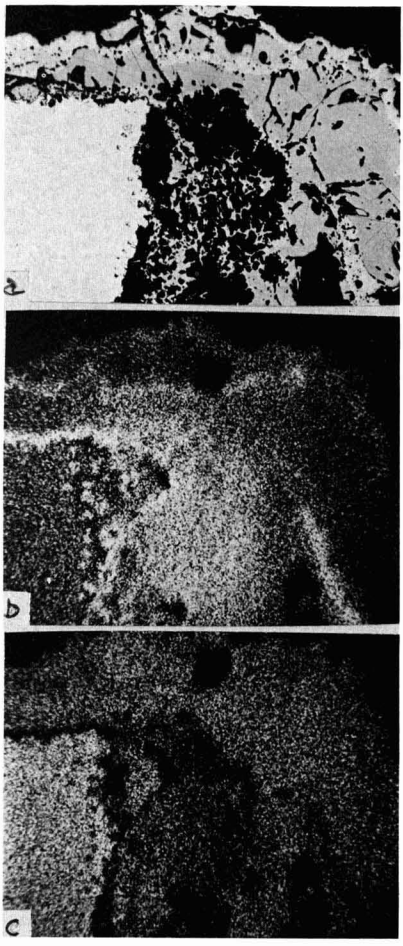


Fig. 8. Cross section of scale formed on Fe-18.0% Cr by 5-hr oxidation at 1200°C: a, optical; b, KαCr image; c, KαFe image. Magnification *ca.* 120X.

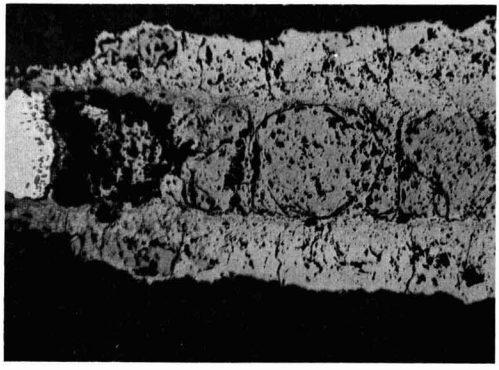

Fig. 9. Cross section of scale formed on Fe-18.0% Cr by 50-hr oxidation at 1200°C. Magnification 75X.

which is now possible, occurs. Figure 9 shows that the growth of type (ii) scale remains unchecked, causing the alloy to be completely converted into oxide. The inner region of this large nodule is again very friable and contains many pores. However, most of these are probably introduced during the metallographic preparation. Internal oxide particles do not appear to have increased in population with the increasing oxidation time.

Finally, the fourth type of scale, (iii), is shown in Fig. 10a, b, and c. The quantitative analyses of the scale (Fig. 10d) indicate the usual layered structure.

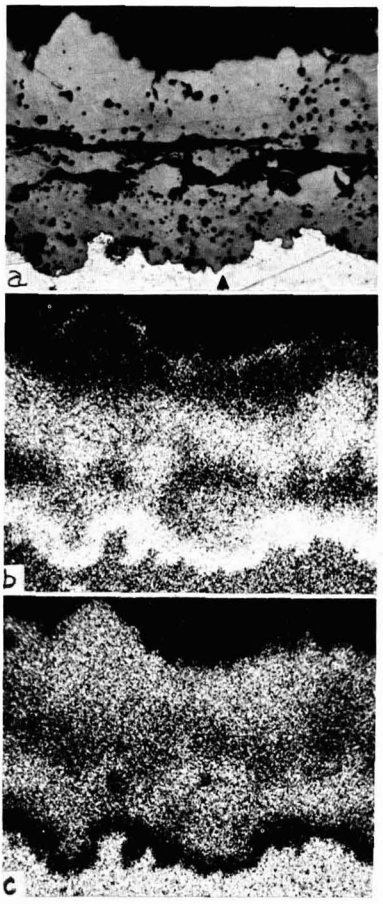


Fig. 10. Cross section of scale formed on Fe-18.0% Cr by 5-hr oxidation at 1200°C: a, optical; b, KαCr image; c, KαFe image. Magnification *ca.* 400X.

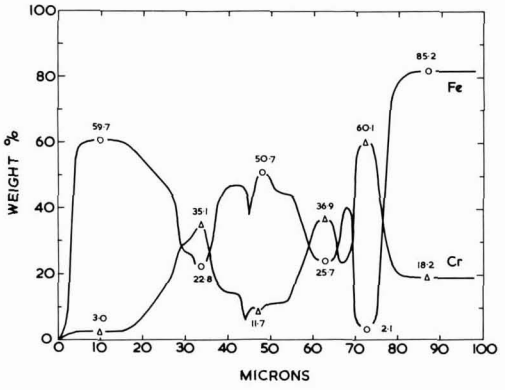


Fig. 10d. Concentration profiles along the line marked in Fig. 10a.

Comparison of these profiles with those for type (i) scale (Fig. 7a, b, or c) indicates a certain similarity. The three outer layers of type (i) scale appear in duplicate in this type (iii) scale, surmounting the usual $Cr_2O_3$ layer at the alloy/oxide interface. Again no internal oxide is present.

## Discussion

*Formation of the protective oxide* $Cr_2O_3$.—The only oxide formed at 800° and 1000°C, and during the first stages of oxidation at 1200°C is $Cr_2O_3$. The growth mechanism of this oxide is presumably similar to that on alloys richer in chromium, namely, predominantly by cationic diffusion as discussed elsewhere (1, 2). Certainly, the parabolic rate constants are of a similar magnitude.

The iron content of the $Cr_2O_3$ scales was always small and decreased with time, the actual weight of iron in the scale remaining constant and equal to that present in the "initial film" as discussed previously (1, 2). No spinel, of the type $FeFe_{(2-x)}Cr_{(x)}O_4$ ($O \leq x \leq 2$), was ever observed metallographically, nor the associated higher iron contents by microanalysis. If this oxide were formed initially, then it must have been rapidly replaced by $Cr_2O_3$.

At 800° and 1000°C, there was in general no cracking of the protective oxide at temperature, no double layers of $Cr_2O_3$ were formed and very little roughening of the alloy/oxide interface occurred. At 1200°C, however, a roughened alloy/oxide interface was formed, and there was ballooning of the $Cr_2O_3$ scale, although this latter could have occurred on cooling the specimen from the oxidation temperature. When cracking of the $Cr_2O_3$ scale occurs at 1200°C, $Cr_2O_3$ is not re-formed as it is with alloys richer in chromium (1,2), because the chromium concentration at the alloy/oxide interface is too low (5). Instead rapid scaling or breakthrough occurs.

*Mechanism of breakthrough.*—At 1200°C, the end of the protective oxidation and commencement of rapid attack occurs at apparently random sites over the specimen surface. The suddenness of the onset of rapid oxidation, together with the observance of only protective $Cr_2O_3$ immediately prior to breakthrough, is indicative of a mechanical cracking mechanism (1, 3-5) rather than a "chemical mechanism" (8-10) for the transformation in oxidation rate. Providing that the $Cr_2O_3$ scale formed initially remains in contact with the alloy, or becomes detached without puncturing, there is no reason why it should not continue to grow. A simple calculation (5) shows that $Cr_2O_3$ is thermodynamically stable with an Fe-Cr alloy containing as little as 0.2% Cr at 1200°C. Calculated chromium concentration profiles (5) which, due to the assumptions made, give the minimum possible chromium concentrations, indicate that the interfacial chromium concentration at 1200°C increases from 4.8% after 10-min oxidation to 5.5% after 5-hr oxidation. Generally, experimentally measured values are not as low as this. Thus, the $Cr_2O_3$ scale formed at the start of oxidation never becomes thermodynamically unstable, and its subsequent failure is simply due to mechanical causes. This is further emphasized, in that at 1000°C where breakthrough does not generally occur, the chromium concentration at the alloy/oxide is calculated to be 2.5% after 10-min oxidation and 7.1% after 5 hr.

Apparently, the loosely attached protective scales balloon from the alloy surface before cracking open so that relatively large areas of the chromium-depleted underlying alloy are eventually exposed; rapid scaling through simple cracks in the protective scale would soon be stifled (1, 3). Presumably the punctured chromium oxide envelope is eventually lost completely from the specimen as it is never observed after breakthrough. In other instances it can stifle the growth of the stratified scale (4) or be slowly incorporated into the growing nodule (2).

Loss of the protective oxide need not occur simultaneously over the whole specimen surface. Cracking of one or two voids initially, followed by very rapid scaling there, would be sufficient to give the observed sudden increases in weight. Intermittent opening of other cavities in rapid succession would then result

in the smooth weight gain/time curves produced. Such failures would be expected randomly, but possibly the development of stratified scale in some places tends to disrupt the protective oxide in nearby locations. Overheating of the specimen may be important under catastrophic oxidation conditions.

It is extremely difficult to isolate one factor as the cause of the loss of protective scale, and probably it is a combination of factors: scale thickness, scale plasticity, alloy ductility, phase changes, adhesion between alloy and oxide and alloy and/or oxide grain growth. Detailed discussion of these factors is given elsewhere (1, 2).

*Growth of stratified scale.*—The scale formed at breakthrough depends implicitly on the chromium concentration at the surface of the underlying alloy when directly exposed to the atmosphere. Generally the higher the bulk alloy chromium content the higher is the chromium content at the alloy/oxide interface when it is exposed, although other factors, oxidation rate, alloy interdiffusion rate, time, are also important (5). Specimen geometry is also sometimes important because larger depletions of chromium are expected near to the specimen edges (chromium being used up from such regions by oxide growth on two or more nearby faces simultaneously) and at locations of thin section. With the present Fe-18% Cr alloy, the chromium concentration at the alloy/oxide interface when breakthrough occurs is near to the borderline between that for formation of type (i) and type (ii) scales. Thus, at the edges of specimens where lower chromium contents are likely type (ii) scales, typical of alloys of lower bulk chromium content, are formed. Over most of the remainder of the surface type (i) scales are formed, while at intermediate locations, type (iii) scales are formed.

At breakthrough, the chromium concentration at the alloy/oxide interface is never high enough for the immediate re-formation of a $Cr_2O_3$ scale as is observed for higher chromium alloys (1, 2) and a mixed iron and chromium oxide is formed. Whether this mixed oxide is the spinel, $FeFe_{(2-x)}Cr_xO_4$ ($O \leq x \leq 2$), or the rhombohedral oxide, $Fe_{(2-x)}Cr_xO_3$ ($O \leq x \leq 2$) or even mixtures of the two is relatively unimportant as both these oxides can vary continually with composition. For the purposes of this discussion, it is assumed that the spinel plays the major role in determining the subsequent oxidation behavior, particularly as this is the more favored phase at chromium levels of this magnitude (11).

Thus, the start of stratified scale growth is the formation of a spinel on the alloy surface exposed by the loss of protective $Cr_2O_3$. Initially the spinel is of uniform composition, but the chromium content of the spinel is dependent on the chromium concentration at the alloy surface when this is exposed; it is lower where type (ii) scales eventually develop than where type (i) scales are formed. The spinel produced in the chromium-rich areas may in fact be the normal spinel as evidenced by its composition (12). The situation at this stage is shown schematically in Fig. 11a, for scales of types (i) and (ii); type (iii) scales are similar to these and are discussed later.

Soon after the spinel is initiated, the faster diffusing iron ions start to segregate at the outer scale surface, leaving a chromium-rich region at the alloy/oxide interface (Fig. 11b), a distribution favored thermodynamically. If the scale is mainly spinel, then the value of $x$ in the formula $FeFe_{(2-x)}Cr_xO_4$ varies through the scale, increasing as the alloy/oxide interface is approached (13). In general, the ionic mobilities in chromite spinels are lower than in ferrite spinels (14) making interdiffusion rates slower in type (i) scales than in type (ii) scales. Thus, in the former scales the segregation is not as complete as in type (ii) scales where the virtually pure spinel magnetite is formed at the surface of the scale, this being further oxidized to $Fe_2O_3$ in a manner similar

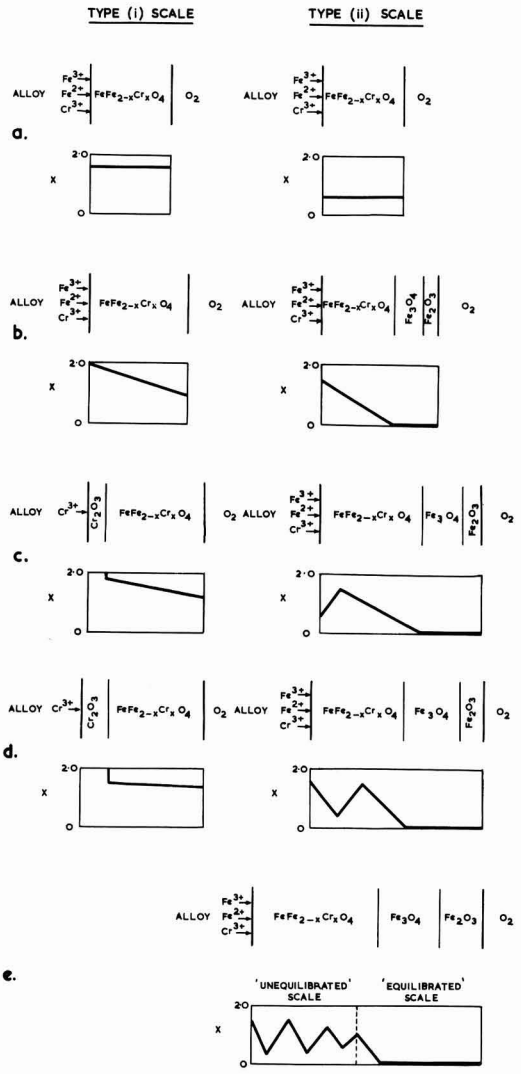


Fig. 11. Schematic diagram of the formation of scales of type (i) and (ii).

to that formed on pure iron. Clearly the over-all growth rate of type (ii) scales will be greater than the more chromium-rich type (i).

When the chromium content of the spinel in the vicinity of the alloy/oxide interface increases it acts as a partial barrier to the continued diffusion of iron ions to the outer scale layers. Consequently, a second iron-rich layer is formed beneath this barrier, resulting in a second chromium-rich barrier layer at the alloy/oxide interface. This is shown schematically for type (ii) scales in Fig. 11c and d. Further growth of type (ii) scales occurs by the continued formation of these iron-rich and chromium-rich oxides, resulting in the complex distribution of alternate iron-rich and chromium-rich layers found in these scales. With type (i) scales, the formation of the chromium-rich spinel at the alloy/oxide interface is closely followed by the formation there of the rhombohedral oxide, $Cr_2O_3$, containing only a very small amount of dissolved iron (Fig. 11c). Iron from the alloy cannot now enter this $Cr_2O_3$ layer at the base of the scale unless

the chromium concentration falls to about 0.2% at 1200°C (5), thus the supply of $Fe^{2+}$ and $Fe^{3+}$ ions to the outer scale layers is terminated. Further scale growth (Fig. 11d) of type (i) scale is, therefore, only the continued thickening of the $Cr_2O_3$ layer, the reaction at the $Cr_2O_3$/spinel interface being

$$3FeFe_{(2-x)}Cr_xO_4 + (6\square''' + 3\square'')_{spinel} = 4Cr_2O_3 + (8\square''')Cr_2O_3$$

where $(\square''')_{spinel}$, $(\square'')_{spinel}$, and $(\square''')_{Cr_2O_3}$ represent trivalent and divalent cation vacancies in the spinel and trivalent cation vacancies in the rhombohedral oxide, respectively.

Scales of type (iii) are formed in an identical manner to those of type (ii) except that several pairs of iron-rich and chromium-rich layers are formed before the scale is healed by a $Cr_2O_3$ layer as described for type (i) scales. Further discussion of scale healing by $Cr_2O_3$ is reserved for the final section.

During later growth of all these scales the undulating chromium and iron concentration profiles tend to approach steady-state conditions. In type (i) scales this is seen in the sequence Fig. 7a-c where interdiffusion has reduced the compositional differences between the three layers. This process is essentially slow because ionic mobilities in the chromium-rich spinels are relatively low. However, it is assisted by the inner $Cr_2O_3$ layer preventing further thickening of the outer spinel layers. Possibly these outer spinel layers are oxidized further to the corresponding mixed rhombohedral oxide.

In type (ii) scales, the levelling out of the compositional differences between iron-rich and chromium-rich layers has to take place simultaneously with the continued growth of these layers. Thus, local activity gradients in the scale, which are not necessarily in the same direction as the over-all activity gradient, are gradually being removed as the scale grows under the over-all activity gradient between alloy and oxidizing atmosphere. Figure 11e shows this situation where the outer scale represents the steady state (a smooth activity gradient) and the inner scale the nonsteady state (an undulating activity gradient), the degree of "equilibration" decreasing as the alloy/oxide interface is approached.

Internal oxidation never occurs behind healed scales because the $Cr_2O_3$ at the alloy/oxide interface is thermodynamically very stable. In other instances, penetration of internal oxide particles into the alloy is never very great because the diffusion rate of oxygen into the alloy is not much faster than the rate of encroachment of the alloy/oxide interface. Incorporation of internal oxide particles into the surface scale would cause further stratification and local concentration gradients in the inner layers.

*Mechanism of scale healing.*—The reasons why stratified scale is healed along the sides of the specimen and not at the edges is not entirely clear. As soon as breakthrough occurs and rapid scaling starts, the chromium depletion established during the initial $Cr_2O_3$ formation is rapidly consumed. However, the alloy is not completely equilibrated as there is still a degree of selective oxidation of chromium during the rapid scaling.

Scale healing is associated with the formation of a continuous layer of the protective oxide, $Cr_2O_3$, in the present system, as opposed to a discontinuous layer or internal oxide of $Cr_2O_3$. After the start of rapid scaling, oxygen produced by dissociation of the surface scale at the alloy/scale interface diffuses into the alloy producing an internal oxide precipitate of $Cr_2O_3$. If the volume fraction of this internal oxide is above a certain critical level, then further formation of $Cr_2O_3$ will occur by sideways growth of the existing internal oxide particles (15). When the volume fraction is below the critical level, new $Cr_2O_3$ internal oxide precipitates are formed deeper in the alloy. Under the former conditions, continued sideways growth of the $Cr_2O_3$ particle results in a continuous "healing" $Cr_2O_3$ layer being formed, providing the rate of encroachment of the alloy/oxide interface is not so fast as to cause the $Cr_2O_3$ particles to be incorporated into the scale before they link up. Where continued nucleation of $Cr_2O_3$ particles occurs, a continuous layer will never be formed and scaling continues unchecked.

Factors governing the formation of this critical volume fraction of internal oxide include: (*a*) the chromium concentration profile in the alloy at the time of breakthrough; (*b*) the alloy interdiffusion coefficient which governs the flux of chromium atoms to the alloy/oxide interface; (*c*) the oxygen diffusion rate in the alloy; (*d*) the oxygen pressure at the alloy/external scale interface; and (*e*) the over-all oxidation rate. Comparing the edges of the specimens with the remainder of the surface, the interdiffusion coefficients, (*b*) and (*c*) above, will be the same. However, the other factors tend to favor healing along the sides of the specimens as compared to the edges of the specimens. Thus the lower local chromium concentrations at the edges of specimens, as discussed earlier, promote more iron-rich spinels in the external scale and therefore faster oxidation rates and higher effective oxygen pressures at the alloy/scale interface. Consequently $Cr_2O_3$ continues to be precipitated as internal oxide rather than form a continuous layer.

In order to understand more quantitatively the formation and healing of scales of this type, more information on diffusion and lattice defects in ternary oxides is required. Using thermodynamic and transport data it is possible at present to predict the final steady-state scaling conditions, but little can be said about the rate at which the steady state is approached or about the scaling behavior during the transient period. Presumably a more sophisticated theoretical approach will permit this.

## Acknowledgments

The authors' thanks are due to Professor T. K. Ross for providing facilities and encouraging this study. They are also indebted to the Science Research Council for providing the electron probe microanalyzer and for a research studentship to one of them (D.P.W.) from October 1962 to September 1965.

Manuscript received May 15, 1967; revised manuscript received July 5, 1967.

Any discussion of this paper will appear in a Discussion Section to be published in the June 1968 JOURNAL.

## REFERENCES

1. D. P. Whittle, Ph.D. Thesis, Univ. of Manchester (1965).
2. G. C. Wood and D. P. Whittle, To be published.
3. G. C. Wood and D. P. Whittle, *Corrosion Sci.*, **4**, 263, (1964).
4. G. C. Wood and D. P. Whittle, *ibid.*, **4**, 293 (1964).
5. D. P. Whittle, G. C. Wood, D. J. Evans, and D. B. Scully, *Acta Met.*, in press.
6. D. Caplan and M. Cohen, *This Journal*, **108**, 334 (1961).
7. D. Caplan, A. Harvey, and M. Cohen, *Corrosion Sci.*, **3**, 161 (1963).
8. G. Bandel, *Arch. Eisenhuttenw.*, **15**, 271 (1941/2).
9. J. O. Edström, *J. Iron Steel Inst.*, **185**, 450 (1957).
10. I. A. Menzies and D. Mortimer, *Nature*, **208**, 1307 (1965).
11. A. U. Seybolt, *This Journal*, **107**, 147 (1960).
12. H. J. Yearian, J. M. Kortwright, and J. Langenheim, *J. Chem. Phys.*, **22**, 1196 (1954).
13. H. J. Yearian, E. C. Randall, and T. A. Longo, *Corrosion*, **12**, 515t (1956).
14. C. E. Birchenall, *Met. Rev.*, **3**, 235 (1958).
15. C. Wagner, *Z. Elektrochem.*, **63**, 772 (1959).

# Electron Diffraction Studies of Active, Passive, and Transpassive Oxide Films Formed on Iron

**C. L. Foley, J. Kruger, and C. J. Bechtoldt**

*National Bureau of Standards, Washington, D. C.*

ABSTRACT

Iron foil specimens were anodically polarized by means of a potentiostat in 1*N* $H_2SO_4$, 0.1*N* NaOH, and a sodium borate-boric acid solution (pH, 8.5). Both passive, active, and transpassive regions of the polarization curve were studied for each solution. The oxide films were examined while still in contact with the iron foil by selected area transmission electron diffraction. Five iron planes were studied: {100}, {110}, {111}, {210}, and {211}, and the epitaxial relationship of the oxide to the iron substrate determined. Evidence was found indicating that in all of the electrolytes used the passive film contained $\gamma$-$Fe_2O_3$, while the nonpassive films did not.

Of prime importance to our understanding of the nature of the phenomenon of passivity is a knowledge of the nature of the passive film. This includes its composition, structure, and relationship to the metal surface on which it was formed. There has not been a concentrated effort to discover the nature of the film, but there have been a few such studies (1-3) of the passive film on iron. Due to the thinness of the films, these studies have involved the use of electron diffraction. Two techniques, in particular, have been used. One is film stripping coupled with transmission electron diffraction; the other is reflection electron diffraction, leaving the film still in contact with the metal surface on which it was formed. The first technique has the advantage that the quality of the patterns obtained allows one to detect the weaker oxide reflections rather easily, but has the disadvantage that the film must be removed from the substrate under rather corrosive conditions. Mayne and Pryor (1) have evidence to show that the removal procedure does not chemically alter the film, although the possibility always exists that subtle changes may have occurred. Another problem associated with film stripping is that the film may change structurally during or subsequent to being detached from the metal surface. For example, stress existing in the film while it is attached to the metal may be relaxed upon stripping, thereby changing the lattice parameter and, as Mayne and Pryor (1) have suggested, may produce recrystallization of the film. The reflection technique, while it does look at films still in contact with the metal, is less able to detect weak oxide reflections because they may be hidden by the elongated stronger metal and oxide reflections.

This study attempts to combine the advantage of reflection diffraction (looking at the film while it is still on the metal) with that of transmission diffraction (greater sensitivity). This is accomplished by producing both passive and nonpassive oxide films on thin metal foils, of the type used so effectively in many recent transmission electron microscopy studies of metals (2). Selected area diffraction enables us to look at double layers of the film (one on each side of the foil) on metal grains of many different crystallographic orientations. The epitaxial relationships between the substrate iron and the film can thus be easily determined for many orientations without the necessity of using large iron single crystals. The film-metal-film "sandwich" doubles the amount of passive film studied and thus increases the possibility of detecting the weaker oxide reflections that are necessary to distinguish between $Fe_3O_4$ and $\gamma$-$Fe_2O_3$. This is of importance since a number of workers have indicated that the $\gamma$-$Fe_2O_3$ plays a role in passivity (3, 5). This "sandwich" would also increase the chances for double diffraction effects, but as will be mentioned later, this did not present a problem in our patterns. The technique now used suffers from the same disadvantage that is present with both of the aforementioned electron diffraction techniques, in that for examination the specimen must be removed from the environment where the film is formed. Thus, there is a possibility that the nature of the film itself has been altered by the time it is studied in the electron diffraction apparatus. Experiments described later indicate that this is not a serious difficulty.

These studies of films formed on pure iron foils have extended the range of systems studied by electron diffraction to include those formed in acidic and basic as well as neutral solutions. The prepassive and transpassive regions of the anodic polarization curve were studied, in addition to the passive region.

## Experimental

The electrolytic cell used for polarizing thin foil specimens to selected potentials by means of a potentiostat is shown in Fig. 1. This cell enabled us to deaerate our solutions with Grade A, 99.99% helium during all experiments. Foil specimens were rolled to a thickness of 0.005 cm from an iron sample obtained

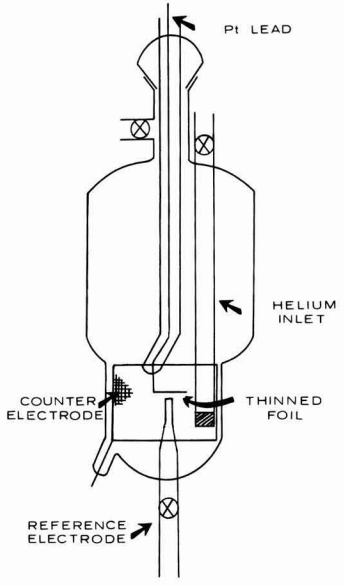


**Fig. 1. Cell used for anodic polarization of foils**

from the Battelle Memorial Institute.[1] After degreasing with ethanol and trichloroethylene, the foil was annealed for 1 hr at 1000°C in a hydrogen atmosphere. The foil specimens were thinned by the Bollman technique (2), using a mixture of one part 70% perchloric acid to twenty parts glacial acetic acid, for the electropolishing solution. Specimens were then rinsed in high-purity methanol and transferred immediately to the electrolytic cell. After 1 min of cathodic reduction to remove any oxide films, the specimen was brought to the desired potential and usually held at this potential for 2 hr. Longer exposures did not give significantly different results.

When the specimen was ready for inspection, it was rapidly removed from the cell, rinsed, and submerged in methanol. The foil was mounted for the electron microscope and selected area diffraction patterns were obtained at an operating voltage of 100 kv. In order to introduce as little contamination and heating into the specimens as possible, the diffraction patterns were taken, during the first 5 min of examination, then electron micrographs of the same area were made, if they were desired.

Three solutions were used in these experiments: a basic solution of 0.1*N* NaOH with a *p*H of 11.4, a nearly neutral solution, which we will refer to as "borate" consisting of 0.15*N* $Na_2B_4O_7 \cdot 10H_2O$ and 0.15*N* $H_3BO_3$ mixed in proportions giving a *p*H of 8.5, and an acidic solution of 1*N* $H_2SO_4$ with a *p*H of 1.1. Using each solution, there were four main groups of experiments: prepassive, passive, passive-decay (initially passive, but then driven potentiostatically to an active potential), and transpassive. The anodic polarization curves used to determine the potentials characteristic of these various regions were determined in a manner similar to that used by Nagayama and Cohen (3).

[1] Gaseous impurities (ppm): $O_2$ (vacuum fusion), 2.1; S (colorimetric), 4 ± 3; C (combustion-conductometric), 3 ± 3; $N_2$ (vacuum fusion), 0.5; $H_2$ (vacuum fusion), 0.3. Major metallic impurities (ppm): Al, 15; Cr, 5; Co, 5; Cu, 7; Ni, 20; P, 9; Si, 10.

The potentials used (*vs.* SCE) are listed in Tables I, II, and III.

A few studies were made on specimens that were formed by exposure to the inorganic passivating solution, 0.1*N* $NaNO_2$. Several other experiments were carried out using the borate and $H_2SO_4$ solutions containing chloride ions.

## Results and Interpretation

The results of our study of oxide films formed in the acidic, basic, and neutral solutions for five of the iron planes are presented in Tables I, II, and III. Figure 2 shows that the patterns obtained for the passive films in the three solutions, plus $NaNO_2$, had the same geometric distribution and differed only in intensity. It should be noted that the observable differences in the patterns are due to the intensity distribution and the difference in thickness of the film. While this figure depicts one iron orientation, the relative quality was similar for all orientations studied.

*Indexing and epitaxy.*—The indexing of each negative plate was accomplished by the standard methods utilizing the sideline technique (6), the iron spots serving as an internal standard. As a check, the angles between various oxide spots were measured and compared with the standard cubic interplanar angles (7). Figures 3-7 show examples of both a passive and a nonpassive film for each plane listed in Tables I, II and III, with a corresponding indexed diagram. A comparison between the epitaxial relationships obtained in our work and other work done in this field is shown in Table IV. The comparison studies listed have all been concerned with films formed by gaseous oxidation.

There were some special problems associated with indexing. The principal one arises because the thickness of the oxide layer [≈ 30Å (8)], makes it possible for reciprocal lattice spikes (9) from more than one oxide layer to intersect the reflecting sphere. In fact,

**Table I. Borate solution**

| | | A | B | C | D | E |
|---|---|---|---|---|---|---|
| | Plane, Fe | {100} | {110} | {111} | {210} | {211} |
| 1. | State and potential | Prepassive, −0.6v or open circuit | | | | |
| 2. | Oxide parameter, in Å | 8.39 | Not determined | Not determined | — | 8.40 |
| 3. | Identification | $Fe_3O_4$ | α-FeOOH | α-FeOOH | No oxide | $Fe_3O_4$ |
| 4. | Epitaxy | | | | | |
| | Oxide plane | $\{\bar{1}\bar{1}4\}$ | — | — | — | $\{01\bar{1}\}$ |
| | Oxide axes parallel to Iron axes | $[1\bar{1}0]$Ox ‖ [010]Fe<br>[100]Ox ‖ [110]Fe | | | | [011]Ox ‖ [111]Fe<br>[111]Ox ‖ [011]Fe |
| 5. | Remarks | No γ-$Fe_2O_3$ | Rings | Rings | Clean | No γ-$Fe_2O_3$ |
| 6. | State and potential | Passive, +0.75v, +0.85v | | | | |
| 7. | Oxide parameter, in Å | 8.3 | 8.32 | 8.29 | 8.33 | 8.31 |
| 8. | Identification | γ-$Fe_2O_3$ | γ-$Fe_2O_3$ | γ-$Fe_2O_3$ | γ-$Fe_2O_3$ | γ-$Fe_2O_3$ |
| 9. | Epitaxy | | | | | |
| | Oxide plane | $\{\bar{1}\bar{1}4\}$ | $\{01\bar{1}\}$ | $\{01\bar{1}\}$ | {100} | $\{01\bar{1}\}$ |
| | Oxide axes parallel to | [221]Ox ‖ [200]Fe | $[0\bar{1}1]$Ox ‖ [001]Fe | [111]Ox ‖ $[1\bar{1}0]$Fe | $[\bar{1}01]$Ox ‖ [001]Fe | Same as above, |
| | Iron axes | [100]Ox ‖ [110]Fe | $[\bar{2}11]$Ox ‖ [111]Fe | [100]Ox ‖ $[01\bar{1}]$Fe | $[11\bar{1}]$Ox ‖ $[2\bar{1}3]$Fe | E—4 plus, |
| | | | | [311]Ox ‖ $[11\bar{2}]$Fe | $[\bar{2}12]$Ox ‖ [100]Fe | [100]Ox ‖ [110]Fe |
| 10. | Remarks | Has γ-$Fe_2O_3$ | Has γ-$Fe_2O_3$ | Has γ-$Fe_2O_3$ | Has γ-$Fe_2O_3$ | Has γ-$Fe_2O_3$ |
| 11. | State and potential | Decay, to −0.6v | | | | |
| 12. | Oxide parameter, in Å | 8.29 | 8.38 | 8.38 | 8.37 | 8.35 |
| 13. | Identification | γ-$Fe_2O_3$ | $Fe_3O_4$ | $Fe_3O_4$ | γ-$Fe_2O_3$ or $Fe_3O_4$ | γ-$Fe_2O_3$ or $Fe_3O_4$ |
| 14. | Epitaxy | | | | | |
| | Oxide plane | $\{\bar{1}\bar{1}4\}$ | $\{11\bar{1}\}$ | $\{01\bar{1}\}$ | {100} | $\{01\bar{1}\}$ |
| | Oxide axes parallel to | Same as above | $[10\bar{1}]$Ox ‖ [001]Fe | Same as above | Same as above | Same as above |
| | Iron axes | A—9 | $[\bar{2}10]$Ox ‖ $[11\bar{1}]$Fe | C—9 | D—9 | E—4 |
| 15. | Remarks | Some γ-$Fe_2O_3$ | Some γ-$Fe_2O_3$ | Some γ-$Fe_2O_3$ | Some γ-$Fe_2O_3$ | Some γ-$Fe_2O_3$ |
| 16. | State and potential | Transpassive, +1.25v | | | | |
| 17. | Oxide parameter, in Å | 8.37 | — | 8.42 | — | 8.39 |
| 18. | Identification | $Fe_3O_4$ | — | $Fe_3O_4$ | — | $Fe_3O_4$ |
| 19. | Epitaxy | | | | | |
| | Oxide plane | $\{\bar{1}\bar{1}4\}$ | — | $\{01\bar{1}\}$ | — | $\{01\bar{1}\}$ |
| | Oxide axes parallel to | Same as above | | Same as above | | Same as above |
| | Iron axes | A—4 | | C—9 | | E—4 |
| 20. | Remarks | No γ-$Fe_2O_3$ | No plates | No γ-$Fe_2O_3$ | No plates | No γ-$Fe_2O_3$ |

**Table II. $H_2SO_4$ solution**

| | | F | G | H | I | J |
|---|---|---|---|---|---|---|
| | Plane, Fe | {100} | {110} | {111} | {210} | {211} |
| 1. | State and potential | | Prepassive, +0.2v | | | |
| 2. | Oxide parameter, in Å | — | — | — | — | 8.37 |
| 3. | Identification | No oxide | No oxide | Some with $\gamma$-FeOOH others clean | No oxide | $Fe_3O_4$ |
| 4. | Epitaxy | | | | | |
| | Oxide plane | — | — | — | | $\{01\bar{1}\}$ |
| | Oxide axes parallel to Iron axes | | | | | $[011]Ox \parallel [111]Fe$ $[111]Ox \parallel [011]Fe$ |
| 5. | Remarks | Clean | Clean | Clean or rings | Clean | No $\gamma$-$Fe_2O_3$ |
| 6. | State and potential | | Passive, +1.4v, + 1.6v | | | |
| 7. | Oxide parameter, in Å | 8.32 | 8.30 | 8.31 | 8.31 | — |
| 8. | Identification | $\gamma$-$Fe_2O_3$ | $\gamma$-$Fe_2O_3$ | $\gamma$-$Fe_2O_3$ | $\gamma$-$Fe_2O_3$ | $\gamma$-FeOOH |
| 9. | Epitaxy | | | | | |
| | Oxide plane | $\{\bar{1}\bar{1}4\}$ | $\{11\bar{1}\}$, $\{01\bar{1}\}$ | $\{01\bar{1}\}$ | {100} | — |
| | Oxide axes parallel to | $[221]Ox \parallel [200]Fe$ | Same as Table I | Same as Table I | Same as Table I | |
| | Iron axes | $[100]Ox \parallel [110]Fe$ | B—9, B—14 | C—9 | D—9 | |
| 10. | Remarks | Has $\gamma$-$Fe_2O_3$ | No $\gamma$-$Fe_2O_3$ | Has $\gamma$-$Fe_2O_3$ | Has $\gamma$-$Fe_2O_3$ | Rings |
| 11. | State and potential | | Decay, open circuit | | | |
| 12. | Spinel parameter | 8.36 | 8.33 | 8.36 | 8.30 | — |
| 13. | Identification | $\gamma$-$Fe_2O_3$ or $Fe_3O_4$ | $\gamma$-$Fe_2O_3$ or $Fe_3O_4$ | $\gamma$-$Fe_2O_3$ or $Fe_3O_4$ | $\gamma$-$Fe_2O_3$ or $Fe_3O_4$ | — |
| 14. | Epitaxy | | | | | |
| | Oxide plane | $\{\bar{1}\bar{1}4\}$ | $\{11\bar{1}\}$, $\{01\bar{1}\}$ | $\{01\bar{1}\}$ | {100} | |
| | Oxide axes parallel to | Same as above | Same as Table I | Same as Table I | Same as Table I | |
| | Iron axes | F—9 | B—9, B—14 | C—9 | D—9 | |
| 15. | Remarks | Some $\gamma$-$Fe_2O_3$ | No $\gamma$-$Fe_2O_3$ | No $\gamma$-$Fe_2O_3$ | Some $\gamma$-$Fe_2O_3$ | No plates |
| 16. | State and potential | | Transpassive, +1.75v | | | |
| 17. | Oxide parameter, in Å | 8.40 | 8.39 | — | 8.37 | — |
| 18. | Identification | $Fe_3O_4$ | $Fe_3O_4$ | $\gamma$-FeOOH | $Fe_3O_4$ | No oxide |
| 19. | Epitaxy | | | | | |
| | Oxide plane | $\{\bar{1}\bar{1}4\}$ | $\{11\bar{1}\}$ | — | {100} | — |
| | Oxide axes parallel to | Same as Table I | Same as Table I | | Same as Table I | |
| | Iron axes | A—4 | B—14 | | D—9 | |
| 20. | Remarks | No $\gamma$-$Fe_2O_3$ | No $\gamma$-$Fe_2O_3$ | Rings | No $\gamma$-$Fe_2O_3$ | Clean |

**Table III. NaOH solution**

| | | K | L | M | N | O |
|---|---|---|---|---|---|---|
| | Plane, Fe | {100} | $\{\bar{1}10\}$ | {111} | {210} | {211} |
| 1. | State and potential | | Prepassive, open circuit | | | |
| 2. | Oxide parameter, in Å | 8.27 | 8.40 | — | 8.40 | — |
| 3. | Identification | $\gamma$-$Fe_2O_3$ | $Fe_3O_4$ | No oxide or has $\alpha$-FeOOH | $Fe_3O_4$ | — |
| 4. | Epitaxy | | | | | |
| | Oxide plane | $\{\bar{1}\bar{1}4\}$ | $\{11\bar{1}\}$ | — | {100} | — |
| | Oxide axes parallel to | $[221]Ox \parallel [200]Fe$ | $[101]Ox \parallel [001]Fe$ | | Same as Table I | |
| | Iron axes | $[100]Ox \parallel [110]Fe$ | $[\bar{2}10]Ox \parallel [111]Fe$ | | D—9 | |
| 5. | Remarks | Has $\gamma$-$Fe_2O_3$ | No $\gamma$-$Fe_2O_3$ some rings | Clean or rings | No $\gamma$-$Fe_2O_3$ | No plates |
| 6. | State and potential | | Passive, +0.5v | | | |
| 7. | Oxide parameter, in Å | 8.31 | 8.33 | 8.31 | 8.31 | 8.30 |
| 8. | Identification | $\gamma$-$Fe_2O_3$ | $\gamma$-$Fe_2O_3$ | $\gamma$-$Fe_2O_3$ | $\gamma$-$Fe_2O_3$ | $\gamma$-$Fe_2O_3$ |
| 9. | Epitaxy | | | | | |
| | Oxide plane | $\{\bar{1}\bar{1}4\}$ | $\{01\bar{1}\}$ | $\{01\bar{1}\}$ | {100} | $\{01\bar{1}\}$ |
| | Oxide axes parallel to | Same as above | Same as Table I | Same as Table I | Same as Table I | Same as Table I |
| | Iron axes | K—4 | B—9 | C—9 | D—9 | E—4, E—9 |
| 10. | Remarks | Has $\gamma$-$Fe_2O_3$ | Has $\gamma$-$Fe_2O_3$ | Has $\gamma$-$Fe_2O_3$ | Has $\gamma$-$Fe_2O_3$ | Has $\gamma$-$Fe_2O_3$ |
| 11. | State and potential | | Decay, to −1.0v | | | |
| 12. | Oxide parameter, in Å | — | 8.40 | 8.36 | 8.35 | — |
| 13. | Identification | — | $Fe_3O_4$ | $\gamma$-$Fe_2O_3$ or $Fe_3O_4$ | $\gamma$-$Fe_2O_3$ or $Fe_3O_4$ | — |
| 14. | Epitaxy | | | | | |
| | Oxide plane | — | $\{11\bar{1}\}$ | $\{01\bar{1}\}$ | {100} | — |
| | Oxide axes parallel to | | Same as above | Same as Table I | Same as Table I | |
| | Iron axes | | L—4 | C—9 | D—9 | |
| 15. | Remarks | No plates | No $\gamma$-$Fe_2O_3$ | No $\gamma$-$Fe_2O_3$ | No $\gamma$-$Fe_2O_3$ | No plates |
| 16. | State and potential | | Transpassive, +1.0v | | | |
| 17. | Oxide parameter, in Å | 8.35 | 8.41 | — | — | — |
| 18. | Identification | $Fe_3O_4$ | $Fe_3O_4$ | No oxide | — | No oxide or has $\alpha$-FeOOH |
| 19. | Epitaxy | | | | | |
| | Oxide plane | | $\{01\bar{1}\}$ | — | — | — |
| | Oxide axes parallel to | Same as Table I | Same as Table I | | | |
| | Iron axes | A—4 | B—4 | | | |
| 20. | Remarks | No $\gamma$-$Fe_2O_3$ | No $\gamma$-$Fe_2O_3$ | Clean | No plates | Rings or clean |

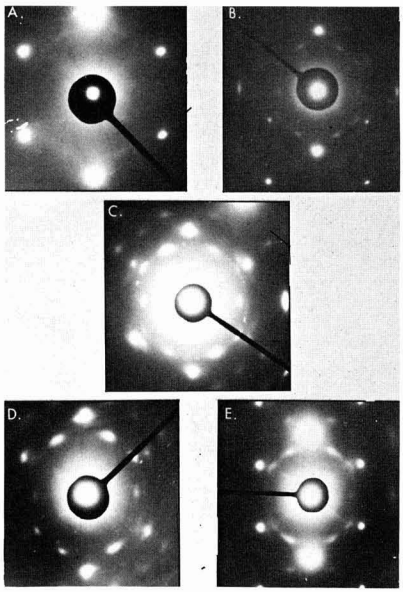


Fig. 2. Comparison of solutions: A, {111} plane shows no oxide after just submerging in borate; B, {111} plane, polarized at +0.75v in borate; C, {111} plane, polarized at +0.5 in NaOH; D, {111} plane, polarized at +1.4v in $H_2SO_4$; E, {111} plane, dipped in $NaNO_2$.

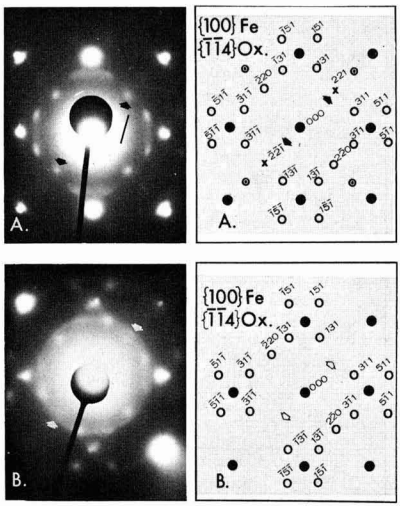


Fig. 3. A, Typical {100} passive pattern; indices are shown for oxide only; black arrows indicate $\gamma$-$Fe_2O_3$ reflections on a passive foil which disappear for nonpassive. B, Typical {100} nonpassive pattern; white arrows show sites where $\gamma$-$Fe_2O_3$ reflections have disappeared. Three oxide levels are represented in both A and B. Note: The oxide orientation is "nearly" $\bar{1}\bar{1}4$. It is composed of reflections on the zero level as well as reflections rel-rodded from above and below. Key: •, iron; ○, spinel $Fe_3O_4$ (or coincident $\gamma$-$Fe_2O_3$ spots in the passive case); X, $\gamma$-$Fe_2O_3$; ⊙, double diffraction.

a number of the patterns could be indexed only by taking this effect into account. An example of this can be seen for {210} iron, where three oxide levels are present (see Fig. 6). Some of the other planes are also interpreted in this manner.

Another difficulty was encountered in indexing films for the {100} substrate. As seen in Fig. 3 the passive

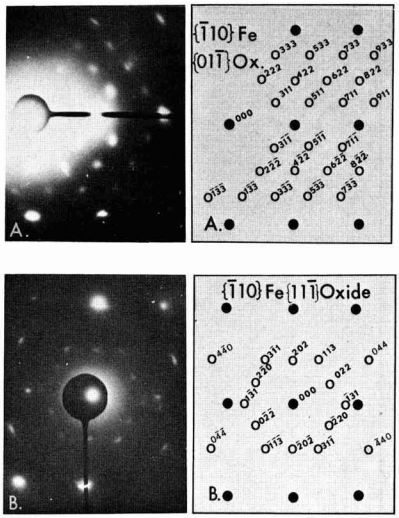


Fig. 4. A, Typical {1̄10} passive pattern; only one oxide layer is represented. B, Typical {1̄10} nonpassive pattern; again, the oxide is nearly {11̄1}, being composed of reflections from more than one oxide layer. Key: •, iron; ○, spinel $Fe_3O_4$ (or coincident $\gamma$-$Fe_2O_3$ spots in the passive case).

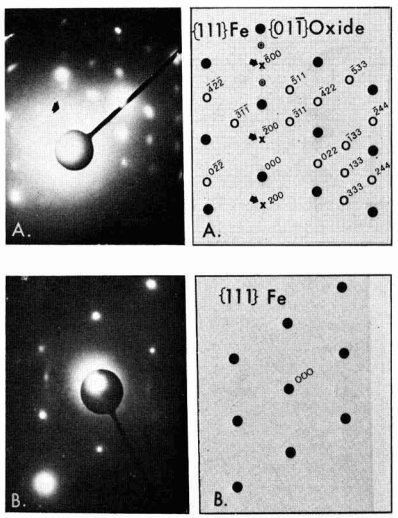


Fig. 5. A, Typical {111} passive pattern. B, The typical {111} nonpassive pattern showed either no oxide (as shown here), or a weaker version of the passive pattern, often incorporating oxide $\alpha$-FeOOH rings. Only one oxide layer is represented in A. Key: •, iron; ○, spinel $Fe_3O_4$ (or coincident $\gamma$-$Fe_2O_3$ spots for the passive case); X, $\gamma$-$Fe_2O_3$.

film appears to have fourfold symmetry, indicating a {100} oxide orientation (this orientation was found in previous studies as indicated in Table IV). Nonpassive films for the {100} iron lose this symmetry, however. In order to explain the disappearance of only one pair of the center oxide spots (marked with arrows in Fig. 3), when the film became nonpassive, it was necessary to consider another orientation for the passive film. A close examination of the passive film pattern revealed a slight, but reproducible difference in the radial distances to the center oxide pairs. The closer pair, having a slightly higher d-value, could then be distinguished as a {221} reflection ($d$ = 2.78), which

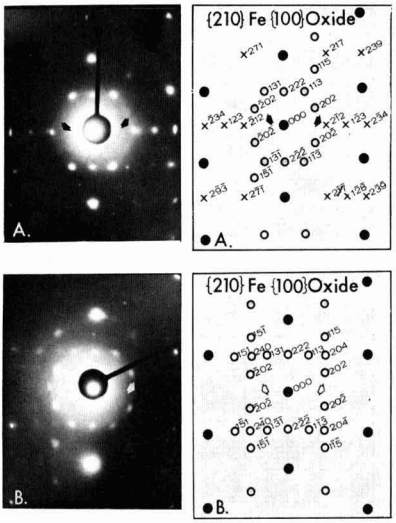


Fig. 6. A, Typical {210} passive pattern; black arrows indicate $\gamma$-$Fe_2O_3$ reflections. B, The {210} nonpassive pattern showed the same structure without the $\gamma$-$Fe_2O_3$ reflections (empty sites indicated by white arrows). Two oxide levels are represented in both A and B, thus the oxide orientation is "nearly" {100}. Key: •, iron; ○, spinel $Fe_3O_4$ (or coincident $\gamma$-$Fe_2O_3$ spots for the passive case); X, $\gamma$-$Fe_2O_3$.

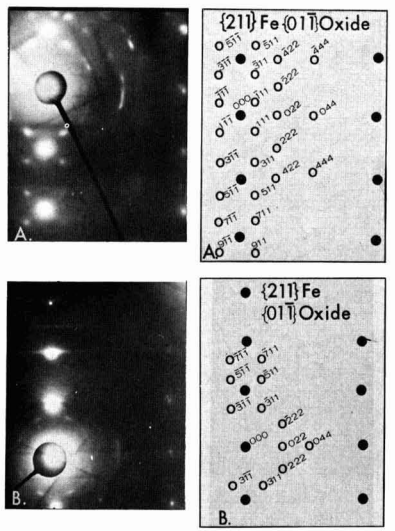


Fig. 7. A, Typical {211} passive pattern; and B, the weaker nonpassive version of the same structure. Only one oxide layer is represented. *Note:* This oxide relationship shows a resemblance to the super lattice reflections (27) perpetrated by partially coherent oxide precipitates. This particular oxide orientation consists of only one oxide level, however, while the super lattice reflections of this type will usually occur only when the foil is tipped a few degrees from a prominent matrix zone. Key: •, iron; ○, spinel $Fe_3O_4$ (or coincident $\gamma$-$Fe_2O_3$ reflections for the passive case).

would disappear when in the nonpassive state. This distinction between certain oxide reflections will be discussed further. When indexed in this manner, the oxide film orientation would be considered as {$\bar{1}$14} in both passive and nonpassive cases.

As seen in Table IV, our work showed the same oxide orientation for both passive and nonpassive films

**Table IV. Epitaxial relationships**

| Reference | Parallel planes | | Parallel axes | |
|---|---|---|---|---|
| | Iron | Oxide | Iron | Oxide |
| This work | {100} | {$\bar{1}$14} P | [200] | [221] |
| | | | [110] | [100] |
| | {100} | {$\bar{1}$14} NP | [010] | [$\bar{1}$10] |
| | | | [110] | [100] |
| Sewell, Cohen, Stockbridge (4) | {001} | {001} | [010] | [1$\bar{1}$0] |
| Haase (6) | {001} | {001} | [110] | [100] |
| Boggs (7) | {001} | {001} | [010] | [011] |
| | | | [$\bar{1}$00] | [0$\bar{1}$1] |
| This work | {$\bar{1}$10} | {01$\bar{1}$} P | [001] | [0$\bar{1}$1] |
| | | | [11$\bar{1}$] | [2$\bar{1}$1], [21$\bar{1}$] |
| | {110} | {111} NP | [001] | [101] |
| | | | [11$\bar{1}$] | [2$\bar{1}$0] |
| Sewell, Cohen, Stockbridge | {011} | {111} | [11$\bar{1}$] | [1$\bar{1}$0], [$\bar{1}$10] |
| Haase | {110} | {011}* | [111] | [112] |
| | | | [100] | [110] |
| Wagner, Lawless, Gwathmey (26) | {011} | {111} | 100 | [$\bar{1}$10] |
| Boggs | {011} | {111} | [$\bar{1}$1$\bar{1}$] | [$\bar{1}$01] |
| | | | [$\bar{1}$12] | [12$\bar{1}$] |
| This work | {111} | {01$\bar{1}$} P | [1$\bar{1}$0] | [111] |
| | | {01$\bar{1}$} NP | [0$\bar{1}$1] | [100] |
| | | | [11$\bar{2}$] | [3$\bar{1}$1] |
| Sewell, Cohen, Stockbridge | {111} | 2 degrees of {210} | [1$\bar{1}$0] | [001] |
| Boggs | {111} | {1$\bar{1}$0} | [01$\bar{1}$] | [001] |
| | {111} | {2$\bar{1}$0} | [01$\bar{1}$] | [00$\bar{1}$] |
| This work | {210} | {100} P | [001] | [$\bar{1}$01] |
| | {210} | {100} NP | [2$\bar{1}$3] | [11$\bar{1}$] |
| | {210} | | [100] | [2$\bar{1}$2] |
| No other studies published on this iron plane. | | | | |
| This work | {211} | {01$\bar{1}$} P | [111] | [011] |
| | | | [011] | [111] |
| | | | [021] | [100] |
| | {211} | {01$\bar{1}$} NP | [111] | [011] |
| | | | [011] | [111] |
| Sewell, Cohen, Stockbridge | {112} | {110} | [1$\bar{1}$1] | [1$\bar{1}$0] |
| Boggs | {112} | {011} | [111] | [3$\bar{1}$1] |

* Determined by the authors from an indexed figure in ref. (6).

for all except the {$\bar{1}$10} substrate orientation. The problem of the {$\bar{1}$10} iron orientation will be discussed later, but it should be noted in Fig. 4 that there is a clear distinction between the passive film orientation and the nonpassive film orientation. This situation is not similar to the {100} substrate where, for reasons mentioned before, the difference between the passive and nonpassive patterns has not been ascribed to a difference in orientations.

Although other iron planes have been studied, *e.g.*, {113} and {301}, the results for these were not significantly different from those listed in Tables I, II, and III, and will not be given a detailed survey here in order to conserve space. The epitaxy for these two orientations is given in Table V.

*Double diffraction.*—Double diffraction effects from the iron were encountered only with the NaOH solution where films formed were relatively thick. The extraneous reflections due to this effect were easy to detect by the method mentioned by Hirsch *et al.* (10).

**Table V. Epitaxy for the {113} and {301} iron orientations. These relationships hold for both the passive (P) and nonpassive (NP) cases.**

| | |
|---|---|
| {113} iron \|\| | {001} oxide P and NP |
| [30$\bar{1}$] iron | \|\| [111] oxide |
| [211] iron | \|\| [3$\bar{1}$1] oxide |
| {301} iron \|\| | {100} oxide P and NP |
| [001] iron | \|\| [10$\bar{1}$] oxide |
| [312] iron | \|\| [$\bar{5}$11] oxide |

The NaOH patterns were then used as a basis for determining all of the double diffraction reflections on each iron orientation. The double layer of oxide viewed (film-metal-film) did not seem to introduce extra reflections for the thinner oxide layers formed in neutral and acidic solutions since double diffraction was not detected for these films.

*Lattice parameters.*—The spinel lattice parameters for each negative were determined by using many $d$-values for different pairs of oxide spots and the parameter calculated for each. Many of the selected area diffraction patterns were found to suffer from a certain amount of pin-cushion distortion (11). In order to correct for the error in lattice parameter determinations introduced by this effect, we measured the degree of distortion using a Palladium standard and used the displacements calculated from this to determine the undistorted values of the radial distances for the oxides. These corrections were small (0-1.25%), but important in distinguishing between $\gamma$-$Fe_2O_3$ (8.32Å) and $Fe_3O_4$ [8.396Å (12)]. The "average" values of lattice parameters listed in Tables I, II, and III, represent values which have been "corrected" for the pin-cushion effect. A number of plates were used to determine each value. Since each oxide spot can be measured with the same absolute accuracy, it is necessary to weight any measurement error in the lattice parameter according to the value of $\sqrt{h^2 + k^2 + l^2}$. This practice has generally been neglected in previous error determinations of the lattice parameters in this system. (Note: A discussion of the structure of $\gamma$-$Fe_2O_3$ follows.) A statistical analysis of the lattice parameter data taking this weighting factor into account showed a maximum error of ± 0.02Å on the parameter values.[2]

It should be noted that, in general, the spinel parameters are much lower for the passive state (Tables I, II, and III, line 1) than for the transpassive or prepassive states. Whenever indications of $\gamma$-$Fe_2O_3$ have been found on most of the films for a particular group (see lines 5, 10, and 15), the lattice parameter is very near the $\gamma$-$Fe_2O_3$ value (8.32Å). Previous studies have verified this result for films formed in chromate solutions (1) and by gaseous oxidation (4).

The lattice parameters found for passive-decay films usually fall nearly midway between these for $\gamma$-$Fe_2O_3$ and $Fe_3O_4$, indicating a transition state. The decay patterns sometimes showed faint $\gamma$-$Fe_2O_3$ reflections, but not consistently.

*Distinction between $\gamma$-$Fe_2O_3$ and $Fe_3O_4$.*—The structures of the two oxides $Fe_3O_4$ and $\gamma$-$Fe_2O_3$ are closely related, $\gamma$-$Fe_2O_3$ being a pseudospinel probably having the lithium "spinel," $LiFe_5O_8$, type structure. $\gamma$-$Fe_2O_3$ has all of the reflections of the $Fe_3O_4$ spinel structure, plus additional reflections which probably result from ordered vacancies or ordered substitution of protons for ferrous ions in certain of the special positions, 16d, Fd3m of the spinel structure. This substitution has the effect of reducing the structure to primitive cubic and, as a result, introduces mixed even-odd indices reflections for the $\gamma$-$Fe_2O_3$ (12, 20). In some $\gamma$-$Fe_2O_3$ preparations (14, 15), including the standard sample used in this laboratory,[3] faint extra reflections can be detected which can be indexed using a tetragonal cell (with $c_o = 3\ a_o$, where $a_o$ equals $a_o$ of the cubic cell). However, the principal lines of this pattern occur in the order of magnitude one would expect for the $LiFe_5O_8$ type structure, and, therefore, a close relation is evident. Bloom and Goldenberg (21) claim that the tetragonal cell occurs with the incomplete removal by oxidation of ferrous ions. In this paper, $\gamma$-$Fe_2O_3$ is regarded as cubic. In addition to the additional mixed even-odd reflections the $d$-values and angles for $\gamma$-$Fe_2O_3$ reflections are sufficiently different from those of the nearby $Fe_3O_4$ reflections to be easily identified. The $\gamma$-$Fe_2O_3$ reflections obtained for our patterns were closely matched to the standard values (16) and were easily distinguished from the standard values for $Fe_3O_4$ (17). We would label the oxide film on a particular iron orientation as "$\gamma$-$Fe_2O_3$" only if it had these extra spots and a lower lattice parameter.

*Validity of electron diffraction studies.*—There have been objections raised to the study of passive films out-of-solution, no matter what the technique. The most serious of these involved the possibility that the films undergo chemical or structural changes in the interval between formation and observation.

For our work, this objection can be met in a number of ways. First, after a passive film has been formed by anodic polarization, the circuit can be open for a considerable length of time before the specimen's potential relative to SCE will drop below the value characteristic of the passive region. A series of experiments in $H_2SO_4$ showed a decay time of more than 7 min when left in an acidic environment. Since our specimens were removed from solution and mounted in an evacuated chamber within 5 min, it seems reasonable to assume that the passive film had remained intact. This hypothesis was checked by passivating a specimen, removing it from solution, treating it in the same manner as required for electron diffraction work, and then replacing it in solution: the potential still remained in the passive range.

Second, the films formed in NaOH were very thick and difficult to dissolve (as can be seen in the decay experiments for this group, Table III). Since the patterns found for foils prepared in $H_2SO_4$ and borate were similar to those for the NaOH prepared foils, it is again reasonable to assume that the passive condition exists for foils prepared in all three solutions when they are under examination.

Finally, prepassive and transpassive films gave different results from those observed for passive films. If the passive films were changed during handling and observation, it is most likely that they would have become nonpassive. This did not happen for any of the NaOH films and occurred only rarely for the other films.

The possibility that the $\gamma$-$Fe_2O_3$ is formed by exposure to air does not seem apparent here as the exposure of the specimens to air and the vacuum environment of the diffraction apparatus is not great enough to produce the sort of lattice parameter variations as noted by Sewell, Stockbridge, and Cohen (4). Since all of the specimens receive approximately equal exposure, the considerable lattice parameter variations found between passive and nonpassive films could not be explained in this manner.

*Effect of chloride ions.*—When chloride ions were added to the solutions used, rings were always detected in the diffraction patterns of the films formed. These rings were found to be due to $\gamma$-FeOOH, in agreement with the previous work of Mellors *et al.* (18) for passive films formed in the presence of chloride in inorganic inhibitor solutions. Table II indicates that $\gamma$-FeOOH was also detected in some cases when films were formed in the active region. Since the $\gamma$-FeOOH was randomly oriented, it seems likely that it formed by precipitation from the solution rather than by direct growth on the metal surface.

## Discussion

This study shows that the structure and composition of the anodic passive film formed on iron is not dependent on the *p*H of the electrolyte, but only on the orientation of the surface on which it is formed. The

[2] The "weighting" factor is necessary since the lattice parameter is a function of $\sqrt{h^2 + k^2 + l^2}$ and the distortion is greater near the center and on the edges of the patterns. The negative plates were oriented and the same oxide and iron spots on each were used to approximate the actual distortion pattern. Then by casting an undistorted grid on the pattern, the percentage of "pull" on each spot could be calculated.

[3] This analysis was made from a sample kindly lent to the authors by Dr. M. C. Bloom, Naval Research Laboratory.

passive film gives electron diffraction patterns of $\gamma$-$Fe_2O_3$, whether it be formed by anodic polarization or by the use of an inorganic passivating solution and in each case shows the same epitaxial relationships to the iron substrate. Since the $\gamma$-$Fe_2O_3$ pattern contains all of the reflections of $Fe_3O_4$, it is possible that it is present along with the $\gamma$-$Fe_2O_3$. This assumption has its basis in the work of Nagayama and Cohen (2) who have suggested that it exists at the metal interface.

The interpretation of two oxide phases in the passive film is not new experimentally (1) nor is it unexpected theoretically (5). As was mentioned earlier, however, this study extends the pH range of the solutions studied from the neutral region of past studies to both the acidic and basic regions and shows that regardless of mode of formation, the nature of the film remains essentially the same.[4] More important, perhaps, than presenting evidence supporting the presence of $\gamma$-$Fe_2O_3$ in the passive film, are the results of this study obtained in the prepassive and transpassive regions showing the absence of $\gamma$-$Fe_2O_3$ and the presence of only $Fe_3O_4$. Had this not been found, the presence of $\gamma$-$Fe_2O_3$ in the passive film could be considered as only an interesting fact, but one not necessarily related to its being passive.

Since the presence of $\gamma$-$Fe_2O_3$ in the passive film appears related to the passive state of the metal, what special property does it have that differentiates it from the very similar $Fe_3O_4$ which we find in the nonpassive films? A recent suggestion has been made by Bloom and Goldenberg (21) who point out that a major difference between the two oxides is the great difference in their electrical conductivity, the $Fe_3O_4$ being a better conductor by many orders of magnitude. As Hoar (22) has pointed out, most current ideas concerning the conductivity of the passive film on iron consider it as being a good electrical conductor. This idea is mainly based on the fact that in going to the transpassive region large currents are easily passed, indicating a film of high conductivity. When the transpassive region is reached, this study shows that the film is no longer $\gamma$-$Fe_2O_3$, but is the relatively good conductor $Fe_3O_4$. In agreement with this we find that low conductivity $\gamma$-$Fe_2O_3$ is absent in these active films. Since $\gamma$-$Fe_2O_3$ is always associated only with a passive film, and it is a poor conductor, then passivity must require a film with an insulating outer layer if it has more than one layer. Recent kinetic studies from this laboratory (8) lend support to this hypothesis. However, no direct measurement, to our knowledge, has been made of the conductivity of the very thin outer $\gamma$-$Fe_2O_3$ layer in the passive film in order to settle this question. Another difference noted by Bloom and Goldenberg (21) is that $\gamma$-$Fe_2O_3$ does not have the formula, $Fe_2O_3$, but is probably similar to the lithium spinel $LiFe_5O_8$, the lithium being replaced by hydrogen to give $HFe_5O_8$. The structure of $HFe_5O_8$ can be derived from the $Fe_3O_4$ structure by systematically replacing four iron atoms in the special positions, 16d and Fd3m of the spinel structure with protons. The specific positions to be filled are: (5/8, 5/8, 5/8), (1/8, 7/8, 3/8), (3/8, 1/8, 7/8), and (1/8, 3/8, 7/8). These are the special positions 4b of the space group $P4_33$. The other positions of the spinel structure can be assigned to other sets of special positions of this space group (12). This revised structure would give, as does $LiFe_5O_8$, the extra reflections that were found in this study.

The other aspect of passivity dealt with in this study is the epitaxial relationship between films formed in the prepassive, passive, and transpassive regions of the anodic polarization curve and the iron substrate. The most unexpected finding is that a {110} iron surface bears a different epitaxial relationship to the film formed on it, depending on whether the film is passive or active. This is not true for any of the other substrate orientations studied, where both passive and nonpassive films gave the same epitaxial relationships. This special behavior of the {110} orientation agrees with previous studies which showed that, of all the other orientations studied, it exhibited greater pitting tendency (23) and that the passive films formed on it had larger numbers of breakdown sites (24). Both of these earlier findings also agree with the present result that the {110} plane showed a lesser tendency to retain the passive state on removal of the potential difference across the cell. This was usually not the rule for other substrate orientations, where the decay films would sometimes show similarities to the passive films.

The origin of this special behavior by the {110} plane (the closest packed plane in the bcc structure) is obscure. Attempts were made to establish any relationship between how well the metal ions in the oxide lattice matched the underlying atoms in the metal lattice and this change of orientation. Based on a simple matching of hard sphere crystal models, it appeared that the passive oxide orientation was a "better match" than the nonpassive. It is difficult, however, to relate the degree of misfit between oxide and substrate to film properties. This was shown by an investigation of the problem of misfit for another system (25), where it was not possible to relate the degree of oxide film-metal substrate misfit to protectiveness in a consistent manner. One would expect that the geometrical relationship between the film lattice and the metal lattice must determine the strain in the film and, hence, the grain size and the number and nature of imperfections. All of these will modify the intrinsic electrical characteristics of the film and determine the film's permeability to the movement of ions and, hence, its protective properties.

## Conclusions

1. $\gamma$-$Fe_2O_3$ is present in all passive films independent of the pH of the solution in which the films are formed, or the orientation of the iron substrate.
2. Films formed in the prepassive or transpassive regions of the polarization curve contain the $Fe_3O_4$ spinel structure and not the $\gamma$-$Fe_2O_3$ structure.
3. The epitaxial relationships between spinel film and substrate on all the orientations studied are the same for both passive and nonpassive films, with the exception of the {110} plane, which has different oxide orientations for the two states.

## Acknowledgments

The authors are grateful to D. Ballard for his help with the preliminary diffraction and to Mary Ann Giles who obtained the majority of the diffraction patterns used in this paper. They are also indebted to Brian Joiner for his aid in the statistical analysis of their data.

Manscript received Feb. 21, 1967.

Any discussion of this paper will appear in a Discussion Section to be published in the June 1968 JOURNAL.

## REFERENCES

1. J. E. O. Mayne and M. J. Pryor, *J. Chem. Soc.*, **1949**, 1831.
2. P. B. Hirsch, A. Howie, R. B. Nicholson, D. W. Pashley, and M. J. Whelan, "Electron Microscopy of Thin Crystals," p. 32, Butterworths, London (1965).
3. N. Nagayama and M. Cohen, *This Journal*, **109**, 781 (1962).
4. P. B. Sewell, C. D. Stockbridge, and M. Cohen, *ibid.*, **108**, 933 (1961).
5. K. J. Vetter, *ibid.*, **110**, 597 (1963).
6. O. Haase, *Z. Naturforsch*, **11a**, 46 (1956).

[4] One study of films formed in very concentrated $H_2SO_4$ gives very different results. This work by Riggs (19) studying films thick enough to be detected by x-ray diffraction found them to be composed of various sulfates. Such layers are not the thin films usually referred to as passive. Their different composition is not surprising considering the unusual environment.

7. Hirsch, Howie, Nicholson, Pashley, and Whelan, *op cit.*, p. 112
8. J. Kruger and J. P. Calvert, *This Journal*, **114**, 43 (1967).
9. Hirsch, Howie, Nicholson, Pashley, and Whelan, *op. cit.*, p. 132.
10. *Ibid.*, p. 117.
11. C. E. Hall, "Introduction to Electron Microscopy," pp. 131-4 McGraw-Hill Book Co., New York (1953).
12. H. E. Swanson, H. F. McMurdie, M. C. Morris, J. H. DeGroot, E. H. Evans, S. J. Carmel, Standard X-Ray Diffraction Powder Patterns, NBS Report #9367 (1966).
13. R. W. G. Wyckoff, "Crystal Structures," Vol. 3, pp. 75-85, Interscience Publishers, Inc., New York, (1965).
14. D. R. Dasgupta, Geol. Survey, Calcutta, India.
15. Schrader and Buttner, *Z. anorg. u. allgem. chem.*, **320**, 205 (1963).
16. Haul and Shoon, *Z. Phys. Chem.*, **44**, 216 (1939).
17. E. Z. Basta, *Min. Mag.*, **31**, 431 (1957).
18. G. W. Mellors, M. Cohen, and A. F. Beck, *This Journal*, **105**, 322 (1958).
19. W. E. Boggs, *ibid.*, **114**, 32, (1967).
20. O. L. Riggs, Jr., *Corrosion*, **20**, 275t (1964).
21. M. C. Bloom and L. Goldenberg, *Corrosion Sci.*, **5**, 623 (1965).
22. T. P. Hoar, D. C. Mears, and G. P. Rothwell, *ibid.*, **5**, 279 (1965).
23. J. Kruger, *This Journal*, **106**, 763 (1959).
24. J. Kruger, *ibid.*, **110**, 654 (1963).
25. K. R. Lawless and A. T. Gwathmey, *Acta Met.*, **4**, 153 (1956).
26. J. B. Wagner, K. R. Lawless, and A. T. Gwathmey, *Trans. Met. Soc. AIME*, **221**, 257 (1961).
27. Hirsch *et al.*, op. cit. p. 323.

# Passivation of Aluminum by Chromate Solutions

**M. A. Heine and M. J. Pryor**

*Metals Research Laboratories, Olin Mathieson Chemical Corporation, New Haven, Connecticut*

ABSTRACT

Passive films of $\gamma$-$Al_2O_3$ formed on aluminum by chromate solutions exhibit lower ionic resistance and higher electronic resistance than amorphous thermal films of the same thickness. The low ionic resistance is attributed to the formation of some crystalline $\gamma$-$Al_2O_3$ of very low ionic resistance at the oxide solution interface. The high electronic resistance is attributed to the inclusion of some protons in the passive film. A detailed mechanism for the passivation process is advanced.

Despite the numerous studies of the passivation of ferrous metals by chromate solutions, comparatively little has been published on the mechanism by which they inhibit the corrosion of aluminum. Mears and Brown (1) in an early study reported that chromates were effective in polarizing the local anodes on aluminum but did not specify a detailed mechanism. Later Edeleanu and Evans (2) suggested that chromate ions and aluminum underwent a redox reaction to form aluminum oxide and chromic ions. One of the authors (3) subsequently conducted an electrochemical-electronoptical study of inhibition of the corrosion of aluminum by sodium chromate solutions within the *p*H range of 2.5-9.5. The passive films were found to be somewhat thicker than the air-formed oxide film on aluminum and were duplex in nature, with an underlying layer of amorphous $\gamma$-$Al_2O_3$ being overlaid by a few angstroms of microcrystalline $\gamma$-$Al_2O_3$ exhibiting sharp spotty diffraction patterns.

It was deduced that passive films grew for a few hours on initially film-free aluminum with inverse logarithmic (or logarithmic) kinetics and thereafter thickened at a somewhat slower rate. This observation was considered to support a high field growth mechanism for the passive film with the enhanced field being supplied by the high adsorbed charge density in chromate solutions as compared with dry oxidation. Aluminum ions migrating to the oxide-solution interface were considered to be oxidized to $\gamma$-$Al_2O_3$, with the chromate ions being reduced to the trivalent condition. It was further suggested that passivation was a kinetic balance between film growth and film dissolution, the former being sensitive to chromate concentration and the latter to *p*H.

At the time when the former study (3) was conducted, techniques were not readily available to determine the ionic and electronic resistance of thin surface films on aluminum. Consequently, the earlier study was not able to throw light on any differences in conduction characteristics between passive (chromate) and amorphous thermal films of similar average thickness. In the intervening years such techniques have been developed in the writers' laboratory and chloride degradation of $\gamma$-$Al_2O_3$ films has been extensively studied (4-7). Accordingly, the primary purpose of the present work was to study the a-c resistance characteristics of passive films formed on aluminum by chromate solutions. The results have been compared with those obtained previously on thermal and barrier layer anodic films of similar thickness so that some more detailed view of the defect structure of passive films and its relation to the passivation process could be formed. The effects of chloride ions on the resistance of passive films has also been studied with a view to determining why chromates are so effective in preventing corrosion of aluminum by chloride ions.

## Experimental

*Materials.*—The aluminum used was in the form of annealed 0.37 mm thick sheet having a purity of 99.997%. The impurities were 0.001% Cu, 0.001% Fe, 0.001% Si. All passivating chromate solutions were made up from A.R. grade chemicals and distilled deionized water and were adjusted to *p*H 6 by the addition of sodium dichromate unless otherwise indicated. All studies were carried out at 25° ± 0.05°C.

*Experimental methods.*—Passive films were mainly formed in 1.0M sodium chromate solution on aluminum specimens carrying an original air-formed oxide film and on caustic etched (and essentially film free) aluminum. The air-formed oxide films were formed by 24 hr exposure to dry air of 6 $cm^2$ aluminum specimens that had originally been etched in 0.5*N* NaOH solution at room temperature for 15 min followed by

less than 1 sec immersion in 50% nitric acid at 85°C. This surface pretreatment produces a slightly scalloped, reproducible, surface having a roughness factor of 1.2 and has been described in detail previously (8). The advantage of this particular surface is that reproducible, high resistance, contamination free, oxide films may be subsequently formed on it by a variety of oxidation processes. Essentially film-free aluminum surfaces were obtained as a starting condition by etching the specimens in 0.5*N* sodium hydroxide solution for 15 min, rapidly rinsing in distilled deionized water, and immediately inserting the specimens into the passivating chromate solution.

Film resistance studies were carried out at frequencies from 1-100 kc using a General Radio Type 716-C capacitance bridge and associated type 716-P4 guard circuit; the measurements were conducted in a separate solution of molar sodium chromate at *p*H 7 as has been described in earlier publications (6, 7). A 50 mv p-p signal was employed throughout with masked specimen areas of 0.02 cm². The neutral chromate solution will form thin films having a thickness greater than around 20-25Å (the passive film thickness) in a uniform manner, thereby permitting a-c resistance profiles to be obtained at various frequencies. In the case of passive films formed by simple immersion in 1.0M chromate solution, resistance profiles could not be obtained by this method because the initial films were already at their terminal passive thickness. Accordingly, after forming passive films by simple immersion for a period of 24 hr at 25°C they were thickened slightly by constant current anodizing in 1.0M sodium chromate solution at *p*H 6.0. Constant current anodizing was performed at 1 $\mu$a/cm². The potential of the specimen was monitored until the total film thickness was around 37Å. The times required to form the 37Å thick passive films varied between 45 and 90 min depending on the particular solution used and the surface condition prior to passivation. The additional passive film so produced was compact and quite dissimilar to the porous thick films produced at much higher voltages in chromates (3). Under no condition was the potential of the specimens during anodic polarization permitted to rise above +1.0v on the hydrogen scale. Such films could then be thinned back to around 20-25Å in 1.0M sodium chromate solution at *p*H 7, and resistance profiles developed for the exterior portions of the passive films. A simple analogue of a capacitor with a parallel resistance was used to represent the electrical behavior of the films. Corrections for solution resistance were made at all frequencies.

Some experiments were conducted on specimens carrying passive films that had not been thickened anodically. These films were formed in 1.0 and 0.01M sodium chromate both free from and containing one tenth and equal concentrations of sodium chloride solution. Passive films were formed on 6 cm² specimens carrying an original air-formed oxide film by simple immersion for 6 hr in the passivating chromate solution of varying chromate and chloride ion concentrations. The specimens were again masked to expose an area of 0.02 cm²; the thickness and a-c resistance of these films were determined at 1 kc only by immersion in fresh solutions of 1.0M sodium chromate solution at *p*H 6 since here, thinning rate of the films is at a minimum.

## Results

Plots of parallel a-c resistance *vs.* thickness[1] at frequencies of 1, 10, and 100 kc are shown in Fig. 1-3. These results all pertain to passive films formed in 1.0M sodium chromate at *p*H 6 which had been subsequently thickened to around 37Å by constant current anodizing at 1 $\mu$a/cm². Each figure contains experimental points determined on quadruplicate specimens both freed from and carrying an original air-formed oxide film.

[1] From capacitance measurements at 1 kc.

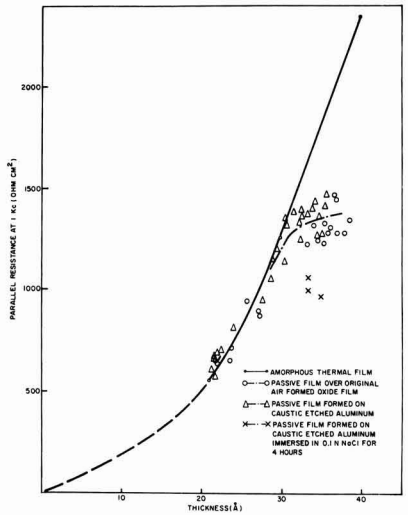


**Fig. 1. Relation between parallel a-c resistance at 1 kc and thickness of an amorphous 350°C thermal film and of passive films formed on aluminum in 1.0M sodium chromate solution at *p*H 6 and at 25°C.**

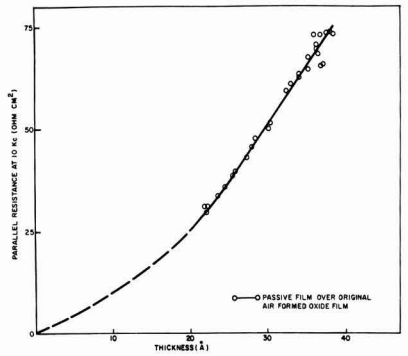


**Fig. 2. Relation between parallel a-c resistance at 10 kc and thickness of passive films formed on aluminum in 1.0M sodium chromate solution at *p*H 6 and at 25°C.**

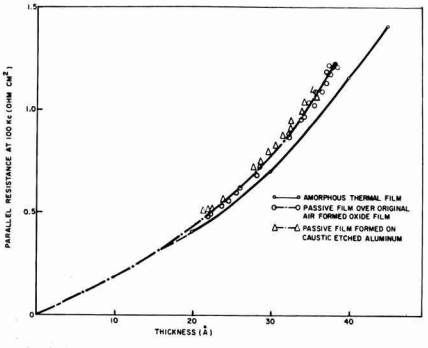


**Fig. 3. Relation between parallel a-c resistance at 100 kc and thickness of an amorphous 350°C thermal film and of passive films formed on aluminum in 1.0M sodium chromate solution at *p*H 6 and at 25°C.**

In Fig. 1 and 3 the parallel resistance results on the passive films are compared with previous results obtained on amorphous thermal films of the same average thickness (8) (350°C for 20 hr at $P_{O_2}$ = 76 Torr). These in turn are identical to resistance results also obtained previously on amorphous barrier layer anodic films formed in neutral ammonium tartrate solution (6, 8). It may be seen from Fig. 1 that, at a frequency of 1 kc, the a-c resistance of the passive films is identical to that of thermal and barrier layer anodic films until a film thickness of around 30Å has been achieved; thereafter, and at higher thicknesses, the a-c resistance of the passive films becomes much less than that of amorphous thermal films. The resistance profile of passive films at 1 kc was not affected by whether the passivation was conducted on specimens carrying a 20Å air-formed oxide film or on essentially film-free aluminum. Also included in Fig. 1 are three points representing the total resistance of specimens carrying a 35Å thick passive film which has been formed as described above and which had then been immersed in 0.1M sodium chloride for 4 hr at 25°C. Such immersion is known to produce no change in the thickness, crystallographic structure or topography of $\gamma$-$Al_2O_3$ films on aluminum (5). A significant reduction in a-c resistance of the passive films at 1 kc was observed.

At the highest frequency studied in this work, *i.e.*, 100 kc, substantially different results were obtained (Fig. 3). Again, the results obtained on passive films were compared with results obtained previously on amorphous thermal films (8, 9) and on barrier films formed in neutral ammonium tartrate (6, 7). Figure 3 shows that the high-frequency a-c resistance of the passive films is significantly higher than that exhibited by amorphous thermal films. Again, the results in Fig. 3 are individual points from quadruplicate specimens with the two initial surface conditions. Also, the results obtained are independent of whether the passive films were formed on top of an original air-formed oxide film or on caustic etched aluminum. The experiment in which the passive film formed in 1.0M sodium chromate at *p*H 6 and the specimen then exposed for 4 hr to 0.1M sodium chloride solution at 25°C was repeated. At 100 kc, exposure to chloride solution produced no detectable lowering of film resistance.

At 10 kc (Fig. 2) the results on the passive films more closely parallel the results of 100 kc than at 1 kc. Such behavior has been noted previously in barrier layer anodic films exposed to sodium chloride solution (5).

It is also possible to obtain from the previous experiments information on the kinetics by which the various films are thinned by the 1.0M sodium chromate solution at *p*H 7.0 from their initial thickness of around 37Å to their terminal thickness of around 25Å. In such instances the measurement of capacitance as a function of time permits calculation of the average thickness of oxide removed at any interval of measurement. The thinning rates of the 350°C thermal film together with those of 37Å thick passive films grown on aluminum freed from and carrying an original air-formed oxide film are shown in Fig. 4.

A final series of experiments was conducted on passivation in 1.0 and 0.01M sodium chromate solutions at *p*H 6 with and without various additions of sodium chloride as described earlier. The a-c resistivity results on replicate specimens at 1 kc are shown in Fig. 5. In 1.0M sodium chromate solution at *p*H 6, the simultaneous presence of a chloride ion concentration of 0.1M resulted in, at best, a slight drop in film resistivity. A significant drop in film resistivity was observed when the chloride concentration in the chromate solution was increased to 1.0M. In all experiments, the aluminum remained passive throughout. In the absence of chloride the initial film resistivity in 0.01M sodium chromate was only around 70% of that in the 1.0M chromate solution. The presence of

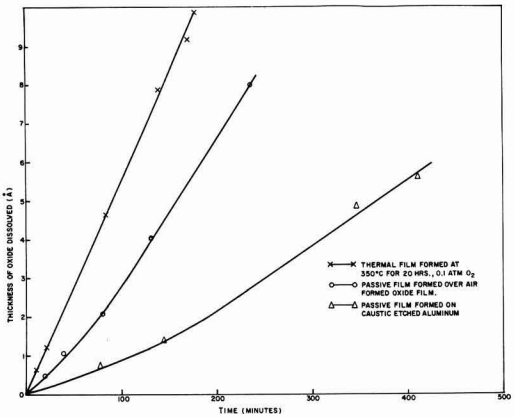


**Fig. 4. Relation between time and average oxide thickness removed in 1.0M sodium chromate solution at *p*H 7 for an amorphous 350°C thermal film and for passive films formed in 1.0M sodium chromate solution at *p*H 6 on aluminum carrying and freed from its original air-formed oxide film.**

chloride ions at a concentration in 0.001M resulted in no change in low-frequency film resistivity; further, the simultaneous presence of 0.01M sodium chloride resulted in a slight rise in film resistivity, although the magnitude of the rise is of somewhat dubious experimental significance. The addition of chloride to the passivating chromate solutions had no effect on film resistivity at 100 kc as had been observed in Fig. 3 and in past work (5-7).

## Discussion

The primary objectives of the present work were: (*a*) to improve understanding of how chromate solutions alone passivate aluminum and (*b*) to obtain information on why chromate ions are so effective in preventing corrosion of aluminum by chloride solutions. The low-frequency (1 kc) a-c resistance profiles of passive films (Fig. 1) show that passive film resistance is identical to that of amorphous thermal films until the film thickness exceeds around 30Å. Thereafter and at higher thicknesses low frequency a-c resistance of passive films is substantially less than that of amorphous thermal and barrier layer anodic films. At best, at the natural passive film thickness of around 25Å a-c resistance at 1 kc can be no higher than that of the less protective thermal films and may well be less. Against this background it is not surprising that identical results were obtained at

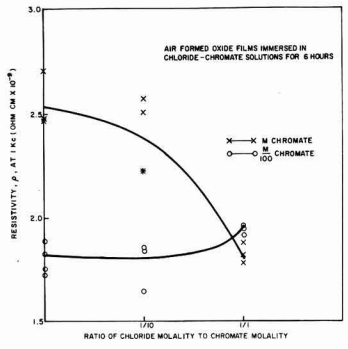


**Fig. 5. Effect of chloride ion concentration on the parallel resistivity at 1 kc of passive films formed on aluminum by 1.0 and 0.01M sodium chromate solutions at *p*H 6.**

1 kc irrespective of whether the aluminum specimens carried an air-formed oxide film or were initially freed from oxide by etching in caustic soda.

Very similar low-frequency resistance profiles have been observed previously on thermal films formed at high temperatures in excess of 450°C (8). A marked reduction in the slope of the resistance/thickness curves, almost identical to that in Fig. 1, occurred when well-defined crystals of $\gamma$-$Al_2O_3$ nucleated and grew at the amorphous oxide-metal interface. Electronoptical studies of the thermal $\gamma$-$Al_2O_3$ crystals (8) showed the presence of extensive faulting, and it was suggested that enhanced ionic conduction took place at these internal surfaces. Crystalline $\gamma$-$Al_2O_3$ also forms during passivation in chromates but at the oxide-solution interface. Figure 1 suggests that this crystalline oxide also has a very low resistivity at 1 kc compared with amorphous $\gamma$-$Al_2O_3$ and that a significant quantity in terms of average thickness must be present before it is easily detected by the capacitance-loss method. Since natural passive films, formed without auxiliary anodic polarization, also show crystals at the oxide-solution interface it is almost certain that these films do not have as high an a-c resistance at 1 kc as amorphous thermal films of identical thickness.

Considerable previous study has been devoted to clarifying the interpretation of the frequency dispersion of the a-c resistance of films of $\gamma$-$Al_2O_3$ (5-7). Most impurity defects in $\gamma$-$Al_2O_3$ appear to have characteristic relaxation times of around $10^{-4}$ sec (4). Accordingly, details in the a-c resistance *vs.* thickness curves seen at frequencies below 10 kc but not above 10 kc pertain to ionic relaxation effects and are related to d-c ionic conduction through the films. Details seen above 10 kc similarly are related to d-c electronic conduction through the films.

Against this background it appears that the amorphous part of the passive film has a virtually identical ionic resistance to that of a similar thickness of amorphous $\gamma$-$Al_2O_3$ formed thermally. When crystalline $\gamma$-$Al_2O_3$ forms at the outer surface of the amorphous film during passivation it exhibits much lower ionic resistance, similar to that of the crystalline portion of thermal films formed above 450°C and probably for the same reasons (8). This observation explains why a deviation from inverse logarithmic growth kinetics, calculated from potential data, was observed after a few hours in earlier work (3). The earlier corrosion potential measurement sensed ionic resistance of the film in a crude and approximate fashion (3). As long as the passive film grew by a high field mechanism and as long as the oxide so produced had ionic resistance characteristics similar to those of barrier layer anodic films, growth kinetics should be inverse logarithmic with time (10). However, as some crystalline oxide of much lower ionic resistivity was produced then the potential measurements will not sense this new oxide quantitatively and growth kinetics calculated from such electrochemical measurements will deviate from an inverse logarithmic law.

From the foregoing it is clear that considerations of ionic resistance alone provide no explanation for the unusually protective nature of passive films on aluminum. Indeed, the passive films will exhibit somewhat inferior ionic resistance to amorphous thermal films, the relative inferiority increasing with the proportion of crystalline $\gamma$-$Al_2O_3$ in the over-all passive film. However, Fig. 4 indicates one area of the complex process of passivation where the presence of crystalline $\gamma$-$Al_2O_3$ may be helpful. It may be seen that the dissolution rate of the outer crystalline portion of passive films formed on aluminum either carrying or freed from an original air-formed oxide film is much less than that of the underlying amorphous $\gamma$-$Al_2O_3$. Since passivation by chromates is believed to involve a kinetic balance between film formation and film dissolution (3) any factor that retards film dissolution should aid in increasing passive film thickness. Similar low dissolution rates of crystalline $\gamma$-$Al_2O_3$ have been observed previously in studies of duplex thermal films formed above 450°C and possible reasons for this behavior have been advanced (8). Similar reasons are believed to be valid for crystalline $\gamma$-$Al_2O_3$ formed during passivation. The linear slope of the dissolution curve for the passive film formed on aluminum carrying an original air-formed oxide film is only slightly less than that for the 350°C thermal film. The linear slope of the dissolution curve for the passive film formed on caustic etched (and essentially film-free) aluminum is much lower than either of the other two curves. No convincing explanation can be offered for this behavior at the present time. The effect cannot be related to an effect of surface preparation on the amount of crystalline phase because the low frequency resistance-thickness curves are identical for the two surface conditions (Fig. 1).

The high frequency (100 kHz) a-c resistance *vs.* thickness curves (Fig. 3) throw additional light on the reasons for the highly protective nature of passive films on aluminum. At all thicknesses studied a-c resistance at 100 kc was significantly higher for passive films formed in chromate solutions than for similar thickness amorphous films formed thermally at 350°C (8) or anodically in ammonium tartrate solution (6, 7). Crystalline $\gamma$-$Al_2O_3$ does not reduce high-frequency a-c resistivity of duplex thermal films formed above 450°C (8, 9) and from Fig. 3 exhibits similar behavior when formed in chromate solutions. Again no effect of initial surface condition was found in these experiments. The form of the a-c resistance *vs.* thickness curves at 100 kc for thermal and barrier layer anodic films is a very accurate parabola (9) for distances up to 90Å from the oxide-metal interface. At greater thicknesses the resistance is a linear function of thickness (6, 7). Heine and Sperry (9) interpreted these results as meaning that 90Å is the limit of thickness of $\gamma$-$Al_2O_3$ at which a conductivity effect due to excess metal arising from the proximity of the metal substrate disappears. At thicknesses lower than this value, conductivity is an inverse function of distance from the metal interface (on account of the parabolic nature of the $R_p$ *vs.* thickness curve) and so the concentration of excess metal current carriers must also vary inversely with distance from the metal interface. Heine and Sperry (9) accepted the earlier model of Grunberg and Wright (11) for the probable defect structure in the vicinity of the oxide-metal interface, *i.e.*, an F′ center structure with excess metal existing as missing oxygen ions with two electrons trapped per oxygen vacancy. Since high-frequency a-c resistance singularities have been related to similar singularities in electronic d-c resistance (5-7) the foregoing implies that electronic conduction through these films to a thickness of 90Å is controlled primarily by the loosely bound electrons in the F′ center defect structure. The form of the 100 kc a-c resistance *vs.* thickness curve for passive films is also a parabola from Fig. 6 but with a greater slope than that for thermal films. This implies higher electronic resistance at any thickness due to the presence of somewhat fewer loosely bound electrons. Such defect structure could logically arise from the relatively uniform incorporation of some water or $H^+$ in the $\gamma$-$Al_2O_3$. $\gamma$-$Al_2O_3$ is a defect spinel with a close packed fcc oxygen lattice. The cation lattice is poorly understood, but could well contain a number of vacant sites. If a $H^+$ were to enter the oxide, either in one of the vacant cation sites or interstitially, one electron would have to be added for electrical neutrality and electronic resistance would decrease. Such is clearly not the case from Fig. 3. If however, a proton were to replace an aluminum ion, two electrons would have to be removed to maintain electrical neu-

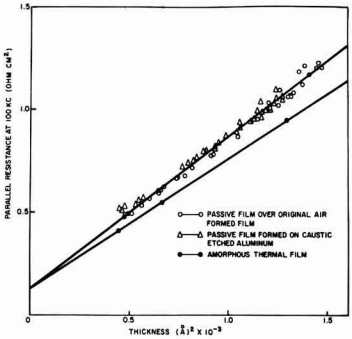


**Fig. 6. Relation between parallel a-c resistance at 100 kc and (thickness)$^2$ of an amorphous 350°C thermal film and of passive films formed on aluminum in 1.0M sodium chromate solution at pH 6 and at 25°C.**

trality, and electronic resistance would increase without any change in ionic resistance. This explanation is consistent with the experimental data in Fig. 1 and 3. Calculations from earlier data (4) would suggest a substituted $H^+$ concentration of around 1 pt in $10^5$ or less. Similar explanations can be derived for the substitution of water, but the present work provides no means of distinguishing these alternatives.

From the foregoing considerations a more detailed mechanism for the passivation of aluminum by chromate solutions may now be advanced. First a redox reaction appears to be involved in passivation as suggested by Edeleanu and Evans (2). Chromate ions from solution are likely strongly and specifically adsorbed on the metal, if it is originally film free, or on an air-formed oxide film as is the more normal condition. This contention is supported by the earlier detection of $Cr^{6+}$ on the surface of passivated iron (11). The adsorbed charge density from the small divalent $CrO_4^=$ ion should be higher than that pertaining during dry oxidation from the formation and adsorption of the energetically more probable O′ ion. Accordingly, a higher than limiting field should exist across any pre-existing air-formed oxide film. Ionic migration will accordingly commence. As migrating aluminum ions arrive at the oxide-solution interface they become oxidized to $\gamma$-$Al_2O_3$ with $Cr^{6+}$ ions becoming reduced to $Cr^{3+}$ although the latter species has not been detected to date. The film will thicken until the limiting field of somewhat less than $10^7$ v/cm is re-established. The amorphous portion of the passive film appears to be formed at field strengths significantly above the limiting field strength; the outer crystalline portion of the passive film appears to form at field strengths only slightly above or at the limiting field.

Because the passive film is duplex in nature the passivation reaction does not proceed in an identical manner to the more widely studied anodic film formation. During the time when the passive film is amorphous, electrochemical information indicates that the growth kinetics are logarithmic or inverse logarithmic, *i.e.*, in accord with a high field mechanism. The amorphous part of the passive film has the same ionic resistance at any thickness as a thermal or a barrier layer anodic film. Simultaneously it exhibits higher electronic resistance than comparable thermal films probably due to inclusion of small quantities of $H^+$ or water and so is more protective. As the low ionic resistance crystals appear at the outer surface of the passive film, electrochemical measurements do not sense the new low-resistance film adequately, and kinetics calculated from these measurements appear to deviate from the former growth law. However, the new crystalline film still contributes to the high electronic resistance of the passive film, being indistinguishable in this respect from the amorphous part of the passive film. It further dissolves in the passivating solution at a lower rate than the amorphous substrate and tends to protect against the competitive film dissolution process. Excellent evidence of this may be found from earlier work. Capacitance measurements (sensitive to the presence of both crystalline and amorphous $\gamma$-$Al_2O_3$) showed that passive film thickness was constant between *p*H 6 and 9 (6). Electrochemical measurements (3), not as sensitive to the presence of low ionic resistance $\gamma$-$Al_2O_3$ crystals, had been interpreted (erroneously) as meaning that passive film thickness is at a maximum at *p*H 6 and decreases with increasing or decreasing *p*H. These observations can now be reconciled as follows. Passive film thickness from capacitance measurements is not *p*H dependent between 6.0 and 9.0 (6). However, ionic resistance by electrochemical measurement (3) does decrease with increasing *p*H above 6.0. It appears that the proportion of low resistance crystalline $\gamma$-$Al_2O_3$ phase must be at a minimum at *p*H 6 and increases as the *p*H moves in the alkaline or acid direction. This contention is supported by earlier potential-time curves (3) which showed that serrated potential-time traces, characteristic of the formation of crystalline $\gamma$-$Al_2O_3$, initiated at lower potentials when *p*H was moved from 6.0 in either direction. Furthermore, the onset of these serrations (crystal formation) was dependent at constant *p*H on the chromate concentration, occurring at lower potentials as the chromate solution was diluted. Accordingly, the proportion of crystalline $\gamma$-$Al_2O_3$ in the film, being *p*H (minimum at *p*H 6.0) dependent and chromate concentration dependent (decreasing with increasing concentration) has a marked influence on the electrochemical properties of the over-all film. The proportion of crystals has little or no effect on the total thickness of film or on its very high electronic resistance both of which are important components of its unusual protective action. The proportion of crystalline phase profoundly modifies ionic resistance of the film which decreases with increasing proportion of crystals. This effects the electrochemical response of the passivated aluminum more than the protective action of the duplex film since an increasing proportion of crystalline $\gamma$-$Al_2O_3$ phase also implies a reduction of the rate of dissolution in the passivating medium.

Finally, there remains the question of the means by which chromate solutions prevent corrosion of aluminum by chloride ions in such an effective manner. The influence of chloride ions on aluminum covered with amorphous $\gamma$-$Al_2O_3$ has been studied in some detail earlier by the authors (5-7). In the absence of chromate, chloride ions can enter the $\gamma$-$Al_2O_3$ lattice, create cation vacancies and lower ionic (1 kc) resistance without changing electronic (100 kc) resistance. $\gamma$-$Al_2O_3$ containing small amounts of substituted Cl′ also dissolves more rapidly in sodium chromate at *p*H 7 than unsubstituted $\gamma$-$Al_2O_3$. The effect of the simultaneous presence of chromate and chloride ions on aluminum is presented in Fig. 5 at chromate concentrations of 1.0 and 0.01M. The study was confined to one frequency (1 kc) which is sensitive to chloride inclusion in the film and to the natural passive film thickness (around 25Å in both solutions). First, it may be seen that the resistivity of the passive film in 0.01M chromate is only about 70% of that in 1.0M chromate. The passive film thicknesses are identical from capacitance measurements, and the difference in resistivity may be attributed to a higher proportion of crystalline $\gamma$-$Al_2O_3$ of low ionic resistance in the more dilute passivating solution. When the two chromate solutions contain sodium chloride at a concentration of one tenth the chromate concentration, *i.e.*, 0.1 and 0.001M, respectively, no significant change in passive film thickness or resistivity is seen at 1 kc. When passivation is conducted in the two chromate solutions with equal concentrations of sodium chloride (1.0 and 0.01M) the thickness of the

passive film again remains constant. However, passive film resistivity decreases in the concentrated (1.0M) solutions and remains essentially unchanged in the dilute (0.01M) solutions. The effects of the chloride in the simultaneous presence of chromate could be due to one of two causes: (*a*) a reluctance of chloride to enter the crystalline $\gamma$-$Al_2O_3$ and penetrate to the amorphous layer where its effect at 1 kc should be large. Such behavior has been noted in high-temperature crystalline $\gamma$-$Al_2O_3$ (8); and (*b*) an adsorption effect whereby chromate prevents simultaneous adsorption of chloride on the film surface. In the absence of specific adsorption of $Cl'$ ions their entry into the $\gamma$-$Al_2O_3$ lattice is not considered possible.

In order to distinguish between these alternatives, passive films were formed in 1.0M chromate on aluminum as described earlier and thickened anodically to around 35Å thereby increasing the amount of crystalline $\gamma$-$Al_2O_3$. After this treatment the specimens were rinsed and immersed in chromate free 0.1M NaCl solution at *p*H6 for 4 hr. The low-frequency (1 kc) resistance of the total film was then measured in the standard manner at *p*H 6 in the absence of film thinning. The results in Fig. 1 show a marked decrease in ionic resistance for these specimens. If this result is compared with the fact that the same concentration of chloride (0.1M) when present in combination with 1.0M sodium chromate permitted growth of a passive film of undiminished resistivity at 1 kc (Fig. 5), it is clear that explanation (*a*) is untenable. Indeed the stability of passive film formed in the combined presence of chromate and chloride must be due to a relative adsorption effect whereby the chromate ions are specifically adsorbed on the growing oxide so strongly that they will displace chloride from the surface at least up to a certain critical concentration level. The fact that the relative critical chloride concentrations differ with the chromate concentration also supports such a view. This conclusion is consistent in part, with views expressed on chromate and chloride adsorption on passive iron by Matsuda and Uhlig (12). It receives direct experimental support from the zeta potential studies of O'Connor *et al.* (13) on corundum, $\gamma$-$Al_2O_3$ and Al·O·OH which indicated a much stronger specific adsorption for divalent $CrO_4''$ ions on these oxides. This conclusion also indicates that the protection against chloride corrosion is only obtained in the simultaneous presence of chromate and that once the latter is removed, film degradation by chloride ions can proceed in a normal fashion.

### Acknowledgment

The authors wish to acknowledge, with thanks, the financial support of this work by the Aluminum Division of the Olin Mathieson Chemical Corporation and their permission to publish the results.

Manuscript received Nov. 3, 1966.

Any discussion of this paper will appear in a Discussion Section to be published in the June 1968 JOURNAL.

### REFERENCES

1. R. B. Mears and R. H. Brown, *This Journal*, **97**, 75 (1950).
2. C. Edeleanu and U. R. Evans, *Trans. Faraday Soc.*, **65**, 683 (1949).
3. M. J. Pryor, *Z. Elektrochem.*, **62**, 782 (1958).
4. J. J. McMullen and M. J. Pryor, First International Congress on Metallic Corrosion, p. 52, Butterworths, London (1961).
5. A. F. Beck, M. A. Heine, D. S. Keir, D. van Rooyen, and M. J. Pryor, *Corrosion Sci.*, **2**, 133 (1962).
6. M. A. Heine and M. J. Pryor, *This Journal*, **110**, 1205 (1963).
7. M. A. Heine, D. S. Keir, and M. J. Pryor, *ibid.*, **112**, 24 (1965).
8. A. F. Beck, M. A. Heine, E. J. Caule, and M. J. Pryor, *Corrosion Sci.*, In press.
9. M. A. Heine and P. R. Sperry, *This Journal*, **112**, 359 (1965).
10. A. Guntherschulze and H. Betz, *Z. Physik*, **71**, 106 (1933).
11. N. Hackerman and R. A. Powers, *This Journal*, **100**, 314 (1953).
12. S. Matsuda and H. H. Uhlig, *ibid.*, **111**, 156 (1964).
13. D. J. O'Connor, P. G. Johansen, and A. S. Buchanan, *Trans. Faraday Soc.*, **52**, 229 (1956).

# Theory of Organic Corrosion Inhibitors

## II. Electrochemical Characteristics of Iron in Acidic Solutions Containing Ring-Substituted Anilines

**Francis M. Donahue,[1] Akitane Akiyama,[2] and Ken Nobe**

*Department of Engineering, University of California, Los Angeles, California*

### ABSTRACT

The effect of aniline and aniline derivatives on the electrochemical characteristics of iron in $H_2SO_4$ has been studied using relaxation techniques. Armco iron corrosion was found to be inhibited primarily by an adsorption mechanism. However, evidence was noted which suggested a contribution from a "surface chelate." Evidence for surface chelation was more pronounced in the case of zone-refined iron which showed a transition from a nearly "pure adsorption" to a predominant surface chelation process. Subsequent loss of inhibition with time by some organics has been attributed to charge transfer processes associated with the surface chelate.

An understanding of the structure-corrosion inhibition relationship of organic compounds may be obtained by: (a) empirically correlating observed corrosion rates of metals in the presence of inhibitors with physico-chemical measurements or correlation parameters [e.g., see ref. (1-4)]; (*b*) a detailed study of the electrochemical behavior of inhibited metal dissolution (5, 6); and (*c*) measurement of adsorption properties of metal-solution interfaces (2, 7).

An unequivocal solution to the structure-corrosion inhibition relationship is not to be anticipated from any of these techniques alone. In fact, unless the nature of the dissolution reaction itself is well under-

[1] Present address: Department of Chemical and Metallurgical Engineering, The University of Michigan, Ann Arbor, Michigan.
[2] Permanent address: Department of Applied Electrochemistry, Tokyo Institute of Technology, Tokyo, Japan.

stood, very little of fundamental significance can be gained from studies of inhibition. Therefore, this laboratory has undertaken the task of simultaneously studying the inhibited and uninhibited behavior of iron in acidic solution. The first paper in this series (4) was concerned with correlation of adsorption and inhibition behavior of organic compounds with phenomenological constants derived from physical-organic chemistry. Another paper (8) is associated with the detection and role of intermediates in the dissolution process. This paper and the one to follow (9) are associated with the electrochemical characteristics of inhibited dissolution and a study of empirical correlations of inhibitor data, respectively. A "final" paper (10) is a study of the uninhibited kinetics of iron. It is the authors' purpose to investigate in a systematic manner with several electrochemical techniques the structure-corrosion inhibition relationship of a series of organic compounds on two different iron samples.

The present paper considers the effect of the addition of organic compounds on the observed electrochemical behavior of iron. Thus, observations of the open-circuit potential (corrosion potential), polarization behavior, and differential capacitance will be used in the manner described below to deduce the role of the organic in the inhibition process.

The various theories of inhibition by organic compounds have been adequately reviewed in the literature (11, 12) and, hence, are not considered here. Whereas chemisorption was assumed as the mode of inhibition in the "Theoretical" aspect of this series (4), no assumptions are made with respect to the mode of inhibition here.

Kaesche (5) has suggested that observations of the shift of the open-circuit potential in the presence of an inhibitor permits the specification of which partial process is influenced by the inhibitor. In summary, his postulates are these: (*a*) shifts of the open-circuit potential in the positive direction indicate predominant interference with the anodic partial process; (*b*) shifts in the negative direction, the cathodic partial process is affected; and (*c*) no shift in open-circuit potential, both processes are affected to the same extent. The analysis tacitly assumes near constancy of the respective Tafel slopes, *i.e.*, no change in mechanism of the partial processes in the presence of the inhibitor. Therefore, mere measurements of open-circuit potentials cannot describe unequivocally the interaction of the organic with the partial processes, and it is necessary to polarize the electrode to verify the Tafel slope constancy.

Bockris (13) has suggested the following mechanism for iron dissolution

$$Fe + OH^- \rightleftarrows (FeOH)_{ads} + e^- \quad [1]$$

$$(FeOH)_{ads} \rightarrow (FeOH)^+ + e^- \quad [2]$$

$$(FeOH)^+ \rightarrow Fe^{+2} + OH^- \quad [3]$$

where step [1] is in quasi-equilibrium, step [2] is rate limiting, and step [3] is fast. In the light of this mechanism and techniques which have recently been developed (8), the rate constants for step [1] may be calculated from anodic charging curves under certain circumstances, *e.g.*, Armco iron in 1N $H_2SO_4$, and the rate of disappearance of the adsorbed intermediate may be deduced from decay measurements. In this manner the question of "deactivation" of the metal surface may find a partial resolution (5). Thus, an inhibitor which "stabilizes" the iron atom in the lattice will cause a shift in the equilibrium given by [1] and, thereby, change the ratio of the rate constants. From the theoretical development given before (8), this effect should be characterized by a decrease in adsorption pseudocapacitance (*i.e.*, surface coverage of intermediate) and an alteration of the shape of the charging curve.

If the effect of the inhibitor is on the adsorbed intermediate, *e.g.*, some sort of chelation mechanism, the evaluation is less direct. Consider the following

$$(FeOH)_{ads} + n\,I \rightleftarrows [(FeOH) \cdot I_n]_{ads} \quad [1a]$$

$$[(FeOH) \cdot I_n]_{ads} \rightarrow [(FeOH) \cdot I_n]^+ + e^- \quad [1b]$$

In step [1a] the adsorbed intermediate interacts with $n$ molecules of inhibitor I (at this point it is unnecessary to stipulate whether the inhibitor is adsorbed) to form a complex which is adsorbed on the surface. To the extent that the complex can undergo charge transfer, *i.e.*, step [1b], and desorb as a complex ion, a postulated inhibitor may in fact be an accelerator (see Experimental Results below). Likewise, the value of the equilibrium constant of [1a] ought to determine the extent of inhibition provided that the rate of [1b] is much slower than [2]. In addition, the values of the rate constants for [1a] should intimately affect the measured values of the rate constants for [1]. For example, should the rate constants for [1a] be much less than those of [1], then the anodic charging curve would be insensitive to the presence of the inhibitor. On the other hand, if the rate constants for [1a] (especially the forward constant) are equal to or greater than those of [1], then the charging curve should undergo a significant change in shape. Unfortunately, no theoretical analysis of the scheme suggested here has been worked out. However, such an alteration of the charging curve would be partial support for such a mechanism.

Since the rate-determining step for hydrogen evolution on Armco iron has been shown to be the first electron transfer step (14), such an analysis for the cathodic partial process is precluded. However, "deactivation" of the surface for hydrogen evolution would reveal itself in an alteration of the cathodic Tafel slope.

A simple blocking of the surface by adsorption of the inhibitor would decrease the area available to the respective partial processes and thereby decrease the apparent exchange currents in an identical fashion. Therefore, the open-circuit potential and Tafel slopes would remain unaltered. However, the adsorption pseudocapacitance would decrease linearly with increasing adsorption of the organic [provided the surface coverage of (FeOH) was less than 0.1 (8)]. In the same manner, the apparent double layer capacitance would also decrease on increasing adsorption of organic.

The foregoing discussion gives a rather qualitative picture of how one might attempt to ascertain information pertinent to the mode of inhibition of organic compounds using electrochemical techniques. In the text to follow an example of this approach is given.

## Experimental

The details of the experimental equipment and the procedure are given elsewhere (10). The materials used were Armco iron and a sample of zone-refined iron which was donated by the American Iron and Steel Institute (designated as Bar 65A) and prepared in rod form by Battelle Memorial Institute. The electrodes were of cylindrical form and were rotated at constant speed.

The organic compounds were purified before use by distillation at reduced pressure in a nitrogen atmosphere or by recrystallization (p-Toluidine). Boiling point ranges were $\leq 2°C$ and the melting point of p-Toluidine was 42°-43.5°C.

The determination of the rate constants was by the technique previously described (8).

## Results and Discussion

Figure 1 shows the effect of the addition of organic compounds on the open-circuit potential of Armco iron. The solid line shows behavior of uninhibited iron (10) for comparison. Aniline and p-Toluidine show deviation in the negative direction, while the remainder exhibit positive deviations. However, with the exception of p-Toluidine, the deviations are smaller

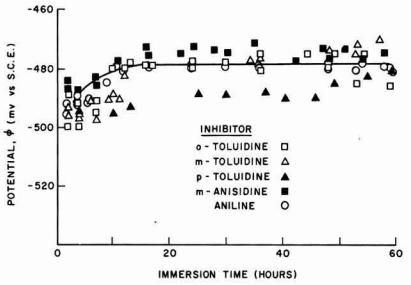


**Fig. 1. Open-circuit potential of Armco iron in the presence of 0.3M aniline and ring-substituted anilines. The solid line describes the behavior of uninhibited iron (10).**

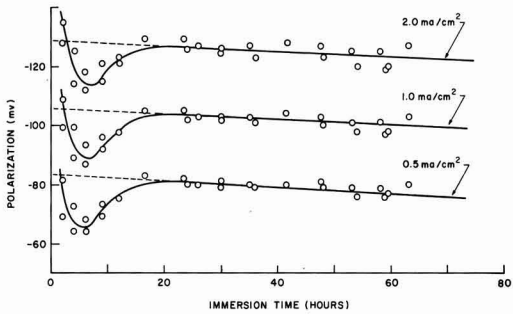


**Fig. 2. Cathodic polarization behavior of Armco iron electrodes in the presence of 0.3M aniline.**

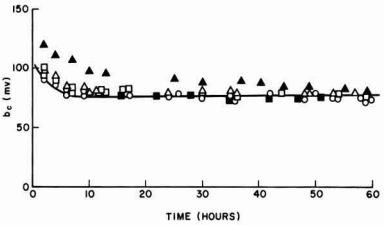


**Fig. 3. Cathodic Tafel slopes for aniline and ring-substituted anilines as a function of time of immersion. Solid line shows the data for uninhibited iron (10). See Fig. 1 for designation of symbols.**

than about 5 mv, which are smaller than those of Kaesche (5), and are not considered to be sufficient to permit ascribing any specific interaction with one or the other partial process.

Figure 2 shows the typical cathodic pulse polarization behavior observed for Armco iron. The minimum in polarization is characteristic of unannealed Armco iron electrodes (10) and does not reflect any effect of the inhibitor.

Figure 3 shows the variation of cathodic Tafel slope with time for inhibited Armco iron [again the solid line is presented to allow comparison with the uninhibited work (10)]. It can be seen that the inhibited samples (except p-Toluidine) follow the behavior of the uninhibited samples. This suggests that the cathodic partial process is essentially unaffected (in terms of reaction mechanism) by the presence of most of the organics. This is not true of p-Toluidine, which only approaches the uninhibited behavior as a limit at long immersion times. This behavior of p-Toluidine is consistent with other observations with this compound. Although it is chemically related to the other ring-substituted anilines, its behavior at the iron electrode seems to be quite anomalous.

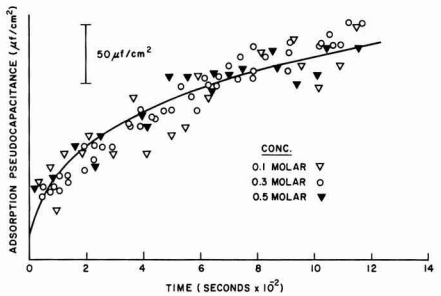


**Fig. 4. Adsorption pseudocapacitance observed during anodic polarization of iron in the presence of aniline. Solid line is curve for uninhibited iron (8). Current density, 1 ma/cm².**

One aspect of Fig. 3 which deserves comment at this time is the observation of rather low cathodic Tafel slopes. Values between 100 and 120 mv have been most frequently reported. In fact, previous work on this system (Armco iron/$H_2SO_4$) in this laboratory gave slopes of 100 mv (15). However, those experiments were usually completed within 2 hr after the samples were immersed. Those observations are in accord with the present work if one examines Fig. 3 at short times. Likewise, Kaesche (5) noted a range of Tafel slopes of 83-92 mv for uninhibited samples whose polarization data were obtained after 5 and 7 hr immersion time, again, in accord with the curve shown in Fig. 3. This underlines the need for investigators to stipulate at what time following immersion their data were obtained. Unless this is done, comparison of data among investigators may not be meaningful.

It has been shown elsewhere (8) that the slow achievement of a steady-state potential during anodic polarization is associated with the slow build-up of the surface concentration of the intermediate species (FeOH). It was also shown that an indirect measurement of this build-up could be made by determining the adsorption pseudocapacitance during the polarization by superimposing short galvanostatic pulses on the already existing signal. Figures 4 and 5 show the experimental results for aniline at three concentrations and some ring-substituted anilines, respectively. The agreement between the inhibited samples and their approximation to the uninhibited case is quite revealing as shown in Fig. 4 and 5. From this it may be surmised that the energetics of the initial electron transfer (see Eq. [1] above) seem to be independent of the presence of the organic or its chemical structure. Again it should be noted that p-Toluidine is an exception.

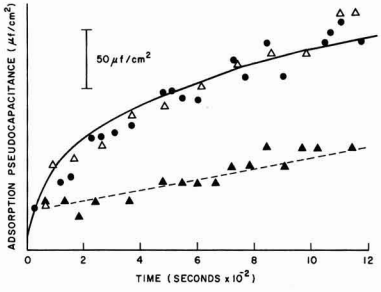


**Fig. 5. Adsorption pseudocapacitance observed during anodic polarization of iron in the presence of some ring-substituted anilines. Solid line is curve for uninhibited iron (8). Current density, 1 ma/cm². Compounds are: 0.1M as-received aniline (●), 0.3M m-Toluidine (△), 0.3M p-Toluidine ▲.**

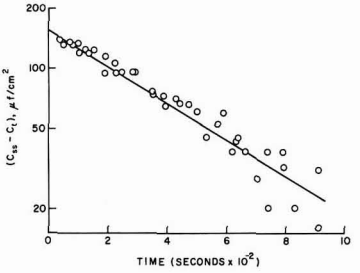


Fig. 6. Experimental test of Eq. (15), ref. (8) for an iron electrode in the presence of 0.3M aniline.

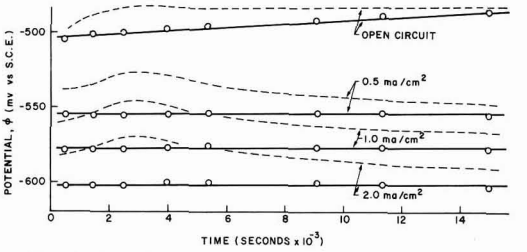


Fig. 7. Electrode potential (open circuit and cathodic pulse polarization) during the relaxation following anodic polarization. Inhibitor: 0.3M aniline. Dashed line shows the results for uninhibited iron (10).

From the comments in the preceding paragraph, it is anticipated that an estimation of the rate constants from the adsorption pseudocapacitance data would approximate that which has been found for the uninhibited case (8). Figure 6 shows the results which were obtained for two different Armco iron electrodes in the presence of 0.3M aniline. The slope of the line, *i.e.*, the sum of the rate constants of Eq. [1], was 2.1 x $10^{-3}$ $sec^{-1}$, which was within 10% of the average value obtained for the uninhibited samples (8).

Thus far all of the suggested electrochemical techniques have been able to supply answers to the specific questions which have been posed. In addition to the mere presentation of answers, the picture which the results suggest is self-consistent, *i.e.*, the open-circuit potential and both the anodic and cathodic polarization measurements suggest a nonspecific, "nondeactivating" mechanism for the effect of the organic on the electrochemical behavior of iron.[3] In addition, it has been possible to eliminate a fast "chelation" step (*e.g.*, see Eq. [1a]). However, the results have not been able to differentiate between a simple blocking mechanism such as might be envisioned in a chemisorption mechanism and a slow "chelation" step (Eq. [1a]).

The resolution of the problem is at least theoretically at hand. If the chelation process proceeds at a reasonable rate (from the rapid convergence of the inhibited and uninhibited cathodic Tafel slopes, it seems reasonable to assume that whatever process is operative it probably has a relaxation time which is less than an hour), then measurements of the decay of adsorption pseudocapacitance following the cessation of anodic polarization ought to show the presence of the chelate. Two pieces of information are available from the previous analysis for uninhibited iron (8): (*A*) The decay relaxation time is about an order of magnitude larger than the charging case; (*B*) the decay data are not as reproducible as charging data. The first observation suggests that it is possible to observe the equilibration of [1*a*] during decay even if we could not detect it during the charging process. The second observation suggests that at the present state of the experimental method one can, at best, only qualitatively evaluate the chelation effect. The experimental results obtained for the decay experiments [see Eq. (16) of ref. (8)] are not shown since the reproducibility was even poorer than those obtained in the uninhibited case (8) and would not lend anything to the discussion.

Another series of measurements are available during the decay process which has not been considered previously. Short (~5 sec) cathodic pulses can be applied to an electrode which is relaxing following the cessation of anodic polarization without perturbing the relaxation process and, thereby, determine the polarization characteristics during the relaxation (10). It has been suggested that (FeOH) catalyzes, *i.e.*, increases the apparent exchange current, the hydrogen evolution reaction (h.e.r.) (15). Since an electrode during the relaxation process has a varying amount of (FeOH) on its surface, the potential associated with a given current density should increase with decreasing (FeOH) if such an hypothesis is correct. On the other hand, if the (FeOH) does not catalyze the h.e.r. or is unavailable for such a catalysis, the potential for a given value of current density should remain constant. Figure 7 compares an uninhibited and an aniline-inhibited iron sample. In the uninhibited sample (dashed line) it can be seen that at times greater than 1 hr (the time corresponding to the achievement of a steady-state open-circuit potential) the previous hypothesis (15) finds experimental support, *i.e.*, the adsorbed (FeOH) affects the h.e.r. In the case of the inhibited sample, however, catalysis is essentially absent. It does not seem likely that such a result can be explained except in terms of a "surface chelation" process.

It was suggested at the outset that measurements of adsorption pseudocapacitance on open circuit should permit an estimation of the coverage of the inhibitor. However, capacitance measurements of Armco iron displayed a large intrinsic scatter from electrode to electrode which has tentatively been ascribed to "surface defects" (10). The same phenomena have been observed in the inhibitor study so that at present the capacitance technique is of no benefit in determining surface coverages of the inhibitor on unannealed Armco iron electrodes.

The zone-refined iron has not been considered in the preceding discussion. It has already been noted that the zone-refined sample undergoes a rather rapid equilibration of step [1], *viz.*, about $10^3$ times more rapid than Armco iron (8). Therefore, it is not possible to evaluate the purer sample in the same manner as that given above.

It has been observed that zone-refined iron in 1*N* $H_2SO_4$ achieves a steady-state potential in less than 5 sec for anodic (8) and cathodic polarization (10). Therefore, in contrast to the Armco iron, it is possible to obtain steady-state polarization data for zone-refined iron with minimum perturbations of the quiescent (open-circuit) conditions of corrosion.

The open-circuit potentials of zone-refined iron were not as reproducible as those for Armco iron both in the presence and absence of aniline. However, in presence of aniline zone-refined iron was always more negative than in the uninhibited case. Consequently, from the analysis of Kaesche (5) it may be deduced that aniline affects the cathodic partial process more than the anodic partial process. This is a different result than had been obtained in the case of the Armco iron (see above).

Figure 8 shows the variation of cathodic Tafel slope for zone-refined iron in the presence and absence of aniline. At times greater than about 20 hr, the slope of the former deviates from that associated with the uninhibited case. Figure 9 shows the variation of the corrosion rate under the same circumstances. A com-

[3] These comments are not true for p-Toluidine, and for the present that compound will be omitted from any generalizations.

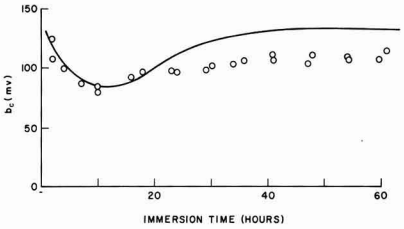


**Fig. 8. Cathodic Tafel slope of zone-refined iron in the presence of 0.3M aniline. The solid line represents the behavior of the uninhibited iron (10).**

parison of these two graphs is illuminating. In the vicinity of the deviation of cathodic Tafel slopes it is seen that the corrosion rate of uninhibited iron begins to "run away," *i.e.*, the shape of the curve for uninhibited iron in Fig. 9 suggests an autocatalytic process. Such a process and the conditions under which it could be realized have been considered elsewhere (10). Let it suffice here that inhibited iron behaves in a "regular" fashion, *i.e.*, at times beyond 20 hr it does not behave much differently than it did at shorter times, and that the "deviation" is more associated with uninhibited iron. Therefore, it is difficult to attempt to rationalize the significance of the Tafel slope deviations.

The rate-determining step for h.e.r. on high-purity iron in the absence of inhibitors has been shown to be slow discharge (16-18). If this is also the rate limiting step in the presence of the inhibitor (a question which remains unanswered), then an inhibitor which decreases the Tafel slope (see Fig. 8) and decreases the corrosion rate must simultaneously decrease the activation barrier and depress the exchange current. For the foregoing observations to prevail, the depression of the exchange current must be very large. An alternate possibility exists which is more intimately associated with the anodic partial process and, hence. will be considered further below.

The anodic Tafel slope for the uninhibited zone-refined iron has been found to be $47 \pm 2$ mv (10) while in the presence of 0.3M aniline, slopes of $55 \pm 3$ mv were obtained. This increase in Tafel slope suggests a mode of inhibition involving an interposition of organic into the charge transfer process for the anodic reaction. This is consistent with the mechanism suggested above if the equilibration of [1a] is fast and is shifted toward the right, *i.e.*, the surface concentration of free (FeOH) is low, and the bulk of the dissolution comes from [1b].

This suggestion of an interposition of the organic in the anodic charge transfer process may help clarify the observations of cathodic Tafel slope deviations and modes of inhibition. If one allows the possibility of the generation of surface sites, which are preferred for adsorption, during the natural corrosion process, then it does not seem unreasonable to suggest that the equilibrium by [1] will be adjusted such that the surface concentration of (FeOH) would increase. In turn the rate of the dissolution reaction would increase and, thereby, beget more surface sites, etc., until the process would tend toward autocatalytic behavior. Tentatively, the h.e.r. process has been neglected, but in fact its exchange current is also increased (10). Therefore, if one could introduce a species which could simultaneously trap the (FeOH) and consume the surface sites (by an appropriate adsorption mechanism) this "autocatalytic" process could be stifled. As was suggested above, the results indicate that the aniline does fill this dual role, *i.e.*, the aniline adsorbs on the surface and complexes with the (FeOH) on the surface.

In contrast to Armco iron, zone-refined iron has reproducible open-circuit capacitance behavior. Therefore, in the latter case, one may deduce the effective surface coverage of the inhibitor. If one assumes that the adsorption of the organic compound "insulates" that part of the metal-solution interface, then the relationship between the capacitance in the presence and absence of inhibitor and the surface coverage is

$$C_i = (1 - \theta)\, C_u \qquad [4]$$

where the subscripts i and u correspond to the inhibited and uninhibited cases, respectively, and $\theta$ is the surface coverage of inhibitor. Therefore, the ratio $C_i/C_u$ is a measure of the surface coverage. If adsorption is the only mode of inhibition, then the ratio of the inhibited rate to the uninhibited rate (at any time) should be the same as that for the capacitance ratio.

The capacitance-time behavior of the inhibited zone-refined iron is shown in Fig. 10. It is seen that the capacitance of uninhibited iron has a higher $C$-$t$ slope than inhibited iron. This is consistent with the suggestion that the inhibition process decreases the rate of appearance of the intermediate (FeOH).

Table I is a collection of data from Fig. 9 and 10 and provides an indication of the extent to which adsorption alone contributes to the inhibition. Considering the approximativeness of the numbers used in the calculation, the correspondence between the ratios of capacitance and corrosivity at times $\leq$ 20 hr is good and suggests a predominantly adsorption mechanism. However, at times greater than 20 hr, the differences between the two can be ascribed to surface chelation as described above.

A detailed tabulation of the observed corrosion rates with time for Armco iron as well as the LFER correlation of the data is given elsewhere (9). The data

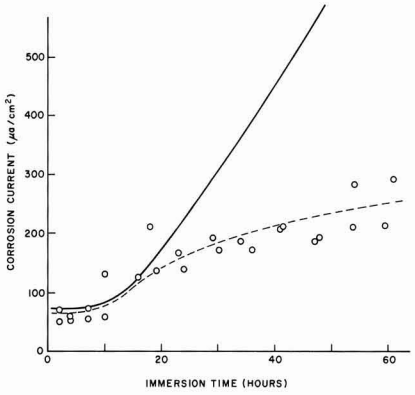


**Fig. 9. Corrosion current obtained by extrapolating the cathodic polarization curve to the corrosion potential for zone-refined iron samples in the presence of 0.3M aniline. The solid line shows the behavior of the uninhibited iron (10).**

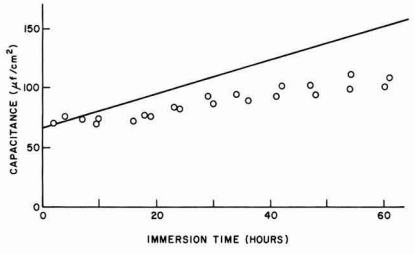


**Fig. 10. Capacitance-time behavior of zone-refined iron in the presence of 0.3M aniline. The solid line represents the behavior of the uninhibited iron (10).**

Table I. Comparison between the capacitance and corrosivity ratios for aniline-inhibited zone-refined iron

| Time, hr | $C_i/C_u$* | $r_i/r_u$** | $\theta$*** |
|---|---|---|---|
| 2 | 1.00 | 0.95 | 0.00 |
| 5 | 0.97 | 0.95 | 0.03 |
| 10 | 0.93 | 0.91 | 0.07 |
| 20 | 0.85 | 0.82 | 0.15 |
| 30 | 0.79 | 0.60 | 0.21 |
| 40 | 0.76 | 0.44 | 0.24 |
| 50 | 0.72 | 0.38 | 0.28 |
| 60 | 0.71 | 0.33 | 0.29 |

* Data from Fig. 10.
** Data from Fig. 9.
*** From Eq. [4].

showed that meta- and para-toluidine lost inhibition with time (para- before the meta-) until both were acting as accelerators. Mere loss of inhibition would derive from an exclusion of the organic from the surface; acceleration suggests a definitive role for the organic. These results may be explained in terms of reaction [1b] becoming the dominant dissolution reaction. The reason for the shift from [2] to [1b] is not clear, but is probably a complex interaction between the stability of the surface chelate and its oxidation propensity. This may be seen in Fig. 5 where the p-Toluidine is seen to deviate from the behavior of the other inhibitors and the uninhibited case. It is suggested that the rate of equilibration of [1] would be very slow due to the intervention of steps [1a] and [1b] to yield the complex ion with iron in the divalent state.

A final comment concerning purification of the organic should be made. During the course of this work, it was found that 0.1M aniline in the as-received state (brownish-colored liquid) gave nearly identical inhibition as 0.3M of the redistilled (clear) aniline. Therefore, it is suggested that only purified compounds should be used when studying the effect of organic compounds on electrochemical properties of metals.

## Conclusions

The results of electrochemical measurements of Armco iron and zone-refined iron in the presence of aniline and its ring-substituted derivatives have shown that deactivation of the iron lattice (5) is not the model by which the anodic partial process is altered. Instead, there is an equilibrated "capture" of the monovalent intermediate, *i.e.*, (FeOH), in some sort of surface chelate. However, at low coverages of the intermediate, the inhibition is essentially a blocking (adsorption) mode.

The effect of aniline derivatives on the hydrogen evolution reaction is essentially an adsorption mode. In the case of the zone-refined iron the drastic alterations in h.e.r. exchange current were more associated with the absence of the intermediate (FeOH) due to the presence of surface chelate than any deactivation of the cathodic partial process, *per se*.

The work presented here shows the utility of the multifaceted electrochemical approach to the problems of ascertaining the effects of organics on the electrochemical properties of active metals. An analysis of the structure-inhibition relationship is given elsewhere (9).

## Acknowledgment

This work has been supported by the Corrosion Research Council, Project 14. Partial support was received from the University of California Sea Water Desalination Program.

Manuscript received Sept. 6, 1966.

Any discussion of this paper will appear in a Discussion Section to be published in the June 1968 JOURNAL.

## REFERENCES

1. R. C. Ayers and N. Hackerman, *This Journal*, **110**, 507 (1963).
2. H. F. Finley and N. Hackerman, *ibid.*, **107**, 259 (1960).
3. P. F. Cox, R. L. Every, and O. L. Riggs. *Corrosion*, **20**, 299t (1964).
4. F. M. Donahue and K. Nobe, *This Journal*, **112**, 886 (1965).
5. H. Kaesche and N. Hackerman, *ibid.*, **105**, 191 (1958).
6. R. R. Annand, R. M. Hurd, and N. Hackerman, *ibid.*, **112**, 144 (1965).
7. E. Blomgren, J. O'M. Bockris, and C. Jesch, *J. Phys. Chem.*, **65**, 2000 (1961).
8. F. M. Donahue and K. Nobe, *This Journal*, **114**, 682 (1967).
9. F. M. Donahue and K. Nobe, *ibid.*, **114**, 1012 (1967).
10. F. M. Donahue and K. Nobe, To be published.
11. N. Hackerman and A. C. Makrides, *I.E.C.*, **46**, 523 (1954).
12. N. Hackerman, Symposium Europeen sur les Inhibiteurs de Corrosion. Comptes Rendus. Universita Degli Studi Ferrara, Ferrara, 1961, p. 99.
13. J. O'M. Bockris, D. Drazic, and A. R. Despic, *Electrochim. Acta*, **4**, 325 (1961).
14. M. A. V. Devanathan and Z. Stachurski, *This Journal*, **111**, 619 (1964).
15. F. M. Donahue and K. Nobe, Proceedings of the Second International Congress on Metallic Corrosion, NACE, Houston, 1966, p. 916.
16. J. O'M. Bockris and D. Drazic, *loc. cit.*, **7**, 293 (1962).
17. J. O'M. Bockris and D. F. A. Koch, *J. Phys. Chem.*, **65**, 1941 (1961).
18. E. J. Kelly, *This Journal*, **112**, 124 (1965).

# Corrections

The titles and authors of the following papers, "Effect of Hydrogen Absorbed by Electrode and Electrolyte on Hydrogen Coverage" by David J. Ben-Daniel and Fritz G. Will, pp. 909-915 and "Primary and Solvent Isotope Effects in the Anodic Evolution of Oxygen" by Mark Salomon, pp. 922-926 were inadvertently omitted from the Table of Contents of the September 1967 issue of the *Journal*.

# Theory of Organic Corrosion Inhibitors

## III. LFER Correlation of Inhibition of Armco Iron by Ring-Substituted Anilines

**Francis M. Donahue[1] and Ken Nobe**

*Department of Engineering, University of California, Los Angeles, California*

ABSTRACT

The corrosion rates of Armco iron in the presence of ring-substituted anilines were shown to obey a LFER predicated on inhibition by adsorption. Deviations from the adsorption correlation were shown for p-Toluidine at times greater than 20 hr and for m-toluidine in excess of 30 hr. These deviations tended toward an acceleration which has been attributed to an oxidative propensity of the "surface chelate." Since 0-Toluidine was found to follow the adsorption correlation, it was concluded that adsorption of the organic was parallel to the electrode surface. Adsorption data on Hg where the orientation was shown to be parallel to the electrode surface were also correlated by the LFER theory.

Recently, the authors have proposed a correlation between adsorption of and/or inhibition by organic compounds and physical-organic chemical substituent constants (1). Correlating such parameters was not completely new since Hackerman and Hurd (2) had plotted the degree of inhibition for ring-substituted N-methylanilines *vs.* the Hammett substituent constant as early as 1961. However, no previous formalism had been developed for plotting inhibition *vs.* substituent constants.

In essence, the "theory" states that, if inhibition (or adsorption) of organic compounds is determined by the electronic distribution in the "anchoring" group of the adsorbate, then it should be amenable to a "Linear Free Energy Relationship" treatment. The term "anchoring" has been placed in quotation marks here and previously (1) for two pragmatic reasons:

(*A*) If one is to investigate electron distributions in an organic molecule, he ought to focus his attention on one atom within that molecule and note variations in the electron density due to variations of a substituent elsewhere in the molecule. Therefore, the choice of the "marked" atom is somewhat arbitrary, although a certain atom in some molecules, *e.g.*, the nitrogen in alkyl substituted pyridines, suggests itself. In physical-organic chemistry the marked atom is invariably the reaction site.

(*B*) In studies of corrosion inhibition the term "anchoring" atom has been used extensively, and the authors feel that one may use such a term provided it is not taken literally [see Discussion, p. 888, of ref. (1)]. Therefore, to remove such an improper interpretation the quotation marks have been and will continue to be used.

Cox and co-workers (3) following the reasoning of Hackerman and Makrides (4) demonstrated a correlation between degree of inhibition for ring-substituted anilines and n.m.r. chemical shift for the amine hydrogens (a measure of the nitrogen electron density). This correlation should have lent considerable support to the authors' theory (1) since Suhr (5) and Dyall (6) had shown correlations between n.m.r. chemical shifts for amine hydrogens and the Hammett substituent constant. However, neither the corrosion inhibition data (3) using Eq. [15b] (1) nor the chemical shifts (3) were found to correlate with the substituent constants. Since Dyall (6) had studied six of the ring-substituted anilines which Cox (3) had observed, it is noteworthy that the results of the two investigators show essentially no correlation with each other. The difference in solvents between the two investigators is probably not the source of the discrepancy since Dyall's work in $CCl_4$ and acetonitrile gave good internal checks. Unfortunately, the authors cannot resolve the discrepancies in the n.m.r. work and, hence, will have to forego any further critique until more work in this interesting area is published.

However, the authors can address themselves to the corrosion inhibition data of Every and Riggs (7). The authors have observed previously that impure organics, *i.e.*, those used in the as-received state without further purification, yield misleading results (8). In neither the paper under discussion (7) nor in previous work by those investigators (9, 10) was mention made of purification of the organics prior to inhibition studies. Likewise, their representation of the degree of inhibition (7) is derived from an integral corrosion rate *i.e.*, the total weight loss after 24 hr in the presence of inhibitor is compared with the uninhibited weight loss for the same duration. Unless the weight loss-time curves have the same shape (an unsubstantiated assumption), such a measurement is not indicative of the over-all efficacy of the inhibitor. Consider Fig. 1 as an example. Using the integral corrosion rate technique, all three inhibitors (a, b, and c) show about a 25% protection at 24 hr. However, only "b" will show this degree at any other time while "a" will give a higher value of protection at longer times and "c" will soon be an accelerator.

From the previous derivation (1) the instantaneous rate, *i.e.*, the slope of the curves in Fig. 1 or the corro-

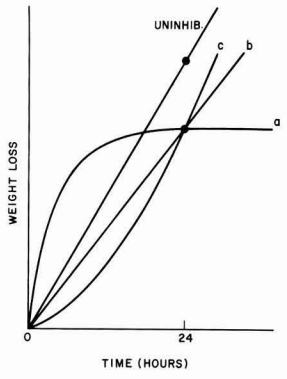


**Fig. 1. Schematic representation of weight loss-time curves for three inhibitors compared with an uninhibited sample.**

[1] Present address: Department of Chemical and Metallurgical Engineering, The University of Michigan, Ann Arbor, Michigan.

sion current from polarization measurements, should be correlated with the substituent constant. Consequently, simple weight loss measurements are an unsatisfactory method of testing the theory unless a sufficient number of data points can be obtained such that a differentiation of curves like those shown in Fig. 1 may be effected. Electrical resistance probes (11) can be used effectively for this purpose under certain conditions.

An important aspect of the proposed theory (1) has been questioned recently (12). Due to an apparent misunderstanding of the usage of "anchoring" group (see comments above), it was suggested by Annand that observations such as those by Blomgren and Bockris (13), who concluded from their results that the adsorption of ring-substituted anilines on mercury was parallel to the electrode surface and was attached to the surface by $\pi$-bonds from the aromatic nucleus, negated our entire analysis. On the contrary, Fig. 2 shows that Eq. [9c] (1) correlates the data of Blomgren (13) quite well when the organic was at the high concentration. The deviations at the lower concentration could be due to slow adsorption or just the intrinsic reproducibility of their measurements coupled with the nature of the ordinate of Fig. 2. The main point here is that for a case which had already been shown to proceed by parallel adsorption the theory prevails. The data followed the correlation because the conjugated system which interacted with the surface was composed of the six carbon atoms and the nitrogen atom. Therefore, the electron density at nitrogen was directly coupled to the density at the aromatic nucleus [see p. 526 of ref. (4)]. This strongly suggests that the organic which adsorbs is unprotonated in support of Hackerman's hypothesis (4) which has been questioned by Blomgren (13). The latter's comments were perhaps premature since dissociative adsorption, *i.e.*, fragmentation of the anilinium ion into free amine and proton at the surface, cannot be ruled out provided equilibrium is maintained with the anilinium ions in the double layer.

## Results and Discussion

Table I shows the instantaneous corrosion rate of Armco iron specimens as a function of immersion time in solutions containing 0.3M organic in 1*N* $H_2SO_4$ (8). It may be seen that all of the organics show a minimum in corrosion rate in the region of 20-30 hr immersion. From the previous discussions (8) it can be seen that the inhibition process is a combination of a number of coupled chemical and electrochemical processes. It is not known at present why this coupling should be optimum after this period of immersion. However, it is noteworthy (although perhaps fortuitous) that this same time was observed for the transition from adsorption to "chelation" control in the case of zone-refined iron (8).

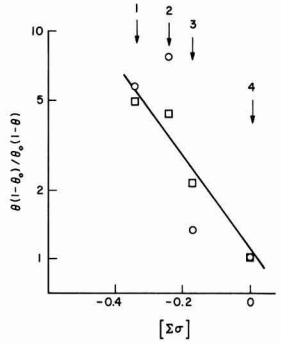


**Fig. 2. Electrocapillary measurements of Blomgren (13) *vs.* substituent constants for substituted anilines. 1, 2,6-dimethyl-; 2, 2,3 dimethyl-; 3, 0-Toluidine; 4, Aniline. Circles, $10^{-3}$ M; squares, $10^{-2}$ M.**

**Table I. Corrosion current ($\mu$a/cm$^2$) obtained from cathodic pulse polarization of Armco iron in 0.3M solutions of inhibitor in 1*N* $H_2SO_4$. Data are from previous work (8).**

| | Inhibitor | | | | | |
|---|---|---|---|---|---|---|
| Time, hr | None | Aniline | o-Toluidine | m-Toluidine | p-Toluidine | m-Anisidine |
| 2 | 105 | 62 | 75 | 66 | 87 | 44 |
| 4 | 98 | 82 | 95 | 89 | 92 | 62 |
| 6 | 85 | 82 | 91 | 85 | — | 68 |
| 8 | 75 | 69 | 84 | 83 | — | 70 |
| 10 | 65 | 58 | 73 | 79 | 85 | 63 |
| 15 | 60 | 47 | 58 | (60) | 87 | 42 |
| 20 | 60 | 45 | 57 | (58) | — | 38 |
| 25 | 60 | 46 | 56 | 56 | 95 | 38 |
| 30 | 60 | 47 | 58 | 65 | 101 | 40 |
| 35 | 60 | 47 | 62 | 65 | 110 | 38 |
| 40 | 60 | 46 | — | — | 115 | 42 |
| 45 | 60 | 46 | 60 | — | 115 | 43 |
| 50 | 60 | 49 | 61 | 61 | 112 | 43 |
| Symbol for figures | ← | ○ | □ | △ | ▲ | ■ |

( ) represents an estimate from an $i_{corr}$-$t$ curve.

The previously suggested processes associated with the effects of organic compounds on the electrochemical properties of iron will be repeated here with the same notations as before for the convenience of discussion (8).

$$Fe + OH^- \rightleftarrows (FeOH)_{ads} + e^- \quad [1]$$

$$(FeOH)_{ads} + n\,I \rightleftarrows [(FeOH) \cdot I_n]_{ads} \quad [1a]$$

$$I + S_{ads} \rightleftarrows I_{ads} + S \quad [1a']$$

$$(FeOH)_{ads} + n\,I_{ads} \rightleftarrows [(FeOH) \cdot I_n]_{ads} \quad [1a'']$$

$$[(FeOH) \cdot I_n] \rightarrow [(FeOH) \cdot I_n]^+ + e^- \quad [1b]$$

$$(FeOH)_{ads} \rightarrow (FeOH)^+ + e^- \quad [2]$$

$$(FeOH)^+ \rightarrow Fe^{+2} + OH^- \quad [3]$$

$$[(FeOH] \cdot I_n]^+ \rightarrow [FeI_n]^{+2} + OH^- \quad [3a]$$

Steps [1a'] and [1a''] have been added for completeness. The symbol S denotes the solvent or any specifically adsorbed electrolytic ions.

In the previous analysis (8), step [1a'] would be the mode of inhibition which has been designated as "blocking" or adsorption. Steps [1a] and [1a''] are the surface chelate modes. If the process described by [1a''] was the dominant mechanism for the production of chelate, then the formation of chelate would be enhanced by increased coverage of both adsorbed inhibitor and reaction intermediate. Since increased coverage of intermediate leads to product formation via step [2], the chelation process, *i.e.*, [1a''], must be fast or the surface coverage of adsorbed inhibitor must be high for inhibition to be maintained. Assuming the foregoing to be correct, *i.e.*, chelate forms by [1a''] and that the equilibria of [1] and [1a'] are shifted toward the right as adsorption sites are generated by dissolution (8), then the importance of chelation ought to increase with increasing immersion time. The extent to which [1] and [1a'] are shifted to the right relative to each other and the stoichiometry of [1a''], *i.e.*, whether $n \geq 1$, will determine whether inhibition will increase, decrease, or remain constant. Thus, until one may ascertain the critical parameters associated with [1], [1a'], and [1a''], only a qualitative discussion of the causes of the observed phenomena can be made.

From the foregoing discussion, it should not be assumed that the mechanism given by [1a] has been ruled out. On the contrary, such a mechanism is still attractive since organic is more readily available from the solution than it would be via some sort of surface diffusion mechanism. On the other hand, the fact that adsorbed organic is indeed present and the organic

and intermediate are assumed to gravitate toward the same surface sites suggest a preference for [1a"].

In the previous study it was noted that both adsorption and surface chelate functioned in a more or less concerted manner to achieve inhibition (8). Likewise, it was suggested that acceleration of corrosion was associated with the oxidative propensity of the surface chelate. The theory which was previously derived (1) predated the experiments, and, hence, did not anticipate stability of surface chelates as playing a role in inhibition. Therefore, the analysis was proposed on the basis of only an adsorption mechanism. Consequently, the theory must be re-evaluated in the light of the experimental observations.

Although the bulk of the "theoretical" paper (1) was associated with adsorption phenomena, the actual applicability of the concept is more universal than might be thought initially. Little and co-workers (14) have shown correlations between chronopotentiometric quarter wave potentials for substituted phenylferrocenes and directly substituted ferrocenes and substituent constants. As noted in the previous paper (1), correlations have likewise been observed for the fifth wave oxidation potential for substituted anilines (15). Chen (16) has demonstrated a Linear Free Energy Relationship (LFER) between complex ions and the $pK$'s of the liquids. The authors mentioned most of this work in passing (1); however, it did not seem important at that time to dwell on areas which then seemed unrelated to corrosion inhibition. The subsequent experimental work (8) showed this view to be short-sighted.

In a very naive sense, [1a] and [1a"] may be viewed as "two dimensional complex ions" or surface chelate (8). Consequently, the stability constant for the complex will be intimately related to the $pK$ of the ligand (organic) provided the three-dimensional work of Chen may be translated to the surface chelate. The $pK$'s of these compounds parallel the Hammett substituent constant. Therefore, the shift in equilibrium of [1a] or [1a"] should vary directly with the substituent constant. Since it was postulated above that inhibition was dependent on the stability of the surface chelate, by deduction it was again seen that inhibition is directly correlatable to a substituent constant.

Likewise, the oxidative propensity of the complex ion may be viewed in the light of Little's work (14). Here the iron of the complex undergoes a single electron oxidative transfer with retention of the structure of the complex. This is identical in form to [1b]. Consequently, extrapolating Little's results to the case under consideration, one deduces that the oxidative propensity of the complex ought to be a function of the substituent constant as well.

In summary, it can be seen [and experimentally demonstrated to an extent (8)] that an organic such as a ring substituted aniline compound is capable of performing the following functions at a corroding electrode: (*a*) chemisorbing on the surface; (*b*) forming a more or less stable complex with a corrosion intermediate and effectively removing the intermediate from the dissolution sequence; (*c*) formation of a complex as in (*b*) with a finite oxidative propensity. Each of these processes taken alone is theoretically capable of being correlated with a substituent constant with an unique value of $\rho$ for each process. Since each of these separate functions derive their stability (or lack of it) from the electronic distribution throughout the molecule, it seems reasonable to suppose that as the electron density is varied in a family of molecules the relative contribution to each of these possibilities will change in a monotonic fashion. For example, a molecule with the greatest tendency for adsorption will probably have a small tendency for formation of the surface complex (one may view this molecule as being in a "stable" state while adsorbed) and, consequently, will have a negligible contribution to oxidation of the complex. On the other end of the spectrum one may envisage a molecule with a great affinity for the lattice ion, but a negligible tendency for long-lived adsorption. Such a molecule would function as an accelerator to corrosion. It would be fortuitous, indeed, if the $\rho$'s for these respective processes were identical.

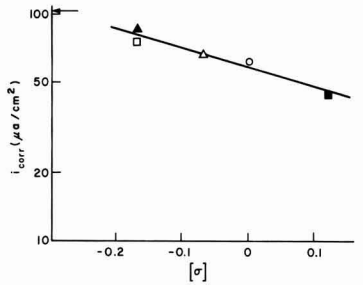


**Fig. 3. Corrosion rate as a function of substituent constant for Armco iron electrodes after 2 hr immersion. Arrow denotes uninhibited rate. Symbols for compounds are given in Table I.**

The comments immediately above suggest that attempts to formalize organic corrosion inhibitors in terms of a single correlation are not likely to succeed. Such a pessimistic outlook would be justified if the only data available to the investigator were the respective corrosion rates and correlation parameters. However, as was noted here and previously (8), each of these three functions, *viz.*, adsorption, complexation, and acceleration, can be determined to a degree by the supporting electrochemical measurements.

For electrodes in the solution for a short period of time, *e.g.*, 2 hr, it may be assumed that the adsorption step has essentially equilibrated. Since the results with most of the organics did not indicate a fast chelation process, even under conditions of high coverage as in the anodic charging experiments (8), it may be assumed that contributions from the chelate were minimal, thereby negating the oxidative mode as a contributor as well. Therefore, a LFER correlation under these conditions should describe the adsorption mode of inhibition and yield a value of $\rho_{ads}$ for future use. Figure 3 is a correlation plot made under those conditions. It is noteworthy that the ortho substituent [a Taft $\sigma^*$ was used for the correlation, see ref. (1)] obeys the adsorption LFER correlation. This rules out a perpendicular orientation with the nitrogen as the "anchoring" group. It suggests, but does not prove, a parallel orientation toward the surface.

Figure 4 shows a correlation plot for data after 25 hr immersion. This is the region where the minimum corrosion rate had been observed. The solid line, which was purposely drawn parallel to the line in Fig. 3, is meant to describe the adsorption "component" of the various functions described above. From the plot

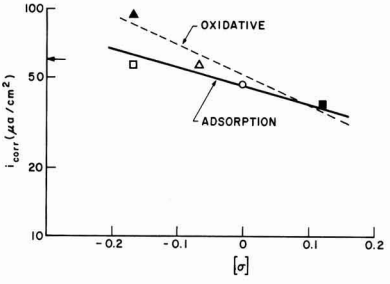


**Fig. 4. Corrosion rate as a function of substituent constant for Armco iron electrodes after 25 hr immersion. Symbols for compounds are given in Table I.**

it seems that an adsorption mode still describes the behavior of all the compounds except p-Toluidine which at this time is involved in an acceleration on the order of 50%. Therefore, it may be concluded that p-Toluidine is functioning in the oxidative mode. A second line (dashed) is drawn with the naive suggestion that this may describe the oxidative mode. However, such a correlation line cannot be drawn at this time. That adsorption is the main mode for the remaining organics corroborates the previous kinetic measurements (8).

## Conclusions

The results presented herein show the validity of a LFER correlation for ring-substituted anilines in terms of corrosion inhibition. The results also demonstrated the necessity for supporting electrochemical measurements. This need was underlined when the analysis of the data suggested the existence of eight possible chemical and electrochemical reactions in the over-all scheme. Such a scheme could be deduced from corrosion rate measurements alone, but the supporting electrochemical measurements permitted definitive mechanisms to be ascribed to the various organics as a function of immersion time.

The observation that adsorption was the primary mode of inhibition by the organics studied lends support to an earlier hypothesis by Hackerman and Makrides (4); however, the results for the zone-refined iron in the presence of aniline (8) present a new challenge to this hypothesis which should be pursued further. The correlation of the work of Blomgren (13) with the current theory and the agreement of the O-Toluidine with the other compounds suggests parallel adsorption of free amine at the metal surface.

## Acknowledgment

This work has been supported by the Corrosion Research Council, Project 14. Partial support was received from the University of California Sea Water Desalination Program.

Manuscript received Sept. 6, 1966.

Any discussion of this paper will appear in a Discussion Section to be published in the June 1968 JOURNAL.

## REFERENCES

1. F. M. Donahue and K. Nobe, *This Journal*, **112**, 886 (1965).
2. N. Hackerman and R. M. Hurd, "1st Intl. Congr. on Metallic Corr. London," p. 166, Butterworths, London (1962).
3. P. F. Cox, R. L. Every, and O. L. Riggs, *Corrosion*, **20**, 299t (1964).
4. N. Hackerman and A. C. Makrides, *Ind. Eng. Chem.*, **46**, 523 (1954).
5. H. Suhr, *Z. Elektrochem.*, **66**, 466 (1962).
6. L. K. Dyall, *Australian J. Chem.*, **17**, 419 (1964).
7. R. L. Every and O. L. Riggs, *Materials Protection*, **3**, 46 (1964).
8. F. M. Donahue, A. Akiyama, and K. Nobe, *This Journal*, **114**, 1006 (1967).
9. O. L. Riggs and R. L. Every, *Corrosion*, **18**, 262t (1962).
10. O. L. Riggs and F. J. Radd, *ibid.*, **19**, 1t (1963).
11. A. J. Freedman, E. S. Troscinski, and A. Dravnieks, *ibid.*, **14**, 175t (1958).
12. Discussion of ref. (1) by R. R. Annand and the authors' reply, *This Journal*, **116**, 633 (1966).
13. E. Blomgren and J. O'M. Bockris, *J. Phys. Chem.*, **63**, 1475 (1959).
14. W. F. Little and others, *J. Am. Chem. Soc.*, **86**, 1376 (1964); *ibid.*, **86**, 1382 (1964).
15. I. Fox, R. W. Taft, and J. M. Schempf, Technical Report No. 22, Office of Naval Research, Contract Nour 656 (05) Project NRO55-328, June 1959.
16. Y. T. Chen, *Z. physik Chem.*, **220**, 231 (1962).

# Mechanism of the Corrosion Inhibition of Stainless Steel in Sulfuric Acid by Sodium Molybdophosphate

**E. A. Lizlovs**

*Research Laboratory, Climax Molybdenum Company of Michigan, Inc., A Subsidiary of American Metal Climax, Inc., Ann Arbor, Michigan*

## ABSTRACT

Sodium 12-molybdophosphate inhibits the corrosion of an actively corroding type 430 stainless steel sample in sulfuric acid by first polarizing the sample to the primary passivation potential. After this potential is reached, the stainless steel sample passivates spontaneously. From the potentiodynamic polarization curves it was deduced that the addition of sodium molybdophosphate to the sulfuric acid does not significantly alter the anodic characteristics of the type 430 steel in sulfuric acid. The experimental results were in agreement with the electrochemical theory for the passivator-type inhibitors.

The corrosion inhibiting properties of the molybdates are well known, and a considerable amount of research has been devoted to the subject. The inhibiting properties of the heteropolymolybdates, on the other hand, are far less known. Exploratory studies conducted at this Laboratory showed that sodium molybdophosphate or molybdophosphoric acid was an effective corrosion inhibitor for stainless steel in a sulfuric acid medium. In addition, the inhibition of corrosion of the actively corroding stainless steel sample was accompanied by the formation of the intensely blue reduced form of the molybdophosphate ion. Therefore, it was suspected that the molybdophosphates might be passivating-type inhibitors, the theory for which has been presented by Stern (1). Further work by Makrides and Stern (2) and by Makrides (3) demonstrated the validity of the theory for the inhibition of corrosion of type 410 stainless steel and pure iron by ferric sulfate. This investigation was undertaken to clarify the corrosion inhibition mechanism of the molybdophosphate ion.

## Experimental Procedures

Commercial grade, type 430 stainless steel was used for all experiments. The construction and preparation of the electrodes is described elsewhere (4). All po-

tentials reported are for the saturated calomel electrode.

Two series of experiments were performed with type 430 stainless steel. One series consisted of the potentiodynamic polarization studies, and the other series was primarily concerned with the potential measurements of the corroding specimen.

Potentiodynamic studies were conducted in 1.05*N* $H_2SO_4$ containing 0.010, 0.100, 1.0, 3.0, and 6.0g of sodium 12-molybdophosphate ($Na_3PMo_{12}O_{40}\cdot nH_2O$) per liter of solution.[1] All experiments were performed in argon-purged solutions at 29.6°C, and the test solution was stirred magnetically. The potential scanning rate was approximately 0.15 mv/sec.

The minimum amount of the inhibitor necessary to passivate an actively corroding sample was determined by the slow addition of 1.05*N* $H_2SO_4$ solution containing 50 mg of $Na_3PMo_{12}O_{40}\cdot nH_2O$ per milliliter to 2100 ml of 1.05*N* $H_2SO_4$ test solution containing the corroding specimen. The potential of the sample was recorded on a strip-chart recorder. The transition from the active to the passive state was marked by a rapid and sharp potential rise from the active to the passive values.

The approximate amount of inhibitor necessary to maintain the passivity was established by passivating the type 430 electrode potentiostatically at +0.50v for 1, 10, and 60 sec, and 2 hr in a solution of 1.05*N* $H_2SO_4$ acid containing 0, 10, and 100 mg of the inhibitor per liter of solution. The potential decay was recorded after the discontinuation of passivation. The procedures for potentiostatic passivation and determination of the passive-film breakdown times are described elsewhere (4).

## Results

The addition of sodium molybdophosphate to 1.05*N* $H_2SO_4$ resulted in a very pronounced change in the appearance of the potentiodynamic polarization curves for the type 430 stainless steel. The potentiodynamic curves for the pure 1.05*N* $H_2SO_4$ and for the sulfuric acid containing 0.100 and 6.0 g/l of sodium molybdophosphate are shown in Fig. 1 through 3. With an increased sodium molybdophosphate content, the oscillations in the polarization current became increasingly larger, the measured critical current density ($I_{cr}'$) became smaller, and a progressively more extensive cathodic loop appeared on the polarization diagrams. For a sodium molybdophosphate concentration of 6 g/l, the measured polarization current remained negative up to the potential of +0.456v. The cathodic loop usually terminated at the equilibrium potential for the molybdophosphate/reduced molybdophosphate system,

[1] Since the exact molecular weight of the $Na_3PMo_{12}O_{40}\cdot nH_2O$ is not known, the inhibitor concentrations are expressed in grams per liter rather than in molarity or normality. Approximate molarity can be calculated by assuming that the molecular weight of the $Na_3PMo_{12}O_{40}\cdot nH_2O$ is 2000 (see Table I).

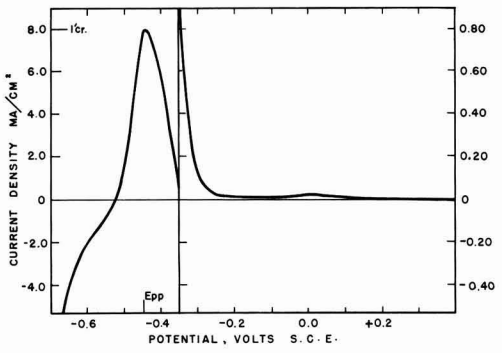


Fig. 1. Potentiodynamic polarization curve for type 430 stainless steel in stirred 1.05*N* $H_2SO_4$ at 29.6°C.

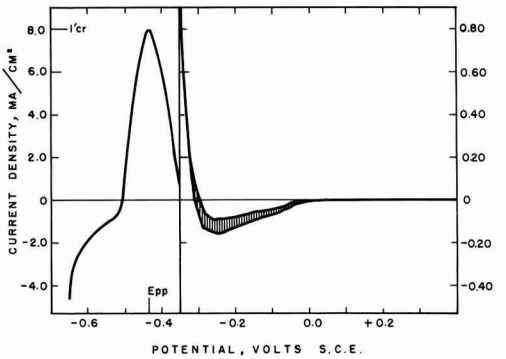


Fig. 2. Potentiodynamic polarization curve for type 430 stainless steel in stirred 1.05*N* $H_2SO_4$ containing 0.100 g/l of $Na_3PMo_{12}O_{40}\cdot nH_2O$ at 29.6°C.

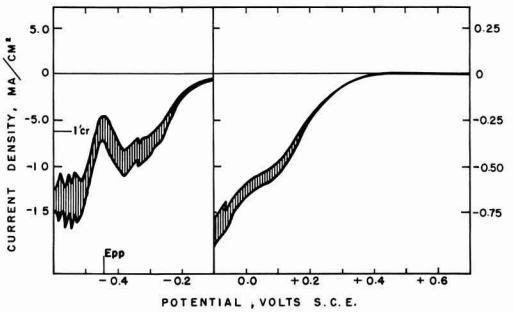


Fig. 3. Potentiodynamic polarization curve for type 430 stainless steel in stirred 1.05*N* $H_2SO_4$ containing 6.0 g/l of $Na_3PMo_{12}O_{40}\cdot nH_2O$ at 29.6°C.

that is, at the potential exhibited by the platinum wire electrode in the test medium. This cathodic loop was due to the reduction of the molybdophosphate ion on the passive type 430 electrode. The oscillations in the cathodic current were dependent on the stirring rate of the solution. In stagnant solutions, no oscillations occurred and the current was considerably smaller.

The most striking feature of the polarization diagram was the presence of the anodic dissolution region even at the most concentrated solution used (Fig. 3). The increased amounts of sodium molybdophosphate depressed the anodic dissolution region; nevertheless, the height of this region was estimated as being unchanged and was approximately equal to that seen for pure sulfuric acid. The potentials ($E_{pp}$), corresponding to the measured critical current density, remained exactly the same for all concentrations of sodium molybdophosphate as for pure sulfuric acid. For the most concentrated solution (6 g/l of sodium molybdophosphate) no net anodic current was observed, and the measured critical anodic dissolution current was actually negative. The measured critical anodic current density and the corresponding primary passivation potentials are summarized in Table I. Average values are given when the current could not be determined exactly because of the oscillations.

The transpassive behavior of the type 430 stainless steel was not affected by the sodium molybdophosphate. The oxidation of the reduced molybdophosphate should occur in the transpassive region, but because of the small amount of the reduced form present, the oxidation current of this compound could not be de-

Table I. Measured critical current densities and primary passivation potentials for various concentrations of $Na_3PMo_{12}O_{40} \cdot nH_2O$ in 1.05*N* $H_2SO_4$

| Concentrations of $Na_3PMo_{12}O_{40} \cdot nH_2O$ g/l | Approximate molarity* | Measured critical current density, ma/cm² | Primary passivation potential, v SCE† |
|---|---|---|---|
| 0 | 0 | 8.0 | −0.440 |
| 0.010 | $5 \times 10^{-6}$ | 8.8 | −0.440 |
| 0.100 | $5 \times 10^{-5}$ | 8.0 | −0.435 |
| 1.0 | $5 \times 10^{-4}$ | 5.8 | −0.435 |
| 3.0 | $1.5 \times 10^{-3}$ | 1.5 | −0.435 |
| 6.0 | $3 \times 10^{-3}$ | −5.8 | −0.440 |

* Calculated assuming the approximate molecular weight of 2000.
† SCE is saturated calomel electrode.

tected in the presence of a much larger transpassive current.

Successive additions of sodium molybdophosphate to the 1.05*N* $H_2SO_4$ solution gradually polarized the corrosion potential of the freely corroding type 430 sample in the noble direction, until the critical potential was reached (Fig. 4). This critical potential was the same as the primary passivation potential determined by potentiodynamic studies, −0.440 to −0.435v. Once this potential was reached, passivation of the corroding electrode resulted. The passivation process was evident by a rapid change of the electrode potential from the active to passive values. The final potential of the electrode was about the same as the potential of a platinum electrode in the same solution, +0.492v. The minimum amount of sodium molybdophosphate needed to passivate freely corroding type 430 stainless steel in stirred 1.05*N* $H_2SO_4$ was determined to be 3.540 g/l ($1.8 \times 10^{-3}$M). However, this amount was dependent on the stirring rate of the solution. In quiescent solutions the electrode continued to corrode even in solutions containing 6 g/l of sodium molybdophosphate.

The passive-film breakdown times for the type 430 stainless steel in 1.05*N* and in 1.05*N* $H_2SO_4$ containing sodium molybdophosphate are given in Table II. As Table II shows, the inhibitor concentration of 10 mg/l apparently represents the borderline concentration for maintenance of the passivity of type 430 steel after prior passivation. The experiments were not performed with more dilute solutions because of the increasing possibility of hydrolytic decomposition of more dilute solutions of molybdophosphate ion.

## Discussion

The behavior of the type 430 stainless steel in sulfuric acid containing various amounts of sodium molybdophosphate is an agreement with Stern's electrochemical theory for the passivating-type inhibitors (Fig. 1 through 3). As the sodium molybdophosphate concentration is increased, the measured current becomes more negative because of the increased total reduction current. Nevertheless, the anodic dissolution region and the presence of the critical anodic current is clearly indicated even at sodium molybdophosphate concentrations of 6 g/l (Fig. 3), where the cathodic partial current at $E_{pp}$ is greater than the critical anodic current, and consequently the total measured current is cathodic. The most striking feature is that $E_{pp}$ remains unchanged for all concentrations of sodium molybdophosphate and is the same as for the pure sulfuric acid (−0.435v). The critical anodic current density can be estimated to be approximately the same in the presence of molybdophosphate as in the pure acid. Furthermore, the critical current densities for the two most dilute solutions, where the effect of the reduction current of the molybdophosphate is expected to be negligible at $E_{pp}$, are essentially the same as for the pure acid (Table I). Hence, it can be concluded that the anodic dissolution characteristics of type 430 stainless steel in 1.05*N* $H_2SO_4$ are not affected by the sodium molybdophosphate additions to the acid. The main function of the inhibitor is to polarize the steel until the corrosion potential coincides with the primary passivation potential. Further polarization then results in spontaneous passivation of the stainless steel sample (Fig. 4) with the final potential value being determined by the redox potential of the molybdophosphate/reduced molybdophosphate system. Thus, the molybdophosphate ion belongs to the passivating class of inhibitors. As the corrosion potential becomes more noble, corrosion rates increase until the critical value of 8.0 to 8.8 ma/cm² is reached. The corrosion rates at any corrosion potential up to $E_{pp}$ in the presence of molybdophosphate ion should be the same as the corrosion rates at the corresponding potentials under potentiodynamic conditions in pure sulfuric acid. The corrosion rates of type 430 steel in the passive state are negligible as can be seen from the polarization diagram shown in Fig. 1, and these rates are also expected to be negligible in inhibited solutions.

According to well-known electrochemical principles, any corroding metal for which the measured critical current density is positive will corrode actively in that medium. On the other hand, if the measured critical current density is zero or negative, the metal will undergo spontaneously active-passive transition. Furthermore, if the potentiostatic (or potentiodynamic) polarization curve for a metal in a corrosive medium is characterized by a cathodic loop, a corroding metal can continue to corrode actively or remain passive, depending on the conditions under which it is exposed to the corrosive medium. No spontaneous transition from one state to the other can take place. The results from this investigation are again in agreement with the theoretical principles above. A spontaneous passivation occurred in a solution containing 6.0 g/l of molybdophosphate for which $I_{cr}'$ is negative (Fig. 3). At the inhibitor concentration of 3.0 g/l no spontane-

Table II. Passive-film breakdown times for the type 430 stainless steel in 1.05*N* $H_2SO_4$

| Passivation time | Concentration of $Na_3PMo_{12}O_{40} \cdot nH_2O$ mg/l | Passive-film breakdown times |
|---|---|---|
| 1 sec | 0 | 5-6.8 sec |
| | 10 | 7-10 sec |
| | 100 | 13.4 sec |
| 10 sec | 0 | 21-47 sec |
| | 10 | 32-49 sec |
| | 100 | 114 sec |
| 1 min | 0 | 2-5 min |
| | 10 | 4-8 min |
| | 100 | No breakdown |
| 2 hr | 0 | 38-53.5 min |
| | 10 | 38 min for one sample<br>No breakdown for two other samples |

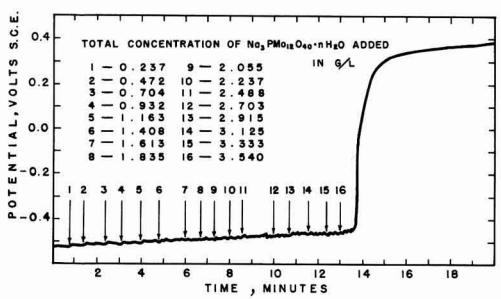


Fig. 4. Effect of successive additions of sodium molybdophosphate on the potential of actively corroding type 430 stainless steel in stirred 1.05*N* $H_2SO_4$ at 29.6°C.

ous passivation is expected; however, the value of $I_{cr}'$ is close to zero (Table I), and small changes in experimental conditions can be expected to result in spontaneous passivation. Increase of sodium molybdophosphate concentration to 3.540 g/l indeed resulted in the spontaneous passivation (Fig. 4). No spontaneous passivation is expected for the 1.0 and 0.100 g/l concentrations, but if the sample were passivated in these solutions, a stable passive state should result because of the prominent cathodic loops present on the polarization curves for these solutions (Fig. 2). This conclusion was also verified by the experiments, and no breakdown of passivity was obtained in these solutions if the sample had been passivated. On the other hand, the specimen continued to corrode actively after cathodic activation and no repassivation occurred. The solution containing 0.010 g/l of the sodium molybdophosphate represents the borderline case. The potentiodynamic polarization curve has a cathodic loop, but this loop is not very pronounced. A small change in experimental conditions can be expected to result in the retention or loss of passivity after the passivation treatment. This again is in accord with experimental observations. In very dilute solution a partial hydrolytic decomposition of the molybdophosphate ion can be expected. Therefore, the retention of the passivity in a dilute solution such as 0.010 g/l ($5 \times 10^{-6}$M) may be partially due to some form of molybdate ions.

The effectiveness of the molybdophosphate ion as a passivating agent depends on the ease of its reduction. Earlier observations in this Laboratory have shown that the molybdophosphate ion is very easily reduced to an intensely blue compound. Because of its ease of reduction it is quite corrosive to many metals, including molybdenum, tungsten, and copper. Because of the diffusion control of the reduction reaction in the important potential range around $E_{pp}$, the passivating process is drastically influenced by the rate of transport of the inhibitor to the surface of the corroding specimen. The minimum amount of the molybdophosphate necessary to passivate the specimen will therefore be strongly dependent on the hydrodynamic characteristics of the system. However, once the passivation occurs, the rate of mass transfer no longer has a significant effect and the passivity will be retained in quiescent solutions.

The minimum amount of molybdophosphate ion necessary to passivate any metal or alloy in acid solution, aside from the hydrodynamic considerations discussed above, will usually depend on the magnitude of the anodic critical current density. For stainless steels more alloyed than type 430, considerably smaller quantities of the sodium molybdophosphate will be needed for passivation. On the other hand, for metals with very large critical current requirements, no amount of the inhibitor will be sufficient to affect the active-passive transition, and the only effect will be the acceleration of the corrosion rate. Thus, for iron, which has a critical current density of about 600 ma/cm$^2$ in 1$N$ $H_2SO_4$ (5), no amount of sodium molybdophosphate is expected to effect passivation. Exploratory studies showed that no passivation of iron electrode occurred in vigorously stirred 1.05$N$ $H_2SO_4$ containing as high as 50 g/l of sodium molybdophosphate. The results from this investigation were in agreement with the results of Makrides and Stern, and Makrides for the ferric sulfate system (2, 3).

Manuscript received Nov. 17, 1966, revised manuscript received June 19, 1967. This paper was presented at the Philadelphia Meeting, Oct. 9-14, 1966.

Any discussion of this paper will appear in a Discussion Section to be published in the June 1968 JOURNAL.

REFERENCES

1. M. Stern, *This Journal*, **105**, 638 (1958).
2. A. C. Makrides and M. Stern, *ibid.*, **107**, 877 (1960).
3. A. C. Makrides, *ibid.*, **108**, 412 (1961).
4. E. A. Lizlovs, *Corrosion*, **22**, 297 (1966).
5. M. Prazak, V. Prazak, and Vl. Cihal, *Z. Elektrochem.*, **62**, 739 (1958).

# The Nonelectrolytic Deposition of Titanium on Columbium Alloys from Fused Salts

**J. B. Steinman, R. V. Warnock, C. G. Root, and A. R. Stetson**

*Solar Division, International Harvester Company, San Diego, California*

ABSTRACT

A high-temperature cell was designed for deposition of metallic coatings on refractory alloy substrates. The deposition of titanium from fused chloride and fluoride salts onto columbium alloys was investigated at several temperatures from 800° to 1100°C. The as-deposited coatings were generally dense and adherent and exhibited excellent side-to-side and edge uniformity. An explanation of the driving force and a mechanism for nonelectrolytic deposition is proposed, and an activation energy for deposition is calculated.

Considerable work has been directed toward the development of a process for the production of high-purity titanium and, alternatively, toward deposition of a uniform titanium coating from a molten salt bath. Studies at the National Bureau of Standards (1) produced titanium coatings 0.001- to 0.002-in. thick by electrolysis of a fused salt bath containing $NaTiCl_4$, KCl, and LiCl. Current densities up to 200 amp/ft$^2$ were used and the deposit was largely dendritic. Using an all-fluoride bath, $K_2TiF_6$ and NaF, Stetson was able to deposit a fairly uniform titanium coating by the electrolytic method (2). However, electrolytic deposition of titanium from a fused salt bath has produced primarily dendritic growths rather than smooth coatings.

Gill, Straumanis, and Schlecten first observed the corrosion of titanium in NaCl to form "pyrosols," and the subsequent use of these sols in the titanium coating of steels, copper, nickel, and cobalt (3-5). Alpert used scrap titanium, a partially reduced $TiCl_3$-$TiCl_2$ mixture, and NaCl to produce a titanium bath which reportedly gave coatings up to 0.02-in. thick on nickel,

iron, and tantalum (6). Stetson and Moore (7) successfully plated titanium on the columbium alloys, D43 and B66, with a $K_2TiF_6$, NaCl, LiF, Ti bath. This bath was run nonelectrolytically between 1010° and 1093°C and gave 0.0007 in. of titanium alloy plate in 20 hr.

The nonelectrolytic deposition of chromium, aluminum, nickel, titanium, silicon, and vanadium has been observed by the authors to occur from fused salt baths.

In the present work, an investigation of nonelectrolytic titanium plating was conducted. All fluoride, $K_2TiF_6$-LiF-NaF-Ti and all chloride, $TiCl_3$-NaCl-$BaCl_2$-Ti baths were investigated at two active salt concentrations and two temperatures. Additional work has shown that the baths will plate well without the addition of $K_2TiF_6$ or $TiCl_3$; however, the equilibration period before acceptable deposits and deposition rates can be obtained is approximately three days compared with one day for the baths with active salt additions. Two additional temperatures were investigated with a 5 m/o (mole per cent) $K_2TiF_6$ bath in an effort to determine the activation energy for deposition. Smooth, uniform, titanium alloy coatings up to 0.007-in. thick were obtained in 16 hr at 1093°C.

A special plating cell was designed for use in this project, and provisions were made for control of the atmosphere above the baths at all times.

### *Materials*

All chemicals used in this work were of reagent or better grade. The barium chloride was vacuum dried at 150°C to eliminate hydrated water. All other chemicals were used as supplied. Commercially pure titanium sheet was used to fabricate the cylindrical titanium source used in each bath.

Cb752 (Cb-10W-2.5Zr) and D43 (Cb-10W-1Zr-0.1C) were used as the substrate alloys. Both alloys were obtained as 0.020-in. thick sheet and were in the duplex heat-treated condition (solution treated, cold reduced 25%, and aged). Table I shows chemical analyses of the as-received columbium alloys.

Two bath concentrations were investigated in the fluoride system and one in the chloride system. The fluoride baths consisted of 5 m/o $K_2TiF_6$, (28.0 w/o $K_2TiF_6$, 34.6 w/o LiF, 37.4 w/o NaF) and 20 m/o $K_2TiF_6$ (65.1 w/o $K_2TiF_6$, 16.8 w/o LiF, 18.1 w/o NaF) dissolved in LiF-NaF eutectic. The chloride baths were prepared by dissolving 5 m/o $TiCl_3$ in a eutectic mixture of $BaCl_2$-NaCl to give a 6.4 w/o $TiCl_3$, 27.8 w/o NaCl, and 65.8 w/o $BaCl_2$ bath. Sufficient titanium metal, in the form of a cylinder, was provided to effect reduction of the baths and to maintain metallic titanium in contact with the bath at all times. The melts weighed approximately 1600g and gave a bath depth of approximately 8 in.

### *Equipment*

A high-temperature plating cell was designed for deposition of metallic coatings on refractory alloy substrates. Provisions were made to ensure positive control of the argon inert atmosphere and to prevent atmospheric contamination of the bath during insertion and extraction of specimens. The cell was designed to operate in the temperature range 427°-1150°C (800°-2100°F) in a gas fired furnace with a temperature control of ± 5°C. A schematic diagram of the cell is shown in Fig. 1.

The bottom part of the cell is 0.125-in. Inconel 600 tube that has been aluminized. The upper chamber

**Table I. Chemical analysis of the as-received alloys**

| Alloy | Oxygen, ppm | Hydrogen, ppm | Nitrogen, ppm | Carbon, ppm | Tungsten, w/o | Zirconium, w/o |
|---|---|---|---|---|---|---|
| D43 | 221 | 1 | 19 | 935 | 9.8 | 1.1 |
| Cb752 | 52 | 6 | 42 | 10 | 9.97 | 2.5 |

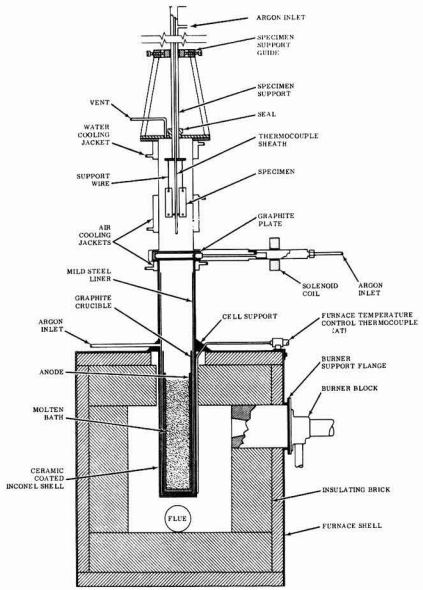


**Fig. 1. Schematic diagram of fused salt plating cells**

was fabricated from type 321 stainless steel and is separated from the lower bath chamber by a graphite gate valve actuated magnetically by a solenoid coil. This arrangement permits insertion and removal of specimens while continuously purging the lower chamber with argon.

The specimens, 2.0 x 0.5 x 0.020 in., are hung on tantalum wires welded to the Inconel specimen support rod which enters the cell through a Teflon compression seal. The cell top, through which the specimen support rod passes, is bolted to the upper chamber flange and is sealed with an O-ring.

The bath is contained in a National Carbon Company ATJ grade graphite crucible with an ID of 2.875 in. This grade of high-density graphite has proven impermeable to the salt mixtures at operating temperatures. The graphite crucible is placed in a mild steel liner which is, in turn, placed inside the Inconel retort. The bottom half of the crucible is wrapped in 0.002-in. molybdenum foil to prevent formation of the iron-carbon eutectic and subsequent fusion of the liner to the Inconel retort.

The furnace is gas fired using an Eclipse Tempered Air Burner. The temperature is controlled by a Barber-Coleman controller operating on the output of a chromel-alumel thermocouple in a protective sheath attached to the outside of the retort. The internal bath temperature is monitored by means of a tantalum-sheathed chromel-alumel thermocouple which enters the bath through the specimen support rod. Water and air cooling jackets are available for cooling the upper chamber but were not used in this work.

### *Procedure*

The entire weighed salt mixture is placed in the graphite crucible into which has been inserted a cylindrical sheet of pure titanium (this is the titanium source in the deposition reaction). The molybdenum-wrapped crucible is then placed in a liner which is, in turn, placed in the cell. After assembly, the cell is purged with argon (99.997% argon) for 4 hr (the time required to decrease the oxygen level in the cell effluent to <5 ppm) with an argon flow of 8 cfh. The furnace is then fired and the cell temperature brought to about 450°C and held for 16 hr. This procedure permits elimination of volatile impurities present in the salt mixture. The temperature is brought to 1093°C

Table II. Titanium deposition on Cb752 from a 5 m/o $K_2TiF_6$ bath

| Time, hr | Average weight gain in mg/cm² | | | |
|---|---|---|---|---|
| | 799°C (1470°F) | 872°C (1600°F) | 982°C (1800°F) | 1093°C (2000°F) |
| 1 | 1.0 | 1.9 | 5.0 | 11.2 |
| 2 | 1.5 | 2.9 | 7.1 | 14.4 |
| 4 | 2.1 | 5.7 | 11.2 | 23.6 |
| 16 | 4.3 | 12.4 | 29.2 | 50.0 |

where the salt is fused and allowed to "equilibrate" (establish a uniform temperature, become homogeneous, and reach the proper valence state).

The bath preparation procedure is slightly modified in the case of the chloride baths. The anhydrous reagent grade $BaCl_2$ contains some water of hydration even after heating to 150°C in a vacuum drying oven. The remaining moisture is eliminated by heating the NaCl-$BaCl_2$ solvent to 1100°C in a stream of argon in the fused salt cell. The $TiCl_3$ is then added in a polyethylene bag suspended from the specimen support wires. The polyethylene decomposes and is vaporized.

To insert the specimens, the top of the cell is removed (with the gate valve closed). The specimens, hung on the tantalum support wires, are introduced into the upper chamber which is then sealed, and purged with argon for 15 min. The gate valve is then opened, and the specimens are lowered into the bath. For removal, the specimens are raised out of the bath into the upper chamber and the gate valve is closed. The specimens are allowed to cool in the argon atmosphere in the upper chamber for 5 min before the cell is opened and the specimens removed. The adherent salt is readily removed from the specimens after a short period of soaking in hot water.

## Experimental Results

Titanium deposition studies were carried out in two different fused salt systems: the all-fluoride system and the all-chloride system. The carrier salt composition for a given system remained the same throughout the studies while the active salt percentage was varied.

*The all-fluoride system.*—A series of plating runs was made in both the 5 and 20 m/o $K_2TiF_6$ baths. Four temperatures were investigated in the case of the former and the two standard temperatures, 982° and 1093°C (1800° and 2000°F) for the 20 m/o bath. The temperatures studied in the 5 m/o bath included 799°, 872°, 982°, and 1093°C (1470°, 1600°, 1800°, 2000°F). The data from the runs in the 5 m/o $K_2TiF_6$ bath are shown in Table II and plotted in Fig. 2.

The series of plating runs in the 20 m/o $K_2TiF_6$ bath at 982° and 1093°C produced results very similar to those from the 5 m/o bath. The deposition ranged from a low of 4.4 mg/cm² in 1 hr at 982°C to a high of 80 mg/cm² in 16 hr at 1093°C. Both macroscopically and microscopically the coatings were similar to those deposited from the 5 m/o $K_2TiF_6$ bath.

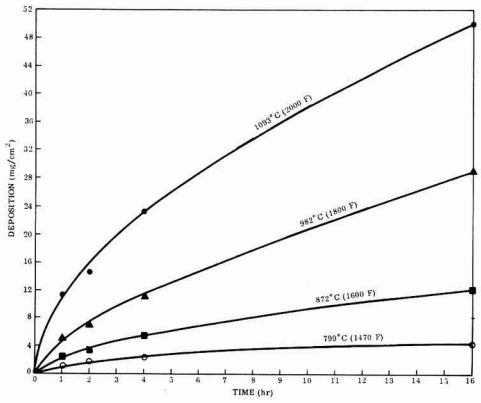


Fig. 2. Deposition *vs.* time; titanium deposition from a 5 m/o $K_2TiF_6$ bath on Cb752 alloy.

Table III. Titanium deposition on Cb752 from a 5 m/o $TiCl_3$ bath

| Time, hr | Average weight gain (mg/cm²) | |
|---|---|---|
| | 982°C (1800°F) | 1093°C (2000°F) |
| 1 | 2.5 | 6.5 |
| 2 | 4.5 | 8.4 |
| 4 | 7.5 | 14.9 |
| 16 | 16.6 | 36.0 |

Table IV. Titanium deposition on D43 alloy

| Bath | Time, hr | Weight gain (mg/cm²) | |
|---|---|---|---|
| | | 982°C | 1093°C |
| 5 m/o $K_2TiF_6$ | 2 | 6.8 | — |
| | 4 | 7.6 | — |
| 5 m/o $TiCl_3$ | 2 | 4.7 | 6.3 |
| | 4 | 9.1 | 13.8 |

*All-chloride system.*—A 5 m/o $TiCl_3$ bath was investigated at 982° and 1093°C. A series of runs was completed at each temperature on the Cb752 alloy, and the data are presented in Table III and plotted in Fig. 3.

The deposition rate in this chloride bath was found to be somewhat lower than that found in the all-fluoride system.

Two- and four-hour runs were made in the baths studied using D43 specimens. Results are shown in Table IV.

Comparison of this data with that for Cb752 shows the rate of titanium alloy formation to be slightly higher on Cb752 in two of the three comparable cases. While substrate composition should have a considerable influence on diffusion controlled deposition, little substrate effect was seen in this case since the alloys are quite similar. There is a possible exception which might be caused by the only compositional difference in the alloys. This one notable difference is the carbon content of the D43 which makes this alloy precipitation hardened (ZrC precipitates). The carbon in the alloy could influence the initial titanium deposition rate because of the possible formation of TiC. However, this effect was not seen in the present work.

The deposition rate curves for all the baths are generally parabolic in shape and fit an equation of the form, $W^2 = kt$, where $W$ is the weight gain, $k$ is a rate constant, and $t$ is the time. The rate constants are a function of temperature and for the 5 m/o $K_2TiF_6$ bath ranged from 1.1 at 799°C to 131 mg²/cm⁴ hr at 1093°C.

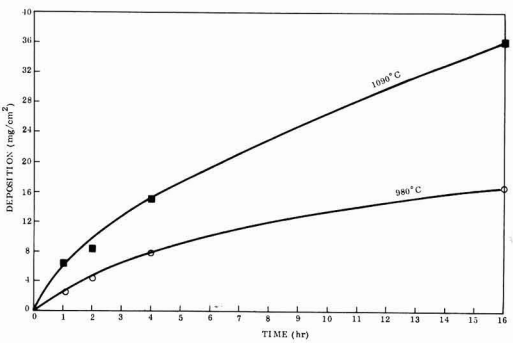


Fig. 3. Deposition *vs.* time; titanium deposition from a 5 m/o $TiCl_3$ bath on Cb752 alloy.

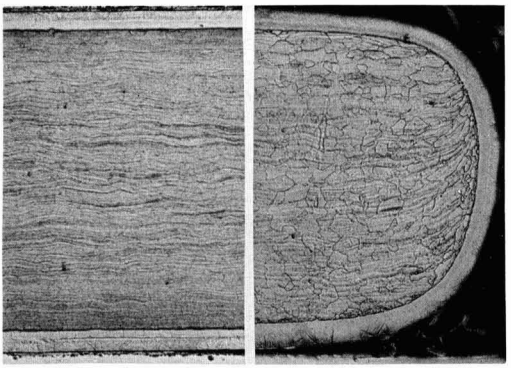

Fig. 4. Cb752 substrate (0.020 in.) with a titanium alloy coating applied in the all-fluoride bath at 1093°C (2000°F) in 4 hr: A (left), note the uniformity of thickness from side to side of the specimen; B (right), edge coating uniformity is shown. Magnification *ca.* 100X.

All of the deposits were smooth, adherent, and presented a shiny macroscopic appearance. Figure 4 shows a photomicrograph of a typical titanium-coated specimen. The side-to-side and edge uniformity should be noted.

Microhardness traverses were made on typical specimens from each of the baths studied in both fluoride and chloride systems. Results were similar for all baths, and a typical microhardness traverse is shown in Fig. 5. The average hardness of the as-received Cb752 alloy is 280 Knoop Hardness Number (50-g load).

A representative group of Cb752 specimens, coated with titanium in different baths, was subjected to bend ductility tests at minus 73°C. In all cases, the specimens bent without fracture or visible signs of cracking as did the uncoated standards. The titanium alloy coating remained intact.

As noted earlier, the baths were protected by an argon atmosphere at all times. It was found that any exposure of the bath to the air resulted in decreased plating rates. For example, exposure of the molten bath surface for less than 5 min resulted in as much as a 75% decrease in plating rates and a concomitant loss in coating quality. Shih and co-workers (8) claimed that the presence of oxygen in a Ti-NaCl or KCl bath was necessary for plating and indicated that poor coatings on iron resulted when no oxygen was present.

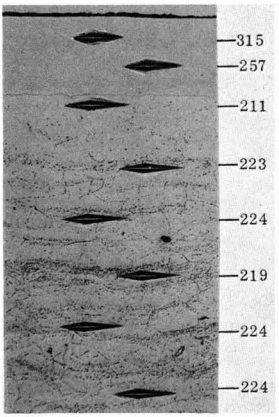


Fig. 5. Titanium coated Cb752 substrate; plated in 5 m/o $TiCl_3$ bath for 16 hr at 1093°C (2000°F). Magnification *ca.* 200X.

While it was not possible to completely exclude oxygen from the fused salt baths in this investigation, all practical precautions were taken to prevent its introduction. It should be noted that the titanium deposition rates in this study were two to four times greater than any reported in the literature.

## Discussion of Results

The fused salt baths investigated in this work produced smooth, adherent titanium alloy deposits on both Cb752 and D43 alloys. Close examination of the specimen cross section seen in Fig. 4 shows two different structures. The single-phase region adjacent to the substrate is probably columbium-rich, beta titanium alloy. The outer, Widmanstatten-like structure is a very dilute solid solution of columbium in transformed beta titanium alloy and was not evident on thinner coatings which showed the single-phase, beta structure only.

The substrate was also affected by the coating treatment. Examination of the microhardness traverse in Fig. 5 shows a loss in substrate hardness. This loss, in all cases, was most pronounced in the area immediately adjacent to the coating and was as much as 25% in some cases. The decrease in hardness was greater at higher temperatures and longer times. This phenomena may be explained by the "interstitial sink effect" (9). This term is used to describe the potential for migration and the equilibrium partition of an interstitial element as a result of the difference in the partial molal free energies of the element in two adjacent metallic layers.

The Cb752 alloy is basically a solid solution strengthened alloy depending on oxygen in solution plus a small distribution of $ZrO_2$ precipitates. These precipitates are readily seen in the as-received alloy with the aid of electron microscopy. A similar examination of the titanium-coated alloy revealed a large reduction or complete elimination of this precipitate for varying depths below the coating-substrate interface depending on the coating time and temperature. The distribution of oxygen between columbium and titanium may be calculated by considering the partial molal free energies of solution. This partition at 1500 K (at equilibrium) in a titanium-coated Cb752 alloy is:

| | Columbium | Titanium |
|---|---|---|
| Oxygen, ppm | 1 | 1000 |

In an effort to fully characterize the plating chemistries, periodic chemical analyses were performed on the operating baths. Comparison of the observed data (weight per cent titanium in the bath) and theoretical weight per cents, as a function of oxidation state, gave an indication of the valence state of the titanium in a bath. Previous work reported in the literature (10, 11) indicated that the predominant reduction product in a $K_2TiF_6$ bath, similar to those used in this work, was $Ti^{+3}$. Analyses and calculations have shown the average valence in the fluoride baths to be generally between +2 and +3, while the predominant species in the $TiCl_3$ baths was found to have an average valence of +2.2. Kreye and Kellogg (12) reported $Ti^{+2}$ as the dominant species in an NaCl-KCl-$TiCl_3$ melt at 760°C. They also observed a slightly lower $Ti^{+2}$ concentration at 782°C with a corresponding increase in the $Ti^{+3}$ species. These findings are in accord with the +2.2 average valence in the present work and might also explain the somewhat higher plating rates found in the $K_2TiF_6$ baths compared with the chloride system. With an average valence of +2.2, the chloride baths were not in as fully reduced a condition as were the fluoride baths when in the +3 or lower state.

The parabolic nature of the deposition rate indicates that the deposition is controlled by diffusion into the metal substrate. A diffusion controlled hypothesis is supported by considering the difference in chemical

activity between the titanium in the source and the titanium in solution in the columbium. The activity of the titanium in solution in the columbium is lower than the activity of the titanium in the source. The decrease in activity from the pure to the alloyed state is then the probable driving force for deposition. It was also noted that the deposition rate was highly temperature dependent, increasing with increasing temperature. This behavior would be expected in a diffusion-controlled reaction as the diffusivity increases with the temperature. Further, if the deposition were diffusion controlled, the rate constant, $k$, from the equation

$$W^2 = kt \quad [1]$$

could be described by the Arrhenius equation and expressed by:

$$k = A\ (\exp) -\frac{Q}{RT} \quad [2]$$

where $A$ is a constant, $Q$ might be called the "activation energy for deposition," $R$ is the universal gas constant, and $T$ is the absolute temperature. If the diffusion hypothesis is correct and Eq. [2] accurately describes the rate constant, an Arrhenius plot of $\ln k$ *vs.* $(1/T)$ should yield a straight line. Such a plot is shown in Fig. 6 for the 5 mole per cent $K_2TiF_6$ bath and is seen to be linear. An activation energy for deposition was determined graphically from Fig. 6 and is 46 kcal/mole. This may be compared to the activation energy for diffusion of titanium in columbium which ranges from about 61 kcal/mole in pure columbium to 39 kcal/mole in pure titanium (13) while the activation energy for diffusion of complex titanium ions in fused salt solutions is expected to be only 6-10 kcal/mole (14). This further supports the hypothesis that the rate-determining step is interdiffusion of the titanium and the basis metal.

Straumanis *et al.* (15) determined the activation energy for diffusion of titanium into an iron substrate. A value of 32 kcal/mole may be calculated from their reported data. This may be compared with the value of 46 kcal/mole determined in the present work and designated, "the activation energy for deposition." More precisely, the latter value, 46 kcal/mole, reflects the activation energy for diffusion of titanium in a columbium alloy, and a comparison of the two values indicates that a titanium alloy coating may be developed more easily on an iron substrate than a columbium substrate under similar conditions if nearly equal frequency factors (A) are assumed. Preliminary work was undertaken to substantiate this conclusion, and results are presented in Table V.

No runs were performed which lasted over 60 min; however, as might be expected, the initial titanium deposition rate is faster on iron than on columbium by a factor of 1.4 to 2. In general, diffusion activation energies of metals in substitutional solid solution are proportional to the melting point, and deposition rates should also be proportional to melting points. An approximately linear relationship between titanium deposition rate and substrate melting point has been observed (over an 1800°C substrate melting point range) in other work by the authors.

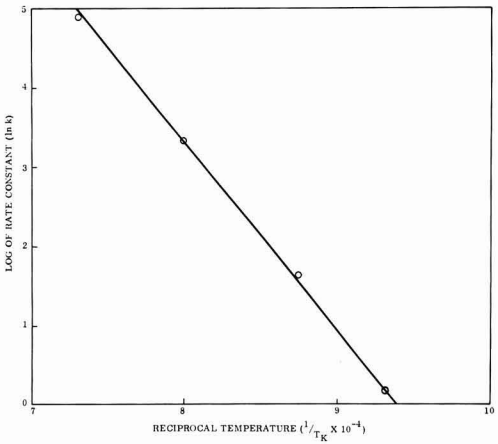


Fig. 6. Arrhenius plot ln $k$ *vs.* reciprocal absolute temperature

Table V. Titanium deposition on 1010 steel from a 20 m/o $K_2TiF_6$ bath

| Time, min | Average weight gain (mg/cm²) at 982°C |
|---|---|
| 2 | 0.8 |
| 6 | 1.9 |
| 15 | 3.4 |
| 30 | 4.0 |
| 60 | 6.9 |

There are several possible mechanisms (of which three are most apparent) which could account for the deposition of titanium on columbium alloys with the subsequent formation of a titanium-rich titanium/columbium alloy at the specimen surface. One such mechanism is an oxidation reduction type in which reactions similar to the following might occur:

$$3Cb\ (alloy) + 5TiF_3 \rightarrow 3CbF_5 + 5Ti$$

or

$$2Cb\ (alloy) + 5TiCl_2 \rightarrow 2CbCl_5 + 5Ti$$

Interdiffusion of the titanium and columbium would then produce the observed alloy coating. The operation of this oxidation-reduction mechanism should result in a decreased substrate thickness, an over-all weight loss or slight weight gain (depending on the coefficients in the redox equation chosen), and the accumulation of columbium in the bath.

Another possibility is a disproportionation reaction leading to the production of titanium metal. A possible representation is:

$$Ti + 6F^- + 3TiF_6^{-2} \rightarrow 4TiF_6^{-3}$$

$$Cb + 4TiF_6^{-3} \rightarrow 3TiF_6^{-2} + 6F^- + (Ti\text{-}Cb\ alloy)$$

This mechanism should be dependent on $TiF_6^{-3}$ concentration and would presumably decrease to a negligible rate with decreasing temperature. As long as sufficient titanium is present to support the deposition rates observed, interdiffusion rates would still control the plating rate. It is possible that some $TiF_4$ would be lost from the bath as a gaseous species; however, it would more probably be retained as a complex $F^-$ ion.

The remaining possible mechanism is the diffusion of dissolved or finely dispersed titanium in the melt into the columbium substrate; for example

$$Ti + Cb\ (alloy) \rightarrow TiCb\ (alloy)$$

Again, the deposition rate should be a function of the ease of interdiffusion of titanium and the substrate material and should decrease with increasing alloy thickness. All of the suggested mechanisms would be temperature dependent.

The oxidation-reduction type mechanism can be eliminated because no decrease in substrate thickness occurs and a positive weight gain is always observed for a coated specimen.

Straumanis, Shih, and Schlecten (15) stated that they were able to differentiate between a disproportionation type reaction and one in which dispersed titanium metal or $TiO_x$ reacted to form the alloy coating. They concluded that the coating was formed by direct impact of dispersed titanium or $TiO_x$ particles in the melt with the surface to be coated.

When examining the possibility of the dissolved or finely dispersed titanium theory, it is interesting to note that recent work (16) has demonstrated the ex-

istence of true solutions of metals in their own halide salts at elevated temperatures. Although no data are available for solutions of titanium in titanium-fluoride or chloride melts, it is quite possible that such systems do exist. X-ray diffraction analysis of melt samples in the present investigation failed to show the presence of any free titanium or titanium oxides in the bath. This does not, though, eliminate the possibility of dissolved titanium metal.

Sufficient data are not available from the present work to determine whether disproportionation of a reduced titanium complex at the specimen surface or mechanical adherence of free titanium metal is the coating mechanism. Evidence for both mechanisms exist, and neither may be ruled out at this time.

### Acknowledgments

The authors are indebted to Messrs. Warren Johnson and Gail Eichelman for helpful discussions and technical direction on this program. The work described was supported by the Chemical Engineering Branch (MATC), Manufacturing Technology Division, Air Force Materials Laboratory, Wright-Patterson Air Force Base, Ohio on Contract AF33(615)-3173.

Manuscript received Dec. 27, 1966; revised manuscript received May 18, 1967. This paper was presented at the Philadelphia Meeting, Oct. 9-14, 1966.

Any discussion of this paper will appear in a Discussion Section to be published in the June 1968 JOURNAL.

### REFERENCES

1. G. B. Wood, P. A. Krasley, K. Schere, and A. Brenner, Electrodeposition of Titanium. U. S. Department of Commerce, National Bureau of Standards, ASTIA-AD 56206 (1 October 1954).
2. A. R. Stetson, U. S. Pat. No. 3,024,174.
3. C. B. Gill, M. E. Straumanis, and A. W. Schlecten, *This Journal*, **102**, 42 (1955).
4. *Ibid.*, 81.
5. M. E. Straumanis and A. W. Schlecten, *ibid.*, **102**, 131 (1955).
6. M. B. Alpert, U. S. Pat. No. 2,734,003 (Feb. 7, 1956).
7. A. R. Stetson and V. S. Moore, Technical Documentary Report No. RTD-TDR-63-4006, Part III (1965).
8. S. T. Shih, M. E. Straumanis, and A. W. Schlecten, *This Journal*, **103**, 395 (1956).
9. A. G. Metcalfe and J. S. Dunning, Solar Report RDR-1392 (July 1965).
10. J. G. Wurm, L. Gravel, and R. J. A. Potvin, *This Journal*, **104**, 301 (1957).
11. M. E. Siebert and M. A. Steinberg, *J. Metals*, **2**, (September 1956).
12. W. C. Kreye and H. H. Kellogg, *This Journal*, **104**, 504 (1957).
13. C. S. Hartley, J. E. Steedly, and L. D. Parsons, "Binary Interdiffusion in Body-Centered Cubic Transition Metals," Diffusion in Body-Centered Cubic Metals, ASM (1965).
14. S. Senderoff, and G. W. Mellors, *ibid.*, **113**, 66 (1966).
15. M. E. Straumanis, S. T. Shih, and A. W. Schlecten, *This Journal*, **104**, 17 (1957).
16. J. Lumsden, "Thermodynamics of Molten Salt Mixtures," Academic Press, London and New York (1966).

# Electrolytic Reductive Coupling

## XV. Electroreductions of Aqueous Concentrated Solutions of Diethyl Maleate in the Presence of Sodium or Tetraethylammonium Cations[1]

**Manuel M. Baizer and John P. Petrovich**

*Central Research Department, Monsanto Company, St. Louis, Missouri*

ABSTRACT

Concentrated solutions of diethyl maleate in dimethylformamide-water containing sodium or tetraethylammonium *p*-toluenesulfonate were electrolyzed at constant current. The yields of diethyl succinate and of tetraethyl butanetetracarboxylate were determined. At a given concentration of supporting cation and of bulk water less hydrodimer is formed in the presence of sodium than in the presence of tetraethylammonium cations. These results are related to previous suggestions concerning the influence of the degree of hydration of the supporting cations upon the nature of the electroreduction products.

It has been suggested (2) that during the electroreduction of concentrated aqueous solutions of acrylonitrile the presence of alkali metal cations ($M^+$), which are simultaneously discharged, leads to substantial yields of propionitrile [1] because of concomitant chemical reactions, whereas the replacement of $M^+$ by quaternary ammonium cations ($R_4N^+$), which are not discharged at the operating cathode potential, permits the attainment of very high yields of adiponitrile [2].

$$CH_2{=}CHCN + 2\bar{e} + 2H_2O \xrightarrow{M^+(H_2O)_x} CH_3CH_2CN + 2\,\overline{OH} \quad [1]$$

[1] For Part XIV see (1).

$$2CH_2{=}CHCN + 2\bar{e} + 2H_2O \xrightarrow{R_4N^+} NC(CH_2)_4CN + 2\,\overline{OH} \quad [2]$$

Recently Feoktistov and co-workers (3) and, independently, Gillet (4) have offered an alternate explanation for the change in the distribution of reduction products when one replaces supporting electrolytes containing $M^+$ by those containing $R_4N^+$. They have pointed out that alkali metal cations are hydrated while quaternary ammonium cations are not. As a consequence, Gillet has argued, when the acrylonitrile molecule, aligned with the $\beta$-carbon atom on

Table I. Electrolysis of 43.0g of diethyl maleate at a mercury cathode 20°-25°, 1.00 amp for 3 hr

| Run | Catholyte | | | Esters recovered | | | | | | | Apparent losses | |
|---|---|---|---|---|---|---|---|---|---|---|---|---|
| | G salt | Ml $H_2O$ | Ml DMF | G diethyl maleate | G diethyl succinate | Equiv. amp hr | Curr. eff, % | G hydrodimers* | Equiv. amp hr | Curr. eff, % | G diethyl maleate equiv. | Amp hr. |
| 1 | 19.4A[a] | 16 | 80 | 22.6 | 2.41 | 0.743 | 24.8 | 13.0 | 2.01 | 67.0 | 5.0 | 0.25 |
| 2 | 19.4A | 22 | 74 | 21.2 | 4.96 | 1.53 | 51.0 | 10.7 | 1.67 | 55.5 | 6.1 | −0.20 |
| 3 | 30.1B[b] | 16 | 80 | 20.6 | 0.81 | 0.25 | 8.2 | 15.6 | 2.42 | 80.5 | 6.0 | 0.33 |
| 4 | 30.1B | 22 | 74 | 22.4 | 2.16 | 0.67 | 22.2 | 14.6 | 2.27 | 75.5 | 3.8 | 0.06 |
| 5 | 15.5A + 6.0B | 22 | 74 | 20.5 | 1.62 | 0.50 | 16.7 | 15.1 | 2.34 | 78.0 | 5.8 | 0.16 |
| 6 | 19.4A | 30 | 66 | 25.0 | 5.33 | 1.64 | 54.9 | 8.84 | 1.37 | 45.7 | 3.8 | — |
| 7 | 30.1B | 30 | 66 | 22.3 | 1.93 | 0.60 | 19.8 | 13.9 | 2.16 | 72.0 | 4.8 | 0.24 |
| 8[c] | 36.1B | 36 | 79 | 9.21[c] | 3.51 | 1.18 | 36.2 | 10.3 | 1.59 | 53.0 | 4.8 | 0.23 |

[a] Sodium *p*-toluenesulfonate.
[b] Tetraethylammonium *p*-toluenesulfonate.
[c] Initially 5.0 ml of diethyl maleate was included in the catholyte. The remainder, to a total of 25.8g (0.15 mole), was added in the course of the run. Acetic acid had to be added dropwise to maintain the desired pH.
* Identified by comparison of vpc retention time with samples previously prepared (7). Two isomers in a ratio of *ca* 93/7 (presumably meso-/dl) were obtained.

the cathode surface, is being reduced[2] the final anionic intermediate which is just leaving the cathode surface has an opportunity to react at the $\beta$-carbon atom with water when $M^+(H_2O)_x$ is the counterion [1], whereas it has an overwhelming opportunity to react with a second acrylonitrile molecule when $R_4N^+(H_2O)_o$ is the counterion.

The purpose of the work reported here was to test the effect of (supporting) cation hydration on the yield of hydrodimer prepared from an activated olefin whose electroreduction occurs at a cathode voltage at which simultaneous cation discharge is unambiguously avoided. While several monoactivated olefins $CH_2$=CHX (where X is an electron-withdrawing group) are available which reduce at a considerably more positive cathode voltage than is required for $Na^+(H_2O)_x$ discharge, they may, like methyl vinyl ketone, undergo under the conditions of electrolysis various chemical side reactions which complicate the interpretation of the results. Because its reduction occurs at a voltage at least 0.7v more anodic than that of $Na^+(H_2O)_x$, its polarography has been extensively[3] studied (6), its electrolytic hydrodimerization to tetraethyl butanetetracarboxylate has been reported (7), and its side reactions during reduction are minimal, diethyl maleate was chosen as the model activated olefin for this study.

## Experimental

*Reagents.*—Diethyl maleate (Matheson Scientific, Superior) was used as received. Vpc and nmr analyses showed that it contained about 8% diethyl fumarate. Tetraethylammonium *p*-toluenesulfonate (Alfred Bader Company) was recrystallized from acetone and dried *in vacuo* at 60°. Sodium *p*-toluenesulfonate was prepared from the acid and base and dried as above. The dimethylformamide (DMF) was redistilled through a Vigreau column at atmospheric pressure.

*Equipment.*—The electrolysis cell and associated apparatus have been described (1). A mercury cathode, area 55 $cm^2$, was used throughout. Vpc analyses of the products obtained from the electrolyses were carried out using an F and M Model 300 instrument; the column contained 1% silver nitrate and 18% Carbowax 20M on 35-48 mesh Chromosorb W and was used at 125° (for "low boilers") and at 225° (for "high boilers").

*Procedures.*—The electrolysis data are summarized in Table I. The catholytes contained 43.0g (0.25 mole) of diethyl maleate, 0.10 mole of sodium (19.4g) or tetraethylammonium *p*-toluenesulfonate (30.1g), and 96 ml of a DMF-water mixture; the total volume was *ca.* 150 ml. The anolytes were saturated aqueous solutions of the same electrolyte present in the catholyte. The electrolyses were conducted at a constant current of 1.00 amp for 3 hr. The cathode voltage in the several experiments was −1.19 to −1.30v (SCE). Acetic acid was available for dropwise addition to the catholyte in order to maintain the pH at 7-8 (measured externally on Alkacid paper). Usually no acid addition was needed, indicating that saponification of the ester was rapid enough to provide a buffering effect. No hydrogen was evolved. At the end of the electrolysis the catholyte was separated from the mercury, diluted with 200 ml of ice water, and extracted with three 100 ml portions of methylene chloride. The combined extracts were washed with three 100 ml portions of water and dried over anhydrous magnesium sulfate. The filtered solution was heated on a water bath to remove methylene chloride and then fractionated through a 2-ft Vigreau column to a vapor temperature of 50° (18 mm) to remove the bulk of the residual DMF. The remaining crude mixture of esters was fractionated through a semimicro apparatus having a vacuum-jacketed 6-in. Vigreau column. The following fractions were collected: (*i*) to 115° (20 mm), (*ii*) 115°-118° (20 mm), (*iii*) to 153° (0.25 mm), (*iv*) 156°-161° (0.25 mm), (*v*) pot residue.[4] Each fraction[5] was analyzed by vpc first at 125° to determine DMF, diethyl maleate, diethyl succinate, and diethyl fumarate and then at 225° to determine tetraethyl butanetetracarboxylate and its ratio to the lower boiling components.

## Discussion of Results

At a given level of proton donor (water) concentration in the catholyte, all other conditions being the same, more hydrodimerization occurs in the presence of tetraethylammonium than of sodium (run 3 *vs.* 1; run 4 *vs.* run 2). The hydrodimerization is less sensitive to increasing water concentration when tetraethylammonium is used than when sodium is used, *e.g.*, the yield of hydrodimer in run 7 is 89.5% of its value in run 3, whereas the yield in run 6 is only 68.3% of its value in run 1. Further the addition of tetraethylammonium to a catholyte containing sodium (run 5) is capable of elevating the yield of hydrodimer substantially. These results lend support to the proposal (3, 4) that, in effect, adsorption of tetraalkylammonium on the mercury cathode leads to the establishment of a water-poor zone close to the cathode surface.[6] The substantial yield of hydrodimer ob-

[2] In the over-all two-electron process the acrylonitrile may during the uptake of the first electron react simultaneously at the -CN or $\alpha$-carbon atom with a molecule of water from the bulk of solution [5].
[3] Professor Wawzonek has pointed out that the polarography of diethyl maleate in tetralkylammonium electrolytes has not been previously reported. While this information will be later presented separately in a paper describing work which is currently in progress, it may be stated now that in aqueous dimethylformamide no significant differences were found in the polarographic behavior using sodium or tetraethylammonium supporting electrolytes.
[4] This was always negligible, indicating that no oligomers higher than the hydrodimer had been formed.
[5] This procedure gave more satisfactory results than the attempted vpc analysis of the crude mixture directly.
[6] This may likewise explain the reported excellent yield of adiponitrile from acrylonitrile in an amalgam reduction in the presence of aqueous acid and tetraethylammonium *p*-toluenesulfonate (8).

tained (run 8) even when the concentration of diethyl maleate in the catholyte at a given time is relatively low and the concentration of water relatively high emphasizes again the need for caution in predicting the products of an electrochemical reduction; this is particularly true when activated olefins are involved.

Since all runs were carried out at the same constant current density, the rates of generation of the reduced intermediates were the same. If formation of hydrodimer occurred *via* radical coupling of anion-radicals or (after neutralization with water) their derived radicals, the yield of hydrodimer should not be affected by the nature of the supporting cation nor by the relatively small over-all changes in water concentration. The experimental results are better accommodated by the proposal (9) that the coupling is the result of an anionic attack of a reduced species upon an unreduced molecule. Whether this is a two-step (9) or a concerted process (1) is still a moot question. It is also not known at present whether the hydrodimerization of 1,2-diactivated olefins proceeds by the same mechanism as the hydrodimerization of monoactivated olefins: this problem is under investigation in this Laboratory.[7]

Finally, it is instructive to examine (Table I) the apparent losses of diethyl maleate and to compare these with the coulombic input not accounted for in the form of reduced products isolated. In run 1, *e.g.*, the "missing" 0.25 amp hr is equivalent to 0.81g diethyl succinate or 1.61g hydrodimer. Assuming complete loss of these reduced esters through saponification[8] there is still considerable diethyl maleate to account for. The facile saponification of the latter ester is well known (6); it was of interest to be able to estimate whether part of the saponified maleate (as half-ester or diacid) was being reduced in the course of the electrolysis and was causing a shift of the cathode v to a more negative value than it would have had in the absence of saponification, or whether part of the diethyl succinate already formed was being later saponified. A study[9] of the kinetics of diethyl maleate/diethyl succinate[10] saponification showed a rate ratio of $k_m/k_s = 20$. Even if all the diethyl succinate had been present from the start (run 1) and the cathode surface had a pH of *ca.* 13, less than 0.2g of diethyl succinate would have been saponified in 3 hr; however, all of the unrecovered ester can be accounted for by saponification of diethyl maleate under the same conditions. Therefore, the "excess" current was most probably used in the reduction of ethyl hydrogen maleate.

Manuscript received March 29, 1967; revised manuscript received *ca.* June 12, 1967.

Any discussion of this paper will appear in a Discussion Section to be published in the June 1968 JOURNAL.

REFERENCES

1. J. P. Petrovich, J. D. Anderson, and M. M. Baizer, *J. Org. Chem.*, **31**, 3897 (1966).
2. M. M. Baizer, *This Journal*, **111**, 215 (1964).
3. L. G. Feoktistov, A. P. Tomilov, and I. G. Sevast'yanova, *Soviet Electrochemistry*, **1**, 1165 (1965).
4. I. E. Gillet, Abstracts 17th Meeting of CITCE, Tokyo-Kyoto, September 1966, p. XXV.
5. F. Beck, *Chem. Ing. Techn.*, **37**, 607 (1965).
6. P. J. Elving and C. Teitelbaum, *J. Am. Chem. Soc.*, **71**, 3916 (1949); R. Takahashi and P. J. Elving, *Electrochim. Acta*, **12**, 213 (1967).
7. M. M. Baizer and J. D. Anderson, *This Journal*, **111** 223 (1964); A. P. Tomilov and L. V. Kaabak, *Zhur. Obshchei Khim.*, **33**, 731 (1963).
8. F. Matsuda, *Tetrahedron Letters*, 6193 (1966).
9. M. M. Baizer, *ibid.*, 973 (1963).
10. G. C. Jones and T. H. Ledford, *ibid.*, 615 (1967).

[7] After this manuscript was submitted for publication, a possibly relevant paper appeared (10) concerning the participation of the $\alpha$-carbon atom in electrolytic reductive couplings of activated olefins. In 1,2-bis-activated olefins the $\alpha$-$\beta$-carbon atoms are of course equivalent.

[8] The half-ester or diacid would not have been extracted by methylene chloride from slightly alkaline solution.

[9] The rates of ester saponification were followed to > 50% reaction by vpc analysis using an XE-60 on Teflon column at 115°. In a typical experiment the appropriate ester and diphenylmethane, the vpc internal standard, were dissolved in a DMF solution containing 30g of tetraethylammonium *p*-toluenesulfonate and 30 ml of 10% aqueous tetraethylammonium hydroxide and diluted to 100 ml with DMF. The reaction flasks were thermostated at 25°. At appropriate times a 1 ml aliquot was removed, neutralized with acetic acid, and analyzed directly by vpc for unreacted diester. The second order rate constants obtained by this method for diethyl maleate and diethyl succinate were $2.1 \times 10^{-3}$ and $1.0 \times 10^{-4}$ liter mole$^{-1}$ sec$^{-1}$, respectively. The estimated error in $k$ is $\pm$ 0.2.

[10] It was assumed that the rate of saponification of the hydrodimer was too low to affect the conclusions.

# Electrolytic Oxidation of Aromatic Amines

S. Wawzonek and T. W. McIntyre

*Department of Chemistry, University of Iowa, Iowa City, Iowa*

ABSTRACT

The electrolytic oxidation of anilines at a rotating platinum electrode in acetonitrile in the presence of pyridine involved a two electron change and formed azobenzenes. Evidence for the mechanism was the voltammetric behavior of hydrazobenzenes, *p*-phenylenediamine and 4,4'-dimethoxyazobenzene and the formation of azobenzenes in macroscale oxidations. The behavior of anilines in the absence of pyridine was more complex since the amine acted as a base and formed a salt which was not easily oxidized. Exceptions were the weakly basic *o*-nitroaniline, *p*-nitroaniline, 2,4-dinitroaniline and the reversible systems, *o*-phenylenediamine and *p*-phenylenediamine; two electrons were involved for these examples.

The electrolytic oxidation of aromatic amines was studied in acetonitrile at a microrotating platinum electrode to determine whether this reaction could be used to prepare azobenzenes on a macroscale.

Voltammetric studies of aromatic amines in acetonitrile have been carried out with aniline (1), 2-aminoanthracene, 2-fluorenamine, 1- and 2-naphthylamine (2), *p*-phenylenediamine (3, 4), 9-amino-10-phenylanthracene (5) and dimethylanilines (4, 6). A stepwise oxidation is reported for *p*-phenylenediamine (3) and a one-electron oxidation change is suggested for the dimethylanilines (4, 6) and 9-amino-10-phenylanthracene (5).

Large-scale oxidations of anilines have been carried out mainly in aqueous acid and basic media. The former usually leads to polymeric products or nitrogen free compounds, (7-10). In alkaline solution *p*-toluidine and 2,4-dimethylaniline gave the corresponding

azobenzenes at an iron anode (11). If one or both of the N-hydrogens are replaced by alkyl groups, dimeric products result (12, 13).

## Experimental

*Apparatus.*—The voltammetric data were obtained with a Sargent Model XXI polarograph and were corrected for *iR* drop across the cell. All measurements were made in a water thermostat at 25° ± 0.1°.

Resistances were measured with a Wheatstone bridge circuit which contained an audio oscillator signal generator and a head set as a null indicator. A variable capacitor was placed in one arm of the bridge circuit to balance the capacitance effects of the cell. An input voltage of 1v (a.c.) and a signal of 1000 Hz was used.

The indicator electrode was a platinum bead electrode, which had an exposed area of 1.0 $mm^2$. This microelectrode was constructed by sealing a No. 20 platinum wire into a 6 mm glass tube parallel to the axis of rotation; the exposed wire was then fused flush with the glass surface. The platinum electrode was rotated at 600 rpm with a Sargent Synchronous Rotator and cleaned before each run by the procedure of Kolthoff and Coetzee (14).

The solutions (25 ml volumes were used) were studied in a cylindrical shaped cell with an external Ag/0.1M $AgClO_4$ reference electrode connected to the cell through a fine glass frit.

The large-scale electrolyses were carried out in two different cells. One cell was an H-cell, which had a medium glass frit separating the two compartments of equal volume (100 ml). One compartment contained a cylindrical platinum gauze anode, which could be rotated at high speed, and the other compartment contained a stirred mercury pool cathode. This cell was also provided with a compartment for a reference electrode for controlled potential electrolysis.

The second cell consisted of a tall beaker 14.5 cm high and 7 cm in diameter. A Coors porous cup (7.5 by 2.6 cm with a wall thickness of 2 mm) was placed inside as the cathode compartment.

A Heath-Kit IP-12 battery eliminator was used as a direct current source with a variable voltage range of 0-15v. For controlled potential electrolysis the manual apparatus described by Lingane (15) was used. An L&N Student Potentiometer was employed as the voltage measuring device.

Infrared spectra of cast films were recorded using a Perkin-Elmer spectrophotometer.

*Chemicals.* Acetonitrile was purified by method E of Coetzee *et al.* (16).

Pyridine was purified by refluxing with solid potassium hydroxide and fractionally distilling through a Fenske column; the center fraction (60%) was collected.

Lithium and sodium perchlorate (G. F. Smith and Company) were dried under vacuum at 80° and stored over phosphorous pentoxide.

The various anilines, hydrazobenzenes, and azobenzenes studied were either obtained commercially or synthesized by appropriate methods given in the literature.

*Electrolytic oxidations.—p-Nitroaniline.* p-Nitroaniline (1.0g)) was dissolved in 90 ml of acetonitrile (0.5*M* pyridine, 0.5*M* sodium perchlorate) and electrolyzed in the H-cell using a rotating platinum gauze anode and a mercury pool cathode. The solution was degassed with nitrogen before and during the electrolysis. At an applied potential of 10v, a current of 0.3 amp was obtained, which decreased to a final value of 0.05 amp in 4 hr. The anolyte was concentrated to 20 ml and 30 ml of water was added. The precipitated material was collected and extracted with 100 ml of cold acetone. The acetone was removed, and the residue was chromatographed on alumina in benzene-chloroform mixtures. The first fraction gave reddish brown crystals (0.26g, 39.2%), mp 220°-222°. The infrared spectrum was identical with that of an authentic sample of 4,4'-dinitroazobenzene. The second fraction from the column was *p*-nitroaniline.

*p-Chloroaniline.*—Oxidation of *p*-chloroaniline (1.0g) was carried out under conditions similar to those used for *p*-nitroaniline. At an applied voltage of 10v a current of 0.15 amp was obtained which decreased to a final value of 0.01 amp in 14 hr.

The anolyte was concentrated to 10 ml and poured into 500 ml of methylene chloride. The methylene chloride was filtered and extracted with two 100-ml portions of cold 5% hydrochloric acid solution. The aqueous extract was evaporated to dryness and 0.32g of *p*-chloroaniline was recovered as the hydrochloride. The methylene chloride extract was dried over anhydrous sodium sulfate, concentrated and chromatographed on alumina with benzene-chloroform mixtures. The first fraction contained 0.165g (24.3%) of 4,4'-dichloroazobenzene, which was identified by comparison of its infrared spectrum with that of an authentic sample. The melting point of the product after recrystallization from methanol was 185°-187°. The second fraction from the column gave 0.053g (7.8%) of a red crystalline compound, which had a melting point of 258°-260d° after recrystallization from toluene. This product produced a violet color when dissolved in concentrated sulfuric acid and gave a NH band in the 3200-3500 $cm^{-1}$ region in the infrared region. These properties agree with those of 2,5-di-*p*-chlorophenylaminobenzoquinonedi-*p*-chlorophenylimine [tetra-*p*-chloroazophenine (I)] (17).

A similar electrolysis of *p*-chloroaniline in the absence of pyridine and using 0.5*M* lithium perchlorate gave an acidic anolyte at the conclusion of the reaction. Products isolated were starting material (20%) and tar.

*2,4-Dichloroaniline.*—The electrolysis was conducted at 10v using the beaker cell with a platinum anode and a copper cathode. The initial current of 0.25 amp decreased to 0.05 amp in 4 hr. During the electrolysis the anolyte turned reddish brown and the azo compound precipitated. The mother liquor was concentrated and poured into water. The resulting product was extracted with hot benzene (200 ml) and chromatographed on alumina. The first fraction consisted of azo compound and was combined with the precipitated fraction. Recrystallization from methanol gave 2,4,2'4'-tetrachloroazobenzene; mp 161°-162°; yield, 30.0%. The infrared spectrum was consistent with this structure.

*p-Anisidine.*—Oxidation was carried out in a similar fashion to that used for *p*-chloroaniline using 0.5*M* lithium perchlorate. The residue in benzene was chromatographed on alumina and gave 4,4-dimethoxyazobenzene (5.2% yield) which melted at 162°-163° after recrystallization from a benzene-(30°-60°) petroleum ether mixture. The infrared spectrum was identical with that of an authentic sample.

The second fraction gave an 8.6% yield of dark red crystals melting at 236°-237°. These crystals gave a red-violet color with concentrated sulfuric acid and had an NH band in the 3200-3500 $cm^{-1}$ region of the infrared. These properties are in agreement with di-*p*-anisidinobenzoquinone-di-*p*-methoxyphenylimine (I) (tetra-*p*-methoxyazophenine) (18). The remaining oxidation products were resinous in nature.

*Aniline and p-chloroaniline.*—A solution of *p*-chloroaniline (0.5g) and aniline (3.0g) in 60 ml of acetonitrile and 10 ml of pyridine containing 0.5*M* sodium perchlorate was electrolyzed in a beaker containing a porous cup cathode compartment. The anode was a platinum screen and the cathode was a copper wire. The solution was purged with nitrogen and a potential of 8.0v was applied to the cell. The original current of 0.1 amp decreased to 0.05 amp after 4 hr. In this period the anolyte changed from an orange to a reddish-

brown color, and the anode became coated with a brown-black tar.

The anolyte was concentrated to 30 ml and poured into ether (30 ml). The ether solution was filtered, concentrated to 50 ml and chromatographed on alumina (grade I). The first fraction consisted of azo compounds which were rechromatographed. The second fraction gave a dark red solid (0.21g) which, on recrystallization from benzene, melted at 234°-236° and gave a violet color in concentrated sulfuric acid. This compound was halogen free and agreed in all respects with di-(phenylamino) benzoquinone-diphenylimine (azophenine) (19). The mixed azo compounds when rechromatographed twice on alumina using a 1:1 mixture of benzene-(30°-60°)petroleum ether gave azobenzene (0.243g) which melted at 68°-69° and *p*-chloroazobenzene (0.86g) melting at 88°-89° [ref. (20), 87.5°]. The infrared spectrum was similar to that for azobenzene and 4,4'-dichloroazobenzene.

*p-Chloroaniline and 2,4-dinitroaniline.*—A solution of *p*-chloroaniline (0.5g), 2,4-dinitroaniline (1.0g) in acetonitrile (80 ml) and pyridine (5 ml) containing 0.5*M* sodium perchlorate was electrolyzed under nitrogen in the H-cell at a controlled potential of +0.80v *vs.* the Ag/0.1*N* $AgClO_4$ electrode, using a rotating platinum anode and a mercury pool cathode. The initial current of 0.15 amp decreased to 0.05 amp in 8 hr. The anolyte was concentrated to 20 ml, poured into water (50 ml), and extracted with ether (500 ml). The ether extract was washed with 100 ml of 5% hydrochloric acid and 100 ml of water. The acid extract gave the hydrochloride of *p*-chloroaniline (0.11g). Removal of the ether gave a solid which was dissolved in a minimal amount of 1:1 benzene-chloroform mixture and chromatographed on alumina. The first fraction gave 4,4'-dichloroazobenzene (0.102g) melting at 184°-186°, and the second fraction gave 2,4-dinitroaniline (0.921g) melting at 178°-179° after crystallization from ethanol (92.1% recovery). No cross product was isolated.

*p-Chloroaniline and p-nitroaniline.*—This mixture was treated in a similar fashion to that described in the preceding paragraph using a controlled potential of +0.7v, 4,4-Dichloroazobenzene (22.8%) and *p*-nitroaniline (90%) were obtained together with resinous material.

*Hydrazobenzene.*—This compound (2.0g) was oxidized in a beaker (100 ml) containing a porous cup cathode compartment. The cell was wrapped with aluminum foil to keep out light, and the solution was deaerated during the electrolysis with nitrogen. The resulting solution when processed in the usual manner gave azobenzene (0.216g), dark brown polymeric material and a black crystalline residue similar to aniline black.

*4,4-Dichlorohydrazobenzene.*—The electrolysis was performed in a similar manner to that for hydrazobenzene. The anode solution gave an 82% yield of 4,4'-dichloroazobenzene.

*4,4-Dimethoxyazobenzene.*—The electrolysis and processing of the oxidation product was similar to the above procedure. The anolyte gave starting material (55%) and brown resinous material.

## Results

The voltammetric behavior of various anilines in acetonitrile containing 0.5*M* sodium perchlorate in the presence and absence of pyridine is given in Table I. Half-wave potentials corrected for the *iR* drop are reported against an external silver 0.1*M* silver perchlorate reference electrode.

Most of the compounds exhibited normal S-shaped waves in the absence of pyridine. In the presence of this compound the curves reached a current plateau which decreased near the end of the voltage scan. This behavior is associated with film formation on the electrode surface for, if the current-voltage curve is retraced without cleaning the microelectrode, the limiting current is substantially reduced. Waves were also encountered as peaks and are probably caused by an immediate coating of the electrode. The decrease in current was not caused by the oxidation of pyridine since this compound when pure does not give an oxidation wave in acetonitrile. In order to evaluate the number of electrons involved in the oxidation, hydroquinone and bromide ion were studied under similar conditions, and the data are given in Table I.

To aid in formulating an electrode mechanism a series of hydrazobenzenes and azobenzenes was studied under similar conditions, and the data are given in Table II.

**Table I. Voltammetric behavior of substituted anilines in acetonitrile containing 0.5*M* sodium perchlorate.[a] (*vs.* Ag/0.1*N* $Ag^+$)**

| Compound | Conc, millimolar | $+E_{1/2}$ | $I_l$[d] | 2mM $+E_{1/2}$ | Pyridine $I_l$[d] |
|---|---|---|---|---|---|
| Aniline | 0.43 | 0.54 | 10.1[b] | 0.54 | 13.2[c] |
| *o*-Nitroaniline | 0.23 | 1.07 | 15.0[b] | 1.03 | 15.0[b] |
| *p*-Nitroaniline | 0.40 | 1.03 | 14.2 | 0.95 | 16.9[b] |
| | 1.00 | 0.97 | 7.0 | | |
| | | 1.14 | 7.0 | | |
| *m*-Nitroaniline | 0.32 | 0.90 | 8.6 | 0.88 | 17.2[b] |
| *p*-Bromoaniline | 0.33 | 0.61 | 8.3 | 0.62 | 17.5[b] |
| *m*-Bromoaniline | 0.40 | 0.70 | 8.5[b] | 0.64 | 8.5[c] |
| *p*-Chloroaniline | 0.40 | 0.60 | 8.3 | 0.61 | 17.1[b] |
| *o*-Anisidine | 0.62 | 0.34 | 8.7[b] | 0.36 | 20.0[b] |
| *p*-Anisidine | 0.23 | 0.26 | 6.5 | 0.24 | 7.1 |
| | | | | 0.42 | 6.7 |
| | | | | 1.03 | 7.6[b] |
| 2,4-Dinitroaniline | 0.35 | 1.48 | 18.8 | 1.41 | 18.7[b] |
| 2,4-Dichloroaniline | 0.50 | 0.78 | 8.6 | 0.74 | 16.7[b] |
| *sym*-Trichloroaniline | 0.55 | 0.95 | 10.3 | 0.87 | 18.9 |
| *o*-Phenylenediamine | 0.82 | 0.08 | 7.2 | 0.09 | 25.8[c] |
| | | 0.76 | 7.8 | | |
| *m*-Phenylenediamine | 0.40 | 0.26 | 7.0[c] | 0.24 | 7.0 |
| | | | | 0.41 | 5.1[c] |
| *p*-Phenylenediamine | 0.44 | −0.10 | 7.1 | −0.10 | 7.1 |
| | | 0.44 | 6.3 | 0.15 | 6.5 |
| 2,2'-Diaminobiphenyl | 0.27 | 0.51 | 8.4 | 0.48 | 5.2[c] |
| | | 0.87 | 4.0[c] | | |
| Ethylphenylamine | 0.30 | 0.40 | 8.8 | 0.43 | 16.4[b] |
| N,N-diethylaniline | 0.40 | 0.34 | 9.6 | 0.36 | 18.5 |
| N,N-diethyl-*p*-chloroaniline | 0.33 | 0.47 | 8.9 | 0.47 | 9.5 |
| N,N-dimethylaniline | 0.30 | 0.35 | 10.8 | 0.36 | 20.5 |
| N,N-dimethyl-*p*-chloroaniline | 0.64 | 0.49 | 10.4 | 0.48 | 13.4 |
| | | | | 1.08 | 2.3 |
| Hydroquinone | 1.00 | 0.68 | 16.7 | 0.42 | 16.6 |
| Tetra-n-butyl-ammonium Bromide | 0.96 | 0.42 | 5.4 | | |
| | | 0.74 | 2.8 | | |

[a] Normal S-shaped wave.
[b] Plateau followed by a decrease in current.
[c] Peak
[d] $I_l = i_l/C$.

**Table II. Voltammetric behavior of azobenzenes and hydrazobenzenes in acetonitrile containing 0.5*M* sodium perchlorate[a] (*vs.* Ag/0.1*N* $Ag^+$)**

| Compound | Conc, millimolar | $+E_{1/2}$ | $I_l$[d] | 2 mM $+E_{1/2}$ | Pyridine $I_l$[d] |
|---|---|---|---|---|---|
| Azobenzene | 0.48 | 1.33 | 18.4 | Coating[c] | |
| Hydrazobenzene | 0.44 | 0.18 | 10.1 | 0.05 | 18.5 |
| | | 1.35 | 7.7 | | |
| 4,4'-Dichloro-azobenzene | 0.21 | 1.44 | 17.4 | Coating[c] | |
| 4,4'-Dichloro-hydrazobenzene | 0.46 | 0.26 | 11.0 | 0.16 | 19.2 |
| | | 1.44 | 10.4 | | |
| 4,4'-Dimethoxy-azobenzene | 0.74 | 0.98 | 18.0 | 0.98 | 18.0 |
| | | | | 1.25 | 25.8[b] |
| 4,4'-Dinitro-azobenzene | 0.29 | No wave | | No wave | |
| 2,2',4,4'-Tetra-nitroazobenzene | 0.34 | No wave | | No wave | |
| 2,2'4,4'-Tetra-chloroazobenzene | 0.21 | 1.59 | 17.8 | Coating[c] | |
| *sym*-Hexachloro-azobenzene | 0.29 | 1.63 | 17.8 | Coating[c] | |

[a] Normal S-shaped wave.
[b] Plateau followed by a decrease in current.
[c] Small bump in the c-v curve.
[d] $I_l = i_l/c$.

**Table III. Large-scale electrolytic oxidations of primary aromatic amines[a] and hydrazobenzenes[a]**

| Compound | Supporting electrolyte, 0.5*M* | Products (per cent yield) |
|---|---|---|
| *p*-Nitroaniline | $NaClO_4$ | 4,4'-Dinitroazobenzene (39.2%) |
| *p*-Chloroaniline | $NaClO_4$ | 4,4'-Dichloroazobenzene (24.3%); tetra-*p*-chloroazophenine (7.8%) |
| *p*-Chloroaniline[b] | $LiClO_4$ | Tar |
| 2,4-Dichloroaniline | $NaClO_4$ | 2,2',4,4'-Tetrachloroazobenzene (30.1%) |
| *p*-Anisidine | $LiClO_4$ | 4,4'-Dimethoxyazobenzene (5.2%) tetra-*p*-methoxyazophenine (8.6%) |
| Aniline and *p*-Chloroaniline | $NaClO_4$ | Azophenine (7.0%); azobenzene (8%); *p*-chloroazobenzene (83%) |
| Hydrazobenzene | $NaClO_4$ | Azobenzene (10.8%) |
| 4,4'-Dichlorohydrazobenzene | $NaClO_4$ | 4,4'-Dichloroazobenzene (82%) |

[a] The electrolysis were run in a nitrogen atmosphere, and pyridine (0.1M) was added unless otherwise indicated.
[b] No pyridine was added.

In further studies of the mechanism of oxidation macroscale oxidations of several anilines were carried out in acetonitrile, and the results are reported in Table III.

## Discussion of Results

Comparison of the limiting currents for the oxidation of the anilines in the presence of pyridine with that for hydroquinone and bromide ion indicates that the majority of the examples involve a two-electron change. The lower values observed for aniline, *o*-nitroaniline, m-bromoaniline, m-phenylenediamine, and 2,2'-diaminobiphenyl were caused by coating of the electrode.

The electrode reaction suggested by the two-electron change using aniline as an example is the following

(*a*) $C_6H_5NH_2 - e \rightarrow C_6H_5NH_2^{\cdot +}$

$C_6H_5NH_2^{\cdot +} + \text{pyridine} \rightarrow C_6H_5NH\cdot + C_5H_5NH^+$

(*b*) $2C_6H_5NH\cdot \rightarrow C_6H_5NHNHC_6H_5$

$2C_6H_5NHNHC_6H_5 - 2e + 2\ \text{pyridines} \rightarrow C_6H_5N{=}NC_6H_5 + 2C_5H_5NH^+$

(*c*) $C_6H_5NH\cdot \leftrightarrow HN{=}\langle\cdot\rangle{-}H$

$C_6H_5NH\cdot + HN{=}\langle\cdot\rangle{-}H \rightarrow C_6H_5NH\langle\rangle NH_2$

$C_6H_5NH\langle\rangle NH_2 - 2e + 2\ \text{pyridines} \rightarrow C_6H_5N{=}\langle\rangle{=}NH + 2C_5H_5NH^+$

The extent to which reactions (*b*) and (*c*) occur will depend on the substituents present.

In agreement with this mechanism is the oxidation of hydrazobenzenes (Table II) and *p*-phenylenediamine (Table I) in the presence of pyridine at more negative potentials than those for the anilines, and the formation of azobenzenes and azophenines (I) in the macroscale oxidations (Table III)

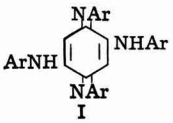


I

Further evidence is the appearance of a third wave in the oxidation of *p*-anisidine at approximately the same point as that for 4,4'-dimethoxyazobenzene. A similar wave was not observed for other azobenzenes because of coating of the electrode.

Diethylaniline and dimethylaniline in the presence of pyridine would involve coupling in the *p*-position in a manner to that suggested by Adams (6)

$R_2NC_6H_5 - e \rightarrow R_2NC_6H_5^{\cdot +} \leftrightarrow R_2\overset{+}{N}{=}\langle\cdot\rangle{-}H$

$R_2\overset{+}{N}{=}\langle\cdot\rangle{-}H + 2\ \text{pyridines}$

$\rightarrow R_2N\langle\rangle\langle\rangle NR_2 + 2C_5H_5\overset{+}{N}H$

$R_2N\langle\rangle\langle\rangle NR_2 - 2e \rightarrow R_2\overset{+}{N}\langle\rangle{=}\langle\rangle{=}\overset{+}{N}R_2$

The oxidation of N-ethylaniline and N-*p*-nitrobenzylaniline could proceed in the same fashion or could give rise to a hydrazine which would be oxidized further. Large-scale oxidation of *p*-nitrobenzylaniline formed the hydrazine together with polymers (21).

*p*-Phenylenediamine and *o*-phenylenediamine which behave reversibly in aqueous medium are oxidized stepwise to the quinoneimine (3). In the presence of pyridine *o*-phenylenediamine behaves differently and shows an abnormally high wave. A similar behavior has been observed in aqueous acetate buffer solution (22) and has been ascribed to the formation of a diaminophenazine which is oxidized further. Another possible explanation is further oxidation of the resulting *o*-quinonediimine to muconontrile since

$\langle\rangle(=NH)_2 - 2e + 2C_5H_5N \rightarrow HC(=CHCN)\text{-}HC(=CHCN) + 2C_5H_5NH^+$

such a reaction is reported to take place in the oxidation of *o*-phenylenediamine by lead tetraacetate (23).

The oxidation of the anilines in the absence of pyridine is more complex. The aniline itself acts as a base and converts the cation radical into the free radical and a salt which would not be easily oxidized

$ArNH_2 - e \rightarrow ArNH_2^{\cdot +}$

$ArNH_2^{\cdot +} + ArNH_2 \rightarrow ArNH\cdot + ArNH_3^+$

Exceptions are the nitroanilines and are discussed later. The free radical thus formed would couple and form the corresponding hydrazobenzenes and N-arylphenylenediamines as mentioned earlier. The latter compound would lead to an N-arylquinonediimine which is considered to be the precursor of the varied products obtained in the oxidation of anilines (24). This formation of N-arylphenylenediamines may be favored in the absence of pyridine since tars were mainly formed on a large scale under these conditions.

Hydrazobenzenes (Table II) formed under these circumstances would be oxidized further to azobenzenes. This process occurs in the absence of pyridine by a two step process.

$$C_6H_5NHNHC_6H_5 - e \rightarrow C_6H_5\overset{+\cdot}{N}HNHC_6H_5$$

$$C_6H_5\overset{+\cdot}{N}HNHC_6H_5 - e \rightarrow C_6H_5N = NC_6H_5 + 2H^+$$

These reactions would be modified to a certain extent by the aniline and would give oxidation waves with unequal heights. The second wave which occurs at the same point as azobenzene is not caused by this compound since the addition of pyridine to the same solution gave one oxidation wave. Azobenzenes under similar circumstances caused coating of the electrode and gave no oxidation waves except for 4,4'-dimethoxyazobenzene. The oxidation products formed from azo compounds are unknown since large-scale oxidations in acetonitrile gave tars.

*o*-Nitroaniline, *p*-nitroaniline, and 2,4-dinitroaniline gave a two electron wave in the absence of pyridine. This behavior suggests that the cation radical, because of the decreased basicity of these compounds, loses a proton easily and forms the radical which dimerizes to the hydrazo compound.

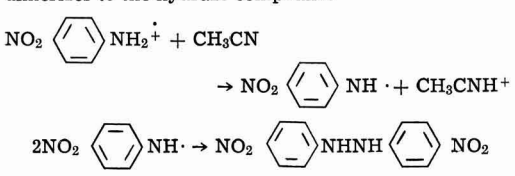

The latter would be oxidized further to the azo compound. A two-step process was actually observed with *p*-nitroaniline at higher concentrations.

Analyses of the current-voltage curves for *p*-bromoaniline and *p*-anisidine in the absence of pyridine gave values of 0.0645 and 0.049, respectively, for the slope which are in fair agreement with the initial one electron step postulated. The addition of pyridine causes the reaction to become more irreversible since *p*-bromoaniline gave a value of 0.0734. *p*-Anisidine is an exception under similar conditions since it gives a stepwise oxidation and a slope of 0.057 for the first wave. This value is in good agreement with the one-electron step involved.

Large-scale oxidations of the anilines at a platinum electrode in acetonitrile (Table III) were in agreement with the electrode mechanisms mentioned; azobenzenes, azophenines, and tars were obtained since the potential was not controlled. The potentials applied, however, gave similar initial currents to those obtained under controlled potential conditions.

Hydrazobenzenes on large-scale oxidation gave azobenzenes as expected. In the oxidation of hydrazobenzene itself, the product was accompanied by tar and aniline black since the potential was not controlled.

No products involving pyridine were isolated in the oxidation of the anilines, and this result eliminates the possible formation of a cation as the initial product

$$ArNH_2 - 2e \rightarrow ArNH^+ + H^+$$

Such an intermediate would be expected to react with pyridine, since pyridine is in excess, and form a hydrazonium salt. Further evidence against this cation is the crossed coupling of two anilines. A mixed azobenzene was obtained only with aniline and *p*-chloroaniline which are oxidized at approximately the same point. Mixtures of *p*-chloroaniline with *p*-nitroaniline and with 2,4-dinitroaniline when oxidized at controlled potential gave only 4,4'-dichloroazobenzene.

## Acknowledgment

The authors wish to acknowledge the support of the U. S. Army Research Office under Contract DA-31-124-ARO-D-406, and Grant No. DA-ARO(D)-31-124-G351.

Manuscript received Feb. 20, 1967; revised manuscript received *ca.* June 12, 1967. This work was abstracted in part from the Ph.D. Thesis of T. W. McIntyre. February 1967.

Any discussion of this paper will appear in a Discussion Section to be published in the June 1968 JOURNAL.

## REFERENCES

1. H. Lund, *Acta Chem. Scand.*, **11**, 1323 (1957).
2. E. S. Pysh and N. C. Yang, *J. Am. Chem. Soc.*, **85**, 2124 (1963).
3. M. T. Melchior and A. H. Maki, *J. Chem. Phys.*, **34**, 471 (1961).
4. A. Zweig, J. E. Lancaster, M. T. Negalia, and W. H. Jura, *J. Am. Chem. Soc.*, **86**, 4130 (1964).
5. G. Cauquis, J. Badoz-Lambling, and J. Billon, *Bull. Soc. chim. France*, **1965**, 1433.
6. E. T. Seo, R. F. Nelson, J. M. Fritsch, L. S. Marcoux, D. W. Leedy, and R. N. Adams, *J. Am. Chem. Soc.*, **88**, 3498 (1966).
7. F. Goppelsroeder, *Compt. rend.*, **81**, 408 (1875); **82**, 228, 1392 (1876).
8. L. Gilchrist, *J. Phys. Chem.*, **8**, 531 (1904).
9. J. W. Shipley and M. T. Rogers, *Can. J. Res.*, **B17**, 147 (1939).
10. T. Yasui, *Bull. Chem. Soc., Japan*, **10**, 306 (1935).
11. F. Goppelsroeder, *Compt. rend.*, **82**, 1199 (1876).
12. S. Goldschmidt and F. Nagel, *Ber.*, **64**, 114 (1931).
13. F. Fichter and E. Rothenberger, *Helv. Chim. Acta*, **5**, 168 (1922).
14. I. M. Kolthoff and J. F. Coetzee, *J. Am. Chem. Soc.*, **79**, 1852 (1957).
15. J. J. Lingane, "Electroanalytical Chemistry," p. 202, Interscience Publishers, Inc., New York (1953).
16. J. F. Coetzee, G. P. Cunningham, and D. K. McGuire, *Anal. Chem.*, **34**, 1139 (1962).
17. D. G. H. Daniels and B. C. Saunders, *J. Chem. Soc.*, **1953**, 822.
18. *Ibid.*, **1951**, 2112.
19. O. N. Witt and E. G. P. Thomas, *J. Chem. Soc.*, **43**, 112 (1883).
20. E. Bamberger, *Ber.*, **29**, 103 (1896).
21. S. Wawzonek, T. H. Plaisance, and T. W. McIntyre, *This Journal*, **114**, 588 (1967).
22. P. J. Elving and A. F. Krivis, *Anal. Chem.*, **30**, 1648 (1958).
23. K. Nakagawa and H. Onoue, *Chem. Commun.*, **1965**, 396.
24. S. Goldschmidt and B. Wurzschnitt, *Ber.*, **55**, 3216 (1922).

# High-Temperature Oxidation

## IV. Zirconium and Hafnium Carbides

**Joan B. Berkowitz-Mattuck**

*Arthur D. Little, Inc., Cambridge, Massachusetts*

ABSTRACT

The oxidation of ZrC was studied at temperatures of 1130°-2160°K and oxygen partial pressures around 3.9 and 20 Torr. The rate of oxidation was monitored with a thermal conductivity cell. Independent measurements were made of net weight gain and quantities of $CO(g)$ and $CO_2(g)$ evolved. Oxidation was shown to be nonpreferential, *i.e.*, zirconium was oxidized at the same rate as carbon. Gas phase diffusion control imposed by the experimental system was frequently encountered. Where it was possible to observe a true chemically controlled reaction rate, the kinetics appeared to be linear. Microscopic examination of the oxidized specimens revealed preferential oxidation along grain boundaries. Between 1130° and 1560°K this preferential oxidation resulted in intercrystalline fracture. At higher temperatures stresses were apparently sufficiently relieved so that the samples remained intact. The oxidation of HfC between 1790° and 2000°K, at oxygen pressures near 10 Torr, was also found to be linear and preferential along grain boundaries.

The oxidation of zirconium carbide was studied by Margrave and Kuriakose (1) at temperatures of 550°-650°C in oxygen at 1 atm. The oxidation was found to be linear, with an activation energy of 16.7 ± 1.7 kcal/mole.

Bartlett, Wadsworth, and Cutler (2) studied the weight gain of sized powders of zirconium carbide in air, oxygen, and oxygen-helium mixtures at temperatures of 450°-580°C, and oxygen pressures of 6.5 x $10^{-5}$ to 1 atm. Stoichiometric oxidation of ZrC to $ZrO_2$ and gaseous oxides of carbon was assumed. The data were interpreted on the basis of two parallel independent processes: a parabolic diffusion reaction involving the partial replacement of interstitial carbon in the ZrC lattice with oxygen, and a linear surface reaction occurring at the ZrC-$ZrO_2$ phase boundary. Both processes occur simultaneously, with the diffusion reaction predominating at short times and the surface reaction becoming rate controlling as oxidation proceeds. The activation energies were calculated as 53 kcal/mole for the diffusion process and 46 kcal/mole for the surface reaction. Water vapor, in the presence of oxygen, was found to accelerate the rate of the surface reaction while leaving its activation energy unchanged. The solid oxidation product was found to be cubic $ZrO_2$, a phase normally thought to be unstable, but which might be stabilized by small amounts of carbon.

Watt, Cockett, and Hall (3) made a single weight change measurement of 49.8 mg/cm² on a solid sample of ZrC of density 6.20 g/cc and 4.8% porosity, exposed to a stream of dry air flowing at 5.3 cm/sec, for 30 min at 800°C.

The present study was undertaken to investigate the oxidation of ZrC and the chemically related HfC at temperatures above 900°C.

### Experimental Method

Cylindrical pellets of ZrC were cut from zone refined bars prepared as described by Westrum and Feick (4). The fabricated bars contained 11.2 w/o carbon. Hafnium carbide powder was prepared by the Carborundum Company from high-purity $HfO_2$ supplied by Wah Chang Corporation. The HfC powder was sintered into bars and arc-melted on a water-cooled copper hearth using a water-cooled tungsten electrode. In order to minimize loss of carbon during melting, the operation was conducted in an atmosphere of argon containing 3.14% of ethylene and 11.4% of hydrogen. The resulting material was carbon deficient, corresponding to a composition $HfC_{0.952}$ (5).

The anticipated products of the oxidation of ZrC and HfC were the permanent gases, $CO(g)$ and $CO_2(g)$, in addition to the refractory metal oxides. Due to the evolution of permanent gases, the thermal conductivity method described in previous publications (6-8) had to be modified to study the oxidation. A known mixture of helium and oxygen was passed through the reference side of a thermal conductivity cell (6) and over an inductively heated carbide pellet supported on $ThO_2$ fingers by three point contact. A portion of the oxygen in the gas stream reacted with the pellet to produce oxides of the metal and carbon. The effluent gas was therefore depleted in oxygen, but enriched in $CO(g)$ and $CO_2(g)$. The latter was removed by passage through a weighed Ascarite bulb, and the remaining mixture of $CO(g)$, $O_2(g)$, and He entered the sampling side of the thermal conductivity cell (6). Finally, the $CO(g)$ was oxidized to $CO_2(g)$ over copper oxide powder at 500°C, and the $CO_2(g)$ produced was collected in a second weighed Ascarite bulb. The signal from the thermal conductivity cell in this case was therefore not directly related to the rate of oxygen consumption as in previously studied systems (6-8), but instead reflected the difference between the rate of total oxygen consumption and the rate of formation of $CO(g)$. The calibration constant, relating the electrical signal to the difference in gas pressure on the two sides of the cell is the same for both CO and $O_2$ in He. Hence, evolution of CO depresses the signal, as compared to simple removal of oxygen.

### Results

*Zirconium carbide.—Oxidation kinetics.*—The experimental data are summarized in Table I. The signal from the thermal conductivity apparatus was constant with time in every experiment. However, only in the case of experiment XII-1 did this reflect true chemically controlled linear oxidation kinetics. In the other experiments more than 90% of the oxygen passed over the carbide pellet reacted with it, and the controlling process was therefore probably the rate of arrival of oxygen gas at the sample surface. At higher pressures and/or higher gas flow rates, a greater proportion of the carbide would have been converted to oxides.

In Table I, the "initial" weights were taken after degassing at 2200°K in pure helium until the signal from the thermal conductivity cell indicated that no permanent gases were being evolved. The surface areas were calculated from micrometer measurements of the height and diameter of the cylindrical pellets. Temperatures were measured optically and corrected for an emissivity of 0.7, determined by comparing

Table I. Summary of experimental data on ZrC

| Expt. | Initial weight, g | Geometric surf. area, $cm^2$ | Temp, °K | Oxygen pressure, Torr | Exposure time, min | Net weight change $W_o$, (g) | CO formed $W_{CO}$ (g) | $CO_2$ formed $W_{CO_2}$ (g) | C consumed $W_c$ (g) | Zr consumed $W_{Zr}$ (g) | Zr/C |
|---|---|---|---|---|---|---|---|---|---|---|---|
| XII-8 | 0.446 | 1.103 | 1130 | 22.9 | 51 | — | 0.0001 | 0.0611 | — | — | — |
| XII-5 | 0.5645 | 1.394 | 1260 | 20.4 | 128 | — | — | 0.0709 | — | — | — |
| XII-3 | 0.6963 | 1.493 | 1560 | 21.2 | 62 | — | 0.0289 | 0.0399 | — | — | — |
| X-31 | 0.5864 | 1.310 | 1860 | 9.1 | 129 | 0.0402 | 0.0438 | 0.0220 | 0.0248 | 0.1852 | 7.47 |
| X-29 | 0.7073 | 1.450 | 1940 | 8.1 | 120 | 0.0366 | 0.0405 | 0.0145 | 0.0214 | 0.1652 | 7.72 |
| XII-1 | 0.7051 | 1.500 | 1970 | 25.9 | 112 | 0.0851 | 0.0968 | 0.0356 | 0.0510 | 0.388 | 7.60 |
| X-27 | 0.6361 | 1.252 | 2070 | 8.5 | 124 | 0.0389 | 0.0464 | 0.0175 | 0.0236 | 0.1780 | 7.55 |
| X-16 | 0.6840 | 1.388 | 2070 | 8.5 | 119 | 0.0402 | 0.0540 | 0.0073 | 0.0252 | 0.1862 | 7.39 |
| VII-8 | 0.6643 | 1.528 | 2100 | 3.0 | 180 | 0.0207 | 0.0242 | 0.0079 | 0.0126 | 0.0949 | 7.54 |
| X-25 | 0.6812 | 1.371 | 2165 | 8.9 | 120 | 0.0356 | 0.0523 | 0.0072 | 0.0244 | 0.1710 | 7.01 |

surface temperatures with ultrasonically drilled black body cavity temperatures under oxidizing conditions. Oxygen partial pressures in helium are given; the total pressure was close to 1 atm in every experiment. The carrier gas flow rate was 58.6 cc/min in every experiment, corresponding to a linear flow velocity in the neighborhood of the sample of 1.9 cm/sec, except VII-8 where a flow of 51.5 cc/min was used.

From the measured net weight change of the carbide on oxidation, and the observed weight changes $W_{CO_2}$ and $W_{CO}$ in the Ascarite bulbs, the total amounts of carbon and zirconium consumed were readily calculated, on the assumption that the only oxidation products were $CO_2(g)$, $CO(g)$, and $ZrO_2(s)$. The formation of $ZrOC(s)$ cannot be precluded, but since it is isostructural with ZrC, no positive evidence was obtained for its presence. The total weight of carbon consumed, $W_c$, is given by

$$W_c = \frac{[C]}{[CO_2]} \cdot W_{CO_2} + \frac{[C]}{[CO]} \cdot W_{CO} \qquad [1]$$

where the symbols in brackets represent molecular weights. The total weight of zirconium, $W_{Zr}$, that has been converted to oxide is calculated from the measured weight change, $W_o$, and the derived carbon consumption

$$W_{Zr} = \frac{[Zr]}{2[O]} (W_o + W_c) \qquad [2]$$

The ratio of the number of grams of zirconium consumed to the number of grams of carbon consumed during oxidation is shown in Table I to have an approximately constant value of 7.5 ± 0.2. Since the corresponding ratio in the ZrC starting material is 7.6, it would appear that the oxidation of ZrC is stoichiometric. That is, for each zirconium atom converted to oxide, a single carbon atom is also converted to oxide.

*Structural changes during oxidation.*—The reason that weight change data were not given for pellets XII-8, XII-5, and XII-3 is that at these relatively low temperatures the pellets were broken apart by the oxidation process. At the end of each experiment, the grain boundaries of the ZrC were seen to be outlined by a white material, identified by room temperature x-ray as monoclinic $ZrO_2$. The growth of the oxide in pre-existing cracks and grain boundaries of ZrC undoubtedly creates enough stress to fracture the carbide. At higher temperatures, as discussed below, significant grain boundary oxidation was observed, but stresses are apparently sufficiently relieved so that fracture does not occur.

Pellet XII-1 for which true kinetic data had been obtained was mounted and polished for metallographic examination.

Figure 1a shows the specimen at a magnification of ca. 4X. The gray outer rim is the oxide, and the inner white circular area is the surface of carbide. To the naked eye, the outer oxide coating looked white and chalky, and the inner surface from which the oxide coating was polished off, looked bright and metallic. A mottled rim is clearly visible along the oxide-alloy interface in the figure and the remaining photomicrographs focus on portions of this interface. In Fig. 1b, at a magnification of *ca.* 30X, the oxide fills the entire upper half of the photograph, and the alloy the lower. The oxide is obviously growing preferentially along grain boundaries in the carbide, and enveloping individual alloy crystallites. The structure of the bulk oxide is very different from that on $ZrB_2$ (8), although after cooling both showed only the x-ray lines for monoclinic $ZrO_2$. On $ZrB_2$ the oxide was seen to grow in a columnar structure; on ZrC, the $ZrO_2$ assumed an equiaxed grain structure very similar to that of the original alloy. Figures 1c and 1d show the oxide alloy interface at a still higher magnification, *ca.* 195X, and one sees even more clearly the preferential oxidation of grain boundaries, and the lateral fingerlike growth of oxide from the boundaries into the crystallite bulk. The reaction zone of intergranular attack was approximately 0.014 ± 0.002 cm in thickness. The outer oxide was about ten times thicker. The mechanism of oxide growth on ZrC at high temperatures appears to be rapid attack at grain boundaries, and slow oxidation of the alloy from the grain boundary surface inward. Figure 1e, at a magnification of *ca.* 345X, shows portions of the alloy completely enveloped by oxide. Finally, Fig. 1f is a view of the alloy surface at a magnification of *ca.* 345X. This surface had been covered with a dense oxide prior to polishing, and one sees here the penetration of the oxide into grain boundaries of the alloy. Between 1126° and 1559°K the grain boundary attack results in intergranular fracture of the alloy. Above 1580°K there is apparently enough plasticity in either alloy, oxide, or both, so that the sample remains intact during oxidation.

*Hafnium carbide.—Oxidation kinetics.*—The experimental data for HfC are summarized in Table II. Since the arc-melted samples were highly irregular in shape,

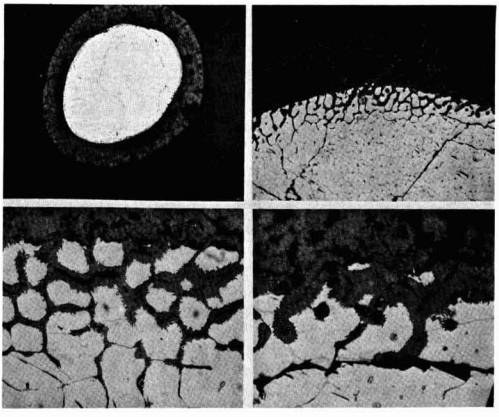

Fig. 1 a-d. Photomicrographs of oxidized ZrC (pellet XII-1); T 196°K; $P_{O_2}$ 25.9 Torr. Magnification: a (top left) ca. 4X; b (top right) ca. 30X; c (bottom left) ca. 195X; d (bottom right) ca. 195X.

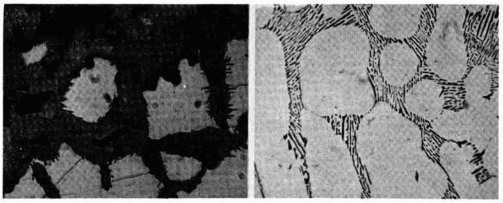

Fig. 1 e-f. Photomicrographs of oxidized ZrC (pellet XII-1); T 196°K; $P_{O_2}$ 25.9 Torr. Magnification: e (left) and f (right) ca. 345X.

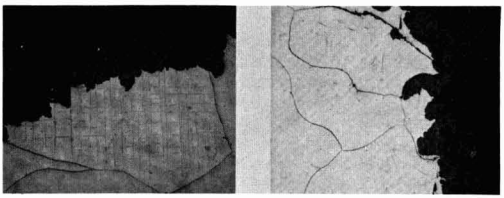

Fig. 2. Photomicrographs of oxidized hafnium carbide pellet XVI-19; temperature 1600°-2000°K; $P_{O_2}$ 11.5 Torr. Magnification ca. 130X.

the geometrically calculated surface areas are only approximate. The surface oxide tended to flake and spall on removal of the sample from the apparatus; and, hence, the measured weight gains are minimum values. From the measured minimum net weight gains, and the weights of CO(g) and $CO_2$(g) in the product gas stream, the minimum ratio of hafnium to carbon oxidized can be calculated, as described above for the oxidation of ZrC. The experimental values of the ratio are given in Table II as 14.1, 10.1, and 15.9, to be compared to an Hf:C ratio in the original alloy of 15.6. Linear oxidation was observed in every case. Flow rates of 119 cc/min, approximately double those used for the ZrC experiments, were employed in order to maintain an adequate supply of oxygen.

At 1280°K in pure oxygen at 1 atm, a hafnium carbide specimen disintegrated into several pieces within 3 min in a manner very similar to that described above for zirconium carbide.

*Metallographic examination of oxide films.*—Pellet XVI-19 was imbedded in plastic and polished for microscopic observation. In the photomicrographs shown in Fig. 2, the oxide is seen to contain considerable porosity. As in the case of zirconium carbide, oxidation appears to be preferential along grain boundaries.

The photomicrograph in Fig. 3 is for a hafnium carbide pellet that had been exposed to a $N_2$-He mixture for an hour and a quarter at a temperature of 1960°K. The $N_2$ apparently contained a small quantity of oxygen, and white $HfO_2$(c) was identified on the surface of the sample by x-ray diffraction. The net weight change of the sample was 0.0024 g/cm², an order of magnitude less than that observed at an oxygen partial pressure of 11.5 Torr at about the same temperature. The oxidation rate was seen to decrease slightly with time, and, although grain boundary oxidation is

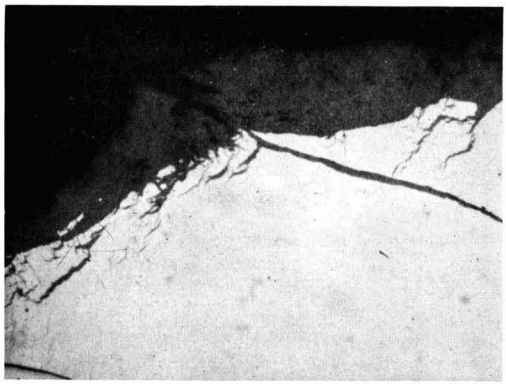

Fig. 3. Photomicrograph of oxidized hafnium carbide pellet XVI-22; temperature 1960°K, low oxygen pressure. Magnification ca. 230X.

apparent in Fig. 3, the oxide seems less porous than that shown in Fig. 2, for oxidation at a higher pressure.

## Discussion

A recent report (9) suggests that grain boundary oxidation is characteristic of iron contaminated ZrC. For material with an impurity level about 1 v/o $Fe_3C$ or about 1.1 w/o, the $Fe_3C$ is found to be segregated at the grain boundaries, and to be oxidized at a much more rapid rate than the ZrC matrix.

A chemical analysis of the zone melted material used in the present study showed an iron contamination level of 0.07% by weight. In order to try to assess the possible influence of iron on the present results, the oxidized and polished ZrC sample shown in Fig. 1 was examined for iron with the electron probe.[1]

An $FeK_{\alpha 1}$ scanning image was taken of the sample, and iron was found to be concentrated in the small circular inclusions visible in Fig. 1, and inhomogeneously in the cracks. Point count analyses take in the inclusions, the cracks, the grain boundaries, and the matrix showed the presence of iron particles of less than 1$\mu$ in size distributed at random in the inclusions and cracks, but failed to reveal the presence of any iron at all in either the grain boundaries or the matrix. The preferential grain boundary oxidation observed in zirconium carbide, therefore, seems to be characteristic of the pure material.

## Acknowledgment

It is a pleasure to thank John Engelke of Arthur D. Little, Inc., for his assistance in obtaining and interpreting the electron probe data, and to acknowledge the invaluable assistance of Richard F. Quigley and Walter Christensen with the experimental work.

Manuscript received Jan. 23, 1967; revised manuscript received May 31, 1967.

Any discussion of this paper will appear in a Discussion Section to be published in the June 1968 JOURNAL.

[1] The electron probe analysis was kindly supplied by Acton Laboratories, 531 Main Street, Acton, Massachusetts.

Table II. Summary of experimental data on HfC

| Expt. | Initial weight, g | Area, cm² | Temp, °K | Pressure, Torr | Time, min | Minimum net weight change, g | CO formed, g | $CO_2$ formed, g | C consumed, g | Minimum Hf consumed, g | Hf/C min |
|---|---|---|---|---|---|---|---|---|---|---|---|
| XVII-4 | 0.5374 | 1.076 | 1790 | 11.5 | 85 | 0.021 | 0.0160 | 0.0254 | 0.0138 | 0.195 | 14.1 |
| XVI-38 | 0.6544 | 1.241 | 1890 | 11.5 | 69 | 0.016 | 0.0232 | 0.0355 | 0.0196 | 0.199 | 10.1 |
| XVI-36 | 0.7511 | 1.032 | 2005 | 11.5 | 43 | 0.022 | — | 0.0191 | | | |
| XVI-19 | 0.6057 | 1.256 | 2000-1600 (continuous drop) | 7.5 | 120 | 0.038 | 0.0340 | 0.0225 | 0.0207 | 0.328 | 15.9 |

REFERENCES

1. A. K. Kuriakose and J. L. Margrave, *This Journal*, **111**, 827 (1964).
2. R. W. Bartlett, M. E. Wadsworth, and I. B. Cutler, *Trans. AIME*, **227**, 467 (1963).
3. W. Watt, G. H. Cockett, and A. R. Hall, *Metaux*, **28**, 222 (1963).
4. E. F. Westrum, Jr., and G. Feick, *J. Chem. Eng. Data*, **8**, 176 (1963).
5. L. A. McClaine, Thermodynamic and Kinetic Studies for a Refractory Materials Program, 4th Semi-annual Progress Report (August, 1963), Contract No. AF 33(616)-7472.
6. J. B. Berkowitz-Mattuck, *This Journal*, **111**, 908 (1964).
7. J. B. Berkowitz-Mattuck and R. R. Dils, *ibid.*, **112**, 583 (1965).
8. J. B. Berkowitz-Mattuck, *ibid.*, **113**, 908 (1966).
9. K. R. Janowski, R. D. Carnahan, and R. C. Rossi, "Static and Dynamic Oxidation of ZrC," TDR-669(6250-10)-3, Aerospace Co., El Segundo, Calif., January, 1966.

# Fundamental Limitations on the Low-Temperature Operation of Electrolytic Devices

**C. A. Angell**

*Department of Chemistry, Purdue University, Lafayette, Indiana*

ABSTRACT

A new approach to the understanding of transport behavior in concentrated electrolyte solutions requires the recognition at low temperatures of a liquid state limiting temperature which is a thermodynamic constant of any solvent-electrolyte solution. The value of this constant, which determines service limits, is a function of electrolyte concentration except at low concentrations where solvent structure may dominate. In this paper the results of workers investigating electrolyte solutions for low-temperature battery applications are used to emphasize the usefulness of the concepts underlying this approach to low-temperature electrolyte problems.

This article considers briefly some implications of recent developments in electrolyte solution transport theory to the practical problems encountered in the use of electrolyte solutions at low temperatures.

*Temperature and concentration dependence of solution transport properties.*—In recent papers (1-3) it has been shown that the temperature dependence and composition dependence of electrical (equivalent) conductance, $\Lambda$, and viscous flow, $\eta$, processes in various concentrated aqueous electrolyte solutions at low corresponding temperatures may be described by equations of the following form

constant composition

$$\Lambda_{(N)}, 1/\eta_{(N)} = A \exp \frac{-k}{T - T_o} \qquad [1]$$

constant temperature

$$\Lambda_{(T)}, 1/\eta_{(T)} = A \exp - \frac{k/Q}{N_o - N} \qquad [2]$$

where $A$, $k$, and $T_o$ in Eq. [1] and $A$, $k/Q$, and $N_o$ in Eq. [2] are constants; $T$ and $N$ are, respectively, the absolute temperature and the equivalent concentration.

A plausible theoretical interpretation discussed in detail elsewhere (1, 4, 5) may be given these equations in terms of the controlling influence on the transport processes, of the liquid configurational entropy content (6). The constants $T_o$ and $N_o$ in this case represent the temperature at fixed composition, and the equivalent concentration at constant temperature, respectively, at which the configurational entropy vanishes.

*Significance of low-temperature electrolyte solution behavior.*—An important result of this treatment which we wish to emphasize in this paper is the realization that, provided crystallization has not already occurred, any electrolyte solution will lose its liquid character and become a glass at a temperature ($\sim T_o$) which in general will be well above 100°K. Where the electrolyte property of interest depends on, or is related to, the fluidity of the substance, this temperature therefore places an absolute lower limit to the serviceability of the material.[1]

Furthermore, it is found that, for many electrolyte mixtures and solutions at temperatures not too far above $T_o$, $T_o$ itself is the only important variable in the transport equation, so that the low-temperature transport properties of such liquids are to a large extent known once $T_o$ is known (3). Thus, the scaling factor to be used in comparing a given property amongst different solutions is, from Eq. [1], $(T - T_o)$.

To illustrate the usefulness of this point, we take an example from the work of Garrett *et al.* (7) who were investigating various strong (presumed fully dissociated) electrolyte solutions for suitability in low-temperature battery applications. Their (uninterpreted) data on the viscosity of some solutions, relative to the viscosity of water at 25°C, are reproduced in Fig. 1(i). The striking feature of the data is, of course, the very rapid rise in solution viscosity at the lower temperatures. In Fig. 1(ii) we show how the use of a $T_o$ value appropriate to each solution in the scaling factor $(T - T_o)$ reduces the data approximately to a single curve. The remaining minor differences seem to be due mainly to variations in the value of the preexponential term A, as seen in the following.

According to Eq. [1], the values of $T_o$ which reduce the solution viscosities as in Fig. 1(ii), should yield a linear plot for the relative viscosities when log $\eta/\eta_o$, (or log $\eta_o/\eta$ to maintain Eq. [1] signs) is plotted against $1/(T - T_o)$. The appropriate semilogarithmic plots are shown in Fig. 2. The various plots are now seen to be differentiated by small changes in the values of the parameter $A$, the plots being linear with essentially equal values of the slope $k$. It must be said, however, that the available data are not sufficiently

[1] The limiting temperature usually imposed by the crystallization temperature is not an absolute limit insofar as suitable additives can usually make crystal nucleation a very improbable process even when thermodynamically favored.

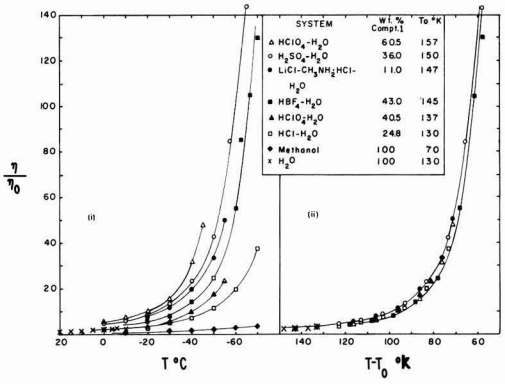


Fig. 1 (i). Viscosities of various electrolyte solutions relative to $\eta_{H_2O}$ at 25°C ($\eta_0$) [after Garrett *et al.* ref. (7)]. Legend gives weight per cent (w/o) of the first component listed: in ternary system, weight per cent of $CH_3NH_2 \cdot HCl$ is 33%; Fig. 1 (ii). Data of (i) scaled by means of the vanishing entropy ($S_c$) temperature $T_o$ [$S_c \rightarrow 0$ as $T \rightarrow T_o$, see ref. (5, 6)].

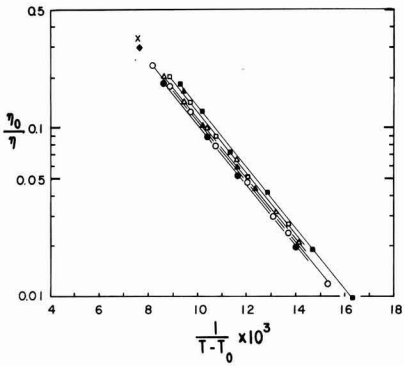


Fig. 2. Plot showing the linear dependence of log (relative viscosity) for the solutions of Fig. 1 on $1/(T-T_o)$ required by Eq. [1]. Points are identified in Fig. 1 legend.

accurate or extensive to conclude that $k$ has the same value for each solution, though the differences apparently cannot be great.

Thus, the low-temperature electrolyte data of Fig. 1(i) are well accounted for by Eq. [1]; it follows that any theoretically guided quest for electrolytes serviceable to very low temperatures must focus attention on the property $T_o$ of the material. We return to this matter shortly.

### *The Case of Specific Conductance*

An interesting situation arises when the low-temperature property of interest is the electrical conductance. For the case of equivalent conductance, the viscosity and conductance at high concentrations follow essentially parallel paths except for small differences in the parameter $k$ (2, 3). However, for practical applications it is the ability of a given volume of the electrolyte to conduct current which is of importance, and one is therefore concerned with the specific conductance, $\kappa$, which is related to the equivalent conductance by

$$\kappa = \frac{\Lambda N}{1000} \qquad [3]$$

whence, from Eq. [2],

$$\kappa = NA' \exp - \left( \frac{k/Q}{N_o - N} \right) \qquad [4]$$

Thus the equation for isothermal specific conductance contains the electrolyte concentration in both preexponential and exponential terms. The preexponential $N$ leads to an increase in conductance with increasing $N$, due to the increase in number density of current carriers, while the exponential $N$ opposes this increase, by raising the $T_o$ value of the solution towards the isothermal temperature, $T$. Thus at $N = 0$, $\kappa = 0$, and eventually, as $N \rightarrow N_o$, $\kappa = 0$. Thus it is clear from Eq. [4] that the specific conductance must go through a maximum, provided the solubility limit of the salt is not first exceeded. The maximum in $\kappa$ observed for many highly soluble salts is, of course, well known (8).

The not-so-obvious consequence of Eq. [4] which is of special interest to the present discussion, is the fact that since the influence of the preexponential $N$ is independent of temperature (provided we are dealing with fully dissociated electrolytes) the maximum in the specific conductance isotherm must shift to lower concentrations at lower temperatures, since $N_o$ decreases with decreasing temperature. Thus attempts to compensate for the low conductances encountered at the low temperatures by raising the electrolyte concentration, are increasingly frustrated the lower the temperature. To observe the effect of concentration on $T_o$, the data for the two compositions of perchloric acid treated in Fig. 1 and 2 may be referred to (see also Table I, discussed below). The effect of temperature on the specific conductance maximum is illustrated adequately by some data on zinc nitrate solutions due to Bak (9) shown in Fig. 3. The effect should be more dramatic at lower temperatures, but suitable data are not available to demonstrate this.

It should be pointed out, in view of the fact that most of the electrolyte solutions whose low-temperature properties were tested by Garrett and co-workers (7) were acids, that although the conductance exhibited is primarily proton conductance, the temperature dependence of the process should still be of the form of Eq. [1]. This will be true because proton conductance requires configurational freedom on the part of the water molecules (primarily freedom to rotate) which, like dielectric relaxation (10), requires an Eq. [1] type of description for the temperature dependence.

### *Factors Determining the Magnitude of $T_o$*

The problem of what determines $T_o$ is therefore fundamental to the question of low-temperature electrolytes. $T_o$ is evidently a thermodynamic property of the material and a parameter of major importance to the understanding of liquid-solid relations. As discussed elsewhere (1) it appears to be the temperature

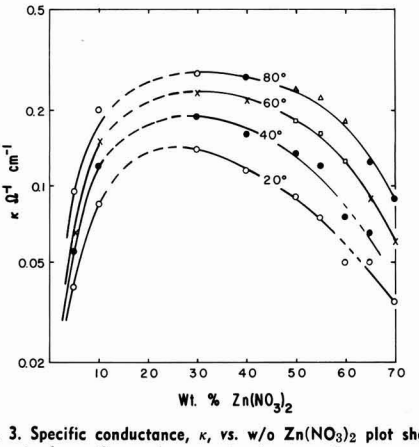


Fig. 3. Specific conductance, $\kappa$, vs. w/o $Zn(NO_3)_2$ plot showing movement of specific conductance maximum to lower concentrations as isotherm temperature decreases [after Bak, ref. (9)].

Table I.

| Liquid | | N equiv. $l^{-1}$, at −70°C[a] | $T_o$ °K |
|---|---|---|---|
| pure, w/o $H_2O$ | | $10^{-7}$ | 130 |
| 40.5 | $HClO_4$ | 5.5 | 137 |
| 43.0 | $HBF_4$ | 7.2 | 145 |
| 24.8 | HCl | 8.0 | 130 |
| 36.0 | $H_2SO_4$ | 9.9 | 150 |
| 60.5 | $HClO_4$ | 10.1 | 157 |

[a] Values of $N$ are calculated using the densities at − 70°C quoted in ref. (7).

at which the "ideal metastable amorphous solid" (11) phase commences to exchange vibrational for configurational degrees of freedom, but it is not clear that this implies a dependence only on bond strength, or cohesive energy, as the interpretation of Turnbull and Cohen (12) suggests. Since the vibration frequencies of the amorphous solid are apparently involved it seems reasonable to enquire about the possible effects of the mass of the constituent particles on $T_o$. Investigations of such possible factors are currently in progress.

Certainly the cohesion among the particles of the material must play a role, and in this connection the difference in $T_o$ values between $H_2O$ and methanol deserves comment.[2] The higher value for $H_2O$ is evidently to be attributed to the more strongly hydrogen-bonded structure of water. The so-called "structure-breaking" solutes may therefore tend to lower $T_o$ at least at low concentrations, while at the same time supplying current carriers. Such properties would seem desirable for low temperature applications, but unfortunately these salts do not produce low eutectic temperatures with water.

It is notable that 24.8% HCl has the same value of $T_o$ as that assigned to $H_2O$. The reason is probably that chloride ion, unlike the oxy- and fluoro-anions of the other acids, can only participate weakly in configuration restricting hydrogen bonding to the water molecules, so that increases in cohesion due to electrostatic effects are largely nullified by a net reduction in hydrogen bonding. HBr and HI solutions may therefore reach still lower $T_o$ values. Apart from HCl, the values of $T_o$ correlate (approximately) with the equivalent concentration, $N$, (Table I) as Eq. [2] predicts. The hydrogen bond contribution will vary from acid to acid and a quantitative correlation is not to be expected.

Figure 1 (i) and (ii) show that the difference in limiting service temperatures (*e.g.*, maximum permissible viscosity, resistance, or relaxation time) is effectively the difference in $T_o$ values. Accordingly, for very low-temperature work, solvents with $T_o$ values lower than that of $H_2O$ would be required, and a non-hydrogen-bonded structure would seem necessary. This leads to something of an impasse however, since a nonhydrogen-bonded structure appears to conflict with the requirement of a dielectric constant high enough to promote electrolyte dissociation. There is room for further experimental work in this area, with systems such as the fluorosulfonic acids in nitrile and mixed alcohol solvents offering interesting possibilities.

[2] The assignment of $T_o$ values to these liquids (see legend Fig. 1) is only approximate because in neither case does the available transport data approach $T_o$ closely enough to permit a solution of Eq. [1] for $T_o$ with confidence. (Solutions of Eq. [1] for $H_2O$ viscosities yield the result $T_o$ = 150°K [F. Gutmann and L. M. Simmons, *J. Appl. Phys.*, **23**, 977 (1952); A. A. Miller, *J. Chem. Phys.*, **38**, 1568 (1963)].) The value, $T_o$ = 130°K assigned to $H_2O$ in this work is based mainly on the observation of the glass transition at 139°K for vapor-deposited vitreous ice [J. McMillan and S. C. Los, *Nature*, **206**, 806 (1965)], (recently confirmed in this laboratory [C. A. Angell, E. J. Sare, and R. D. Bressel, *J. Phys. Chem.*, **71**, 2759 (1967)], and the experience that the experimental glass transition is always observed at a temperature higher than $T_o$ by 5 − 30% dependent partly on molecular complexity. The estimate for methanol is based on the experimental value for the observed glass transition, 110°K [J. A. Faucher and J. V. Koleske, *Phys. Chem. Glasses*, **7**, 454 (1966)] and the known value $T_o$ = 73.5°K for n-propanol [see ref. (10)] for which the measured glass transition temperature is also 110°K.

Figure 1 (i) and (ii) show that the difference in limiting service temperatures (*e.g.*, maximum permissible viscosity, resistance, or relaxation time) is effectively the difference in $T_o$ values. Accordingly, for very low-temperature work, solvents with $T_o$ values lower than that of $H_2O$ would be required, and a non-hydrogen-bonded structure would seem necessary. This leads to something of an impasse however, since a nonhydrogen-bonded structure appears to conflict with the requirement of a dielectric constant high enough to promote electrolyte dissociation. There is room for further experimental work in this area, with systems such as the fluorosulfonic acids in nitrile and mixed alcohol solvents offering interesting possibilities.

Manuscript received Nov. 2, 1966, revised manuscript received June 12, 1967.

Any discussion of this paper will appear in a Discussion Section to be published in the June 1968 JOURNAL.

## REFERENCES

1. C. A. Angell, *J. Phys. Chem.*, **70**, 3988 (1966).
2. C. T. Moynihan, *ibid.*, **70**, 3399 (1966).
3. C. A. Angell, presented at 17th Meeting of the Comite Internationale de Thermodynamique et de Cinetique Electrochimique, Tokyo (CITCE), September (1966).
4. G. Adam and J. H. Gibbs, *J. Chem. Phys.*, **43**, 139 (1965); *J. Chem. Phys.*, **46**, (12) 4673 (1967).
5. C. A. Angell, *J. Phys. Chem*, **70**, 2793 (1966).
6. J. H. Gibbs and E. A. Dimarzio, *J. Chem. Phys.*, **28**, 373 (1958).
7. (a) A. B. Garrett, J. Welsh, S. Woodruff, R. Cooper, and J. Heiks, *J. Phys. Chem.*, **53**, 505 (1949); (b) A. B. Garrett and S. A. Woodruff, **55**, 477 (1951).
8. A. N. Campbell, A. P. Gray, and E. M. Kartzmark, *Can. J. Chem.*, **31**, 617 (1953).
9. B. V. Bak, *Zhur. Obsch. Khim.*, **16**, 395 (1946).
10. D. Davidson and R. H. Cole, *J. Chem. Phys.*, **19**, 1484 (1951).
11. D. Turnbull, "Physics of Non Crystalline Solids," p. 41, J. Prins, Editor, North-Holland Publishing Co. (1965).
12. D. Turnbull and M. H. Cohen, *J. Chem. Phys.*, **34**, 120 (1961).

# A Generalized Expression for the Tafel Slope and the Kinetics of Oxygen Reduction on Noble Metals and Alloys

**D. S. Gnanamuthu and J. V. Petrocelli**

*Applied Research Laboratory, Scientific Research Staff, Ford Motor Company, Dearborn, Michigan*

ABSTRACT

The usually employed expression for the Tafel slope is modified to take into account the potential which is effective in charge transfer within the double layer. The exchange currents and cathodic Tafel slopes are obtained on noble metal electrodes having different number of holes in the d-band. Using the conventional and modified Tafel slopes, possible paths and rate-determining steps are suggested for the cathodic reduction of oxygen.

It has been well established that the oxygen electrode reaction

$$O_2 + 4H^+ + 4e = 2H_2O \quad \text{(acidic)}$$
$$O_2 + 2H_2O + 4e = 4\,OH^- \quad \text{(basic)}$$

is highly irreversible. In fact only a few investigators have been able to establish the thermodynamically reversible potential on the noble metals. In these cases the electrodes were pretreated by methods which produced oxide films on the surface (1-3).

It is very likely that much of the reported data on the cathodic reduction of oxygen and the anodic evolution of oxygen on the noble metals were obtained on oxide covered surfaces (1-5). Since the completion of this work Damjanovic *et al.* (6-8) have obtained cathodic Tafel lines on Pt and Rh. They report different Tafel slopes for prereduced and oxide covered surfaces.

The energetically unfavorable steps in the reduction of oxygen are the endothermic reactions, (*i*) breaking the oxygen bond which requires about 5 ev, and (*ii*) the addition of a second electron to an oxygen atom which requires about 7.0 ev (8a). Although the addition of the first electron to the oxygen atom is exothermic by 1.0 ev, it should be noted that this electronic level

$$O(g) + e \rightarrow O^-(g)$$

lies about 3-4 ev above the Fermi level, when the metal electrode is at equilibrium for the over-all reaction, with reactants and products in their standard states. The reaction path should be dictated by these energetic requirements, and it is reasonable to assume that the chemisorption of the proper species will play a large role in reducing the activation energy. The adsorption energy will, of course, depend on the bond strength and, whether we consider a valence bond or an electrostatic bond, the number of electrons in the d-levels may play an important role.

The object of this study was to determine the effect of the number of holes in the d-band of the electrode on the Tafel parameters and over-all activity for the reduction of oxygen. Since the presence of an oxide on the metal surface may well obscure any metallic electronic structure effects, the data was obtained on prereduced electrodes of Au, Pt, Pd, Ir, Rh, Os, Ru, Pt-Au, and Pd-Au alloys.

It may be noted that McDonald and Conway obtained Tafel slopes for oxygen evolution on a series of Pd-Au alloys, but concluded that any possible effects of d-band structure were probably obscured by the role of surface oxides (5).

### *Tafel Slopes*

It is difficult, if indeed possible, to determine a unique reaction path by means of only Tafel parameters. However, if one reaction path is predominant and one of the elementary reactions (step) in the sequence of elementary reactions is rate determining, the Tafel slope, $b_c$, will be characteristic of the rate-determining step (rds).

The assumption usually made in obtaining the "expected slope" is that the symmetry factor for the rds is 0.5. Riddiford has shown that this assumption may not be in accord with the experimental facts (9). McDonald and Conway have pointed out the possible effect of oxide films on the symmetry factor (5).

We suggest that even if the symmetry factor of the rds is 0.5 and oxide films are absent, the expression generally used to obtain the "expected" Tafel slope (7-13)

$$-b_c = \frac{2.303\,\nu_j}{n_c + \beta_c n_j}\frac{RT}{\mathbf{F}} \qquad [1]$$

may not be correct in some cases. In this expression $n_c$ is the total number of electrons transferred before the rds, $n_j$ is the number transferred in the rds, $\beta_c$ is the symmetry factor of the rds, and $\nu_j$ is the number of times that the rds must occur in order for the over-all reaction to take place once, usually designated the stoichiometric number of the rds.

Although this expression is usually employed, the derivation has not been given (7, 10). For purposes of clarity we shall designate this $b_c$ as the "conventional expected" Tafel slope, (CTS) and present a derivation in order to indicate its limitations and finally derive a more general expression. The latter will be more satisfactory especially for some reaction paths which have been postulated for the oxygen reaction (7).

When the over-all reaction is governed predominantly by one reaction path, and one of the consecutive elementary reactions, a step, is rate determining, the slope may be obtained by assuming "quasi-equilibrium" for all reactions preceding the rds (12) or by considering the passage of the reactants over a series of energy barriers (11). We shall follow the latter approach.

If we have an over-all reaction

$$xX + bB^z + ne \rightarrow wW + cC^{(bz-n)/c} \qquad [2]$$

it is assumed that the completion of this over-all reaction requires the formation and decomposition of $\nu$ identical activated complexes $A^*$, where $\nu$ is an integer. The rate-determining reaction may then be written as

$$\frac{x}{\nu}X + \frac{b}{\nu}B^z + \frac{n}{\nu}e \rightarrow \frac{w}{\nu}W + \frac{c}{\nu}C^{(bz-n)/c} \qquad [3]$$

and $\nu$ is usually called the stoichiometric number of the reaction.

The four states to be considered are: the initial state *I*, the state immediately before the highest energy barrier *P*, the state immediately after this barrier, *Q*, and the final state *F*. A cross section of the energy surface indicating the reaction path is shown, schematically, in Fig. 1.

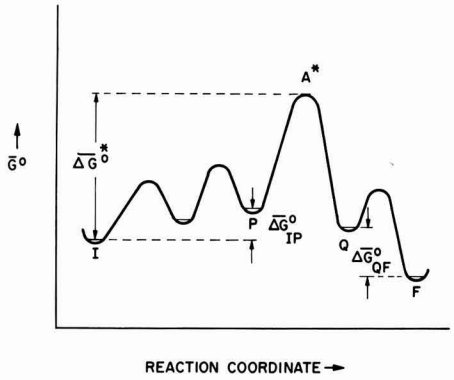


Fig. 1. Standard free energy change in a consecutive reaction path (schematic).

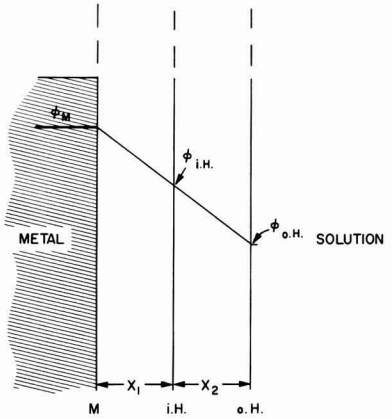


Fig. 2. Distribution of potential in the double-layer (schematic)

The electrical part of the standard free energy of activation in the forward direction is given by

$$\Delta G^{*o}_{Elec} = \sum_i Z_{IP} F \Delta\phi_{IP} + Z_{PQ} F \Delta\phi_{PA^*} \quad [4]$$

where $Z_{IP}$ is the charge of a particle which is transferred from state $I$ to $P$, $\Delta\phi_{IP}$ is the electrical potential difference through which the particle moves in going from $I$ to $P$ and the summation is over all charged particles $i$ which react in order for the rds to occur once. Similarly the second term is for the charged particles which react to form the transition complex $A^*$.

If we let

$$\beta_c = \frac{\Delta\phi_{PA^*}}{\Delta\phi_{PQ}} \quad [5]$$

where $\beta_c$ is the fraction of the potential difference between state $P$ and $Q$ which is effective for the activation of a charged particle $i$. We may write:

$$\Delta G^{*o}_{Elec} = \sum_i Z_{IP} F \Delta\phi_{IP} + Z_{PQ} F \beta_c \phi_{PQ} \quad [6]$$

$\beta_c$ is then the conventional symmetry factor.

If we now identify the electric inner potentials which occur in the various states with those of the metal, $\phi_M$, and the solution, $\phi_S$, and consider only the transfer of electrons, we can write Eq. [6] as

$$\Delta G^{*o}_{Elec} = \frac{n_{IP}}{\nu_j} F [\phi_M - \phi_S] + \frac{n_{PQ}}{\nu_j} F \beta_c [\phi_M - \phi_S] \quad [7]$$

where effectively we assume that the electric potential difference across each barrier is that between the metal and the solution. $n_{IP}/\nu_j$ and $n_{PQ}/\nu_j$ are the number of electrons which are transferred from the metal to the solution prior to the rds and in the rds, respectively, in order for the rate-determining reaction, Eq. [3], to take place once.

For the complete reaction we have

$$\frac{n}{\nu_j} F [\phi_M - \phi_S] = \frac{n_{IP}}{\nu_j} F [\phi_M - \phi_S] + \frac{n_{PQ}}{\nu_j} F [\phi_M - \phi_S] + \frac{n_{QF}}{\nu_j} F [\phi_M - \phi_S] \quad [8]$$

The rate of the forward reaction in terms of current density is

$$i = \frac{n}{\nu} F\kappa \frac{kT}{h} a^{x'}{}_X a^{b'}{}_B e^{\frac{-\Delta G^{*o}_{Chem}}{RT}} e^{\frac{-\Delta G^{*o}_{Elec}}{RT}} \quad [9]$$

where

$$x' = \frac{x}{\nu} \text{ and } b' = \frac{b}{\nu}$$

which for a given reaction may be written as

$$\Delta G^{*o}_{Elec} = -RT \ln i + C \quad [10]$$

substituting Eq. [7] into [10] we obtain

$$\frac{n_{IP}}{\nu_j} F [\phi_M - \phi_S] + \frac{n_{PQ}}{\nu_j} F \beta_c [\phi_M - \phi_S] = -RT \ln i + C \quad [11]$$

and

$$-b_c = \frac{2.303\,\nu_j}{n_{IP} + \beta_c n_{PQ}} \frac{RT}{F} \quad [12]$$

which is identical with Eq. [1], the expression for the CTS.

It will be obvious that Eq. [11] and [12] are only true when the electrons or charges, are transferred from the metal to the solution or *vice versa*. This may not always be the case. In some of the elementary reactions, charges may not cross the total double layer. If the electrons are transferred from the metal to the adsorbed species and the ions are transferred from the adsorbed sites to the solution, or *vice versa*, the above equations must be modified.

Recalling the relative positions of the metal-plane, the inner Helmholtz plane, iH, and the outer Helmholtz plane, oH, shown schematically in Fig. 2, we may designate $\phi_M$, $\phi_{iH}$, and $\phi_{oH}$ as the inner electric potential of these planes (13-15). The diameter of an adsorbed radical or ion in the oxygen electrode reaction will be approximately equal to that of an oxygen atom or ion and will lie in the iH plane.

If we go back to Eq. [6] and substitute it into Eq. [10], the following general expression is obtained

$$\sum_i Z_{IP} F \Delta\phi_{IP} + Z_{PQ} F \beta_c \Delta\phi_{PQ} = -RT \ln i + C \quad [13]$$

Let

$$\Delta\phi_{IP} = f_{IP} \Delta\phi_{MS}$$
$$\Delta\phi_{PQ} = f_{PQ} \Delta\phi_{MS} \quad [14]$$

We have from Eq. [13] and [14]

$$-b_c = \frac{2.303}{\sum_i Z_{IP} f_{IP} + Z_{PQ} \beta_c f_{PQ}} \frac{RT}{F} \quad [15]$$

By this treatment we have retained the conventional definition and concept of the symmetry factor $\beta_c$ as the portion of the change in the standard free energy of the rds which is effective in the activation process. The quantities $f_{IP}$ and $f_{PQ}$ then indicate the fraction of the total electrical potential difference at the metal-solution interface involved in the charge transfer process.

The transfer coefficient for the reaction will be given by

$$\alpha_c = \sum_i Z_{IP} f_{IP} + Z_{PQ} \beta_c f_{PQ} \qquad [16]$$

As a first approximation we will let $\phi_{oH} = \phi_S$ (neglect p·d of the diffuse layer), take $\partial\phi/\partial X$ in the double layer as constant, and take the distance from the metal to the iH plane equal to that from the iH plane to the oH plane.

With these approximations and the usual reasonable assumption that $\beta_c = 0.5$, the "corrected" Tafel slopes, $b'_c$, have been calculated from Eq. [15] for the reaction paths given in Table I. Values of the "conventional" Tafel slopes, $b_c$, are included for comparison. The paths I through XIV have been listed by Damjanovic *et al.* (7); paths XV and XVI have been added.

Since Eq. [15] will yield the "conventional" slope when the values of $f_{IP}$ and $f_{PQ}$ are equal to unity, only paths VI, X, XI, XIII, XIV, XV, and XVI are affected.

To illustrate and clarify the concepts developed here, let us apply Eq. [15] to the Hoar's alkaline path, section VI in Table I, which has received support from Hoar (10) and Damjanovic *et al.* (7).

We assume that step 3 is rate determining so that $\nu_j = 2$. First it should be noted that since this step does not involve electron transfer, the conventional treatment assumes that this is not directly potential dependent. Yet the elementary reaction as written indicates the transfer of charge from the adsorbed site to the solution. Certainly this transfer should depend on $(\phi_{iH} - \phi_S)$, and Eq. [15] takes this into account.

The electrical part of the standard free energy of the various states *I*, *P*, *Q*, and *F* are

| State | $G^o_{Elec}$ |
|---|---|
| *I* | $-2F\phi_M$ |
| *P* | $-F\phi_{1H} - F\phi_M$ |
| *Q* | $-F\phi_S - F\phi_M$ |
| *F* | $-2F\phi_S$ |

The total electrical standard free energy change for the rate-determining reaction

$$\tfrac{1}{2}\,O_2 + 2e + H_2O \rightarrow 2\,OH^-$$

is

$$(\Delta G^o_{Elec})_{Total} = 2F\Delta\phi_{MS}$$

as it should be, and the electrical part of the standard free energy of activation for the forward reaction is

$$\Delta G^{*o}_{Elec} = F\,[\phi_M - \phi_{iH}] + F\beta_c\,[\phi_{iH} - \phi_S] = 0.5F\Delta\phi_{MS} + 0.25F\Delta\phi_{MS}$$

so that

$$\alpha_c = 0.75$$

$$-b'_c = 0.079V \text{ @ } 25°C$$

whereas the conventional slope = —0.059v.

If the reacting species are in fact adsorbed on the metal surface as indicated by the reaction equations, the conventional expected values of $b_c$ used by investigators in their analysis would not yield a correct slope.

## Experimental

The experiments were performed in highly purified solutions at 25°C. The techniques and methods of purification were similar to those described in the literature. Oxygen was maintained at unit pressure and at a constant rate of bubbling. Some data were obtained on rotating electrodes, but they were essentially the same as in the solutions stirred only by oxygen bubbling, except for larger limiting current densities in some cases.

The solutions were 1*N* $H_2SO_4$, 0.1*N* NaOH and various concentrations of $Na_2SO_4$ which were of constant ionic strength but various *p*H values by adding a few drops of diluted $H_2SO_4$ or NaOH.

Pt, Pd, and Au electrodes were 99.999% pure and the other electrodes were 99.9% pure. The Pd-Au and Pt-Au alloys were made in an induction furnace using recrystallized alumina crucible and helium atmosphere. They were cast and rolled to 50% reduction at room temperature, except for some of the Pt rich Au-Pt alloys which were rolled at 1100°C. All alloys

**Table I. Oxygen reaction paths and cathodic Tafel slopes**

| | | | $-b_c$ | $-b'_c$ |
|---|---|---|---|---|
| **I The "Oxide" Path** | | | | |
| 1. $O_2 + 2M$ | → | $2MO$ | ∞ | ∞ |
| 2. $MO + MH_2O$ | → | $2MOH$ | ∞ | ∞ |
| 3. $MOH + H^+ + e$ | → | $M + H_2O$ | 0.118 | 0.118 |
| **II The "Electrochemical Oxide" Path** | | | | |
| 1. $O_2 + 2M$ | → | $2MO$ | ∞ | ∞ |
| 2. $MO + MH_2O + H^+ + e$ | → | $MOH + M + H_2O$ | 0.118 | 0.118 |
| 3. $MOH + H^+ + e$ | → | $M + H_2O$ | 0.039 | 0.039 |
| **III The "Hydrogen Peroxide" Path** | | | | |
| 1. $O_2 + M + MH_2O$ | → | $MOH + MO_2H$ | ∞ | ∞ |
| 2. $MOH_2 + MO_2H$ | → | $MOH + MH_2O_2$ | 0.059 | 0.059 |
| 3. $M + MH_2O_2$ | → | $2MOH$ | 0.03 | 0.03 |
| 4. $MOH + H^+ + e$ | → | $M + H_2O$ | 0.118 | 0.118 |
| **IV The "Metal Peroxide" Path** | | | | |
| 1. $O_2 + M + MH_2O$ | → | $MHO_2 + MOH$ | ∞ | ∞ |
| 2. $M + MHO_2$ | → | $MO + MOH$ | 0.059 | 0.059 |
| 3. $MO + MH_2O$ | → | $2MOH$ | 0.03 | 0.03 |
| 4. $MOH + H^+ + e$ | → | $M + H_2O$ | 0.118 | 0.118 |
| **V The "Electrochemical Metal Peroxide" Path** | | | | |
| 1. $O_2 + M + MH_2O$ | → | $MOH + MHO_2$ | ∞ | ∞ |
| 2. $MHO_2 + H^+ + e$ | → | $MO + H_2O$ | 0.039 | 0.039 |
| 3. $MO + MH_2O$ | → | $2MOH$ | 0.03 | 0.03 |
| 4. $MOH + H^+ + e$ | → | $M + H_2O$ | 0.071 | 0.071 |
| **VI Hoar Alkaline Path** | | | | |
| 1. $M + O_2 + 2\,e$ | → | $MO_2^{-2}$ | 0.059 | 0.118 |
| 2. $M + MO_2^{-2} + 2H_2O$ | → | $2MH_2O_2^-$ | 0.03 | 0.059 |
| 3. $MH_2O_2^-$ | → | $MOH + OH^-$ | 0.059 | 0.079 |
| 4. $MOH + e$ | → | $M + OH^-$ | 0.039 | 0.039 |
| **VII Conway and Bourgault Reaction Path** | | | | |
| 1. $M + MH_2O + O_2$ | → | $MHO_2 + MOH$ | ∞ | ∞ |
| 2. $MHO_2$ | → | $MOH + MO$ | 0.059 | 0.059 |
| 3. $MO + H^+ + e$ | → | $MOH$ | 0.024 | 0.024 |
| 4. $MOH + H^+ + e$ | → | $M + H_2O$ | 0.071 | 0.071 |
| **VIII Alternative Conway and Bourgault Reaction Path** | | | | |
| 1. $M + MH_2O + O_2$ | → | $MOH + MHO_2$ | ∞ | ∞ |
| 2. $MHO_2 + H^+ + e$ | → | $MO + H_2O$ | 0.039 | 0.039 |
| 3. $MO + H^+ + e$ | → | $MOH$ | 0.024 | 0.024 |
| 4. $MOH + H^+ + e$ | → | $M + H_2O$ | 0.039 | 0.039 |
| **IX Riddiford Path** | | | | |
| 1. $O_2 + MH_2O + H^+ + e$ | → | $MHO_2 + H_2O$ | 0.118 | 0.118 |
| 2. $MHO_2 + H^+ + e$ | → | $MO + H_2O$ | 0.039 | 0.039 |
| 3. $MO + MH_2O$ | → | $2MOH$ | 0.03 | 0.03 |
| 4. $MOH + H^+ + e$ | → | $M + H_2O$ | 0.039 | 0.039 |
| **X Krasilshchikov Path (Ni electrodes)** | | | | |
| 1. $O_2 + 2M$ | → | $2MO$ | ∞ | ∞ |
| 2. $MO + e$ | → | $MO^-$ | 0.118 | 0.236 |
| 3. $MO^- + H^+$ | → | $MOH$ | 0.059 | 0.079 |
| 4. $MOH + H^+ + e$ | → | $M + H_2O$ | 0.039 | 0.039 |
| **XI Wade and Hackerman's Path** | | | | |
| 1. $O_2 + 2e + 2M + MH_2O$ | → | $2MOH^- + MO$ | 0.059 | 0.118 |
| 2. $MO + MH_2O + 2e$ | → | $2MOH^-$ | 0.02 | 0.03 |
| **XII** | | | | |
| 1. $O_2 + H^+ + e + M$ | → | $MO_2H$ | 0.118 | 0.118 |
| 2. $MO_2H + H^+ + e$ | → | $MO + H_2O$ | 0.039 | 0.039 |
| 3. $MO + H^+ + e$ | → | $MOH$ | 0.024 | 0.024 |
| 4. $MOH + H^+ + e$ | → | $M + H_2O$ | 0.017 | 0.017 |
| **XIII** | | | | |
| 1. $M + O_2$ | → | $2MO$ | ∞ | ∞ |
| 2. $MO + H_2O$ | → | $MO - H - OH$ | ∞ | ∞ |
| 3. $MO - H - OH + e$ | → | $MO - H - OH^-$ | 0.118 | 0.236 |
| 4. $MO - H - OH^- + H^+$ | → | $MOH + H_2O$ | 0.059 | 0.079 |
| 5. $MOH + H^+ + e$ | → | $M + H_2O$ | 0.039 | 0.039 |
| **XIV** | | | | |
| 1. $O_2 + H^+ + e + M$ | → | $MHO_2$ | 0.118 | 0.118 |
| 2. $MHO_2 + e$ | → | $MO + OH^-$ | 0.039 | 0.039 |
| 3. $MO + H_2O$ | → | $MO - H - OH$ | 0.03 | 0.03 |
| 4. $MO - H - OH + e$ | → | $MO - H - OH^-$ | 0.024 | 0.026 |
| 5. $MO - H - OH^-$ | → | $MOH + OH^-$ | 0.020 | 0.021 |
| 6. $MOH + H^+ + e$ | → | $M + H_2O$ | 0.017 | 0.017 |
| **XV Hoare Path (2)** | | | | |
| 1. $O_2$ (aq) | → | $MO_2$ | ∞ | ∞ |
| 2. $MO_2 + e$ | → | $MO_2^-$ | 0.118 | 0.236 |
| 3. $MO_2^- + H^+$ | → | $MHO_2$ | 0.059 | 0.079 |
| 4. $MHO_2 + e$ | → | $MHO_2^-$ | 0.039 | 0.047 |
| 5. $MHO_2^- + H^+$ | → | $MH_2O_2$ | 0.03 | 0.034 |
| catalytic | | | | |
| 6. $2H_2O_2$ | ⟶ | $2H_2O + O_2$ (ads) | 0.03 | 0.03 |
| **XVI [Quoted by Ives (20)]** | | | | |
| 1. $M + O_2 + e$ | → | $MO_2^-$ | 0.118 | 0.236 |
| 2. $MO_2^- + H^+$ | → | $MO_2H$ | 0.059 | 0.079 |
| 3. $MO_2H + e$ | → | $MO_2H^-$ | 0.039 | 0.047 |
| 4. $MO_2H^- + H^+$ | → | $MH_2O_2$ | 0.03 | 0.034 |
| 5. $MH_2O_2 + e$ | → | $MOH + OH^-$ | 0.024 | 0.024 |
| 6. $MOH + e$ | → | $M + OH^-$ | 0.017 | 0.017 |

were homogenized for 12 hr at the proper temperature and quenched in water to obtain a homogeneous, single phase solid solution. Au-Pt alloys having the following compositions were used (w/o Au): 4.72, 9.66, 17.35, 27.38, 37.25, 49.84, 60.35, 70.13, 80.03, and 89.64. Au-Pd alloys were of the following composition (w/o Au): 9.47, 23.96, 53.89, 67.06, 71.01, 76.90, and 85.8.

The alloy electrodes were cut from the inside of the specimen in order to avoid any possible surface inhomogeneity. The homogeneity of the surface was checked by the electron probe microanalyzer.

Electrodes were metallographically polished, thoroughly cleaned, rinsed, and dried. Acid pretreatments were omitted in order to avoid possible preferential dissolution of alloy constituents. Experiments on pure metals with and without acid treatment showed the same final results.

All the electrodes were prereduced at +0.20v in $H_2SO_4$ and —0.60v in NaOH for 15 min. Since the final results were the same whether the solutions were saturated with oxygen or nitrogen during the reduction, most prereductions were done in an oxygen saturated solution. After prereduction the circuit was opened and the electrode assumed an open-circuit potential, $E_o$, which became steady in about 10 min. The electrode was then cathodically polarized, galvanostatically, from low to high current densities, then from high to low current densities without opening the circuit.

Electrode potential values are given on the standard hydrogen electrode scale.

## Results

*Pure metals.*—The $\eta$ log $i$ curves for oxygen reduction showed a reproducible Tafel relation for all the electrodes in $H_2SO_4$ and NaOH from about $10^{-6}$ amp/cm² to about $10^{-3}$ amp/cm². Concentration polarization became noticeable at these higher current densities under the stirring conditions used. The curves were the same whether obtained from low to high currents or *vice versa*.

Except for Au in $H_2SO_4$ the potential changed very little from the open-circuit value, $E_o$, until the current density reached about $10^{-6}$ amp/cm². The $\eta$-log $i$ relation was not linear in this low current density range. The results for Pt, Pd, and Au are typical and are shown in Fig. 3.

The Tafel parameters are given in Table II. The reported values are the mean of at least six experiments. The values of the slope, $b_c$, were reproducible to better than ±0.005v for all metals in NaOH, to about the same value for Pt and Pd in $H_2SO_4$, and about ±0.01v for the other metals and alloys in $H_2SO_4$. The values of $i_o$ could be reproduced by a factor of ten. Except for Au in $H_2SO_4$, $E_o$ varied by about ±0.02v in $H_2SO_4$ and ±0.01v in NaOH. The $E_o$ of Au varied by about ±0.05v in acid. The overpotential at $10^{-5}$ amp/cm², $\eta^o$, was chosen as a relative index of the "over-all activity" of the electrode for the reduction reaction.

Pt has the highest $i_o$ and activity (lowest $\eta^o$) in both acid and alkaline solutions. Except for Pt, the activity of the metals is greater in NaOH. Since the values of $i_o$ are all quite low, $b_c$ plays the greater role in determining $\eta^o$.

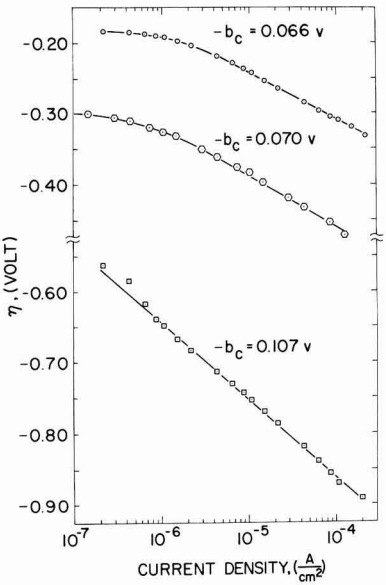


Fig. 3. Overvoltage, $\eta$ — log $i$ relationship in 1*N* $H_2SO_4$. ⊙ Pt; ⊙ Pd; ⊡ Au.

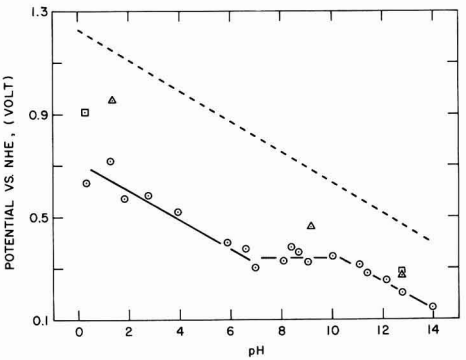


Fig. 4. Open-circuit potential, $E_o$ *vs.* pH. △ Pt; ⊡ Pd; ⊙ Au. Dashed line indicates theoretical potential-pH relationship, calculated from the equation

$$E = 1.23 - \frac{RT}{4F} \ln \frac{(a_{H_2O})^2}{(a_{H^+})^4 (P_{O_2})}$$

Since the values of $b_c$ and $\eta^o$ for Au were significantly different in $H_2SO_4$ and NaOH, more detailed data were obtained for this metal with solutions of different pH values. The results are shown in Fig. 4, 5, and 6.

*Alloys.*—The data for the alloys are shown in Fig. 7, 8, and 9. These figures also include parameters of

Table II. Experimental Tafel parameters

| Metal | No. of holes in d-band | $-b_c$,* volt | | $i_o$, amp/cm² | | $-\eta^o$ [at $10^{-5}$ amp/cm²], volt | | $E_o$ *vs.* NHE, volt | |
|---|---|---|---|---|---|---|---|---|---|
| | | 1*N* $H_2SO_4$ | 0.1*N* NaOH | 1*N* $H_2SO_4$ | 0.1*N* NaOH | 1*N* $H_2SO_4$ | 0.1*N* NaOH | 1*N* $H_2SO_4$ | 0.1*N* NaOH |
| Au | 0.0 | 0.10 | 0.047 | $10^{-13}$ | $10^{-13}$ | 0.74 | 0.35 | 0.70 | 0.21 |
| Pt | 0.58(21) | 0.065 | 0.053 | $10^{-9}$ | $10^{-10}$ | 0.26 | 0.29 | 1.03 | 0.26 |
| Pd | 0.58(22) | 0.070 | 0.046 | $10^{-11}$ | $10^{-12}$ | 0.39 | 0.30 | 0.90 | 0.28 |
| Rh | 1.7 (19) | 0.12 | 0.048 | $10^{-11}$ | $10^{-13}$ | 0.60 | 0.37 | 0.83 | 0.12 |
| Ir | 1.7 (19) | 0.09 | 0.040 | $10^{-11}$ | $10^{-16}$ | 0.47 | 0.41 | 0.91 | 0.18 |
| Ru | 2.2 (19) | 0.08 | 0.051 | $10^{-12}$ | $10^{-12}$ | 0.55 | 0.35 | 0.82 | 0.21 |
| Os | 2.2 (19) | 0.13 | 0.035 | $10^{-10}$ | $10^{-15}$ | 0.58 | 0.35 | 0.98 | 0.20 |

* — $b_c$ reproducible to ± 0.005v in NaOH; ± 0.005v for Pt and Pd in $H_2SO_4$; ± 0.01v for others in $H_2SO_4$.

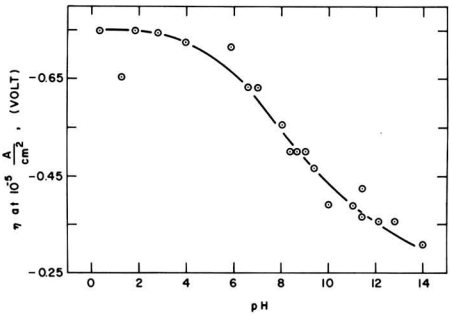


Fig. 5. Activity, $\eta^o$ vs. pH for Au

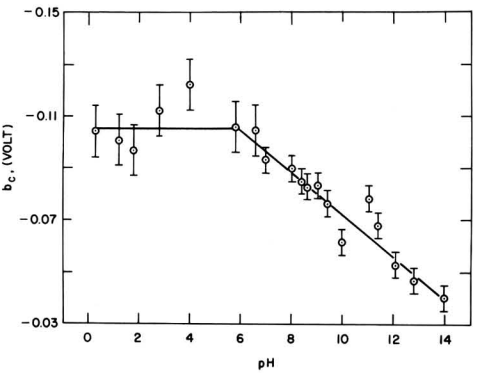


Fig. 6. Tafel slope, $b_c$ vs. pH for Au

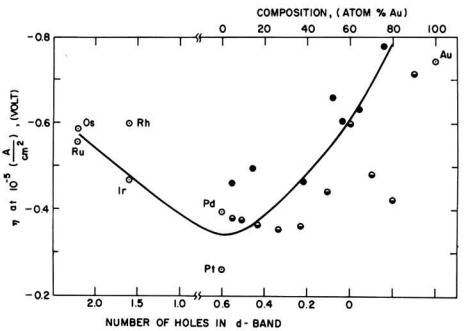


Fig. 7. Activity $\eta^o$ vs. composition and number of holes in d-band; in 1N $H_2SO_4$. ◒ Pt-Au alloys; ● Pd-Au alloys.

the pure metals in order to show the effect of the d-band structure as well as composition.

Pt-Au *alloys in* $H_2SO_4$.—$E_o$ remains close to the value for Pt until about 85 a/o (atomic per cent) Au. The value of $i_o$ remains close to that of Pt until about 60 a/o Au. Surprisingly, $b_c$ changes to that of Au at only about 5 a/o Au. The net effect is a decrease of activity with Au content.

Pt-Au *alloys in* NaOH.—$i_o$ decreases with Au content, while $E_o$ remains close to that of Au for all compositions. $\eta^o$ and $b_c$ do not vary with alloy composition.

Pd-Au *alloys in* $H_2SO_4$.—$E_o$ remains close to that of Pd until about 70 a/o Au. The values of $b_c$, $i_o$, and $\eta^o$ change approximately linearly with Au content from the values of Pd to those of Au, with considerable scatter in the values.

Pd-Au *alloys in* NaOH.—$E_o$ remains close to that of Pd until about 60 a/o Au. The values of $b_c$ and $\eta^o$ are

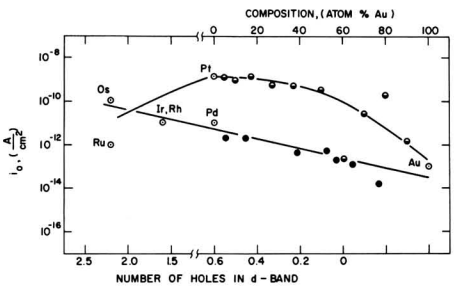


Fig. 8. Exchange current, $i_o$ vs. composition and number of holes in d-band; in 1N $H_2SO_4$. ◒ Pt-Au alloys; ● Pd-Au alloys.

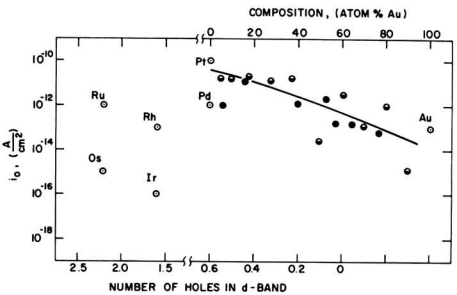


Fig. 9. Exchange current, $i_o$ vs. composition and number of holes in d-band; in 0.1N NaOH, ◒ Pt-Au alloys; ● Pd-Au alloys.

about the same for the two pure metals and show no significant dependency on composition, considering the reproducibility. The $i_o$ values for Pd and Au are about $10^{-12}$ amp/cm² and $10^{-13}$ amp/cm², respectively. The value for the alloys changes approximately linearly with Au content between these two limits.

Any effects due to the number of holes in the d-band (nhd) may be seen from Fig. 7, 8, and 9, by considering the data for the pure metals along with that for the alloys. The large scatter in the values does not allow precise evaluation, but certain consistent trends of the variation of the Tafel parameters $\eta^o$ and $i_o$ are indicated. These trends are shown by the curves drawn in the figures. The trends are much more with the chemical composition-surface structure than with the nhd.

## Discussion

*Open-circuit potential.*—The nonlinear character of $\eta$-log $i$ and the very low rate of change of $\eta$ with log $i$ in the low current density range strongly indicates that the open-circuit potential is either a mixed potential with a "reaction current density" of about $10^{-6.5}$ amp/cm² or that it is a reversible potential for some reaction with an exchange current density of the same value. We believe that the former is the case, in agreement with Hoar and others (16, 16a).

*Reaction mechanisms.*—It is not possible to determine reaction mechanisms by means of $b_c$ and $i_o$. Since the anodic reaction occurs on an oxide surface (5, 6), the anodic slope $b_a$ and $\nu$ could not be obtained on prereduced surfaces. Moreover $E_o$ is about 1V, and hence one cannot use the linear relation between $\eta$ and $i$ to calculate $\nu$ (11).

Values of $b_c$ may be used to eliminate certain reaction paths and indicate possible paths. Many reaction paths can be devised for the oxygen electrode, but we will limit our discussion to those listed in Table I. Taking into account the variations in the reproducibility of the $b_c$ values the possible paths for the metals are summarized in Table III.

**Table III. Possible reaction paths and rate-determining steps corresponding to experimental $b_c$**

| No. | System | Possible paths and rds** | Remarks |
|---|---|---|---|
| 1 | Pt in $H_2SO_4$ | III(2), IV(2), VI(2), VII(2), V(4),* VII(4)* | Damjanovic *et al.* (6) obtained 0.054v on oxide free Pt. Bianchi *et al.* (3) obtained 0.06v on oxide free Pt. |
| 2 | Pt in NaOH | III(2), IV(2), VI(2), VII(2), XV(4),* XVI(3)* | Damjanovic *et al.* (7, 8) obtained 0.065v on oxide covered Pt. Hoar (16) obtained 0.048v |
| 3 | Pd in $H_2SO_4$ | V(4),* VII(4)* | |
| 4 | Pd in NaOH | XV(4),* XVI(3)* | |
| 5 | Au & Rh in $H_2SO_4$ | I(3),* II(2),* III(4),* IV(4),* VI(1),* IX(1),* XII(1),* XIV(1)* | Damjanovic *et al.* (8) obtained 0.06v on reduced Rh and 0.06v on oxidized Rh at low current densities. |
| 6 | Au & Rh in NaOH | XV(4),* XVI(3)* | Hoar obtained 0.048v (16) on Au. Damjanovic *et al.* (8) obtained about 0.100v on oxidized Rh. |
| 7 | Os in $H_2SO_4$ | Refer No. 5 above | |
| 8 | Os in NaOH | II(3),* V(2),* VI(4),* VIII(2),* VIII(4),* IX(2),* IX(4),* X(4),* XII(2),* XIII(5),* XIV(2),* XV(5), XVI(4), III(3), IV(3), V(3), IX(3), XIV(3), XI(2)* | |
| 9 | Ir in $H_2SO_4$ | VI(3), X(3), XIII(4), XV(3), XVI(2) | Damjanovic *et al.* (8) obtained 0.100v on oxidized Ir. |
| 10 | Ru in $H_2SO_4$ | VI(3), X(3), XIII(4), XV(3), XVI(2), V(4),* VII(4)* | |
| 11 | Ru in NaOH | Refer No. 6 above | |

* In these steps electrons are transferred.
** Roman numeral indicates the reaction path and the numeral in parenthesis indicates the rds; refer to Table I.

The continuous variation of $b_c$ with pH for Au is noteworthy. Although data were not obtained for Ru, Rh, Ir, and Os, which also show a fairly large change in slope from acidic to alkaline solutions, it is likely that a similar variation of $b_c$ with pH occurs on these metals. The continuous variation in $b_c$ with pH is very likely due to the presence of at least two alternate reaction paths whose rates are close in value with one path being pH dependent.

There is no apparent relationship of the number of holes in the d-band (nhd) with the activity in NaOH or with $b_c$ in $H_2SO_4$ and NaOH. The exchange current density, $i_o$, does show a trend with nhd in $H_2SO_4$. It does not appear significant, however. The trend in NaOH is even less significant. The activity in $H_2SO_4$ does show a definite trend (Fig. 7), with a maximum activity (minimum $\eta^o$) at Pt and Pd. Our general conclusion is that composition, hence geometric and chemical factors, play the predominant role in this series of metals. These results and conclusions are not at variance with some current views on the role of electronic structure on catalysis (17). It is interesting to note that Brennan *et al.* found that the integral heat of adsorption for oxygen on Pt, Pd, and Rh varied almost linearly with atomic radii (18). On the other hand, Rao *et al.* have reported an increase in surface coverage of oxygen with an increase in the nhd for the same metals used in this work (19).

## Acknowledgment

The authors wish to express their appreciation to the Ford Motor Company for permission to publish this work.

Manuscript received March 20, 1967. This paper was presented at the Dallas Meeting, May 7-12, 1967.

Any discussion of this paper will appear in a Discussion Section to be published in the June 1968 JOURNAL.

## REFERENCES

1. J. O'M. Bockris and A.K.M.S. Huq, *Proc. Roy. Soc., London,* **A237,** 277 (1956); N. Watanabe and M.A.V. Devanathan, *This Journal,* **111,** 615 (1964).
2. J. P. Hoare, *ibid.,* **112,** 849 (1965).
3. G. Bianchi and T. Mussini, *Electrochim. Acta,* **16,** 445 (1965).
4. J. J. Lingane, *J. Electroanal. Chem.,* **2,** 296 (1961).
5. J. J. McDonald and B. E. Conway, *Proc. Roy. Soc.,* **A269,** 419 (1963).
6. A. Damjanovic and J. O'M. Bockris, *Electrochim. Acta,* **11,** 376 (1966).
7. A. Damjanovic, A. Dey, J. O'M. Bockris, *ibid.,* **11,** 791 (1966).
8. A. Damjanovic, A. Dey, and J. O'M. Bockris, *This Journal,* **113,** 739 (1966).
8a. D.F.C. Morris and H. N. Schmeising, *Nature,* **181,** 469 (1958).
9. A. C. Riddiford, *Electrochim. Acta,* **4,** 170 (1961).
10. T. P. Hoar, Proc. 8th Meeting CITCE, 1956, p. 439, Butterworths, London (1958).
11. R. Parsons, *Trans. Faraday Soc.,* **47,** 1332 (1951); G. H. Fraser and R. G. Barradas, *This Journal,* **112,** 462 (1965).
12. B. Lovrecek, *J. Phys. Chem.,* **24,** 817 (1956); J. O'M. Bockris, *ibid.,* **24,** 817 (1956); B. E. Conway, *Trans. Roy. Soc. Canada,* **54,** (111) 19 (1960).
13. R. Parsons, "Modern Aspects of Electrochemistry," Vol. I, J. O'M. Bockris and B. E. Conway, Editors, p. 103; Academic Press Inc., New York (1954).
14. P. Delahay, "Double Layer and Electrode Kinetics," Interscience Publishers, New York (1956).
15. J. R. Macdonald and C. A. Barlow, Jr., *This Journal,* **113,** 978 (1966); "Electrochemistry" (Proc. 1st Australian Conference), Pergamon Press, New York (1964).
16. T. P. Hoar, *Proc. Roy. Soc., London,* **A142,** 628 (1933).
16a. Giner, *Z. Elektrochem.,* **63,** 386 (1959); J. P. Hoare, *This Journal,* **109,** 858 (1962).
17. G. Ehrlich, "Proc. 3rd International Congress on Catalysis," p. 113; John Wiley & Sons, Inc., New York (1965).
18. D. Brennan, D. O. Hayward, and B. M. Trapnell, *Proc. Roy. Soc., London,* **A256,** 81 (1960).
19. M.L.B. Rao, A. Damjanovic, and J. O'M. Bockris, *J. Phys. Chem.,* **67,** 2508 (1963).
20. "Reference Electrodes—Theory & Practice," Edited by D. J. Ives and G. J. Janz, p. 365; Academic Press, New York (1961).
21. D. W. Budworth, F. E. Hoare, and J. Preston, *Proc. Royal Soc., London,* **A257,** 250 (1960).
22. F. E. Hoare and B. Yates, *ibid.,* **A240,** 42 (1957).

# The Kolbe Electrosynthesis of Polydifluoromethylene

**Madeline S. Toy**

*Douglas Aircraft Company, Missile and Space Systems Division, Astropower Laboratory, Newport Beach, California*

In general, dicarboxylic acids, such as malonic acid, do not undergo reactions of Kolbe type, but oxidize to degradation products at anode electrode in an alkaline medium. However, the alkaline salts of the monoester dicarboxylic acids have been reported to give Kolbe type reactions with products being higher dicarboxylic acid esters (1). The electrolysis of dibasic acids in methanol have been reported by Garrison (2) to form polymers, and Kolbe couplings of perfluorinated monobasic acids have been reported by Levin, Chechina, and Sokolov (3). A recent patent describes the production of long-chain perfluoromono- and perfluorodicarboxylic acid esters also through Kolbe couplings (4).

This note reports the anodic synthesis of polydifluoromethylene from a perfluorodicarboxylic acid. Polydifluoromethylene has been prepared by electrolysis of solutions of commercial perfluoroglutaric acid (mp 85°-90°C) with sodium in methanol. The temperature of the experiments ranged from 25° to 55°C and the monomer concentration in absolute methanol ranged from 5 to 25 w/o. The electrolytic cell was equipped with two smooth platinum electrodes. A typical run employed 10% monomer by weight, current density of 40 to 100 ma/cm², and applied voltage up to 40v (depending on the distance between the electrodes and salt concentration). A white loosely adhering coating was formed on the anode in 4 hr. The current density could not be maintained but gradually decreased. After a few hours of electrolysis, a small amount of white flocculent precipitate was observed around the anode. The flocculent precipitate can be slightly increased by occasionally reversing the polarity of the electrodes. The white solid scraped from the anode partially softened at 300°C and was insoluble in solvents, including hexafluorobenzene, chloroform, dimethyl formamide, dimethyl sulfoxide, concentrated sulfuric acid, while the small amount of white solid recovered from the suspension was partially soluble in concentrated sulfuric acid, but not in the other tested solvents. The very strong broad absorption band between 7.9 and 8.7$\mu$ (5) for "Teflon" (trademark of du Pont's polytetrafluoroethylene) is observed in Fig. 1. The anodically synthesized polydifluoromethylene also shows another strong absorption band at 5.6$\mu$ with a weak peak at 2.9$\mu$, indication typical of COOH in fluorocarbons (6). The infrared spectrum (Fig. 1) and the absolutely insoluble characteristics of the white solid scraped from the anode indicate that the polymer is essentially a long perfluorocarbon chain as Teflon, but with carboxylic terminal groups. The estimated molecular weight is low at approximately one thousand by the relative intensities of the CF and CO groups in the infrared spectrum.

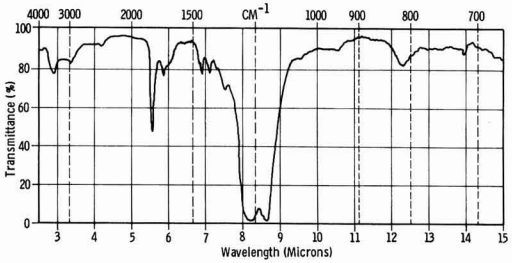


**Fig. 1. Infrared spectrum of anodically synthesized polydifluoromethylene.**

The mechanism of anodic synthesis of polydifluoromethylene from perfluoroglutaric acid appears to involve diradical couplings on the electrode surface.

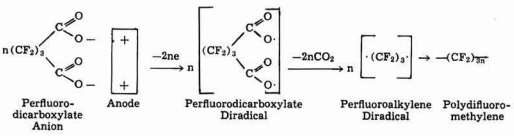


During electrolysis, the perfluorodicarboxylate anions are impelled to the anode, where they give up the ionic charges and possibly exist in a transient phase as a perfluorodicarboxylate diradical having an odd electron on both ends. This diradical at once loses carbon dioxide molecules and gives an equally transient trivalent carbon radical on both ends. This perfluoroalkylene diradical finally achieves stabilization by radical combinations with adjacent diradicals to form a polydifluoromethylene coating on the metal surface.

Manuscript received April 24, 1967; revised manuscript received *ca.* June 22, 1967.

Any discussion of this paper will appear in a Discussion Section to be published in the June 1968 JOURNAL.

## REFERENCES

1. M. J. Allen, "Organic Electrode Processes," pp. 109-111, Reinhold Publishing Co., New York (1958).
2. W. E. Garrison, Jr., *Diss. Abstr.*, **20**, 77 (1959).
3. A. I. Levin, O. N. Chechina, and S. V. Sokolov, *Zh. Obshch, Khim.*, **35**, (10), 1778 (1965).
4. W. Bloechl and H. Kuckertz, German Pat. 1,231-679 (1967).
5. J. D. Simons, Editor, "Fluorine Chemistry," Vol. II, p. 497, Academic Press, New York, (1954).
6. M. I. Bro and C. A. Sperati, *J. Polymer Sci.*, **38**, 289 (1959).

# Oxygen Reduction on a Partially Immersed Rotating Platinum Cathode

R. J. Roethlein and H. J. R. Maget

*DECO Research & Development Laboratory, General Electric Company, West Lynn, Massachusetts*

Reaction rates for an electrochemical process occurring on stationary electrodes in a diffusion controlled region having essentially the same interphase between the conducting electrolyte and the gas phase reactant have been shown by many authors to be associated with mass transport processes through thin electrolyte films (1-5). The reaction zone is confined to a small region near the film-meniscus interphase, and it is evident that these electrodes utilized only a fraction of the total electrode surface area. The bulk electrolyte presents a longer path for the mass transport of the reactant (gas) species to the electrode surface, and the reaction zone is further limited by the increased resistance to ionic flow encountered in the thin film region as the distance from the bulk electrolyte region increases. In order to facilitate a larger portion of the electrode surface area for mass transport processes a rotating electrode structure was investigated.

A circular hydrophobic electrode structure was rotated intermittently through an aqueous electrolyte and a depolarizing gas (oxygen). This procedure extends the region of thin film formation above the electrolyte level causing an increase in the total electrode current. Similar investigations have been carried out by Bonnemay *et al.* (6) in an attempt to separate adsorption from mass transport in electrochemical studies, and Weber *et al.* (7) have used a rotating copper electrode to investigate the mechanism of metal oxidation. The increased currents observed on partially immersed porous electrode has been employed by Bianchi (8) as a convenient basis for a comparative study of electrocatalytic activity of noble metals and for investigations of electrocatalytic processes of various reactant gases.

Therefore this novel electrode structure may not only provide higher diffusion controlled currents but also serve as an effective tool in catalyst evaluation. Further by variation of the rotational speed and depth of immersion this device could be used to determine the relative rates of:

1. The diffusion of a reactant gas across an electrolyte film.
2. Migration parallel to the electrolyte film.
3. Reaction and desorption of reactants into the electrolyte.
4. Adsorption on a dry surface or below the electrolyte film level.

## Experimental

Experiments were carried out in a specially modified Pyrex glass test cell, which contained reference and counter electrode compartments separated from the study electrode section of the cell, Fig. 1. The counter electrode consisted of a large section of platinum black screen, and the reference system contained a dynamic hydrogen reference electrode, which maintained a steady potential near the reversible $H^+/H_2$ potential. The test electrode consisted essentially of a Teflon-bonded platinum black electrode (9) which was cut into a circular disk and then mounted on a tantalum shaft. The shaft was connected by means of an insulated bushing to a multi-speed transmission which has a 600 rpm reversible synchronous motor and a gear train with twelve steps of reduction. By the use of this motor various speeds of rotation could be imposed upon the

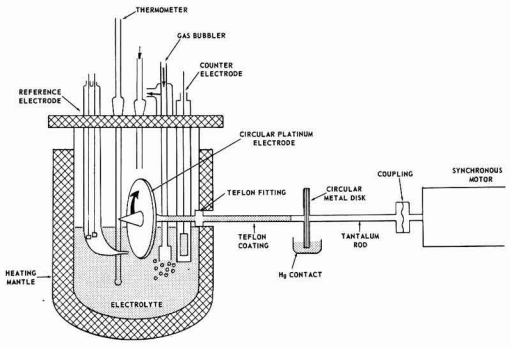


**Fig. 1. Experimental apparatus**

electrode. The study electrode was held vertical on the shaft with two circular Teflon disks which were threaded into the tantalum rod.

Electrical contact was accomplished by having a metal disk connected to the shaft outside of the test cell which then rotated through a pool of mercury. Teflon couplings mounted on the glass inlet port for the tantalum shaft prevented electrolyte leakage from the test cell, but still permitted the metal shaft to rotate freely. Temperature was maintained constant to within a few degrees by means of a variac controlled heating mantel. The study electrode was composed of the same materials generally employed in making Niedrach-Alford-type electrodes, nine parts platinum black to one part of weight of Teflon; pressed on platinum screening. The electrode was pressed at approximately 6200 psi at 700°F for a period of 7.5 min. A thin film of Teflon was sprayed on both sides of the electrode with an aqueous dispersion of (T-30). The actual electrode area on both faces of the disk was approximately 42 $cm^2$ with an average thickness of 10 mils. Measurements of the electrochemical reduction of oxygen were made in $10N$ $H_2SO_4$ at 25°C; both the electrolyte and surrounding atmosphere inside the test cell were kept completely saturated with oxygen gas. The electrolyte was presaturated with oxygen by means of the gas bubbler; however, during test the oxygen was admitted above the electrolyte level. Electrode potential was held constant by means of a Wenking potentiostat.

## Results and Discussion

Performance studies were made of the rate of the electrochemical reduction of oxygen under various conditions. The electrode was held at a constant potential of $+0.600$v *vs.* $H^+/H_2$ and the current recorded for various conditions of electrode immersion and rotational speed. Figure 2 shows a plot of variation in current with the square root of rotational speed for six different immersion depths, 10, 15, 30, 50, 75, and 100% of the total electrode surface below the electrolyte level. When the electrode is totally immersed the electrochemical process is controlled by the bulk diffusion of oxygen through the electrolyte; hence only low currents are obtainable which show only slight increases with rotational speed. As

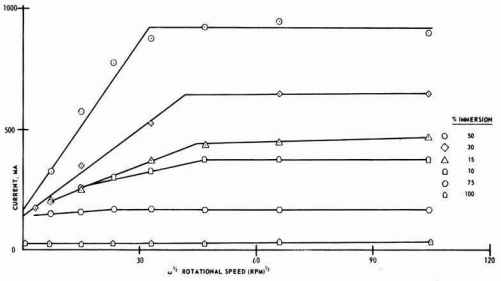


**Fig. 2. Effect of rotational speed and immersion depth on electrode current. $O_2$ reduction; ion-$H_2SO_4$, 25°C; applied potential +0.600v vs. $H^+/H_2$.**

the electrode is raised out of solution there is an immediate increase in current even while the electrode is at rest. This is due to the formation of a thin film of electrolyte in the exposed portion of the electrode matrix, which provides a shorter path for diffusion of oxygen molecules to the catalyst surface (10). Increasing the amount of exposed surface area has no substantial effect on the current while the electrode is at rest. This is due to the fact that the effective "active" area of the thin film portion of the electrode is virtually the same no matter how much of the total electrode surface is above the electrolyte level. The "active" length of the film is dependent mainly on the thickness of the electrolyte film which can produce large ionic resistance variations during current flow. At rest, gravitational forces will cause the liquid film to drain to a constant thickness which is independent of the amount of exposed surface area. When the electrode is rotated a linear increase in current is obtained with the square root of rotational speed up to an optimum value above which there is no subsequent current change with increasing rotational speed.

Observations made of the electrode surface at rest and during rotation show a distinctly hydrophobic surface in that the contact angle is greater than 90° and liquid does not cling to the exposed electrode surface during rotation. However the catalyst matrix beneath the Teflon film does wet, and rotating the electrode brings this wetted section above the electrolyte level. At this point electrolyte in the catalyst matrix drains downward, but has the immediate effect of providing an electrolyte film in the exposed section of the electrode above the level of the electrolyte. Increasing the speed of rotation will tend to counter balance the force of gravity providing a temporary greater film thickness in the region above the electrolyte level. Thus a larger portion of the thin film will be able to support current due to the decreased ionic resistance provided by the increase in film thickness. Eventually increasing the rotational speed will no longer have any effect on the film thickness and electrode current will reach a plateau.

Variations in the amount of electrode surface partially immersed reflect changes in the electrode current during rotation. There is a steady increase in current as the depth of immersion increases up to approximately 50% of the total electrode area; subsequent increases in the per cent of immersion produce a decrease in total electrode current. For immersion depths less than half of the total electrode area smaller portions of the outside perimeter of circular electrode surface are wetted by electrolyte during rotation. As the immersion depth increases the total current increase is due to a geometric increase in electrode area on which the active area of the thin film can be formed. The lower currents obtained for immersions depths greater than approximately 50% are caused by a decrease in the active area of the thin film region since a larger portion of the electrode surface is below the electrolyte level and bulk diffusion controlled.

Manuscript received May 8, 1967; revised manuscript received June 22, 1967.

Any discussion of this paper will appear in a Discussion Section to be published in the June 1968 JOURNAL.

## REFERENCES

1. F. Will, *This Journal*, **110**, 152 (1963).
2. H. J. R. Maget and R. J. Roethlein, *ibid.*, **112**, 1034 (1965).
3. R. J. Roethlein and H. J. R. Maget, *ibid.*, **113**, 581 (1966).
4. D. N. Bennion and C. W. Tobias, *ibid.*, **113**, 589 (1966)
5. R. P. Icztowski, *ibid.*, **111**, 1078 (1964).
6. R. Bonnemay, Paris Meeting on Fuel Cells, February 1965.
7. H. C. Weber, H. P. Meissner, and D. A. Sama, *This Journal*, **109**, 884 (1962).
8. G. Bianchi, *ibid.*, **112**, 233 (1965).
9. L. W. Niedrach and H. R. Alford, *ibid.*, **112**, 117 (1965).
10. R. J. Roethlein and H. J. R. Maget, To be published.

Brief Communication

# Conductivity of KOH and KOH-ZnO Electrolytes from 36° to -66°C

**Charles T. Baker and Isaac Trachtenberg**

*Texas Instruments, Incorporated, Dallas, Texas*

Currently, emphasis is being placed on the research of alkaline batteries using the negative zinc electrode, and more information is needed on the KOH and KOH-ZnO electrolyte systems which are used in such batteries. In this note data are presented on the specific conductivities of various KOH and KOH-ZnO solutions as a function of temperature between 36° and —66°C and on the solubility of ZnO in these KOH solutions. These latter data are in agreement with those of other investigators (1, 2).

All KOH and KOH-ZnO solutions were prepared using reagent grade KOH and ZnO and deionized water. During the preparation and utilization of these solutions, precautions were taken to prevent the introduction of $CO_2$. A Tenney, Jr., Environmental Chamber, Model TJR, was used to control the temperature of the experiments to ±0.5°C. The conductivity measurements were made with an L&N model 4805-50 conductivity cell assembly in conjunction with a General Radio Company impedance comparator, model 1605, using General Radio Company precision resistance and capacitance decade boxes. The cell constant for the conductivity cell was determined by using the solutions and data given by Jones and Bradshaw (3).

In the ZnO solubility studies, at each temperature the sample solution was agitated periodically by means of an ultrasonic bath over a three-day span in order to insure that equilibrium had been established. When samples were needed for analysis, the required amount of solution was extracted from the vessel in the environmental chamber by means of a reduced pressure system.

Results of the conductivity experiments are reported in Fig. 1 and Fig. 2 for 39, 34, 30, and 25% KOH and for 36.3% and 30% KOH saturated with ZnO at temperatures from 36° to —66°C. Both Dirkse (4) and Bodamer (1) have shown that for a particular KOH concentration and temperature, the specific conductivity decreases as the concentration of zinc in solution increases.

The conductivity data point out one major problem which must be considered in the use of alkaline batteries at low temperatures. There will be about a 100 fold change in the internal resistance of the battery which in itself can grossly affect the charge-discharge characteristics of the battery. For the pure KOH solutions, the 30% KOH solution exhibits the best behavior over the temperature range investigated. The 25% KOH solution is equally conductive at temperatures down to —23°C and is slightly more conductive for temperatures down to —36°C, but is limited by a freezing point in the neighborhood of —41°C. The conductivity data for the KOH solutions saturated with

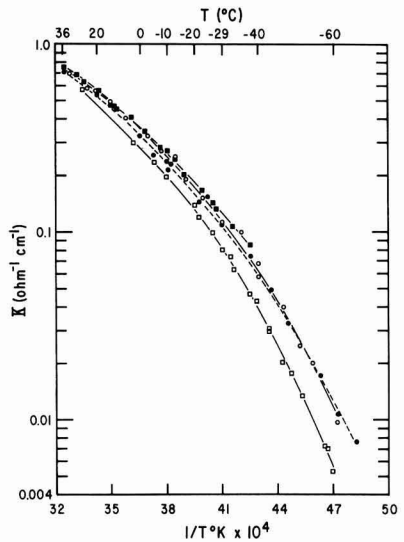


Fig. 1. Specific conductivity of KOH solutions as a function of temperature. ■ 25% KOH; O 30% KOH; ● 34% KOH; and □ 39% KOH.

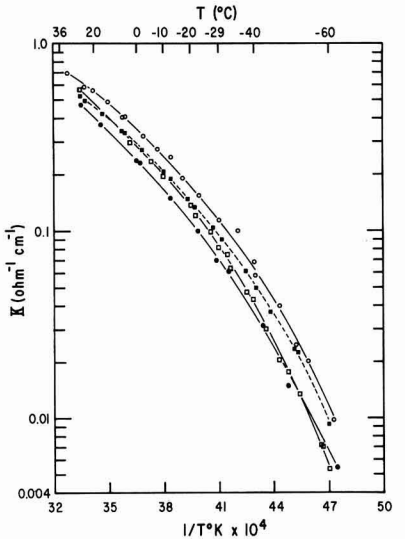


Fig. 2. Specific conductivity of KOH and KOH-ZnO solutions as a function of temperature. O 30% KOH; □ 39% KOH; ● ZnO saturated 36.3% KOH; and ■ ZnO saturated 30% KOH.

Table I. Solubility of ZnO in KOH at 25°C

| % KOH (before saturation) | *M* Zn ions in solution |
|---|---|
| 25 (5.5*M* KOH) | 0.45 |
| 30 (6.9*M* KOH) | 0.64 |
| 34 (8.1*M* KOH) | 0.83 |
| 36.3 (8.7*M* KOH) | 0.95 |

ZnO at these low temperatures are consistent with that reported by Bodamer at the higher temperatures. Addition of ZnO to a KOH solution decreases the conductivity of the solution.

Results of the solubility studies of ZnO in 25, 30, 34, and 36.3% KOH at 25°C are given in Table I and are in agreement with the values reported by Bodamer (1) and Dirkse (2). The effect of temperature on the solubility of ZnO in 36.3% KOH is shown in Table II. As the temperature decreases from 26° to −62°C, the solubility of ZnO appears to be invariant. Bodamer observed the same effect for temperatures between 10° and 95°C. Based on these two sets of data, the over-all heat of solution appears to be close to zero.

Manuscript received July 25, 1967.

Table II. Effect of temperature on the solubility of ZnO in 36.3% KOH

| Temperature, °C | *M* Zn ions in solution |
|---|---|
| −62 | 0.92 |
| −51 | 0.92 |
| −30 | 0.95 |
| −30 | 0.94 |
| −26 | 0.97 |
| −10 | 0.92 |
| 0 | 0.94 |
| +26 | 0.97 |

Any discussion of this paper will appear in a Discussion Section to be published in the June 1968 JOURNAL.

## REFERENCES

1. G. W. Bodamer, "Heat Sterilizable Impact Resistant Cell Development," Jet Propulsion Lab. Contract No. 951296.
2. T. P. Dirkse, *This Journal*, **106**, 154 (1959).
3. G. Jones and B. C. Bradshaw, *J. Am. Chem. Soc.*, **55**, 1780 (1933).
4. T. P. Dirkse, *This Journal*, **102**, 497 (1955).

JOURNAL OF THE ELECTROCHEMICAL SOCIETY

# SOLID STATE SCIENCE

OCTOBER 1967



*Journal of The Electrochemical Society* is the fundamental research journal serving the interdisciplinary interests of chemistry, physics, electronics, biology, medicine, and engineering as they pertain to electrochemistry and to electrochemical phenomena. Written for the research scientist in industry, government, the independent laboratory and the university, it publishes contributed Technical Papers, Technical Notes and Brief Communications describing current basic research of original character, and is edited in two sections: 1) ***Electrochemical Science*** including such areas as batteries, fuel cells, corrosion and corrosion mechanisms, electrothermics and metallurgy, electrodeposition, electroorganic reactions and phenomena, and allied work of theoretical electrochemical nature. 2) ***Solid State Science*** including such areas as dielectrics and insulation, electrothermics and metallurgy, semiconductors, luminescence and related solid state investigations.



## TECHNICAL PAPERS



## TECHNICAL NOTES



## BRIEF COMMUNICATION

# Characterization of Energy Transfer Interactions between Rare Earth Ions

L. G. Van Uitert

*Bell Telephone Laboratories, Incorporated, Murray Hill, New Jersey*

ABSTRACT

Energy transfer studies employing the sodium rare earth tungstates (scheelite structure) indicate a number of modes of, and requirements for, nonradiative interaction. Direct dipole-dipole interactions are prevalent. However, dipole-quadrupole interactions are observed for the states of the larger rare earth ions that lie high in energy. The relation of lifetime ($\tau_e$) to intensity changes with the mode of transfer. Phonon assisted transfer is enhanced by exchange coupling between rare earth ions in nearest or next nearest neighbor positions. Excitation may migrate between Tb ions in such positions when thermally activated and provided a suitable quenching center (*e.g.*, Nd, Eu) is present. Such migration appears to be directional in comparison to transfer by radiation reabsorption. The latter is essentially random. Methods for analyzing lifetime data for transfer interactions are also discussed.

Energy transfer between rare earth (RE) ions is a subject of appreciable current interest for practical as well as theoretical reasons. The use of rare earths for laser and colored television applications have stimulated a desire for a better understanding of transfer. Early work in this field has been discussed by Botden (1). More recent work has been summarized elsewhere (2). Much of the previous work has been limited to demonstrations that transfer does occur and general statements as to the probable mechanisms involved. In fact, however, a sufficiently strong theoretical basis exists for more exacting results to be obtained (3-6). The RE ions are particularly suitable for the study of energy transfer as the absorption and emission due to f-electrons is sharp and the associated oscillator strengths are weak.

Energy transfer is generally associated with multipolar interactions, radiation reabsorption, or exchange. These effects can be identified by examining intensity and lifetime data as a function of the excited (E) and/or the quenching (Q) ion concentration. Intensity values can be obtained by direct measurement under equilibrium conditions, but lifetime is obtained under transient conditions and is somewhat subject to interpretation. Procedures for analyzing lifetime data and the significance of various correlations of intensity and lifetime with E-ion and/or Q-ion concentration are discussed.

### *Materials and Measurements*

Crystals of various members of the series $Na_{0.5}(Y,RE)_{0.5}WO_4$, where RE = Pr, Nd, Sm, Eu, Tb, Dy, and or Er in the combinations indicated in the accompanying figures, were grown from a $Na_2W_2O_7$ flux as described previously (7). The crystals have the scheelite ($CaWO_4$) structure; however, the Na, Y, and RE ions are distributed somewhat randomly over the dodecahedral sites normally occupied by Ca. The compositions were analyzed by x-ray fluorescence methods.

Intensity comparisons were obtained using a standard plaque technique. The intensity of emission of Pr (at 0.487$\mu$ for $Pr^3P_o$), of Sm (at 0.598$\mu$ for $Sm^4F_{5/2}$), of Eu (at 0.614$\mu$ for $Eu^5Do$), of Tb (at 0.544$\mu$ for $Tb^5D_4$), of Dy (at 0.574$\mu$ for $Dy^4F_{9/2}$) and of Er (at 0.552$\mu$ for $Er^4S_{3/2}$) was obtained under ~0.365$\mu$ excitation as provided by a CH4 spotlamp and CS7-54 longwave uv pass filter. The intensity of emission of Er (at 1.56$\mu$ for $Er^4/I_{13/2}$) or Nd (at 1.06$\mu$ for $Nd^4F_{3/2}$) was obtained under 0.43-0.62$\mu$ excitation isolated from the CH4 lamp by a CS3-72 cut-off filter and a $CuSO_4$ solution before the sample. A Gaertner high dispersion spectrometer equipped with an AMINCO microphotometer and S11 detector were employed to record data for the visible region. A Bausch and Lombe No. 33-86-03 monochromator, with a CS7-56 filter at the input, and S1 detector at the output, was used to record data at 1.06$\mu$; and a Bausch and Lombe No. 33-86-04 monochromator, with a CS7-56 filter at the input, and a InAs detector at the output, was used to record data at 1.56$\mu$.

Lifetime data were obtained employing a confocal ellipse laser housing with an EG&G FX12 flashlamp at one focus and the sample at the other. One side of the ellipse was slotted so that the output of the sample could be viewed. A Bausch and Lombe No. 33-86-02, -03 or -04 monochromator equipped with an S1, cooled S11 (~217°K), or cooled InAs (~77°K) detector and oscilloscope were used to obtain photographic recordings of the decay curves. A CS-7-54 filter was placed between the flashlamp and sample when obtaining data in the visible region. A CS-3-72 filter was placed between the lamp and sample in measuring at 1.06$\mu$, but none was used in obtaining data at 1.56$\mu$ A CS-7-56 filter was placed in front of the monochromator for all infrared measurements.

### *Intensity and Lifetime*

The emission spectra of RE ions change little with concentration provided that increasing substitution does not appreciably change the effective crystal field seen by the RE ions. This condition is satisfied when substituting RE ions for others of equivalent radius and valence in the sodium rare earth tungstates.

The probability for de-excitation of the E-species ($P_3$) is equal to the sum of the probabilities for emission ($P_1$) and nonradiative loss ($P_2$). Therefore emission per E-ion ($I$) relative to that obtained under dilute conditions ($I_o$) is

$$I/I_o = P_1/P_3 = P_1/(P_1 + P_2) \qquad [1]$$

If the nonradiative losses are attributable to multipolar transfer, $P_2 \propto (C/C^*)^{\theta/3}$ where $C$ is the Q-ion concentration, $C^*$ is the critical transfer concentration of Q-ions and $\theta$ = 6, 8, or 10 for dipole-dipole, dipole-quadrupole, or quadrupole-quadrupole interactions, respectively (3-6). Substituting into relation [1] and rearranging, one obtains

$$I/I_o = [1 + \beta(C/C^*)^{\theta/3}]^{-1} \qquad [2]$$

where $\beta$ is a constant for each interaction.

Lifetime measurements are obtained under transient conditions and can involve various modes of decay that complicate their interpretation. When there is no interaction between RE ions, the emission decay curve is a single exponential. Lifetime can then be

taken to be the time ($t$) required for the transient intensity ($\Phi$) to fall to $1/e$ (or 0.368) of the value it has at $t = 0$. This relation defines $\tau_e$. If direct multipolar interactions quench the E-species, the decay curve is much more complex. $\tau_e/\tau_o$, where $\tau_o$ is the value of $\tau_e$ under dilute conditions, cannot then be substituted directly for $I/I_o$ in relation [2]. However, this relation can be employed to define an arbitrary lifetime $\tau_a$

$$\tau_a/\tau_o = [1 + \beta'(C/C^*)^{\theta/3}]^{-1} \qquad [3]$$

The relation of $\tau_e$ to $\tau_a$ and the procedure for determining a lifetime ($\tau_i$) which approximates $\tau_a$ from the initial or early slope of the decay curve is discussed in the Appendix. Properly selected values of $\tau_i$ correlate with $I$ and are therefore helpful in characterizing energy transfer interactions.

*Interactions*

Exchange is generally limited to interactions between RE ions in nearest neighbor (nn) or next nearest neighbor (nnn) dodecahedral sites in the scheelites. Six such interactions are permissible (8). Therefore, the fraction of RE ions which, in any event are little affected by exchange is $(1 - x)^6$, where $x$ is the fraction of dodecahedral sites occupied by RE ions. Where RE ions that are exchange coupled (but no others) are quenched, intensity of emission per ion ($I$) will follow this relation and a peak in total emission will be obtained at $\sim x = 0.14$. When direct multipolar interactions are involved, quenching is generally more extensive and relations [2] and [3] tend to be obeyed (8-14). Quenching is even greater when excitation migrates over the E-ion set. If migration is rapid compared to direct transfer, quenching tends to be proportional to Q-ion concentration ($\theta = 3$), since transfer to Q-ions from close lying E-ions becomes the rate limiting step (8-14). Lifetime tends to be a single exponential, but decreases rapidly with Q-ion concentration under these conditions. If radiation reabsorption, self-quenching, or internal relaxation is strong, the foregoing intensity and/or lifetime relations can be altered significantly. Examples are cited under results.

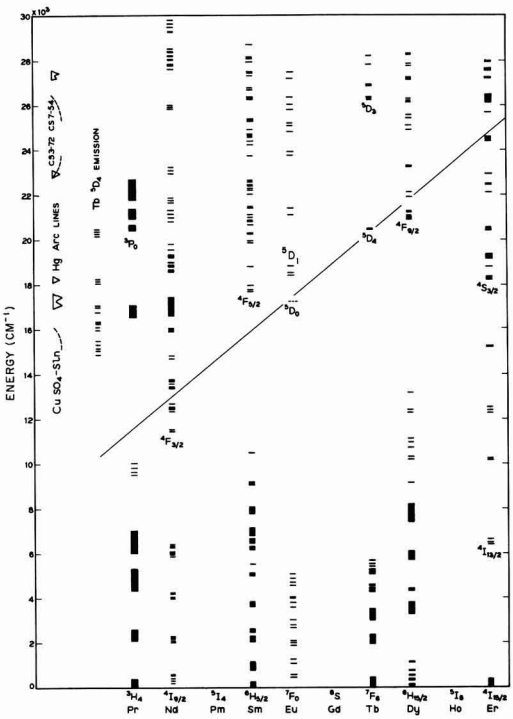


Fig. 1. Energy levels of rare earth ions. Positions on energy of the radiation peaks from the mercury arc source, of emission lines of Tb from $Tb^5D_4$, and of the cut-off frequencies for the CS7-54, CS3-72, and $CuSO_4$ solution filters are also indicated. The diagonal line is a somewhat arbitrary demarcation between manifolds which have been observed to participate in dipole-quadrupole interactions (upper part) and those for which only dipole-dipole interactions have been observed.

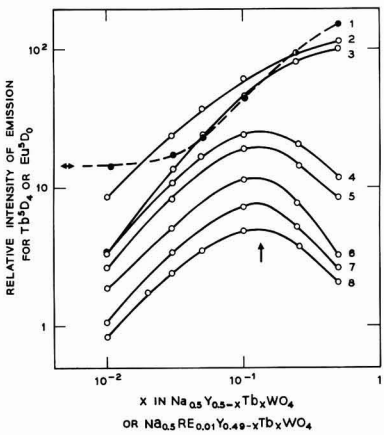


Fig. 2. Relative intensity of emission of Tb from $Tb^5D_4$ (O) at 295°K *vs.* Tb concentration for the following series: curve 3, $Na_{0.5}Y_{0.5-x}Tb_xWO_4$; curves 2, 4, 5, 6, 7, and 8, $Na_{0.5}RE_{0.01}Y_{0.49-x}Tb_xWO_4$ where RE = Dy, Eu, Pr, Sm, Nd, and Er respectively. Curve 1 represents emission from $Eu^5D_0$ (●) for series 4. The reference mark (↔) indicates the intensity of emission for Eu in $Na_{0.5}Eu_{0.01}Y_{0.49}WO_4$.

## Results

The positions in energy of significant excited states of Pr, Nd, Sm, Eu, Tb, Dy, and Er in the tungstates are shown in Fig. 1. The energies of the spectral lines for emission from $Tb^5D_4$ and for emission from the CH4 Hg arc lamp and the cut-off frequencies of the CS7-54, CS3-72, and $CuSO_4$ solution filters employed are also indicated. The diagonal line represents a somewhat arbitrary demarcation between states that have been observed to participate in dipole-quadrupole ($\theta = 8$) interactions (upper part) and those for which only dipole-dipole ($\theta = 6$) interactions have been observed (see Discussion). The manifold designations are those given by Dieke for chlorides (15).

Intensity of emission from $Tb^5D_4$ at 295°K under $0.365\mu$ excitation is shown *vs.* Tb concentration in various series in Fig. 2. All of the Tb intensity data is relative to 100 for $Na_{0.5}Tb_{0.5}WO_4$. Curve 3 is for the series $Na_{0.5}Y_{0.5-x}Tb_xWO_4$ and curves 2, 4, 5, 6, 7, or 8 are for the series $Na_{0.5}RE_{0.01}Y_{0.49-x}Tb_xWO_4$ where RE equals Dy, Eu, Pr, Sm, Nd, or Er, respectively. Dy transfers excitation from $Dy^4F_{9/2}$ (20,900 $cm^{-1}$) to $Tb^5D_4$ (20,500 $cm^{-1}$) and has little quenching effect on $Tb^5D_4$ for the indicated Dy concentration. This is shown by curve 2 lying above curve 3. Eu, Pr, Sm, Nd, and Er, however, increasingly quench $Tb^5D_4$ in the given order. If only direct Tb to Q-ion multipolar interactions occurred, curves 4-8 would all be parallel to curve 3 as the average distance from Tb to Q-ion is not dependent on Tb concentration. In general, the strengths of the multipolar interactions responsible increase with the overlap of Tb emission and RE absorption. However, discrepancies do occur (2, 12).

At high Tb concentrations, excitation may migrate from remote Tb ions to those that are close to Q-ions and thereby enhance the probability for transfer to the latter. This effect accounts for the increased displacement of curves 4-8 from curve 3 at high Tb concentrations. Although Eu, Pr, Sm, Nd, and Er are quite different in quenching power, curves 4-8 all peak at

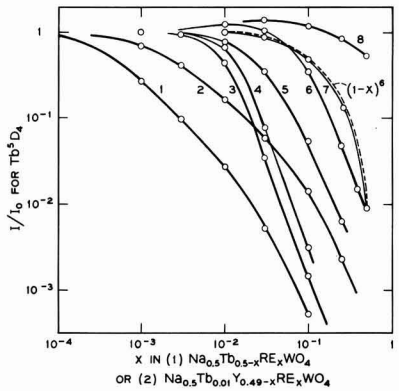


Fig. 3. Normalized emission *per* Tb ($I/I_o$) for emission from $Tb^5D_4$ *vs.* RE concentration for the series 1 $Na_{0.5}Tb_{0.5-x}RE_xWO_4$ and 2 $Na_{0.5}Tb_{0.01}Y_{0.49-x}RE_xWO_4$ where RE = Nd, Eu, or Dy. Curves 1 and 4 are for series 1 Nd at 295°K and 4.2°K, respectively. Curve 3 is for series 2 Nd at 295°K. Curves 2 and 5 are for series 1 Eu and series 2 Eu, respectively, at 295°K. Curve 7 represents both series 1 Eu and series 2 Eu at 4.2°K. The data for both of the latter series fit the relation $(1-x)^6$. Curve 6 represents both series 1 Dy and series 2 Dy at 295°K, and curve 8 represents the comparable data for Dy at 77°K (or 4.2°K).

$x \simeq 0.14$ indicating that the migration is dominated by exchange (8-13). That is, energy may move between $Tb^5D_4$ manifolds only when the Tb-ions are in nearest or next nearest neighbor dodecahedral sites in the tungstates and therefore the chances for such excitation migration depends directly on Tb concentration. When Eu is the Q-species, the excitation lost to Eu by Tb appears as emission from $Eu^5D_o$ (16). The effect on Eu emission is indicated by curve 1 of Fig. 2. Since multipolar transfer from Tb to $Eu_{0.01}$ is rather weak, the large increase in Eu emission at high Tb concentrations is almost entirely due to enhanced transfer due to migration between exchange coupled Tb ions.

$I/I_o$ for emission *per* Tb from $Tb^5D_4$ under 0.365$\mu$ excitation is shown *vs.* RE concentration in Fig. 3 for the series 1 $Na_{0.5}Tb_{0.5-x}RE_xWO_4$ and 2 $Na_{0.5}Tb_{0.01}Y_{0.49-x}RE_xWO_4$ where RE = Nd, Eu, or Dy. Curves 1 and 4 are for series 1 where RE = Nd, 1 Nd, at 295°K and 4.2°K, respectively. Curve 3 is for series 2 Nd at 295°K, curves 2 and 5 are for series 1 Eu and series 2 Eu, respectively, at 295°K while curve 7 which fits the relation $(1-x)^6$, represents both series 1 Eu and series 2 Eu at 4.2°K. Curve 6 represents both series 1 Dy and series 2 Dy at 295°K, and curve 8 represents the comparable data for series 1 Dy and series 2 Dy at 77°K (or 4.2°K). The curves for RE = Nd, Eu, and Dy have been selected as representative of three different energy relations between the E- and Q-ions. For the first Q-species (Nd), there is an exact match between an emission transition of Tb and an absorption transition of Nd originating from the ground state. Therefore transfer from Tb to Nd is not dependent on temperature. The data of curve 3, for series 2 Nd, is fitted by a $\theta = 8$ relation showing that the transfer from Tb to Nd is dipole-quadrupole in character. Curve 1, for series 1 Nd at 295°K shows the additional quenching due to excitation migration between Tb ions in nn or nnn sites (2,12). This migration no longer occurs at 4.2°K as shown by the near coincidence of curves 3 and 4 of Fig. 3.

For the second Q-species (Eu), Tb emission overlaps Eu absorption at 295°K but not at 4.2°K. However, transfer can occur at the lower temperature through simultaneous interaction with the phonon spectrum. The data of curve 5 of Fig. 3, for series 2 Eu, is fitted by a $\theta = 6$ relation indicating that transfer from Tb to Eu is by dipole-dipole interactions at 295°K. Curve 2, for series 1 Eu, shows that excitation migration between Tb-ions is also prevalent at 295°K when Eu is the Q-ion species. At 4.2°K, however, the data for both series 1 Eu and series 2 Eu lie along curve 7 of Fig. 3. This curve follows the relation $(1-x)^6$, indicating that at 4.2°K transfer from Tb to Eu only occurs when these ions are in nn or nnn positions (9).

Dy, the third Q-ion, only acts as a quenching center for $Tb^5D_4$ when quenched itself. The receiving manifold ($Dy^4F_{9/2}$) lies ~400 $cm^{-1}$ above $Tb^5D_4$ (see Fig. 1). Emission from $Tb^5D_4$ to the ground state, the highest emission line in Fig. 1, can match an absorption transition to $Dy^4F_{9/2}$ when Dy (400 $cm^{-1}$) is thermally populated. This occurs at 295°K but not at 77°K. At low Dy concentrations, transfer is predominantly from $Dy^4F_{9/2}$ to $Tb^5D_4$, as indicated in connection with Fig. 2. However, at high Dy concentrations, where Dy is strongly self-quenched, the reverse transfer can be important. Lifetime data show that transfer from $Tb^5D_4$ to $Dy^4F_{9/2}$ is by dipole-dipole ($\theta = 6$) interactions (10). Curve 6, however, is altered by transfer from Dy to Tb for low Dy concentrations. The extent of this transfer is apparent from curve 8, which represents the data for series 1 Dy and series 2 Dy at 77°K where transfer from Tb to Dy is negligible. It is apparent that $I/I_o$ is not dependent on Tb concentration when Dy is the Q-species, even at 295°K.

$I/I_o$ for emission *per* E-ion is shown *vs.* concentration for self-quenching of $Dy^4F_{9/2}$, $Er^4S_{3/2}$, $Sm^4F_{5/2}$, $Nd^4F_{3/2}$, $Pr^3P_o$, and $Tb^5D_3$ by curves 1-6 of Fig. 4A, respectively (8-14). Similar curves for the quenching of $Tb^5D_4$ by multipolar interactions with Er, Sm, Pr, Nd, Eu, and Dy in the series $Na_{0.5}Tb_{0.1}Y_{0.4-x}RE_xWO_4$ are shown by curves 7-12 of Fig. 4B, respectively. Curve 12′ fits the data of curve 12 when the latter are corrected for Dy to Tb transfer (10). The data for curves 1, 2, 4, 7, 11, and 12′ are fitted by $\theta = 6$ relations indicating that the corresponding interactions are dipole-dipole in character. The data for the remaining curves are fitted by $\theta = 8$ relations, indicating that dipole-quadrupole interactions are responsible for transfer in these instances. Curve 2 deviates from a $\theta = 6$ relation toward $\theta = 8$ at high Er concentrations. This is attributable to the combined effects of radiation reabsorption and rapid internal relaxation (13).

Examples of the relation of $\tau_i/\tau_o$ to $I/I_o$ for emission per E-ion are given in Fig. 5. Curves 1 and 2 represent $\tau_i/\tau_o$ and $I/I_o$, respectively, for emission from $Tb^5D_4$ in the series (*a*) $Na_{0.5}Tb_{0.1}Y_{0.4-x}Nd_xWO_4$ (for $Tb^5D_4$, $\tau_o$ = 565 $\mu$sec). Curves 3 and 4 represent $I/I_o$ and $\tau_i/\tau_o$, respectively, for emission from $Tb^5D_4$ in the series (*b*) $Na_{0.5}Tb_{0.1}Y_{0.4-x}Eu_xWO_4$ and curves 5 and 6

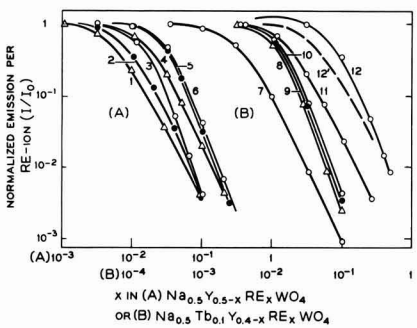


Fig. 4.(A) Normalized emission per E-ion ($I/I_o$) *vs.* E-ion concentration in series (A) $Na_{0.5}Y_{0.5-x}RE_xWO_4$. Emission is from $Dy^4F_{9/2}$, $Er^4S_{3/2}$, $Sm^4F_{5/2}$, $Nd^4F_{3/2}$, $Pr^3Po$, or $Tb^5D_3$ for curves 1-6, respectively. *(B)* Normalized emission *per* Tb ($I/I_o$) for emission from $Tb^5D_4$ *vs.* RE concentration for the series *(B)* $Na_{0.5}Tb_{0.1}Y_{0.4-x}RE_xWO_4$ where RE — Er, Sm, Pr, Nd, Eu, or Dy for curves 7-12, respectively.

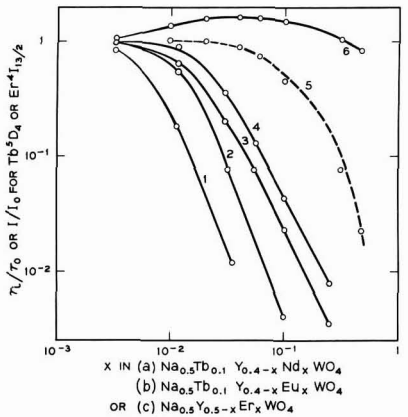


**Fig. 5. Normalized initial lifetime ($\tau_i/\tau_o$) or normalized emission per E-ion ($I/I_o$) for emission from $Tb^5D_4$ or $Er^4I_{13/2}$ vs. Nd, Eu, or Er concentration. Curves 1 and 2 represent $\tau_i/\tau_o$ and $I/I_o$, respectively, for Tb emission from series (a). Curves 3 and 4 represent $I/I_o$ and $\tau_i/\tau_o$ respectively for Tb emission from series (b) and curve 6 and the data following curve 5 are for $\tau_i/\tau_o$ and $I/I_o$ respectively for Er emission from series (c). Curve 5 is the relation $(1-x)^6$.**

approximate $I/I_0$ and $\tau_i/\tau_o$, respectively, for emission from $Er^4I_{13/2}$ in the series (c) $Na_{0.5}Y_{0.5-x}Er_xWO_4$. All data are for 295°K. Moderately high Tb concentrations were employed for series (*a*) and (*b*) to insure fast internal relaxation to $Tb^5D_4$ (11, 12, 17). Further, radiation reabsorption by $Tb^5D_4$ is minimal since less than 10% of the emission from $Tb^5D_4$ is to the ground state. Hence, the relations between $\tau_i/\tau_o$ and $I/I_o$ for these series [(*a*) and (*b*)] are relatively uncomplicated. It can be observed that $\tau_i/\tau_o$ falls outside $I/I_o$ for series (b), which follows a $\theta = 6$ relation, and inside $I/I_o$ for series (*a*), which follows a $\theta = 8$ relation.

All of the strong emission transitions of Er appear to be to the ground manifold. Further, the drain time from higher lying manifolds to $Er^4I_{13/2}$ is small compared to the lifetime of the latter (~4,500 μsec) (13). Hence, the prolonged lifetimes where $\tau_i/\tau_o > 1$, indicated by curve 6 of Fig. 5, for intermediate values of Er in series (c), can be attributed to radiation reabsorption. The $I/I_o$ data for series (c) follows the $(1-x)^6$ relation indicated by the broken line (curve 5). *This indicates that quenching is associated with* interactions between Er ions in nn or nnn positions. The quenching may involve nonradiative excitation migration between exchange coupled Er-ions to Q-ions present as impurities or it may be due to pairing enhancing interaction with the phonon spectrum. In either case, radiation absorbed by the paired Er-ions is not emitted and therefore beyond $\sim Er_{0.1}$, the chances for absorption and re-emission of resonance radiation decreases with increasing Er concentration, resulting in a decline in $\tau_i/\tau_o$ back to ~1.0.

## Discussion

The lifetime $\tau_a$ defined by relation [3] can be approximated by measuring $\tau_i$ from the initial or early slope of the decay curve for emission, as outlined in the Appendix. $\tau_i/\tau_o$ has the same dependence on $C/C^*$ as the corresponding equilibrium intensity measurement $I/I_o$. However, *for multipolar interactions* where other things are equal $\tau_i/\tau_o$ lies at decreasing values of $C/C^*$ relative to the comparable $I/I_o$ curve as $\theta$ increases (see Fig. 5). This displacement is consistent with the fact that, when quenching is strong, the fraction of the total emission yielded up to $t = \tau_e$ (or $\tau_i$) changes from 0.28 to 0.10 to 0.045 on changing from a $\theta = 6$ to 8 to 10 mechanism. Quadrupole effects tend to shift $\tau_i/\tau_o$ to the inside of the comparable $I/I_o$ curve while prolonged drain time to the emitting manifold or radiation reabsorption by this manifold have the opposite effect.

Multipolar interactions generally increase with the overlap of E-ion emission and Q-ion absorption. However, when the overlap is small, processes involving the simultaneous release of energy to the phonon spectrum become competitive. Single phonon processes, for energies up to that of the fundamental stretching frequency (~850 $cm^{-1}$ in the tungstates), do not appear to have drastically reduced probabilities for transfer (12, 13). Further, these and more complex interactions can be facilitated by the mixing effects of exchange.

As shown in Fig. 1, the positions in energy of $Eu^5D_1$ and $Eu^5D_0$ and the emission lines originating from $Tb^5D_4$ are mismatched by ~100 $cm^{-1}$, with the closest emission lines lying below the Eu levels. The closest to a match for a Tb emission line that lies higher in energy than a Eu level ($Eu^5D_0$) is out by ~900 $cm^{-1}$. At 295°K, however, $Eu^7F_1$ (~500 $cm^{-1}$) is populated from $Eu^7F_0$, permitting a match of the Tb emission line at ~16,800 $cm^{-1}$ to the Eu absorption transition $Eu^5D_0$ (17,300 $cm^{-1}$) ← $Eu^7F_1$ (~500 $cm^{-1}$). As a result, multipolar transfer takes place at this temperature (curve 5 of Fig. 3). However, at 4.2°K, $Eu^7F_1$ is not populated, and transfer requires the release of ~900 $cm^{-1}$ *to the phonon spectrum.* $I/I_o$ *follows the* relation $(1-x)^6$ under these circumstances, indicating that the mixing effects of exchange facilitate transfer from Tb to Eu (curve 7 of Fig. 3).

Excitation migration between Tb-ions in nn or nnn positions at 295°K is evident for series 1 Nd and series 1 Eu (curves 1 and 2 of Fig. 3, respectively) but not for series 1 Dy (curve 6 of Fig. 3). Nd and Eu can act as quenching centers as single Q-ions while Dy only does so when it, itself, is quenched. However, as Dy is self-quenched at intermediate concentrations (see curve 1 of Fig. 4) and, therefore, dissipates excitation received from $Tb^5D_4$ by multipolar transfer, it is evident that excitation migration does not occur, even at 295°K, unless a sink that acts directly is present. In contrast to the essentially random movement of excitation by emission and reabsorption, this implies that migration by nonradiative interactions can be directed toward the Q-ion promoting the transfer.

It is apparent from Fig. 4 that both $\theta = 6$ and $\theta = 8$ relations are observed for interactions between RE-ions in the scheelite structure. The manifolds $Pr^3P_0$, $Sm^4F_{5/2}$, $Tb^5D_3$ and $Tb^5D_4$ have been found to participate in dipole-quadrupole interactions. These lie above the diagonal in Fig. 1. The manifolds $Nd^4F_{3/2}$, $Eu^5D_0$, $Dy^4F_{9/2}$, and $Er^4S_{3/2}$ lie below the diagonal. So far the latter have only been found to participate in dipole-dipole transfers. Such interactions may be typical for smaller RE-ions and for the lower lying levels of the larger RE-ions. Dipole-quadrupole interactions seems more likely for the higher lying levels of the larger RE-ions. There seems to be an increased probability for quadrupole interactions when the states involved are strongly perturbed. Perturbation increases with the tightness of the fit of the rare earth into the site it occupies and with the proximity of the manifold involved to the continuum.

## Acknowledgments

The author is indebted to J. E. Geusic and R. N. Thurston for helpful discussions.

## APPENDIX

### *Analysis of Lifetime Data*

The intrinsic lifetime for fluorescence ($\tau_o$) of an excited E-ion state is equal to the time ($\tau_e$) required for the transient intensity of emission ($\Phi$) to decay to $1/e$ (or 0.368) of its initial value when there is no interaction between E-ions or with Q-ions by radiative or nonradiative means. When conditions are ideal, Ln $\Phi$ is linear with time ($t$). However, if multipolar transfer occurs $\tau_e$ will be less than $\tau_o$ and, if emission, corresponding to transitions to the ground manifold of

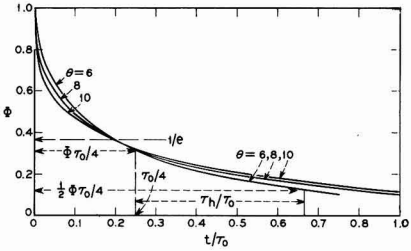


**Fig. 6. Transient intensity ($\Phi$) vs. normalized time ($t/\tau_o$) for relation [5] when $C = C^*$ and $\theta$ is the value indicated. Markings relevant to determining $\tau_h/\tau_o$ are also present.**

the E-ion, is reabsorbed $\tau_e$ will tend to be greater than $\tau_o$.

The probability for de-excitation of the E-species ($P_3$) is equal to the sum of the probability for emission ($P_1$) and the probability for nonradiative transfer ($P_2$)

$$P_3 = P_1 + P_2 \qquad [4]$$

$P_1$ is inversely related to $\tau_o$ (or $P_1 \propto 1/\tau_o$); $P_2 \propto (C/C^*)^{\theta/3}$ as indicated previously; and $P_3$ is inversely related to $\tau_a$, the representative lifetime when both radiative and nonradiative de-excitation occurs. Substituting for $P_1$, $P_2$, and $P_3$ in relation [4] and rearranging, one obtains relation [3] which has the same form as that for intensity, relation [2]. $\theta$ and $\beta/C^*$ can be determined from relation [2]. $\theta$ can also be determined from relation [3] provided one measures the proper lifetime, *i.e.*, $\tau_a$.

$\theta$ and an independent value for $C^*$ can be obtained by fitting accurately measured decay curves to the theoretical expression for decay given by Inokuti and Hirayama (6).

$$\Phi(t) = \exp\left[-t/\tau_o - \Gamma(1 - 3/\theta)\,(C/C^*)\,(t/\tau_o)^{3/\theta}\right] \qquad [5]$$

However, for most materials such a procedure would require greater measurement accuracy than can generally be relied on. $\Phi$ for relation [5] is plotted *vs.* $t/\tau_o$ in Fig. 6 for $C = C^*$ and $\theta = 6$, 8, or 10. The value of $\Gamma(1 - 3/\theta)$ is 1.77, 1.43, and 1.30, respectively, for these curves. The markings relating to $\tau_o/4$ and $\tau_h$ are discussed below. It can be seen that relatively small errors in measuring $\Phi$ can seriously affect one's ability to determine the correct value of $\theta$. It is easier to determine $\theta$ from the concentration dependence of intensity by relation [2] or from the concentration dependence of lifetime by relations 3 or 5.

The dependence of $\tau_e/\tau_o$ on $C/C^*$ for $\theta = 6$, 8, or 10 is shown in Fig. 7 by set (A) curves 1, 2, and 3, respectively. The comparable relations for $\tau_a/\tau_o$ (or $I/I_o$ are shown by set (B), curves 4, 5, and 6, respectively. Curves 1, 2, and 3 were obtained from relation [5] by setting $\mathrm{Ln}\Phi = -1$.

$$\mathrm{Ln}\Phi = -1 = -t/\tau_o - \Gamma(1 - 3/\theta)\,(C/C^*)\,(t/\tau_o)^{3/\theta} \qquad [6]$$

while curves 4, 5, and 6 were obtained from relation

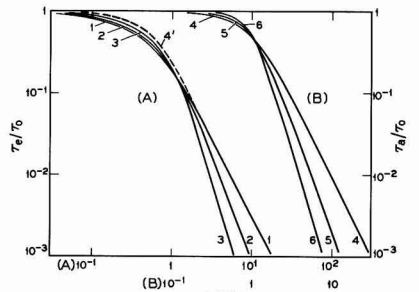


**Fig. 7. Normalized values of lifetime ($\tau_e/\tau_o$ or $\tau_a/\tau_o$) vs. $C/C^*$ calculated from relations [6] or [3], respectively. Curves 1, 2, and 3 are for $\tau_e/\tau_o$ for $\theta = 6$, 8, or 10, respectively, and curves 4, 5, and 6 are for $\tau_a/\tau_o$ for $\theta = 6$, 8, or 10, respectively, when $\beta' = 1.0$. Curve 4′ is obtained from relation (7). Normalized intensity $I/I_o$ follows the $\tau_a/\tau_o$ relation.**

[3] by setting $\beta' = 1$. Curve 4′ is curve 4 brought into coincidence with curve 1 (for $C > C^*$) by assigning $\beta' = 3.2$

$$\tau_a/\tau_o = [1 + 3.2(C/C^*)^2]^{-1} \qquad [7]$$

Curve 1, for $\tau_e/\tau_o$ when $\theta = 6$, deviates up to 30% from curve 4′, $\tau_a/\tau_o$ for $\theta = 6$, over the first order of magnitude of quenching. However, for $C > C^*$, the slope of the curve for either $\tau_a/\tau_o$ or $\tau_e/\tau_o$, from relation [3] or relation [5], respectively, is about equal to $\theta$. For the first order of magnitude of quenching $\tau_e/\tau_o$ can be corrected to $\tau_a/\tau_o$ by comparing the above curves. For stronger quenching, where discrimination between $\theta$ values is much clearer, $\tau_e$ can be employed as a measure of $\tau_a$. However, $\tau_e$ is difficult to determine directly in this region. Therefore, if intensity measurements are impractical, other methods for obtaining lifetime data at high Q-ion concentrations should be considered.

It can be seen from relation [6] that when $t < \tau_o$ and $C > C^*$ the second term of the exponent is dominant and the first can be ignored. Under these circumstances, if $\theta$ is fixed the decay curves for various $C/C^*$ ratios can be reduced to a single representative curve by multiplying the values along the $t/\tau_o$ coordinate (see Fig. 6) by $(C/C^*)^{\theta/3}$. Such relations are shown by curves 4, 5, and 6 of Fig. 8.

Figure 8 has been constructed by plotting $\Phi$ from relation [5], on a logarithmic scale *vs.* $n(t/\tau_o)$, on a linear scale, where $n$ is the scaling factor required to position $\Phi = 0.1$ at $n(t/\tau_o) = 1.0$. The parameter $n(t/\tau_o)$ is only used to graph the theoretical decay curves. In practice, the abscissa is $t$ alone on a scale that suitably displays curve symmetry. Curve 1 is the exponential relation for $C/C^* = 0$. Curve 2 is for $C = 0.28C^*$ and $\theta = 6$, curve 3 is for $C = C^*$, and $\theta = 6$ and curves 4, 5, and 6 are representative for Q-ion concentrations where $C > 2C^*$ when $\theta = 6$, 8, or 10, respectively.

Lifetime calculated from the tangent (1, 2′-5′ or 6′) to the respective curve as drawn is equal in value to $\tau_a$. This value also equals $\tau_e$ for 1, 4′, 5′, and 6′. It is 25% larger than $\tau_e$ for 2′ and 20% larger than $\tau_e$ for 3′. In practice, for the first factor of 5 of quenching, $\tau_a$ can be estimated from $\tau_e$ by adding the correction indicated by superimposing the calculated relations between $\tau_e/\tau_o$ and $\tau_a/\tau_o$. The corrections required are essentially independent of $\theta$ as $\tau_a/\tau_o$ varies in the same manner as $\tau_e/\tau_o$ with $\theta$ (see Fig. 7). However, if there is some question as to the value of $\Phi$ at $t = 0$, the decay curve can be plotted as in Fig. 8 and $\tau_a$ inferred from the proper tangent. For weak interactions (curves 1 and 2) the tangent required to obtain $\tau_a$ averages the points of the curve lying between 10 and

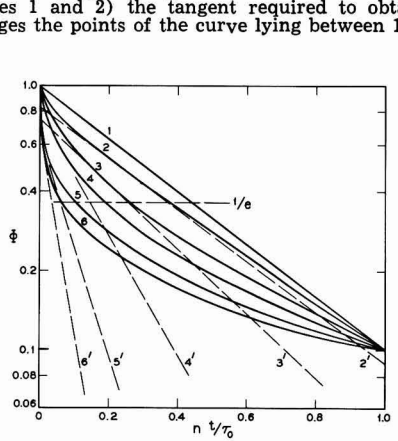


**Fig. 8. Transient intensity ($\Phi$) from relation [5] vs. adjusted time, $n(t/\tau_o)$, where $n$ is the scaling factor required to position $\Phi = 0.1$ at $n(t/\tau_o) = 1.0$. Curve 1 is for $C/C^* = 0$; curve 2 is for $C = 0.28C^*$, $\theta = 6$; curve 3 is for $C = C^*$, $\theta = 6$; and curves 4, 5, and 6 are characteristic for $C > 2C^*$ for $\theta = 6$, 8, or 10, respectively. The tangents 2′-6′ are drawn to indicate the correct value of $\tau_a$. As an aid to reading the theoretical curves, it is noted that for the intercept of $\Phi$ with, i.e., $\tau_e/\tau_o = (1/n)[n(t/\tau_o)$ for the intercept] and for the tangents $\tau_a/\tau_o = [1/(2.3n)]n(t/\tau_o)_{10}$, where $n(t/\tau_o)_{10}$ is the time period elapsed for a tenfold decrease for the coordinate of the tangent along $\Phi$.**

30% of the way along the time coordinate to $\Phi = 0.1$. When quenching is by a factor greater than 5 (*i.e.*, $\tau_e/\tau_o < 0.2$ or $C > C^*$), $\Phi$ at $t = 0$ is generally so obscured by the excitation flash, or in some instances by the rise in $\Phi$ on excitation being prolonged by a finite drain time from higher lying states, that it is difficult to estimate its value accurately. Under these circumstances, the tangent to the initial measurable slope of the decay curve provides a good estimate of $\tau_e$ or $\tau_a$ as long as the lifetime for emission exceeds the decay time of the flash lamp. The symmetry of the appropriate curve of Fig. 8 should be kept in mind when choosing the tangent or otherwise estimating lifetime. The tangents shown in Fig. 8 indicate the slopes to measure to obtain $\tau_a$ in each case. The lifetime derived in this way from the early or initial slope of the decay curve, or by correcting $\tau_e$, is termed $\tau_i$ and is the estimate of $\tau_a$ obtained by observing the foregoing procedures.

### *Other Measures of* $\tau$

As shown in Fig. 7 there is less than 5% difference in $\tau_e/\tau_o$ for $\theta = 8$ and either the neighboring curve for $\theta = 6$ or for $\theta = 10$ over the first order of magnitude of quenching. Obviously it is difficult to characterize transfer interactions from such data alone. Further, even if $\tau_e$ or a comparable defined lifetime is accurately measured the results would be deceiving unless they were properly analyzed. For example $\tau_e$ values employed in place of $\tau_a$ values in relation [3] may indicate the wrong value of $\theta$. As can be seen from Fig. 7, $\tau_e/\tau_o$ for $\theta = 10$, indeed, lies closer to $\tau_a/\tau_o$ for $\theta = 6$ than does $\tau_e/\tau_o$ for $\theta = 6$ itself over the first order of magnitude of quenching.

Nakazawa and Shionoya employ a lifetime ($\tau_h$) which is defined as the time ($t$) required for $\Phi$ to fall from its value at $\tau_o/4$ to one-half of that value, as illustrated for the $\theta = 6$ curve of Fig. 6 (18). This definition effectively limits measurement to the first order of magnitude of quenching. $\tau_h/\tau_o$ bears a relation to $I/I_o$ that is susceptible to analysis. However, the shape of the curve follows a $\theta = 3$ relation regardless of the actual mechanism of quenching. These results are quite similar to those obtained by taking lifetime from the tangent to the decay curve (Ln $\Phi$ *vs.* $t$) at a fixed value of $t$. As can be seen from relation [5], $\theta$ appears in the exponent of $t/\tau_o$ not $C/C^*$; hence, the curves obtained by plotting such data *vs.* $C/C^*$ only change in displacement along the latter coordinate as $\theta$ changes.

Unfortunately, most of the literature concerning lifetime measurements connected with transfer interactions is not clear as to the actual procedure for analyzing data. It is therefore not easy to draw significant conclusions concerning the mechanism of energy transfer involved from such lifetime data alone.

Manuscript received May 1, 1967; revised manuscript received June 23, 1967. This paper was presented at the Dallas Meeting, May 7-12, 1967.

Any discussion of this paper will appear in a Discussion Section to be published in the June 1968 JOURNAL.

## REFERENCES

1. F. J. Botden, *Philips Res. Rept.*, **6**, 425 (1951); **7**, 197 (1952).
2. L. G. Van Uitert and L. F. Johnson, *J. Chem. Phys.*, **44**, 3514 (1966).
3. D. L. Dexter, *ibid.*, **21**, 836 (1953).
4. D. L. Dexter and J. H. Schulman, *ibid.*, **22**, 1063 (1954).
5. D. L. Dexter, *Phys. Rev.*, **26**, 1962 (1962).
6. M. Inokuti and F. Hirayama, *J. Chem. Phys.*, **43**, 1978 (1965).
7. L. G. Van Uitert and R. R. Soden, *J. Appl. Phys.*, **31**, 328 (1960).
8. L. G. Van Uitert, E. F. Dearborn, and J. J. Rubin, *J. Chem. Phys.*, **45**, 1578 (1966).
9. L. G. Van Uitert, E. F. Dearborn, and H. M. Marcos, *Appl. Phys. Letters*, **9**, 255 (1966).
10. L. G. Van Uitert, E. F. Dearborn, and J. J. Rubin, *J. Chem. Phys.*, **46**, 3551 (1967).
11. L. G. Van Uitert, E. F. Dearborn, and J. J. Rubin, *J. Chem. Phys.*, In press.
12. L. G. Van Uitert, E. F. Dearborn, and J. J. Rubin, *J. Chem. Phys.*, **47**, 547 (1967).
13. L. G. Van Uitert, E. F. Dearborn, and J. J. Rubin, *J. Chem. Phys.*, In press.
14. L. G. Van Uitert, E. F. Dearborn, and J. J. Rubin, *J. Chem. Phys.*, **46**, 420 (1967).
15. G. H. Dieke, in "Advances in Quantum Electronics," J. A. Singer, Editor, p. 164, Columbia University Press, New York (1961).
16. L. G. Van Uitert and R. R. Soden, *J. Chem. Phys.*, **36**, 1289 (1962).
17. L. G. Van Uitert and R. R. Soden, *ibid.*, **32**, 1161 (1960).
18. E. Nakazawa and S. Shionoya, Preprints 9/70 International Conference on Luminescence, Budapest 1966.

# Photovoltaic Behavior of the TCNE-THF Solution Charge-Transfer Complex

**P. J. Reucroft, P. L. Kronick, and E. E. Hillman**

*Chemistry Department, The Franklin Institute Research Laboratories, Philadelphia, Pennsylvania*

ABSTRACT

Reversible photoinduced electron transfer in solutions of tetracyanoethylene (TCNE) in tetrahydrofuran (THF) has been shown to lead to a voltaic effect. The photovoltage spectral response peaks at the absorption edge of the charge-transfer band, demonstrating that light capable of promoting charge-transfer must penetrate to the vicinity of the electrode. Maximum power output recorded is in the region of $10^{-10}$ watts for monochromatic light input intensity of $10^{-3}$ w/cm$^2$. A sublinear dependence of photovoltage on light intensity suggests a mechanism of photovoltage production whereby photogenerated ionic species distribute to give concentration gradients, or alternatively a process involving the preferential adsorption of the negative ion species.

The production of photovoltages in organic systems has been widely reported. Thin films of organic solid sandwiched between semitransparent layers of metal have been most commonly investigated (1g). Organic solids studied in this way include aromatic hydrocarbons (1a), organic dyes and pigments (1b, c) and organometallics (1d). Photovoltaic effects in organic crystals in contact with electrolyte solutions as electrodes have also been reported (1e). Photovoltages obtained in layers of electron-donor organic solids in contact with electron-acceptor organic solids have been attributed to photoinduced donor-acceptor interaction (1f). Photovoltages in these systems usually fall in the range $10^{-6}$ to 1v and power outputs in the range $10^{-8}$ to $10^{-17}$w.

In order to explore more fully the role of donor-acceptor interaction in photovoltage production in organic systems and evaluate the potential of organic systems for significant power output, we have investigated the photovoltaic behavior of molecular complexes in solution. The present work deals with the photovoltaic behavior of solutions of tetracyanoethylene (TCNE) in tetrahydrofuran (THF). This system was chosen for the investigation as previous studies on photoinduced electron spin resonance (2a, b) and photoconduction (2b) have provided some understanding of the fundamental processes which take place on illumination. In addition, complicating photochemical reactions are minimal in this system (2c), the main effect of illumination being to promote a reversible photoinduced electron transfer from the electron-donor molecule (THF) to the electron-acceptor molecule (TCNE). Reversible photovoltaic effects were thus expected and were, in fact, found.

## Experimental

Photovoltaic measurements were carried out by illuminating platinum electrodes immersed in the TCNE-THF solutions. A typical cell, used in initial studies, is shown in Fig. 1. The electrodes were constructed from platinum sheet, 0.5 mm in thickness, welded to 2 mm diameter platinum rod. The electrode area and spacing was 2 cm$^2$ and 1 cm, respectively. Solution was introduced into the cell and was in contact with platinum and glass only. After successive freeze-thaw cycles, evacuating after each freezing procedure, the cell was sealed off under a vacuum of 5 x $10^{-3}$ mm Hg. In later experiments, an all-glass cell was used to eliminate solvent attack on the O-ring.

THF, supplied by Matheson, Coleman, and Bell, was purified by distillation from a sodium dispersion under 1 atm of nitrogen. Eastman Kodak White Label TCNE was vacuum sublimed. All measurements were made on freshly prepared solutions.

The experimental arrangement for measuring photovoltage is shown in Fig. 2. A Keithley 610 electrometer, or a Cary vibrating-reed electrometer operating in the 31V mode, was used to measure the photoinduced voltages. Open-circuit photovoltages were usually measured. The power output of the photocell was determined by measuring the photovoltage across a series of shunt resistors, varied from $10^{11}$ to $10^2$ ohms. An Osram 900-W or 150-W xenon light source was used for illumination. Monochromatic light could be obtained from these sources in conjunction with Bausch and Lomb monochromator gratings, Nos. 33-86-07 and 33-86-02. Illumination conditions were arranged so that one electrode received the full

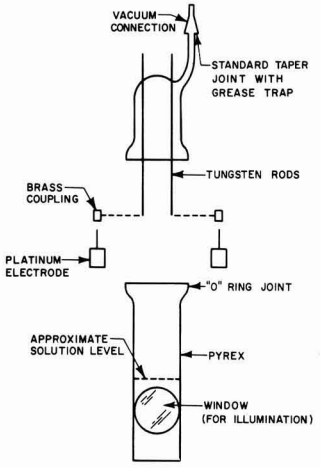


Fig. 1. Cell for photovoltage studies

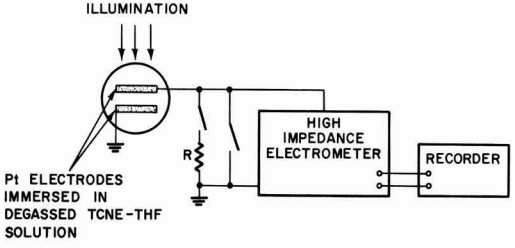


Fig. 2. Schematic of measuring circuitry

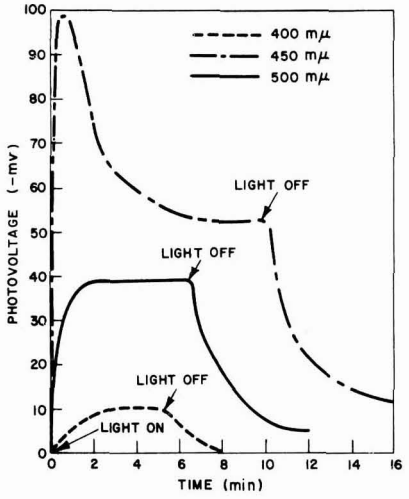


Fig. 3. Photovoltage response of $10^{-1}M$ TCNE-THF solution at various illuminating wavelengths.

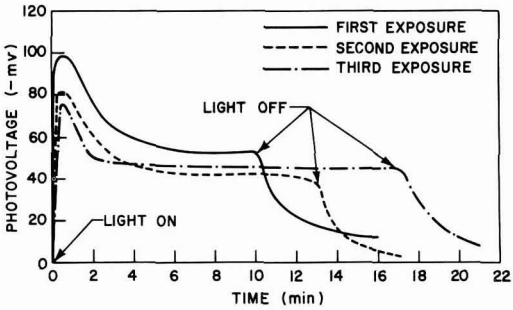


Fig. 4. Reproducibility of photovoltage response of $10^{-1}M$ TCNE-THF solution at 450 mμ.

illumination. Illumination intensities were measured by means of a bismuth-silver thermopile supplied by Eppley Laboratory Inc. Solution spectra were measured with a Cary 14R recording spectrophotometer.

## Results

The photovoltage response is shown in Fig. 3 at three illuminating wavelengths for a $10^{-1}M$ solution of TCNE in THF. The fast rise observed at 450 and 500 mμ reflects the response time of the external circuit. A slower rise was observed at 400 mμ, however, which appears to be a property of the solution system. The electrode attached to the electrometer input (the illuminated electrode) always acquired a negative voltage. Reproducibility and reversibility of the photovoltage is illustrated in Fig. 4.

Similar results were obtained with $10^{-3}$ and 7 x $10^{-1}M$ solutions of TCNE in THF. The $10^{-3}M$ solution responded more slowly and required a dark period for regeneration.

The spectral dependence of the photovoltage for three solution concentrations is shown in Fig. 5. The photovoltage magnitude is corrected to a uniform incident light intensity throughout the spectral region. The absorption spectra of the various solutions is also shown in Fig. 5 illustrating that the photovoltage increases sharply with decreasing wavelength at the absorption edge for each solution. The absorption of TCNE-THF solutions in this spectral region is due to the TCNE-THF charge-transfer band (2b, c, 3). The maxima in the photovoltage curve for the more concentrated solutions demonstrate that light capable of producing charge-transfer must be able to penetrate to the vicinity of the electrode in order to promote photovoltage production. This is only possible at the absorption edge, in the case of concentrated solutions, since wavelengths at the absorption peak are completely absorbed by the solution and do not penetrate to the electrode region. Thus, the photovoltage spectrum decreases again at the onset of strong absorption, the peak photovoltage shifting to longer wavelengths as the concentration increases. The results for the $10^{-1}$ and 7 x $10^{-1}M$ solutions indicated that the peak voltage increases as the TCNE concentration decreases. The peak photovoltage in the case of the $10^{-3}M$ solution was not determined in view of experimental difficulties due to the reduced light output of the source below 380 mμ. A trend toward a peak voltage at least as high as the peak observed for the $10^{-1}M$ solution is suggested, however, from the data at wavelengths longer than 380 mμ.

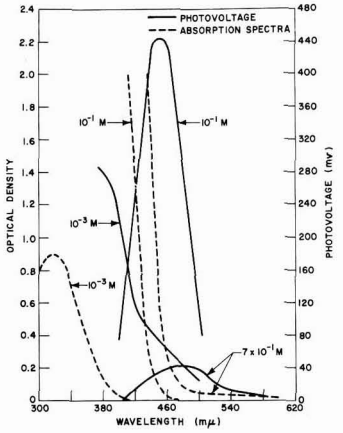


Fig. 5. Photovoltage spectral response and absorption spectra of TCNE-THF solutions (photovoltage corrected to incident light intensity 3.4 mw/cm²).

Maximum power output was obtained from the $10^{-3}M$ solution at 1.6 x $10^{-10}$w, illuminating with monochromatic light. Maximum power output from the 7 x $10^{-1}M$ solution with polychromatic light intensity 0.13w/cm² was 4 x $10^{-11}$w. The photovoltage-current characteristic for a $10^{-3}M$ solution is shown in Fig. 6.

A sublinear dependence of photovoltage on light intensity was generally observed, *i.e.*, $V = K(I)^n$ where

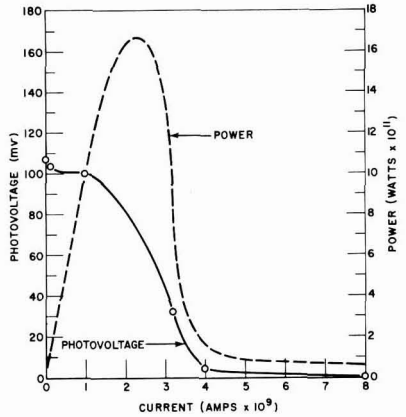


Fig. 6. Power output of $10^{-3}M$ TCNE-THF solution cell (illuminating wavelength 450 mμ; incident light intensity 1.7 mw/cm²).

Table I. Effect of illumination intensity on photovoltage of $10^{-3}$M TCNE-THF solution

| Wavelength, mμ | Intensity, μw/cm² | Photovoltage, mv | Intensity, μw/cm² | Photovoltage, mv | Intensity ratio | Photovoltage ratio |
|---|---|---|---|---|---|---|
| 375 | — | (−) 40 | 202 | (−) 70 | — | 1.7 |
| 400 | 54 | (−) 70 | 832 | (−) 115 | 15 | 1.6 |
| 425 | 112 | (−) 54 | 1370 | (−) 68 | 12 | 1.3 |
| 450 | 141 | (−) 15 | 1662 | (−) 58 | 12 | 3.8 |
| 475 | 204 | (−) 10 | 2495 | (−) 40 | 12 | 4.0 |
| 500 | 183 | (−) 2 | 2080 | (−) 18.5 | 11 | 9.2 |

$n < 1$. This is illustrated by the photovoltage data in Table I at two incident light intensities and the plot of photovoltage against incident light intensity shown in Fig. 7. In this plot $n = 0.62$.

## Discussion

ESR and photoconductiviy studies have shown that the TCNE negative-ion radical and, presumably, the THF positive-ion radical are formed on illuminating TCNE-THF solutions in the TCNE-THF charge transfer band. The TCNE negative-ion radical was identified from the hyperfine splitting of the ESR signal. The positive-ion radical was not detected, possibly because hole migration from $THF^{+}\cdot$ to THF neutral species (present in large excess) leads to broadening of the ESR signal (4). Chemical reaction of $THF^{+}\cdot$ is unlikely, since no permanent changes are detected.

The present data suggest two possible explanations for the production of photovoltages in charge-transfer solutions. In one view the photogenerated ions distribute to give concentration gradients in the vicinity of a platinum electrode yielding a net emf which can be sensed by the electrode. Evidence for this was provided by measurements of photovoltages with the charge-transfer solution stirred and unstirred. An unstirred $10^{-3}$M solution of TCNE in THF gave a photovoltage of 126 mv at 425 mμ. On commencement of stirring, with a Teflon-coated magnetic stirring bar incorporated in the cell, the voltage dropped immediately to 96 mμ and dropped almost to zero on increasing the stirring speed. Assuming that the photovoltage ($V$) follows the Nernst relation

$$V = A \log C + B \qquad [1]$$

where $C$ is the concentration of ionic species and $A$ and $B$ are constants, then taking $C = K'(I)^{1/2}$ (2b, c), where $I$ is the intensity of incident illumination, we have

$$V = \frac{A}{2} \log I + B' \qquad [2]$$

which is a sublinear dependence of photovoltage on illumination intensity. The observation of a sublinear dependence of photovoltage on illumination intensity is thus consistent with this picture, although the intensity data shown in Fig. 7 does not give a good fit to Eq. [2].

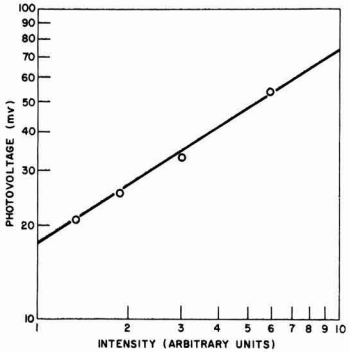


Fig. 7. Photovoltage-illumination intensity relationship for $10^{-1}$ TCNE-THF solution (illuminating wavelength 500 mμ).

Alternatively the photovoltage may arise from the preferential adsorption of one ionic species on the platinum electrode. This would explain the negative potential if it is assumed that the TCNE negative radical-ion is preferentially adsorbed. When light was confined to the solution between the electrodes, erratic results were obtained. This is further evidence that the interaction between the illumination and the charge-transfer species must take place in the vicinity of the electrode for photovoltage production.

Assuming that the photovoltage is directly proportional to the number of ions adsorbed and that Henry's law obtains, *i.e.*, number of ions adsorbed is directly proportional to the ionic concentration in solution, we have

$$V = K(I)^{1/2} \qquad [3]$$

An approximate fit to such a relationship is shown in Fig. 7. This model predicts a saturation effect with increased intensity as a monolayer of adsorbed ions is approached (Langmuir isotherm). Some evidence for this was found at the highest intensities with polychromatic light. The weight of evidence can thus be considered to favor the second explanation.

Further studies on the interaction of ion radical species with the electrode surface and measurements of photovoltages with reference electrodes are needed to settle some of these points, however.

Maximum power output of the TCNE-THF solution cell was on the order of $10^{-10}$w, obtained with the $10^{-3}$M solution. This value is on the upper limit of the range of values reported for organic solid photovoltaic systems (1) and suggests that organic solution systems may have more potential than organic solid systems for significant power output. Attempts were made to improve the power output by supplying ionic additives to the solution which would decrease the internal cell resistance without affecting the photovoltage magnitude or reversibility. This approach was largely unsuccessful.

## Summary and Conclusions

Reversible photoinduced electron transfer in solutions of TCNE in THF leads to the production of voltages which can be sensed by platinum electrodes. The mechanism of photovoltage production is not well understood, but probably involves distribution of photogenerated ionic species leading to a voltaic cell effect, or an effect related to the adsorption of ionic species on the electrode.

Maximum power output from these systems is in the region of $10^{-10}$w for monochromatic illumination intensities of $10^{-3}$ w/cm². This is an extremely low conversion efficiency compared to the values reported for the best inorganic photovoltaic devices (5). Power output is on the high range of values reported for organic systems, however. Solution photovoltaic cells of this type may thus have greater potential in the development of organic photovoltaic devices than the solid systems investigated previously.

## Acknowledgments

Research reported in this publication was supported by the United States Air Force Cambridge Research Laboratories, Office of Aerospace Research, under Contract No. AF19(628)-5511.

Manuscript received May 26, 1967; revised manuscript received July 10, 1967.

Any discussion of this paper will appear in a Discussion Section to be published in the June 1968 JOURNAL.

## REFERENCES

1. (a) H. Inokuchi, Y. Maruyama, and H. Akamatu in "Symposium on Electrical Conductivity

in Organic Solids," p. 69, H. Kallmann and M. Silver, Editors, Interscience Publishers, Inc., New York (1961).
(b) A. Terenin, *ibid.*, p. 39.
(c) B. Rosenberg, *ibid.*, p. 291.
(d) H. Meier and W. Albrecht, *Ber.*, **68**, 64 (1964).
(e) H. Kallmann and M. Pope, *J. Chem. Phys.*, **30**, 585 (1959).
(f) D. Kearns and M. Calvin, *ibid.*, **29**, 950 (1958).
(g) For a recent review see "Organic Semiconductors" by F. Gutman and L. E. Lyons, John Wiley & Sons, Inc., New York (1967).
2. (a) R. L. Ward, *J. Chem. Phys.*, **39**, 852 (1963).
(b) D. F. Ilten and M. Calvin, *ibid.*, **42**, 3760 (1965).
(c) D. F. Ilten, Ph.D. Thesis, University of California, Berkeley (1964).
3. R. Vars, L. A. Tripp, and L. W. Pickett, *J. Phys. Chem.*, **66**, 1754 (1962).
4. J. W. Eastman, G. M. Androes, and M. Calvin, *Nature*, **193**, 1067 (1962).
5. (a) P. Rappaport and J. J. Wysocki, *Acta Electronica*, **5**, 364 (1961).
(b) M. Wolf, *Proc. IRE*, **48**, 1246 (1960).
(c) P. Rappaport and J. J. Wysocki in "Photoelectronic Materials and Devices," p. 259, S. Larach, Editor, Van Nostrand Co., Inc., New York (1965).

# Bismuth in Yttrium Vanadate and Yttrium Europium Vanadate Phosphors

**R. K. Datta**

*Lighting Research Laboratory, General Electric Company, Cleveland, Ohio*

## ABSTRACT

Activation of rare earth vanadate by ions other than rare earths is successfully attempted in the present investigation. $Bi^{+3}$ can be incorporated in the $YVO_4$ and $GdVO_4$ lattice by solid-state reaction. The phosphor $R_{1-x}Bi_xVO_4$ (R = Y,Gd), excited by cathode rays or uv radiation, shows luminescence with a continuous emission band extending from 4000 to 7000Å and peaking at 5670Å. Under 2537Å excitation, the energy is absorbed essentially by Y-O components of the matrix and transferred to the emission centers ($Bi^{+3}$). Under 3650Å excitation, energy absorbed by charge-transfer processes involving (V-O) and (Bi-O) components of the phosphor is transferred to the emission centers ($Bi^{+3}$). The transmission of energy from the absorption to the emission centers under 2537 and 3650Å excitations involved a radiationless process. The phosphor $YVO_4$:Bi can be modified by incorporating $Eu^{+3}$ in the lattice. $YVO_4$:Eu:Bi, when excited by short- or long-wavelength uv radiation, shows emission spectra with sharp $Eu^{+3}$ emission peaks. Under cathode-ray or 3650Å excitation, the $Bi^{+3}$ emission is gradually quenched when $Eu^{+3}$ is incorporated in the $YVO_4$:Bi lattice with a constant level of $Bi^{+3}$ concentration; on the other hand, under 3650Å excitation, the $Eu^{+3}$ emission is enhanced when $Bi^{+3}$ is incorporated in the $YVO_4$:Eu lattice with a constant level of $Eu^{+3}$ concentration. This indicates a radiationless transfer of energy from $Bi^{+3}$ to $Eu^{+3}$ under 3650Å radiation.

In recent years activation of yttrium vanadate ($YVO_4$) by various rare earth ions has become of considerable scientific (1-5) and technological (6-7) interest. The phosphor $YVO_4$:R (R = rare earth), when excited by cathode rays, 2537 or 3650Å radiation, shows a typical, narrow-band spectrum of the corresponding rare earth fluorescence. Datta (8) studied the mechanism of absorption and photoluminescence and postulated that $YVO_4$:Eu is a host-sensitized phosphor. The excitation of the phosphor by uv radiation is due to absorption by two separate processes in the matrix ($YVO_4$). The energy absorbed by the matrix is transferred by a resonance process to the activator ($Eu^{+3}$) which causes excitation of $Eu^{+3}$ ions among levels of the $4f^6$ configuration and thence the final emission from them. O'Connor (5) investigated the laser properties of YVO:$Nd^{+3}$ and suggested transfer of energy from the lattice ($YVO_4$) to $Nd^{+3}$. Although these investigations indicate that $YVO_4$ is a promising matrix which can be activated by various types of activator ions, published reports list phosphors where $YVO_4$ is activated by rare earth ions only. This is probably due to recent interest in color-television phosphor and solid-state laser studies. $YVO_4$:R shows fluorescence of rare earth ions where transitions among the $4f^6$-electron energy levels result in line emission because the shielding effects of outer electrons minimize the perturbing influence of the crystal field. However, possibilities of activating $YVO_4$ with activator ions involving s-, p-, or d-electrons, where considerable perturbation occurs resulting in broad emission bands, cannot be ruled out.

In the present investigation, $Bi^{+3}$ among other trivalent activators (other than the rare earth ions) was substituted for $Y^{+3}$ in the $YVO_4$ lattice in various concentrations. It has been found that $YVO_4$, $GdVO_4$, and their various solid solutions, when activated with $Bi^{+3}$, show a broad emission band under cathode-ray, short- and long-wavelength uv excitations. It has been observed that the function of $Bi^{+3}$ in the phosphor is manifold. It acts as absorption and emission centers in the phosphor. In addition, when coactivated with $Eu^{+3}$ in the $YVO_4$ or $GdVO_4$ matrix, $Bi^{+3}$ acts as a sensitizer for $Eu^{+3}$ emission.

This report (*i*) characterizes the phosphors $YVO_4$:Bi $GdVO_4$:Bi and $YVO_4$:Eu:Bi; (*ii*) qualitatively describes the general function of $Bi^{+3}$ ions in terms of absorption, emission, and excitation of the phosphors under uv radiation with special emphasis on $YVO_4$:Bi and $YVO_4$:Eu:Bi.

## Experimental Procedure

*Sample preparation and composition.*—The raw materials used in this investigation consisted of luminescent grade (99.99-99.999% pure) oxides, such as yttrium oxide, $Y_2O_3$, gadolinium oxide, $Gd_2O_3$, europium oxide, $Eu_2O_3$, bismuth oxide, $Bi_2O_3$, and vanadium pentoxide, $V_2O_5$. In order to obtain the optimum

brightness of luminescence and high reflectance in the visible region, the vanadate should preferably be of stoichiometric composition. The activator(s) was incorporated with $Y_2O_3$ ($Gd_2O_3$) by coprecipitation as the oxalate, which was ignited at about 830°C to form the oxide. This insured uniform distribution of the activators in the phosphor. This oxide and $V_2O_5$ were mixed essentially in stoichiometric proportion (1:1 mole ratio) and fired at about 1000°C for 1½ hr. Additional 1-2 m/o (mole per cent) of $V_2O_5$ in the mixture insures compensation of the loss of $V_2O_5$ due to volatilization during firing. After cooling, the mixture was ground and washed in an ammonia solution to remove any excess $V_2O_5$. The washed and dried phosphor was reheated at ~1100°C for 1 hr. The firings of the phosphors were done in silica crucibles, and the homogeneity of the final products checked by x-ray diffraction analysis. $CuK_\alpha$ reduction from a G.E. diffractometer with a nickel filter was used to investigate all compounds. For precise determination of the change of d-spacing with change in composition of the solid solution series of the system $YVO_4$-$BiVO_4$, diffraction patterns were run at high angle ($2\theta \sim 65°$) region at slow speed (¼ deg/min/in.). Reproducibility of measurement was within ±0.0125°. Composition of the finished phosphors were periodically analyzed by wet chemical method in order to determine the loss of bismuth during firing. The loss ranged from 2 to 6% of bismuth added in the starting compositions; the amount of bismuth in the phosphors described throughout this paper is based on the formulated compositions.

*Spectroscopic measurements.*—Diffuse reflectance spectra of the samples within the range 2500-7000Å were obtained by using $CaF_2$ [1] as standard in a Cary Recording Spectrophotometer, Model No. 14. The emission spectra and the intensity of emission (peak height) measurements were obtained with a direct recording spectroradiometer (10) with a grating monochromator with nearly constant dispersion. The details involved are described elsewhere (8). The excitation spectra were measured using sodium salicylate as standard.

Cathodoluminescence spectra were obtained using a demountable cathode-ray tube operating at a 20 kv anode potential at 17.5 $\mu$a beam current over a standard scan TV raster of 35 $cm^2$ area. Brightness and color points of emission under these conditions were measured using an eye-corrected Weston foot-Lambert meter and G.E. colorimeter (JB 1E), respectively.

*Compositions of the phosphors studied.*—Since the absorption and emission spectra of phosphors may not always be independent of the relative amounts of the activator and coactivator, phosphors with wide range of concentration of $Bi^{+3}$ and rare earth ions were prepared. The compositions of the phosphors can be expressed by the general formula

$$Y_{1-(x+y)}Bi_xEu_yVO_4$$

$x$ and $y$ can vary from 0.000025 to 0.1 and 0 to 0.1, respectively.

The subsequent discussion on the properties of phosphors is generalized and does not pertain to one specific phosphor composition. The exact compositions of the phosphors are described in the text whenever such descriptions are necessary and meaningful. However, reflectance, emission, and excitation spectra are given along with the exact composition of the corresponding phosphor.

## Results and Discussion

*Phase equilibrium relationship.*—Subsolidus studies showed at least 7 m/o of $BiVO_4$ can be dissolved in the $YVO_4$ lattice within the temperature range (830°-1100°C) of sample preparation. This is well within the range of activator concentration used in the present investigation.

*Reflectance spectra.*—($YVO_4$:Eu:Bi).—Figures 1 and 2 show the effects of $Bi^{+3}$ incorporation on the diffuse reflectance spectrum of the phosphor $YVO_4$:Eu. Except for the sharp $Eu^{+3}$ absorption lines in the visible region, the diffuse reflectance spectra of $YVO_4$ and $YVO_4$:Eu are essentially alike. Figure 1 shows the reflectance spectra of samples having a constant concentration (5 a/o [atom per cent]) of $Eu^{+3}$ but different amounts of $Bi^{+3}$, whereas Fig. 2 shows the reflectance spectra of samples having a fixed amount of $Bi^{+3}$ (2 a/o) but different levels of $Eu^{+3}$ concentration. These spectra show that the absorption of the phosphor $YVO_4$:Eu:Bi in the uv region is essentially independent of $Eu^{+3}$ concentration. However, incorporation of $Bi^{+3}$ enhances the absorption at long-wavelength uv radiation. On the basis of the spectra shown in Fig. 1, 2, and 3, it may be suggested that the mechanisms of absorption in the uv region by the phosphors $YVO_4$:Bi (discussed below) and $YVO_4$:Eu:Bi are essentially similar.

($YVO_4$:Bi).—The diffuse reflectance spectra of some of the $YVO_4$:Bi samples studied are shown in Fig. 3. $YVO_4$ shows two absorption bands, namely, at 2500

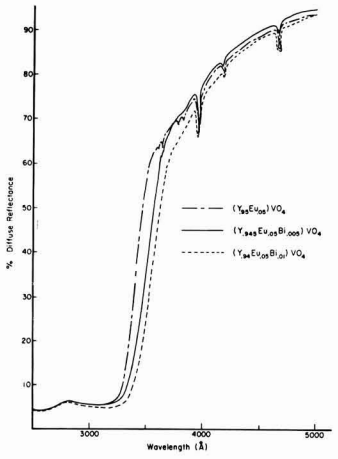


Fig. 1. Diffuse reflectance spectra of $YVO_4$:Eu:Bi samples (constant Eu content).

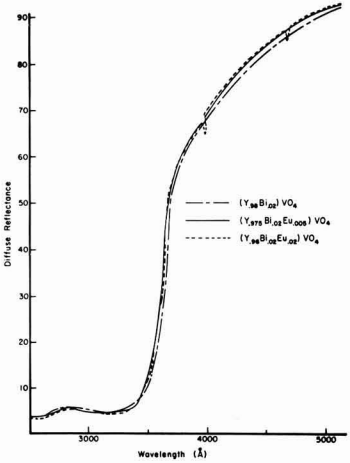


Fig. 2. Diffuse reflectance spectra of $YVO_4$:Eu:Bi samples (constant Bi content).

[1] In addition to higher reflectance in the region 2500-4000A, $CaF_2$ shows better chemical stability in room conditions than the usual reflectance standards, such as MgO, $MgCO_3$, which partly react with atmospheric moisture and lower their reflectance in the uv region even further (9).

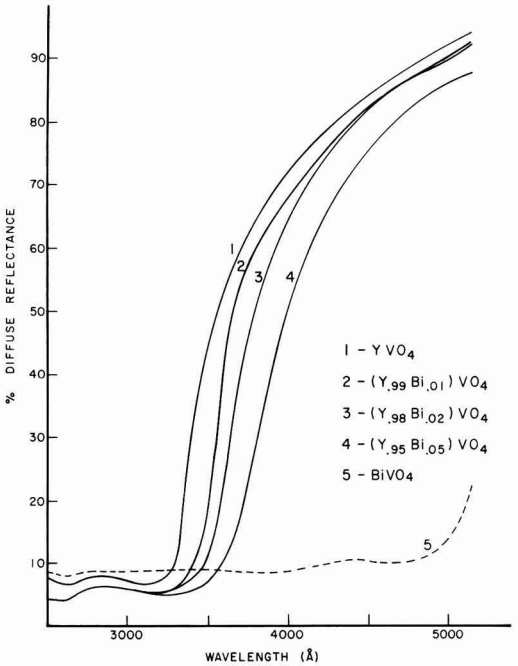


Fig. 3. Diffuse reflectance spectra of $YVO_4$:Bi samples

and 3200Å. These are attributed to charge transfer processes involving Y-O and V-O components of the matrix, respectively (8, 16). Addition of $Bi^{+3}$ in $YVO_4$ shifts the absorption edge toward longer wavelength, whereas the absorption band at 2500Å region remains essentially unchanged. Pure $YVO_4$ shows an absorption edge at about 3200Å with about 60% absorption at 3400Å. Addition of 1 and 2 a/o of $Bi^{+3}$ shifts the edge to 3300 and 3450Å and increases the absorption at 3400Å to about 85 and 90%, respectively (Fig. 3). From a study of the reflectance spectra of $BiF_3$ and $Bi_2O_3$, it has been shown (11) that the absorption of long-wavelength uv radiation due to incorporation of $Bi^{+3}$ in an oxide matrix is mainly caused by charge-transfer states involving bismuth and oxygen. The shift in the absorption edge of $YVO_4$ to longer wavelength due to $Bi^{+3}$ addition, as observed in the present investigation, may be ascribed to the absorption caused by charge-transfer states involving $Bi^{+3}$ and the neighboring eight oxygen atoms of $(YBi)VO_4$ (12).

It can be summarized that $YVO_4$:Bi and $YVO_4$:Eu:Bi show strong absorption of short- and long-wavelength uv radiations. The absorption of short-wavelength uv radiation is due to a charge-transfer process involving the Y-O components (8), whereas the charge-transfer process involving Bi-O and V-O component (8) of the phosphor are responsible for absorption in the 3000-3400Å region. In addition, increase in $Bi^{+3}$ content of the sample causes increased absorption at wavelengths about 3400Å and higher. For the sake of brevity, in the subsequent sections of this paper absorption due to charge-transfer processes involving the Bi-O components is referred to as $Bi^{+3}$ absorption.

In the foregoing discussion little emphasis has been placed on the absorption of short-wavelength uv radiation by the Bi-O components of $YVO_4$:Eu:Bi and $YVO_4$:Bi. However, it is not suggested that such absorption by $Bi^{+3}$ and/or Bi-O is either not taking place or is not important. On the contrary, the absorption of short-wavelength uv radiation by $Bi^{+3}$ incorporated in the $Y_2O_3$ matrix is shown by the

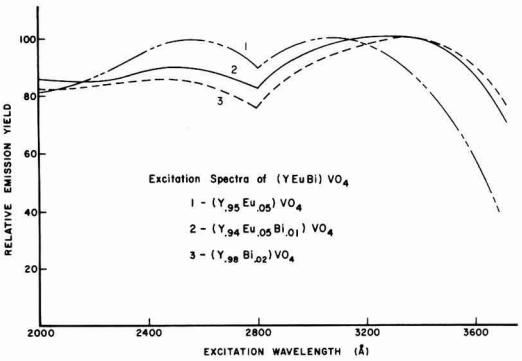


Fig. 4. Excitation spectra of $(YEuBi)VO_4$

diffuse reflectance spectra of $Y_2O_3$:Bi samples (11). The only suggestion made here is that although some (about 20%) absorption of short-wavelength uv radiation is probably caused by Bi and/or Bi-O, such process is not the underlying cause for high efficiency of the phosphor $YVO_4$:Bi under 2537Å excitation. This idea may be indirectly supported by the fact that as the concentration of $Bi^{+3}$ in the phosphor $YVO_4$:Bi increases from 0.75 to 2 a/o, the absorption of the short-wavelength (2537Å) uv radiation and the intensity of emission under 2537Å remain essentially constant.

*Excitation spectra.*—Normalized excitation spectra of the samples $YVO_4$:Bi, $YVO_4$:Eu, and $YVO_4$:Eu:Bi are shown in Fig. 4. The emission spectra of samples with and without $Eu^{+3}$ are quite different. Hence, their response to the photomultiplier tube used in obtaining excitation spectra are also different. Any quantitative comparison of the excitation spectra should be made after necessary correction. However, it may be generalized that these phosphors have continuous broad excitation spectra with two wide maxima at 2600 and 3200Å. These samples respond efficiently to 2537 and 3650Å excitations.

*Emission spectra.*—$(YVO_4:Bi)$.—When excited by cathode-rays, short (2537Å)- or long (3650Å)-wavelength uv radiations, $Bi^{+3}$-activated $YVO_4$ shows luminescence with an emission band extending from 4000 to 7000Å and peaking at 5670Å (Fig. 5). The present investigation does not include any quantitative measurement of the quantum efficiency of the phosphor under different excitations. However, a qualitative evaluation of the emission process can be attempted.

The band shape of the emission spectra of the phosphor $YVO_4$:Bi (Fig. 5) is independent of the exciting source and amount of $Bi^{+3}$. The question now arises whether the emission is from the lattice $(YVO_4)$, $Bi^{+3}$ ions or from the excited Bi-O components. The emis-

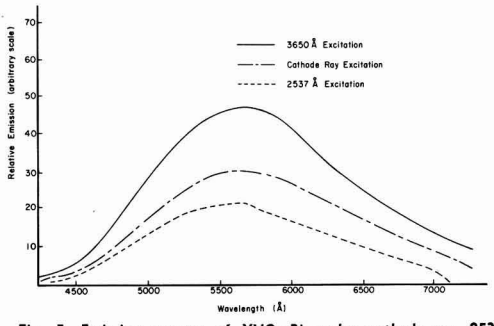


Fig. 5. Emission spectra of $YVO_4$:Bi under cathode-ray, 2537 and 3650Å excitations.

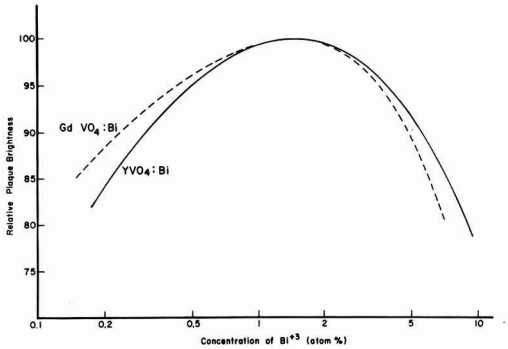


Fig. 6. Plaque brightness vs. activator concentration of $RVO_4$:Bi (R = Gd, Y), 2537Å excitation.

sion spectrum of pure $YVO_4$, excited by cathode rays, 2537 or 3650Å radiations, shows a broad weak emission extending from 4000 to 5500Å region and peaking at about 4375Å. The position of the peak of this emission spectrum is quite different from that of $YVO_4$:Bi. In addition, the intensity of emission of $YVO_4$:Bi is a function of $Bi^{+3}$ concentration. Normalized plots of plaque[2] brightness against logarithm of $Bi^{+3}$ concentration in $YVO_4$ and $GdVO_4$ under 2537Å excitation are shown in Fig. 6. When excited by uv radiation, the optimum concentration of $Bi^{+3}$ is independent of the wavelength of the exciting source. The concentration of $Bi^{+3}$ may be chosen within wide limits (1-10 a/o), the optimum being 1-3 a/o of bismuth substituted for Y or Gd in $YVO_4$ and $GdVO_4$, respectively. When excited under cathode rays, the optimum $Bi^{+3}$ concentration ranges from 0.1 to 0.5 a/o. These indicate that the emission in $YVO_4$:Bi is not a matrix fluorescence; it is related to $Bi^{+3}$ ions and/or Bi-O components.

Most of the $Bi^{+3}$-activated phosphors (sulfides, selenides, carbonates, oxides, silicates, etc.) emit in the blue region, although other emissions, such as green, yellow, red, etc., are known (13). The absorption and emission of trivalent metal ions of the sixth period with $^1S_0$ ($5d^{10}6s^2$) ground state have been discussed in considerable detail by McClure (14). However, no simple correlation between the $Bi^{+3}$ emission and composition and structure of the matrix could be obtained from available literature. McClure (14) suggested a $6s6p \rightarrow 6s^2$ transition for $Bi^{+3}$ fluorescence. These outer sp orbitals of post-transitional metal ions are also actual bonding orbitals. Hence, the energy levels of $Bi^{+3}$ ions are highly perturbed by the anions ($O^{-2}$) of the matrix. In the subsequent discussion this emission is referred to as $Bi^{+3}$ emission.

It should be noted that the emission spectrum of pure $YVO_4$ which extends from 4000-5500Å, is in part coincident with that of the phosphor $YVO_4$:Bi (4000-7000Å region), although their peak positions are different. From the symmetric nature of the emission spectrum of $YVO_4$:Bi, even when the concentration of $Bi^{+3}$ is very low (about 0.7 a/o of yttrium), it can be suggested that the lattice emission ($YVO_4$) is essentially absent. Hence, it can be suggested that the excitation energy absorbed under short (2537Å)- or long (3650Å)-wavelength uv radiation is emitted mostly as $Bi^{+3}$ fluorescence.

($YVO_4$:Eu:Bi).—When $Eu^{+3}$ is incorporated in the $YVO_4$:Bi lattice with a fixed concentration of $Bi^{+3}$, the broad $Bi^{+3}$ emission under cathode rays, 2537 and 3650Å excitations is gradually quenched, and sharp, line emissions of $Eu^{+3}$ appear. The relative intensity of these two emissions are dependent on the relative concentration of these two activators so that concentrations can be varied within a wide range depending on the nature of emission desired.

[2] Powdered samples tightly packed in a flat holder.

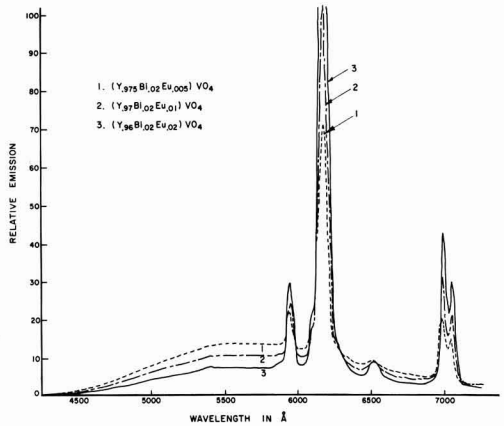


Fig. 7. Emission spectra of $YVO_4$:Eu:Bi under 2537Å excitation

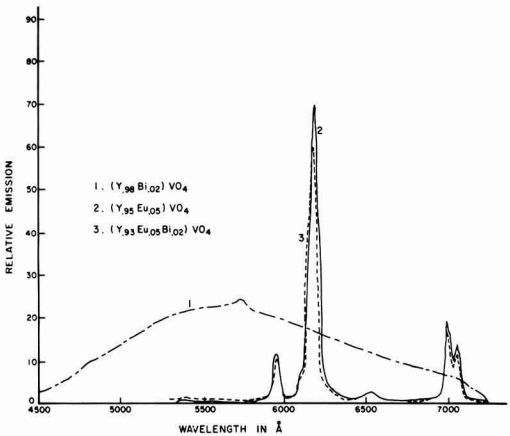


Fig. 8. Emission spectra of $YVO_4$:Eu:Bi under 2537Å excitation

The phosphor $YVO_4$:Eu:Bi behaves differently under different uv excitations, namely, 2537 and 3650Å radiations. These are discussed separately below.

2537Å *excitation.*—When $Eu^{+3}$ concentration is gradually increased in the $Y_{0.95}Bi_{0.02}VO_4$ lattice, the broad $Bi^{+3}$ emission under 2537Å excitation is gradually quenched without any change in the band shape of Bi-emission, and narrow-band $Eu^{+3}$ emissions appear (Fig. 7). When $Bi^{+3}$ is incorporated in the $Y_{0.95}Eu_{0.05}VO_4$ lattice, a very faint $Bi^{+3}$ emission is noticed, and there is little effect on the intensity of $Eu^{+3}$ emission (Fig. 8, 12). With further increase in $Bi^{+3}$ concentration (above 2 a/o) the intensity of $Eu^{+3}$ emission is gradually decreased without any enhancement of $Bi^{+3}$ emission. At higher concentration, $Bi^{+3}$ acts as "killer" for $Eu^{+3}$ emission.

3650Å *excitation.*—When $Eu^{+3}$ concentration is gradually increased in the $Y_{0.98}Bi_{0.02}VO_4$ lattice, the intensity of broad $Bi^{+3}$ emission under 3650Å excitation is decreased, and narrow-band $Eu^{+3}$ emissions appear (Fig. 9, 10). Even 0.5 a/o $Eu^{+3}$ can considerably decrease $Bi^{+3}$ emission of $Y_{0.98}Bi_{0.02}VO_4$ (curve 2, Fig. 10). However, $Bi^{+3}$ emission is never completely quenched, even with $Eu^{+3}$ concentration as high as 5 a/o (curve 5, Fig. 11). When $Bi^{+3}$ is gradually incorporated in the $Y_{0.95}Eu_{0.05}VO_4$ lattice, the emission lines of $Eu^{+3}$ show enhanced intensity, especially the main emission peak at 6190Å. The intensity of this peak shows an increase of almost 200% as $Bi^{+3}$ content of $Y_{0.95}Eu_{0.05}VO_4$ is increased from 0 to

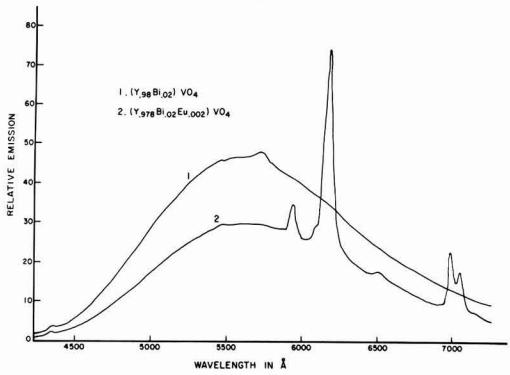


Fig. 9. Emission spectra of $YVO_4$:Eu:Bi under 3650Å excitation

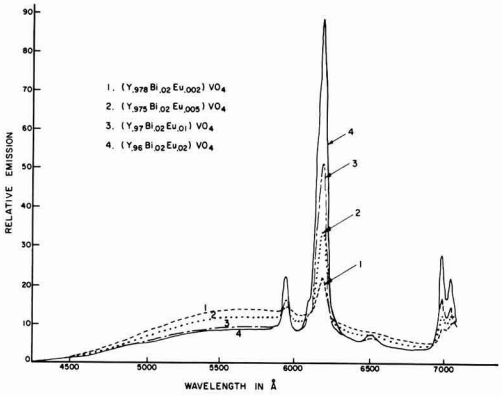


Fig. 10. Emission spectra of $YVO_4$:Eu:Bi under 3650Å excitation

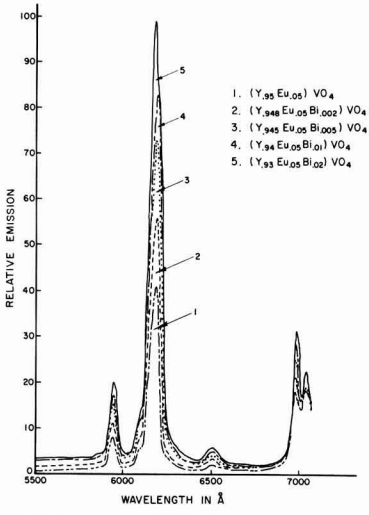


Fig. 11. Emission spectra of $YVO_4$:Eu:Bi under 3650Å excitation

2 a/o. That is, the composition of the phosphor is changed from $Y_{0.95}Eu_{0.05}VO_4$ to $Y_{0.93}Eu_{0.05}VO_4$ to $Y_{0.93}Eu_{0.05}Bi_{0.02}VO_4$ (Fig. 11). Figure 12 shows the effects on the main $Eu^{+3}$ emission peak at 6190Å under 2537 and 3650Å excitations due to incorporation of $Bi^{+3}$ in $Y_{0.95}Eu_{0.05}VO_4$. Because of the difference in

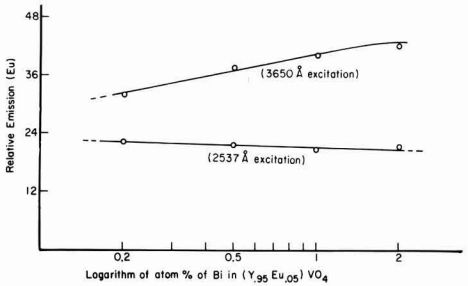


Fig. 12. Relative $Eu^{+3}$ emission of $YVO_4$:Eu:Bi under 2537 and 3650Å excitations vs. $Bi^{+3}$ content of the samples. (The emission is measured from the total area of the peak at 6190Å.)

the intensities of the two exciting sources used in the present investigation, the relative response of the phosphor, $(YEuBi)VO_4$ to these two excitations should not be deduced from Fig. 12 and compared with the data presented in Fig. 4.

## Mechanism of Energy Transfer

It has been suggested in the reflectance spectra section of this paper that in the phosphors $YVO_4$:Bi and $YVO_4$:Eu:Bi the short-wavelength uv radiation is absorbed essentially by the lattice, whereas the long-wavelength uv radiation is absorbed jointly by the lattice (V-O components) and the impurity (Bi-O components) elements. The question now arises: What are the mechanisms involved in the transfer of energy from the absorber to the emitting centers, *i.e.*, $Bi^{+3}$ and $Eu^{+3}$ ions in $YVO_4$:Bi and $YVO_4$:Eu:Bi, respectively? Klick and Schulman (15) discussed two different methods by which energy from the absorbing components can be transferred to the emission centers in photoluminescent phosphors: (*i*) a radiative transfer of energy through the emission of photons from the absorbing matrix and reabsorption by the final emitter; (*ii*) a nonradiative or exchange process associated with resonance between the absorber and emitter.

In the former case, the absorbing species of the phosphor system must be a very good emitter, and the emitting species must be an efficient absorber. In addition, for any significant amount of energy transfer by the radiative process, the emission spectrum of the absorbing species must substantially overlap the absorption band of the emitting species.

In the phosphor $YVO_4$:Bi, the weak emission of the matrix ($YVO_4$) which extends from 4000-5500Å region under uv radiations does not overlap significantly the $Bi^{+3}$ absorption band (3200-4200Å region) of the phosphor. In the phosphor $YVO_4$:Eu:Bi, the emission of $YVO_4$:Bi which extends from 4000 to 7000Å under uv excitations does not overlap the main absorption band (at about 2500Å) of $Eu^{+3}$ ions. Hence, any substantial transfer of energy by a radiative process from $YVO_4$ and $YVO_4$:Bi to the emitting centers, such as $Bi^{+3}$ and $Eu^{+3}$ of the phosphor systems $YVO_4$:Bi and $YVO_4$:Eu:Bi, respectively, can be ruled out.

It may be emphasized that two steps are involved in case of energy transfer by a radiationless or resonance process in photoluminescent phosphors (16): (*i*) energy transfer through the matrix, *i.e.*, from one absorbing group to the other, and (*ii*) energy transfer from the absorbing groups to the activators or emitting centers. Dexter (17) studied the mechanisms and conditions required for a nonradiative transfer of energy through the matrix. The probability of such transfer is a function of the overlap of the wave functions of the absorbing groups and the overlap of the absorption and emission bands of the absorbing groups. It has been shown that such conditions are well satisfied in the $YVO_4$ matrix (16). Blasse (16) studied many host-sensitized $Eu^{+3}$-activated phosphors and suggested several requirements for energy transfer from

the matrix to the emitting centers (activators): (a) overlap between the orbitals of the central cation of the absorbing group and the neighboring activator ions, and (b) some overlap of the emission and absorption of the absorbing and emitting groups, respectively.

Blasse (16) further suggested that by virtue of the arrangements of the ions in the lattice, the requirement of orbital overlap betwen yttrium and vanadium is very well satisfied in $YVO_4$. As a result, $YVO_4$-based phosphors where part of the yttrium is randomly substituted by the activator ion show efficient energy transfer from the absorbing centers ($VO_4^{-3}$) to the emitters. In $YVO_4$:Bi a part of the emission spectrum of $YVO_4$ is overlapped by the absorption band of $Bi^{+3}$. Hence, in case of $YVO_4$:Bi, the short-wavelength (2537Å) uv radiation absorbed by the matrix ($YVO_4$) may well be transferred by a radiationless process (15, 17) to the emitting centers ($Bi^{+3}$) resulting in the excitation of $Bi^{+3}$ ions and the final emission from them ($6s6p \rightarrow 6s^2$ transition). The mechanism of excitation of $Bi^{+3}$ ions under 3650Å radiation is slightly different. In this case, in addition to the transfer of energy from the matrix to the activator centers ($Bi^{+3}$), $Bi^{+3}$ ions themselves absorb the excitation energy and undergo excitation directly. In $YVO_4$:Eu:Bi, the requirement for energy overlap for the transfer of energy from the matrix to the emission centers is satisfied. This is because $Eu^{+3}$ ions show small, sharp absorption lines within the region (4000-7000Å) of continuous emission spectrum of $YVO_4$:Bi under uv excitations. It can be recalled here that both $YVO_4$:Bi and $YVO_4$:Eu are essentially host-sensitized phosphors under 2537Å excitation. The energy absorbed by the matrix is transferred to the emission centers $Eu^{+3}$ and $Bi^{+3}$. When these two activators are present together, as observed in the present investigation, energy absorbed by the matrix is transferred preferentially to $Eu^{+3}$ ions which undergo excitation and the final emission. Since $Eu^{+3}$ and $Bi^{+3}$ ions randomly substitute part of yttrium in the $YVO_4$ lattice[3] and their probabilities of being near the absorption matrix are equal, it is not yet understood why only $Eu^{+3}$ ions are excited. On the other hand, it could be a multistep transfer, *i.e.*, energy from the host is transferred to $Eu^{+3}$ *via* $Bi^{+3}$. However, even with increased $Bi^{+3}$ concentration very little energy absorbed by the matrix is emitted from $Bi^{+3}$.

The emission of $YVO_4$:Eu:Bi under 3650Å excitation is an example of simultaneous host- and impurity (coactivator)-sensitized luminescence (15). In case of impurity-sensitized phosphor, such as $CaSiO_3$:Pb:Mn, energy absorbed by Pb is transferred by a radiationless process to $Mn^{++}$ which undergoes excitation and the final emission (18). In case of host-sensitized phosphors, such as $YVO_4$:Eu and $Y_2WO_6$:Eu, energy absorbed by the matrix ($VO_4^{-3}$, $WO_6^{-6}$) is transferred by a radiationless process to the emission centers ($Eu^{+3}$) (8, 19). In $YVO_4$:Eu:Bi, as observed in the present investigation, energy absorbed by the lattice ($VO_4^{-3}$) and the impurity centers (Bi-O) under 3650Å excitation is transferred to $Eu^{+3}$ ions by a nonradiative or resonance process (15, 20). The idea of transfer of energy is supported by the following observations under 3650Å excitations: (*i*) The broad $Bi^{+3}$ emission of $Y_{0.98}Bi_{0.02}VO_4$ is gradually quenched as $Eu^{+3}$ concentration is increased in the lattice. (*ii*) The $Eu^{+3}$ emission of $Y_{0.95}Eu_{0.05}VO_4$ is enhanced markedly with gradual increase in $Bi^{+3}$ content.

Sensitization of $Eu^{+3}$ emission by other rare earths, such as Tb, is known (21). $YVO_4$:Eu:Bi is probably the first phosphor reported where $Eu^{+3}$ emission is sensitized by a nonrare earth ion ($Bi^{+3}$). This paper describes the photoluminescence of the phosphors $YVO_4$:Bi and $YVO_4$:Eu:Bi. However, for the sake of completeness, the effects of $Bi^{+3}$ addition on color point and brightness of $Y_{0.95}Eu_{0.05}VO_4$ emission under cathode-ray excitation are shown (Table I). Although, because of instrumental limitations, no $Bi^{+3}$ emission was detected in the emission spectra of (YEuBi)$VO_4$ under cathode-ray excitation, data in Table I are more consistent with the introduction of a $Bi^{+3}$ emission (hence the color shift) with little effect on the $Eu^{+3}$ emission intensity.

[3] X-ray diffraction patterns obtained with carefully prepared samples of $YVO_4$ and $Y_{1-(x+y)}Bi_xEu_yVO_4$ to avoid preferred orientation were compared. Absence of any additional reflection in the activated samples was interpreted as a lack of superlattice or long-range order of Bi-Eu or Bi-Y-Eu in $Y_{1-(x+y)}Bi_xEu_yVO_4$. However, short-range order, usually indicated by preferential increase or decrease of intensities of certain reflections over others in a randomly oriented sample, cannot be unequivocally ruled out due to very small concentration of Bi involved.

Table I. Cathode-ray brightness of $YVO_4$:Eu:Bi samples

| Composition | A/O Eu | A/O Bi | Relative brightness | Color coordinates* X | Y |
|---|---|---|---|---|---|
| (YBi)$VO_4$ | — | 0.2 | 100 | 378 | 537 |
| (YBi)$VO_4$ | | 0.5 | 97 | | |
| (YBi)$VO_4$ | | 1.0 | 87 | 380 | 545 |
| (YEuBi)$VO_4$ | 5 | — | 100 | 655 | 336 |
| (YEuBi)$VO_4$ | 5 | 0.1 | 126 | 636 | 351 |
| (YEuBi)$VO_4$ | 5 | 0.2 | 129 | 637 | 352 |
| (YEuBi)$VO_4$ | 5 | 0.5 | 130 | 625 | 361 |
| (YEuBi)$VO_4$ | 5 | 0.7 | 132 | 618 | 367 |
| (YEuBi)$VO_4$ | 2.5 | 0.1 | 110 | 630 | 349 |

* Based on 1931 CIE Chromaticity Diagram.

## Summary and Conclusion

Yttrium vanadate ($YVO_4$) is a well-known matrix for fluorescence of rare earth ions. In the present investigation it has been activated with $Bi^{+3}$. $YVO_4$:Bi is a new phosphor with a broad excitation band extending from 2000 to 3600Å. The phosphor responds very well to cathode rays, 2537 and 3650Å excitation and emits a broad emission band extending from 4000 to 7000Å with a peak at 5670Å. Under 2537Å excitation, energy is absorbed by the Y-O components of the matrix and transferred to $Bi^{+3}$ ions (emission centers) by a radiationless process. The emission of $YVO_4$:Bi is attributed to the $6s6p \rightarrow 6s^2$ transition of $Bi^{+3}$ ions. These sp orbitals are also bonding orbitals. Hence, influence of the oxygen ions surrounding $Bi^{+3}$ ions on emission cannot be ruled out. Under 3650Å excitation, energy is absorbed by charge-transfer processes involving the V-O and Bi-O components of the phosphor. The energy from the matrix (V-O) is transferred by a radiationless process to Bi ions resulting in their excitation and the final emission from them.

When $Eu^{+3}$ is incorporated in the $YVO_4$:Bi lattice, the broad $Bi^{+3}$ emission is gradually quenched under cathode rays, 2537 and 3650Å excitation, and the line emission of $Eu^{+3}$ ions appears. With proper selection of concentration of $Eu^{+3}$ and $Bi^{+3}$, the $Eu^{+3}$ emission is enhanced under 3650Å excitation without showing any appreciable emission of $Bi^{+3}$.

On the basis of these observations, it can be suggested that the photoluminescence of $YVO_4$:Eu:Bi under 3650Å excitation is a result of host and impurity sensitization. The energy absorbed by the matrix (V-O) and the impurity centers (Bi-O) is transferred by a resonance process to the emission centers ($Eu^{+3}$) resulting in the excitation of $Eu^{+3}$ ions among the energy levels of the $4f^6$ configuration and final narrow band emission from them with a peak at 6190Å involving mainly $^5D_0 \rightarrow {}^7F_2$ transition of $Eu^{+3}$. This investigation shows that $Bi^{+3}$ in $YVO_4$:Eu:Bi and $YVO_4$:Bi acts as absorber, emitter, and sensitizer.

## Acknowledgments

The author acknowledges the assistance of Dr. R. L. Brown, T. E. Lusk, and B. Walsh in obtaining emission and excitation spectra, of M. Brines and F. Geraghty who measured cathode-ray brightness. The author also wishes to express his thanks to L. S. Staikoff for x-ray measurements, to T. Luscher for preparing the phosphor and measuring uv brightness, and to Dr. E. F. Apple for many helpful discussions. Dr. T. S. Davis and

V. Thelian helped in preparing the manuscript in the final form.

Manuscript received May 23, 1967; revised manuscript received *ca.* July 3, 1967. This paper was presented at the Dallas Meeting, May 7-12, 1967.

Any discussion of this paper will appear in a Discussion Section to be published in the June 1968 JOURNAL.

REFERENCES

1. L. G. Van Uitert, R. C. Linares, R. R. Soden, and A. A. Ballman, *J. Chem. Phys.*, **36**, 702 (1962.).
2. A. Levine and F. C. Palilla, *Appl. Phys. Letters*, **5**, 118 (1964).
3. L. H. Brixner and E. Abramson, *This Journal*, **112**, 70 (1965).
4. F. C. Palilla, A. K. Levine, and M. Rinkevics, *ibid.*, **112**, 776 (1965).
5. J. R. O'Connor, *Appl. Phys. Letters*, **9**, 407 (1966).
6. A. K. Levine and F. C. Palilla, *Electrochem. Tech.*, **4**, 16 (1966).
7. F. C. Palilla and A. K. Levine, *Appl. Optics*, **5** 1467 (1966).
8. R. K. Datta, *Trans. Metal. Soc. AIME*, **239**, 355 (1967).
9. F. J. Studer, Personal communications.
10. R. L. Brown, *Illum. Engr.*, **61**, 230 (1966).
11. R. K. Datta, In press.
12. W. A. Runciman, *Proc. Phys. Soc.*, **A68**, 647 (1955).
13. F. A. Kroger, "Some Aspects of the Luminescence of Solids," Elsevier Publishing Co., Inc., New York (1948).
14. D. S. McClure, "Solid State Physics," Vol. 9, Academic Press, New York (1959).
15. C. C. Klick and J. H. Schulman, "Solid State Physics," Vol. 5, Academic Press, New York (1957).
16. G. Blasse, *J. Chem. Phys.*, **45**, 2356 (1966).
17. D. L. Dexter, *ibid.*, **21**, 836 (1953).
18. H. J. Schulman, R. J. Ginther, and C. C. Klick, *This Journal*, **97**, 123 (1950).
19. G. Blasse and A. Bril, *J. Chem. Phys.*, **45**, 2350 (1966).
20. P. G. Botden, *Philips Research Rept.*, **7**, 197 (1952).
21. L. G. Van Uitert and R. R. Soden, *J. Chem. Phys.*, **36**, 1289 (1962).

# Ohmic Electrical Contacts to P-Type ZnTe and $ZnSe_xTe_{1-x}$

**M. Aven and W. Garwacki**

*General Electric Research and Development Center, Schenectady, New York*

ABSTRACT

Low resistance electrical contacts to p-type ZnTe and $ZnSe_xTe_{1-x}$ can be made by diffusing Li from a Li salt into the area of the crystal to be contacted and forming an electroless Au deposit on top of the Li-diffused area. The Li-Au contacts stay nearly ohmic down to 35°K and have been used on crystals having carrier concentrations below $10^9$ $cm^{-3}$. It is suggested that the superior behavior of the Li-Au contacts arises from high concentrations of shallow acceptors in the Li-diffused region which narrows the potential barrier between the valence band of ZnTe and the filled band of the contacting material sufficiently to allow tunneling of carriers even at low temperatures.

Fundamental studies as well as device applications of II-VI compounds, particularly the Zn chalcogenides, have been seriously hindered by the difficulties in making low resistance, low noise, ohmic contacts to these materials. In a recent paper Blount *et al.* (1) have reviewed the requirements for obtaining such contacts. In brief, these requirements call for a material for the contact electrode which has a smaller work function than that of the semiconductor if the semiconductor is n-type or larger if the semiconductor is p-type, and which, when diffused into the semiconductor, will act as a dopant providing majority carriers.

Following these guidelines, satisfactory ohmic contacts can be produced to n-type CdS, CdSe, and CdTe by using In or Ga as the contact metal (2). The contacting of n-type ZnS and ZnSe, which have lower work functions (3) and show a greater tendency toward compensation is more difficult. Nevertheless, satisfactory ohmic contacts have been found for low and high resistivity ZnSe (4), low resistivity ZnS (5), and, more recently, even for high resistivity ZnS (1). Low resistivity p-type CdTe and ZnTe have been electroded with moderate success with electroless gold (6-7). The contacting of these compounds in high or even moderate resistivity form, however, has been very difficult. As a consequence, low-temperature electrical transport studies of these materials in high-purity p-type form are very scarce.

In this paper the authors wish to describe the preparation and some characteristics of Li-diffused contacts to high resistivity p-type ZnTe and $ZnSe_xTe_{1-x}$ crystals. Such contacts stay ohmic and noiseless to quite low temperatures and can be used on crystals having very low carrier concentrations.

## Preparation

The crystal to be electroded is etched for 10 to 60 sec in boiling 50% NaOH, rinsed first with hot dilute NaOH, and then with hot distilled water. A small drop of $LiNO_3$ solution ($10^{-4}$ mol/ml) is placed on the crystal in the desired electrode location while the crystal is heated to 40°C in air. The heating is not a necessary requirement, but promotes the evaporation of the solution to dryness. This is particularly useful when applying several electrodes to different sides of the crystal. The crystal is then slowly heated to 320°-350°C in $H_2$ and held there for 20 to 60 sec. As the crystal is heated, the dry $LiNO_3$ deposit melts at 250°C. At about 300°C the liquid melt suddenly reacts with the substrate and appears to penetrate into the crystal, leaving a barely visible gray spot on the surface. Lateral spreading causes the spot to increase to several times the size of the contact area of the original liquid salt droplet. After cooling to room temperature, the crystal is rinsed with distilled water, dried, and an electroless Au deposit is formed (6) on top of the Li-reacted area. If desired, wires can be soldered to the Au deposit with an In or In-Ag alloy, or fastened to it with silver paste.

In a few instances, while electroding very small bar-shaped ZnTe crystals for Hall effect measure-

ments, the lateral spread of the Li-diffused area or, possibly, a fine spray of droplets from the Li solution caused a partial shorting of some of the electrodes to each other. To safeguard against such low resistivity surface channels, the following procedure was adopted for crystals with closely-spaced (less than a few mm) contacts. After forming the Li-contacts, each was covered with a small drop of thermosetting resin (*e.g.*, GE 7031 "Adhesive and Insulating Varnish"). After the resin had set for 30 to 60 min, the crystal was etched for 30 to 45 sec in boiling concentrated NaOH. This removed some 20-50$\mu$ of material from the crystal surface in locations not covered by the resin. After rinsing, the resin was dissolved in a 1:1 mixture of ethyl alcohol and toluene, and a gold dot was deposited on each of the small Li-diffused mesas left by the etching of the surrounding areas. Crystals electroded in such fashion rarely showed any signs of interelectrode shorting. With contacts that were more than a few mm apart, this more complicated procedure was, in most cases, unnecessary.

## Electrical Properties

Figure 1 shows a series of oscilloscope I-V traces obtained between a pair of Au and pair of Li-Au contacts on two ZnTe crystals from the same boule at several temperatures. The resistivity of the crystals was about 10 ohm-cm at room temperature and 200 ohm-cm at 55°K. It can be seen that whereas the Au contacts show a considerable contact resistance already at 300°K (note the different current scales for the Li-Au and the Au sequences), the Li-Au contacts stay relatively low resistance down to 55°K. At 70°K the contact resistance of the Au electrode is so high as to make the current through the crystal unobservably low on the scale employed. Frequently the Au contacts to ZnTe have displayed strongly nonohmic behavior even at room temperature. Investigation of the conditions which produce optimum room temperature Au contacts showed that a 60-sec heating period at 80°-100°C after the forming step led to best results. No heating or heating at higher temperatures produced much inferior contacts. However, Au contacts with even the best room temperature characteristics started rapidly deteriorating at about 150°C and were unusable for Hall effect measurements on high resistivity ZnTe crystals below liquid $N_2$ temperature. The significance of this finding is discussed below.

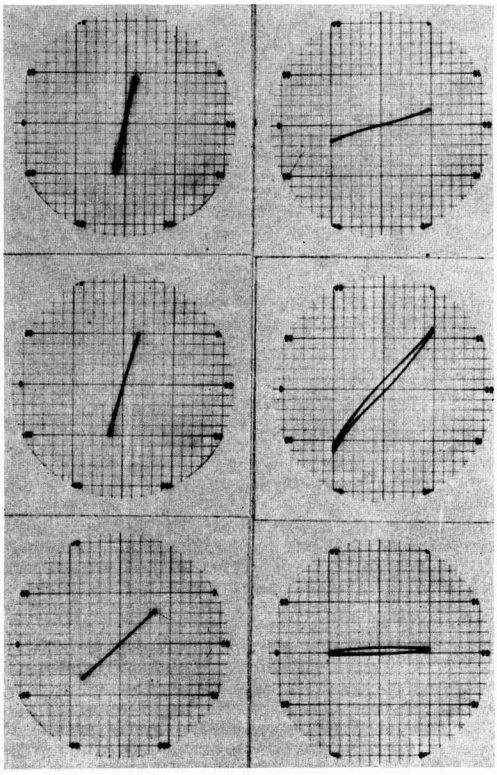

Fig. 1. Current-voltage characteristics obtained between a pair of Li-Au (left sequence) and a pair of Au (right sequence) contacts on ZnTe. Horizontal scale 1v/in. (1 in. corresponds to one large division). The temperatures and vertical scales are, from top to bottom: Li-Au sequence, 300°K, $10^{-3}$ amp/in.; 232°K, $10^{-3}$ amp/in.; 55°K, $10^{-6}$ amp/in.; Au sequence, 300°K, $10^{-4}$ amp/in.; 232°K, $10^{-5}$ amp/in.; 70°K, $10^{-7}$ amp/in.

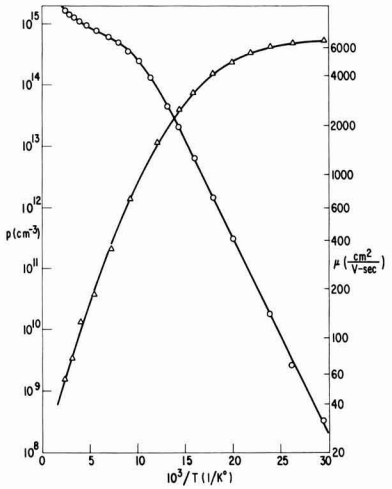


Fig. 2. Temperature dependence of the free hole concentration (circles) and of the Hall mobility (triangles) of an undoped ZnTe crystal.

Figure 2 shows the temperature dependence of the free hole concentration and of the Hall mobility of an undoped p-type ZnTe crystal. Measurements of this type at temperatures below the liquid $N_2$ range have been very difficult before due to the unavailability of suitable contacts. The data in Fig. 2, obtained with a crystal with five Li-Au contacts, have enabled us, for the first time, to extend the measurements to about 35°K. On a reciprocal temperature scale this provides an additional range extending from about $10^3/T = 14$ (pumped $N_2$ temperature) to $10^3/T = 29$. As can be seen in the figure, this is the range in which the log p *vs.* $1/T$ relationship has become linear, and which, therefore, enables one to obtain the acceptor ionization energy with good accuracy. Hall mobility measurements between the liquid $N_2$ temperature and 35°K indicate increasing departure from pure LO phonon scattering (4). Mobility studies in this temperature range thus make it possible to investigate the scattering due to low concentrations of charged impurities.

The forward I-V characteristics at 77°K of a $ZnSe_{0.36}Te_{0.64}$ light emitting p-n junction diode (8) with an In-Hg electrode on the n-type side and either a Li-Au or a Au electrode on the p-type side of the diode are compared in Fig. 3. It can be seen that the Li-Au contact allows a substantially higher current to pass through the diode than the Au contact. The strongly nonideal I-V characteristic of this particular diode even with the Li-Au contacts is due to the high bulk resistance of the p- and n-type sides of the diode.

It has been reported (7) that originally low resistivity Li-doped ZnTe crystals gradually become high re-

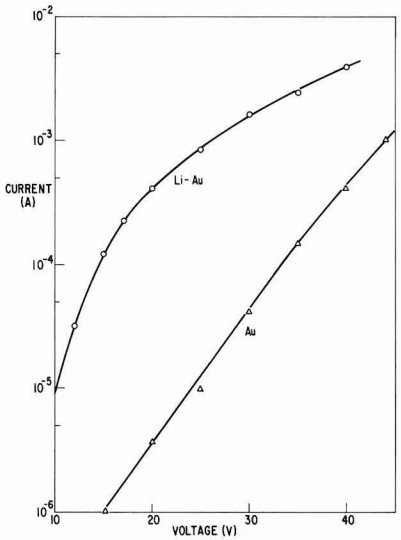


Fig. 3. Forward I-V characteristics of a $ZnSe_{0.36}Te_{0.64}$ light emitting p-n junction diode with an In-Hg electrode on the n-type side and either a Li-Au (circles) or a Au (triangles) electrode on the p-type side.

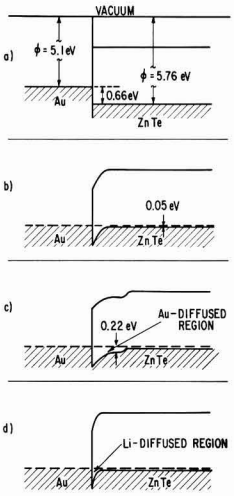


Fig. 4. Band structure of the Au-ZnTe contacts. (a) Relative positions of the Fermi levels in Au and ZnTe; (b) "Noninteracting" Au contact; (c) Au-diffused contact; (d) Li-diffused contact with Au overlay.

sistivity when annealed at even relatively low temperatures. The high ionic mobility of Li and its tendency to associate with other lattice defects in semiconductors is well known (9). In view of this a life test was conducted with a $ZnSe_{0.36}Te_{0.64}$ p-n junction diode in which the I-V characteristic was measured originally, and after (*a*) 264 hr in liquid $N_2$; (*b*) 312 hr at room temperature in vacuum; (*c*) 640 hr at room temperature in air; and finally (*d*) 93 hr at liquid $N_2$ temperature in vacuum, with 30v forward bias. The I-V characteristic was found to be essentially unchanged after each of the indicated periods, indicating the electrical stability of the Li-Au contacts under the test conditions employed.

## Discussion

The shallow acceptor activity in undoped ZnTe and CdTe has generally been attributed to doubly ionizable Zn vacancies (4, 10, 11), which have their first charge state about 0.05 ev above the valence band edge. Acceptor states with ionization energies comparable to that of the Zn vacancy have been observed in Li- and Na-doped ZnTe and CdTe (7). The noble metals Ag, Cu, and Au, on the other hand, have been found to introduce deeper acceptor states, 0.11, 0.15, and 0.22 ev, respectively (4). Using this information in conjunction with the results of the present study leads to the following characterization of the Au and Au-Li contacts.

As shown in Fig. 4a the relative work functions of Au and ZnTe are such (3) as to suggest a barrier of about 0.66 ev between the Fermi level in Au and the valence band edge in ZnTe. Although the presence of surface contamination, surface states, etc., often does not allow one to rely on simple calculation of barrier heights from work function data, it has been shown by several workers (3, 12) that in the case of II-VI compounds this is often not a bad approximation. The band structure resulting from an essentially noninteracting contact (in the sense that the barrier shape and height depends only on the work function difference of Au and ZnTe and the charge density in ZnTe) on undoped ZnTe would then look as shown in Fig. 4b. Due to a moderate concentration of shallow Zn vacancy acceptor states, the barrier height and width are such as to allow a small but measurable current of holes from the metallic contact into the valence band of ZnTe, and *vice versa*, at room temperature. At low temperatures, however, the barrier becomes a serious obstacle to current passage, and the contact becomes high resistance. We believe that the Au contact on undoped ZnTe, processed under optimum conditions, comes close to this case. Figure 4c schematically represents an Au contact in which Au has diffused too far into the crystal and replaced the shallow Zn vacancy acceptors by the deep Au acceptors. In addition to the barrier one now has a high resistivity region under the contact. The structure of the Li-diffused contact is shown in Fig. 4d. Here the high concentration of shallow acceptors in the surface region significantly reduces the barrier width and allows a tunneling current of holes to pass from the external Au electrode into the valence band of ZnTe even at low temperatures. Gold contacts to Li, Na, or P-doped ZnTe work in a similar fashion, except that now the high p-type doping exists uniformly throughout the bulk of the ZnTe crystal rather than just in the Li-diffused surface region.

The external contacts of chemically deposited Au are much superior to simple mechanical electrodes such as silver paste, colloidal graphite, or tungsten wire even on Li-diffused areas on ZnTe crystals. This suggests that the chemical reaction between ZnTe and the solution used to form the electroless Au contacts ($HAuCl_4 \cdot aq$) which consumes a small layer of the ZnTe crystal under the Au solution drop thereby effects a clean-up of the surface immediately beneath the Au deposit. Evidence of the etching action of $HAuCl_4 \cdot aq$ is revealed by microscopic examinations of Au-contacted ZnTe crystals, which show that the Au deposits reside in slightly depressed areas having the appearance of shallow negative mesas.

## Conclusion

It has been shown that electrical contacts to ZnTe and $ZnSe_xTe_{1-x}$ crystals fabricated by a method in which Li is first diffused into the area to be contacted and then an electroless Au deposit is formed on top of the diffused area, are significantly superior to electroless Au contacts. Using the Li-Au electroding technique on undoped ZnTe crystals it has been possible to investigate the electrical transport properties of this material at considerably lower temperatures than has been done previously. $ZnSe_xTe_{1-x}$ p-n junction diodes

electroded with the Li-Au contact on the p-type side have been found to pass substantially higher current at comparable voltages than diodes electroded with the Au alone. It has been suggested that the low contact resistance of the Li-Au contacts arises from the highly Li-doped surface regions of the ZnTe crystals being electroded. In such regions the shallow acceptor concentration is considerably higher than in undoped ZnTe, and hence the barrier separating the valence band of ZnTe from the filled band of the external contacting material is much narrower. This allows a tunneling current to communicate between the crystal and the external electrode even at low temperatures.

### Acknowledgments

The authors wish to thank R. K. Swank and H. H. Woodbury for the many helpful suggestions and stimulating discussions during the course of this work. Work on this paper was sponsored by the Air Force Cambridge Research Laboratories under Contract No. AF-19(628)-4976.

Manuscript received May 22, 1967.

Any discussion of this paper will appear in a Discussion Section to be published in the June 1968 JOURNAL.

### REFERENCES

1. G. H. Blount, M. W. Fischer, R. G. Morrison, and R. H. Bube, *This Journal*, **113**, 690 (1966).
2. R. W. Smith, *Phys. Rev.*, **97**, 1525 (1955).
3. R. K. Swank, *ibid.*, **153**, 844 (1967).
4. M. Aven and B. Segall, *ibid.*, **130**, 81 (1963).
5. M. Aven and C. A. Mead, *Appl. Phys. Letters*, **7**, 8 (1965).
6. D. de Nobel, Thesis, University of Leiden (1958).
7. B. L. Crowder and W. N. Hammer, *Phys. Rev.*, **150**, 541 (1966).
8. M. Aven, *Appl. Phys. Letters*, **7**, 146 (1965).
9. See, *e.g.*, H. Reiss, C. S. Fuller, and F. J. Morin, *Bell Syst. Tech. J.*, **35**, 533 (1956).
10. D. G. Thomas and E. A. Sadowski, *J. Phys. Chem. Solids*, **25**, 395 (1963).
11. L. R. Shiozawa and J. M. Jost, Aeronautical Research Laboratory, USAF, Contract No. AF 33(657)-7399, Final Report, March 19, 1965.
12. C. A. Mead, *Appl. Phys. Letters*, **6**, 103 (1965).

# The Effects of Double Insulating Layers on the Electroluminescence of Evaporated ZnS:Mn Films

**M. J. Russ and D. I. Kennedy**

*Bowmar Canada Limited, Ottawa, Ontario, Canada*

### ABSTRACT

The performance of ZnS:Mn electroluminescent layers deposited between double SiO insulating films is described. The dependence of emission properties on SiO and ZnS film thickness and Mn content are outlined. The relatively bright (700 ft-L) and efficient (1 lpw) emission is interpreted in terms of excursions from equilibrium trap occupation under high field conditions.

A considerable number of investigations of EL (electroluminescence) in thin ZnS films have been carried out using direct contact between the ZnS films and the conducting electrodes. In some investigations a single thin insulating layer has been used between the films and one of the electrodes. In most of the cases the results have shown marked asymmetry with respect to changes in polarity of the applied voltage. This situation has frequently led to difficulties in interpretation of the results. The present experiments were designed to eliminate some of the complexity by using thin insulating layers on both sides of the ZnS films.

In the past there have been a number of reports (1-11) on a-c EL in ZnS thin films. These reports have covered a variety of preparation techniques. Halsted and Koller (1) prepared EL (electroluminescent) ZnS:Mn films by the vapor reaction technique of Studer and Cusano (12), whereas Thornton (2) used the diffusion method of Feldman and O'Hara (13) to prepare ZnS:Mn:Cl and ZnS:Cu:Cl films. Vlasenko and Popkov (4) prepared ZnS:Mn films by separate evaporation and subsequent high-temperature diffusion of the constituents. Using a technique of coevaporation on a heated substrate proposed by Koller and Coghill (14), Antcliffe (15) has prepared EL ZnS:Mn films. Apart from variations in methods of producing the phosphor layer, various types of composite device have been investigated. Several authors (4, 6) have utilized an insulating layer between the phosphor film and the metal electrode. Harper (6) has reported that improved efficiencies and over-all brightness levels can be obtained by the use of an $SiO_2$ film of thickness between 7 and 160Å in this position.

The technique of coevaporation of ZnS and Mn on a heated substrate was adopted for the present experiments because of the simple, one-stage process.

#### *Film Preparation*

High-purity ZnS in either single crystal or compressed polycrystalline form was used as source material and, in the majority of experiments, Mn powder was added to the ZnS crystals in a range of concentrations from 0.04 to 6.0 w/o. To maintain uniform conditions in successive depositions the accurately weighed charges were evaporated to completion.

It was found that in order to obtain high-brightness EL the deposition conditions were critical. Substrate temperatures had to be maintained in the range 250°-300°C. Above 300°C significant crystallization of the ZnS film occurred and this resulted in the formation of an opaque white layer. For substrates maintained at temperatures between 20° and 250°C, only low-level emission was obtained. The critical deposition rate was found to be 1000 Å/min at a pressure of $10^{-5}$ Torr. The source temperature required to maintain this deposition rate at a distance of 7 in. from the substrate was 1230°C as determined by an optical pyrometer. The use of a lower evaporation rate did not permit sublimation of the added Mn, and a higher rate led to poor incorporation of the Mn in the film. This latter condition resulted in the deposition of a film having a black metallic coloration.

When the critical deposition conditions were met it was possible to obtain emission from panels with a range of ZnS film thicknesses and Mn concentrations. In order to obtain panels with a usable brightness, however, it was necessary to control the latter parameters also.

Prior to deposition of the ZnS film a layer of SiO was evaporated onto the unheated tin-oxide coated glass substrate. SiO thicknesses which were varied from 600 to 5000Å were used. Subsequent to the deposition of the phosphor film a second SiO layer was evaporated and finally metal electrodes were deposited. The properties of devices made with this structure were found to be independent of the metal electrode used (Al, Au, and In were each investigated). The results are based on an evaluation of at least 36 devices for each experiment.

## Results

The emission resulting from a-c excitation of the ZnS:Mn films was located in the same region of the spectrum as reported by previous authors. Using a DK-2A spectrophotometer it was found that the peak occurred at 5780Å and the half-width was 450Å.

On first application of voltage to these devices it was found that the emission would grow steadily to a uniform brightness over the active area. This behavior contrasted strongly with previous experiments carried out in this laboratory and elsewhere on structures with no insulating layers or a single such layer. In the latter cases it was found that a "forming" process, in which the phosphor was subjected to a critical near-breakdown electric field, was required to produce over-all luminescence. This "forming" process was attended initially by high currents without the presence of EL, and the emission appeared gradually as the currents fell to lower values. These processes have been discussed by Goldberg and Nickerson (16) and Cusano (17). The use of single insulating layers reduces the severity of the break-in process, and the double layers described in this report virtually eliminate the effect.

*Effects of* SiO *layers.*—Using the deposition conditions described above a 1000Å film of SiO was evaporated on tin-oxide coated glass followed by deposition of a 1.5$\mu$ ZnS:Mn film (Mn concentration in source of 0.6 w/o). This was followed by deposition of SiO stripes which increased in thickness in steps over the range from 220 to 5000Å. Metal electrodes of area $6 \times 10^{-2}$ cm$^2$ were then evaporated to complete the devices.

Figure 1 shows the results obtained on a-c excitation of these films at a frequency of 13 kHz in terms of the dependence on surface brightness on the rms electric field applied across the ZnS film. (This latter parameter was estimated from the total applied voltage using measured results for the dependence of the dielectric constants of ZnS and SiO on film thickness at the frequencies used.) The brightness was measured using a Spectra-Spot brightness meter. All results show a marked dependence of brightness on SiO thickness. As the SiO thicknesses were gradually increased it was found that the observed emission for a given field across the ZnS layers passed through maxima and minima. Although the emission process may be influenced by SiO thickness to some extent, the oscillatory nature of the characteristics pointed strongly to the existence of optical interference effects in the composite structure.

To maximize the observed emission in the above structure it was necessary to use particular values of SiO layer thickness. Utilization of data similar to that shown in Fig. 1 for dependence of brightness on SiO thickness at fixed values of ZnS field showed that the maximum brightness is obtained for an SiO thickness of 650Å. This differs from the theoretical value of 730Å calculated from reported refractive indices for the various layers; the difference probably

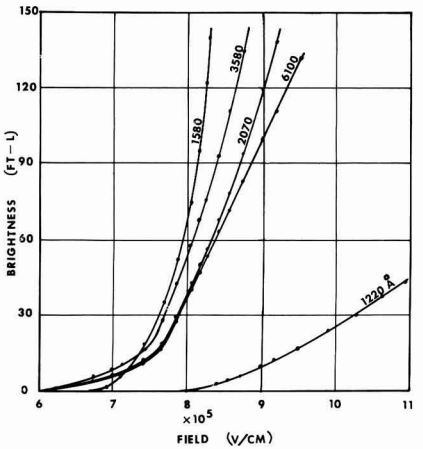


**Fig. 1. Dependence of brightness on ZnS field at 13 kHz for various SiO layers. 1000Å SiO films were used between the ZnS and $SnO_2$ and thicknesses of 220-5100Å of SiO were used between the ZnS and Al.**

results from the complex dependence of refractive index on film composition and thickness in the materials used. By varying the thickness of the SiO layer between the tin-oxide electrode and the ZnS film while maintaining the second SiO layer constant, it was possible to establish an optimum thickness value of 1300Å for the internal SiO layer. This value is in agreement with theory assuming $n_{SiO} < n_{SnO_2}$. A further increase in observed emission would be anticipated if the SiO or tin-oxide layers were replaced with materials with more ideally matched refractive indices.

It is interesting to note that the field strengths applied to the ZnS layers in our devices under routine operating conditions appear to be equal to or slightly higher than values normally used in this type of experiment and also than the reported dielectric breakdown strength for ZnS (4, 18). The calculated field strength values were obtained from separate measurements on SiO and ZnS layers of equivalent thicknesses and may not correspond exactly to the values which occur in composite structure. Nevertheless, the possibility exists that the double SiO layers eliminate one form of breakdown which occurs when direct metal/ZnS contact exists. The highest-efficiency EL in this work was observed when devices were operated in this field regime.

The dependence of brightness on frequency in the range from 1-20 kHz, showed, for all values of SiO thicknesses, a saturation effect above 8 kHz. As the frequency was increased above 13 kHz the average brightness at a given applied field decreased. Although this decrease may be associated with impedance effects in the various layers or with internal heating there is some evidence that it could be caused by failure of the excitation and recombination processes to reach completion within individual half cycles of the applied field.

*Effect of manganese concentration.*—There is little information in the literature on the dependence of ZnS film emission properties on Mn concentration. The majority of published work has been carried out on single values of Mn content in a range between 0.1 and 1 w/o. Vlasenko and Popkov (4) carried out experiments with several Mn concentrations and reported an optimum value of 0.6 w/o. In the present work a range of samples were prepared from sources containing from 0.04 to 6.0% Mn. In all cases the ZnS film thickness was maintained at 1.5$\mu$, and a symmetrical structure with double SiO layers of 700Å thickness was used.

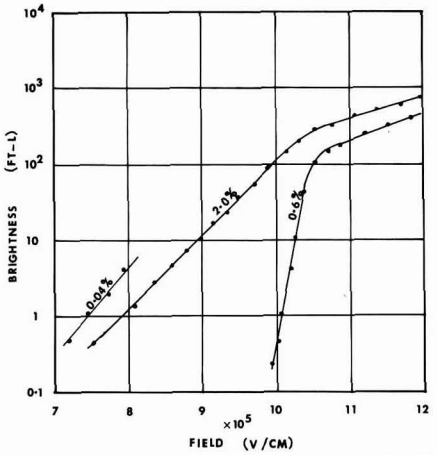


Fig. 2. Dependence of brightness on ZnS field at 13 kHz for various Mn concentrations. A ZnS thickness of 1.5$\mu$ was used in conjunction with double 700Å SiO layers.

Figure 2 shows the dependence of integrated brightness on the applied field at 13 kHz for three Mn concentrations. A considerable improvement in brightness levels was obtained as the Mn concentration increased. The maximum brightness for a phosphor containing 2 w/o Mn was in excess of 700 ft-L compared with 5 ft-L for a 0.044 w/o phosphor. If the Mn concentration was increased to 6%, the maximum brightness was reduced to 10 ft-L, and the panels were found to burn out at low applied voltages; this would appear to be due to the reduction in the resistivity of the phosphor with high Mn content. At 6 w/o Mn the films had a metallic black rather than yellow coloration. In the concentration range from 0.04 to 2.0 w/o the maximum brightness and discrimination ratio increased with increasing Mn content. Although 2% Mn was the maximum level of incorporation which led to repeatably good results using the described procedures it is felt that higher concentrations could be achieved using more sophisticated source materials and deposition procedures. In this case it should be possible to obtain even brighter emission from the devices. The present results are in agreement with Kodzhespirov *et al.* (8) who reported that emission intensities of ZnS:Mn devices increased with increasing Mn content. The maximum concentration used by these authors was 4.0 w/o and the ratio of emission intensity in the high-concentration devices to those with 0.04 w/o Mn was reported to be $10^3$:1.

The dependence of the El output on frequency exhibited little variation as the Mn concentration was altered.

*Effect of* ZnS *thickness.*—There is little information in the literature on the effects of variation of phosphor film thickness on device performance. The results from the present work are shown in Fig. 3. In these experiments the concentration of Mn was maintained at 0.6 w/o, and the film was again sandwiched between 700Å SiO layers. The maximum obtainable brightness increased with ZnS thickness to 1.3$\mu$, but did not increase appreciably thereafter. The discrimination ratio attained a maximum value for films in the region of 1.3$\mu$ in thickness. The figure also demonstrates that the field strength required to develop a given emission intensity falls towards a lower limit as the ZnS film thickness is increased. Vlasenko and Popkov (4) observed that emission intensity increased with increasing film thickness and the field strength at which emission was first discernible to the eye decreased with increasing thickness. The latter authors interpreted the results to be evidence

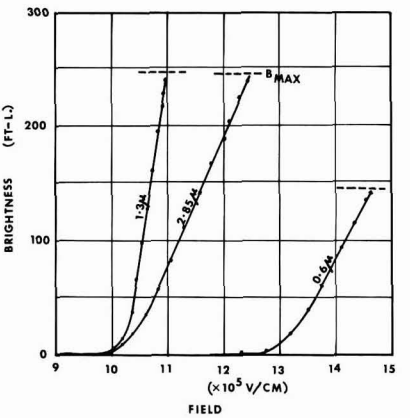


Fig. 3. Dependence of brightness on ZnS field at 13 kHz for various ZnS film thicknesses. A Mn concentration of 0.6 w/o was used and double 700Å SiO layers were employed.

of recombination throughout the bulk of the phosphor.

The dependence of electroluminescent output on frequency was found to saturate for all thicknesses of ZnS layers but, as the ZnS thickness was increased beyond 1.3$\mu$, saturation occurred at successively lower frequencies.

In measurements of I-V curves on a number of panels over a brightness range from 1 to 700 ft-L it was found that the current increased linearly with voltage. As the SiO thickness was decreased or as the Mn content was decreased a given change in applied voltage would produce a greater change in current.

The relationship between brightness and rms applied voltage was measured for a number of films and was found to consist of two exponential regions. The curves, which are illustrated in Fig. 4 for several ZnS thicknesses, obey the following relation

$$B = B_1\left(\exp\frac{V}{V_1} - 1\right) + B_2\left(\exp\frac{V}{V_2} - 1\right)$$

where $B$ is the surface brightness, $V$ is the rms applied voltage, and $B_1$, $B_2$, $V_1$, and $V_2$ are constants. Kolomeitsev *et al.* (9) also found their results to obey this expression.

*Efficiency-voltage characteristic.*—Figure 5 shows the efficiency-voltage curves for several typical de-

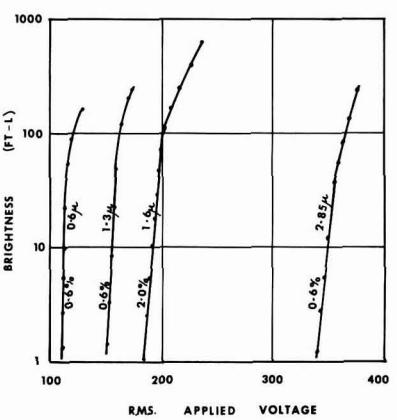


Fig. 4. Dependence on brightness on rms applied voltage for various ZnS film thicknesses and Mn concentrations using 700Å SiO layers.

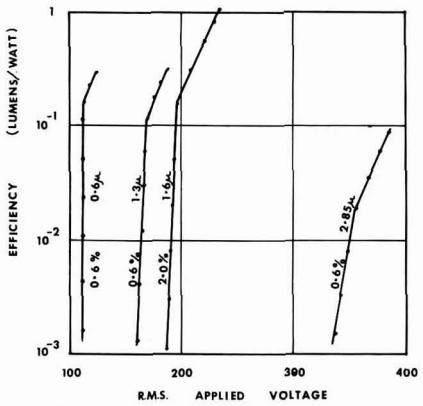


Fig. 5. Efficiency vs. rms applied voltage for various ZnS film thicknesses and Mn concentrations using 700Å SiO layers.

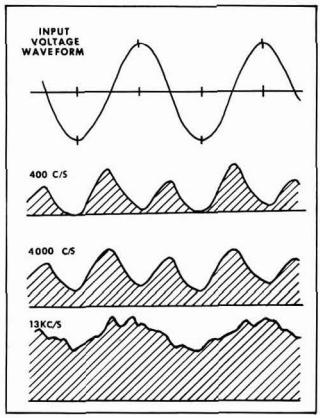


Fig. 6. Tracings of the emission waveforms obtained under sinusoidal excitation at several frequencies from a typical 2% Mn 1.6μ ZnS film.

vices. Once again double SiO layers were used and an excitation frequency of 13 kHz was employed. Emission efficiencies in the range from 0.1 to 1.0 lpw were regularly obtained; the higher efficiency results usually occurred when ZnS with 2 w/o Mn was evaporated, and the devices had the optimum SiO thicknesses for maximum emission.

The reduction in rate of increase of efficiency with applied voltage shown in Fig. 5 was also reported by Kodzhespirov and Kostylev (8). The dependence of efficiency on SiO thickness attained a maximum for values similar to those described in the section dealing with optical effects in these layers. Therefore, the improvement in efficiency can also be associated with these effects. The improvements in efficiency reported by Harper (6) for $SiO_2$ layers were associated with tunneling and accumulation effects in these layers; for these thin films (7-160Å) significant optical enhancement would not be anticipated.

In comparing the performance of thin-film and powder El phosphors it is significant that the efficiency of films increases with applied voltage whereas the efficiency of powder phosphors reaches a peak at approximately one-half of the desirable operating brightness and falls off with further increase of voltage. Although powder cells have exhibited maximum efficiencies of 14 lpw at low brightness, a value of 3 lpw is a more typical efficiency under normal operating conditions. The efficiency of thin-film panels of the type described here operating under similar conditions compares favorably with this value.

*Emission characteristics under sinusoidal and pulsed excitation.*—The shapes of the emission output waveforms were detected by a type 7625 photomultiplier and displayed on a Hewlett-Packard 175A dual-trace oscilloscope. Tracings of photographs of the waveforms obtained under sinusoidal excitation are shown in Fig. 6; the wavetrains progress from left to right of the diagrams. It was noted at low frequencies that there were two emission pulses per cycle of applied voltage and that the maximum emission lagged the maximum voltage for both polarities by 0.6 to 0.8 msec. At 400 Hz the two pulses were distinct but at 4 kHz the emission from a particular pulse did not decay to zero before onset of the succeeding pulse. At 13 kHz the emission pulses appeared only as a slight structure superimposed on a continuous level of emission.

It was found in a number of devices that, although similar time and frequency dependence of the emission peaks occurred, their amplitudes were not always equal. In these cases where the emission pulses were not equal in amplitude it was found that the light output corresponding to positive voltage applied to the tin oxide electrode could exceed the reverse case by up to 50%. Because of the similarity of behavior of the two peaks in all other aspects and because of the independence of results on the nature of the electrodes it is felt that the asymmetry results from nonuniform excitation or emission properties through the ZnS layer or at its interfaces with SiO. The nature of the device fabrication unfortunately introduces asymmetry in two respects. First, the distribution of Mn through the depth of the ZnS film may be nonuniform due to rapid depletion of Mn at the start of evaporation or deposit of an excess at the completion [in previous work (14) the Mn:Zn ratio has been shown to vary from 0.003 to 0.007 to 0.011 in subsequent 1-min deposition intervals]. A second factor arises from the sequential film deposition procedures which involve substrate heating during the ZnS evaporation. This process inevitably introduces inequalities in the properties of the initial and final SiO layers.

Figure 7 shows the response of a panel to symmetrical pulse excitation. Again two pulses per cycle were observed, and the maximum light emission lagged the voltage switching time by about 0.6 msec. Similar results were obtained for the cases where the tin-oxide electrode was pulsed positive and negative with respect to the metal electrode; the only slight distinction occurred in cases where the two emission

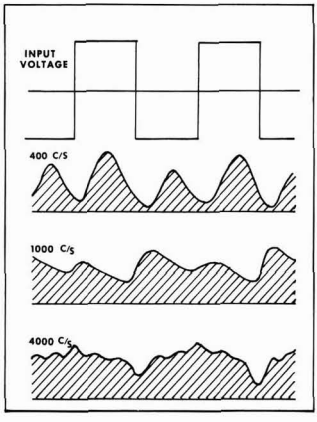


Fig. 7. Tracings of the emission waveforms obtained under symmetrical pulse excitation at several frequencies.

pulses were unequal in amplitude. In the latter case the larger pulse would occur when the tin-oxide layer was switched positive with respect to the metal electrode regardless of the potential at which the metal electrode was held (0 volts or full negative potential). At 400 Hz the two pulses per cycle were distinct but, as higher frequencies were applied, the light emission did not decay to zero between field reversals.

An interesting result was obtained by varying the mark: space ratio of the pulse waveform at a repetition rate in the region of 400 Hz, *i.e.*, below saturation frequencies. At a 50:50 duty cycle it was found that two approximately equal pulses per cycle were obtained, but as the ratio was moved to 85:15 the amplitude of one pulse decreased and the second pulse increased. At 85:15 only a single pulse occurred each cycle and this was approximately twice the size of its counterpart in the 50:50 duty cycle case. The single pulse was found to reach a peak approximately 0.6 msec after the termination of the 85% part of the cycle.

A series of experiments were performed in which the metal electrode was held at ground potential and the tin oxide was pulsed to full positive potential for 15% of each cycle. These experiments were repeated for the same pulse durations but with application of negative pulses to the tin oxide. Both sets of experiments were repeated using longer pulse durations so that the pulse occupied 85% of the cycle times. In all cases the results were similar, and the samples behaved as if the condition in which 85% of the time was spent was the equilibrium state and emission took place only after the applied voltage switched to the 15% state. Figure 8 illustrates two of these cases. It can be seen that the decay to zero emission following each light pulse takes several milliseconds.

*Ageing.*—One major disadvantage of thin-film El panels is their extremely rapid ageing characteristic. Apart from exceptional cases, thin films prepared by the above techniques show a reduction to half initial brightness within tens of operating hours. This figure is similar to values obtained by other authors. Ageing was accelerated by elevating the ambient temperature. It was noted, however, that the lifetime parameter showed distinct variations from one batch of devices to another prepared at a different time but in ostensibly the same manner, whereas from one device to another within any one particular batch there was consistency in ageing characteristics. There is evidence to suggest that this property is related to controlled and uniform manganese incorporation and that the use of more sophisticated material preparation and evaporation procedures may yield significant improvements. It was found that the lifetime of panels capable of several hundred foot-Lamberts could be extended by operation at lower brightness levels. The initial decay of brightness is not truly exponential, and a fast decay occurs during the application of the first few cycles of voltage. Because of this it is almost impossible to establish the true starting time for the decay process and therefore to state the true half-life. In our work we have taken the initial brightness as a value measured within the first minute of field application.

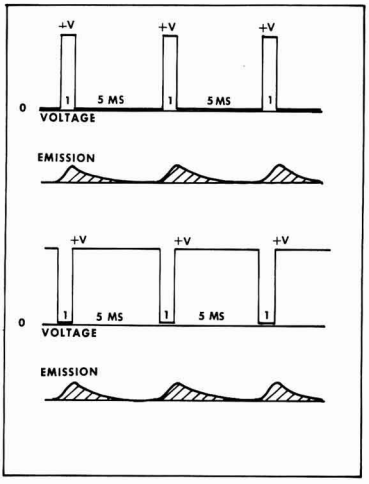


Fig. 8. Dependence of emission waveform on the applied pulse duty cycle.

## Discussion

A great deal of controversy is apparent in recent published work on ZnS films. The majority of workers suggest that the best structure for obtaining efficient emission has a blocking layer at the positive metal electrode while others report that blocking contacts at the cathode are advisable [these points are reviewed in ref. (19)]. In the present work using relatively thick double insulating layers the emission was found in almost every case to be similar for both applied polarities regardless of the nature of the metal electrodes. This result implies that the metal/insulator interface properties are of secondary importance and that the carriers required for the recombination process originate either in the ZnS film itself or in the ZnS/SiO interface barriers, for example, in an accumulation layer of the type described by Harper (6).

The most favored mechanisms for explaining electroluminescence in Zns films include injection effects from adjacent layers (16, 20) or internal p-n junctions (5),and electronic impact ionization (6, 21). It is almost certain that light emission can and does result from these and other processes depending on the film preparation and contact properties. In the case of the present devices where average fields of $10^6$ V/cm exist in the films under the optimum operating conditions one would anticipate a high-field mechanism to be operative. Impact excitation is likely to occur at these fields. The source of carriers for the emission process may be thermally generated electrons, but it is also possible that field effects lead to depopulation of traps in the various parts of the devices and that these could represent a significant contribution (23, 25). It should be noted that an average field of $8 \times 10^5$ V/cm was normally required for the efficient emission process in our layers and that the light output increased typically from 1 to 600 ft-L with a minor increase of field to $1.2 \times 10^6$ V/cm. Although inefficient emission was detected at lower fields its characteristics were different; the bright emission process appeared to have a definite field threshold. (Since there was evidence of space-charge effects in the devices it was possible that nonuniform field distribution occurred within the layers and that considerably higher than the average local fields may have been present.)

The emission from the films was similar to emission from a variety of ZnS:Mn devices and is believed to result from excitation of Mn centers by collision or resonance transfer. It is unlikely that direct field excitation of the Mn center itself occurred because of the high calculated field strength required for this process (22).

The emission waveform was considerably simpler than described results from ZnS films with other activator systems. The secondary peaks often described in work with other films were not observed in the present experiments. After a single step increment in voltage the emission was found to grow to a peak after 0.6 to 0.8 msec and then to decay over a considerably longer time interval. This behavior together with the observations under various applied waveforms could be explained in the following manner.

It is a well-established fact that ZnS films, interfaces, and oxide insulators possess a number of trapping levels with time constants ranging from microseconds to hours. The degree of occupation of these levels in structures such as the present panels is a complex function of applied voltage, ambient temperature, illumination, and past history. On changing the applied voltage a series of events occurs which leads to a new distribution of the carrier population throughout the devices. At first the free carriers and easily excited carriers flood toward their new positions and, more gradually, the deeper levels adjust in population according to a complex time dependence. Some of the adjustment occurs at a rate determined by thermal detrapping, but additional field-enhanced detrapping at fields as low as $5 \times 10^3$ V/cm could also occur (23). The internal field in each part of the structure cannot instantaneously acquire a new equilibrium value when the applied voltage is increased, but rather it will rise to a new value according to a time dependence determined by the level repopulation processes. Based on these premises it is tempting to conclude that it is this gradual field growth after a change in applied voltage which leads to the 0.6 msec delay before peak emission occurs. In other words the required field for the collision process does not appear across the total volume of the main emitting regions until 0.6 msec after application of the required voltage (the 0.6 msec time being a particular property of the present panels under these applied conditions).

As equilibrium is approached the flow of carriers diminishes and this leads to a gradual reduction in the number of excitations and recombinations. This is likely to be the explanation for the observed decay in emitted brightness after the peak value at 0.6 msec. A small residual light emission after equilibrium is established caused by thermally generated carriers entering the high-field regions might also be expected.

The above picture provides a simple and self-consistent explanation of the observed emission waveforms. Under sinusoidal or symmetrical pulse excitation there are equal excursions about each side of an average condition. This creates two major disturbances of equilibrium per cycle and could be expected to lead to two emission pulses per cycle. If the symmetry of the pulse excitation is altered to an 85:15 duty cycle, the equilibrium will be biased predominantly to the 85% condition. This being the case only one major excursion from equilibrium per cycle occurs. The excursion will be larger in magnitude than in the 50:50 duty cycle, and the result would be the observed single emission pulse of larger amplitude following the onset of the 15% parts of the waveform. This situation would occur regardless of the actual voltage experienced by the panel during the 85% part of the cycle.

The frequency dependence of the results is also explained. At high frequencies the 0.6 msec required by the present devices to reach full emission is not available. Instead the emission only grows to part of the maximum value. As the frequency is raised, however, the number of partial emissions per second is increased. These two effects counterbalance until, above 15 kHz the emission per pulse is so weak that the increased repetition rate no longer compensates and the output falls off. At low frequencies the growth of emission to a peak after 0.6 msec followed by a decay may be completed before the end of the applied voltage pulse. The total emission would in this case be simply determined by the pulse repetition rate. This linear emission fall off with reduced frequency was in fact observed.

With no applied field the distribution of occupied traps takes on its field-free form. Under sinusoidal or pulse excitation, parts of the ZnS films and adjacent layers become depopulated during a fraction of each voltage cycle and the population of deeper levels slowly adjusts to a value determined by the average occupation of the shallow levels. This operational equilibrium is different from the field-free case, and the transition from one situation to the other is believed to be responsible for the gradual build-up of emission during the first few cycles of voltage which is frequently described in the literature (26-28).

## Conclusion

The experiments that have been reported have shown that the use of insulating layers on both sides of a ZnS:Mn film can lead to bright and relatively efficient electroluminescence (700 ft-L at 1 lpw). It is considered that the emission results from an impact excitation process which occurs when the various energy states in the device are disturbed from equilibrium under high-field conditions. It is also believed that the present efficient emission occurs in a regime of electric field in which the ZnS layer would normally experience breakdown if placed in direct contact with a metal electrode.

The proposed mechanism for the EL provides a consistent and straightforward explanation of the present observations, and it can also be shown to provide a simple alternative explanation of several other experiments which are described in the literature. The mechanism is amenable to experimental verification although the procedures are complex because of the small range of applied voltage during which the panels pass from 1 to 700 ft-L emission. A study of the time-dependence of the repopulation effects and their relation to ambient temperature, field, and illumination will clarify the situation.

The critical nature of the film deposition parameters required to produce efficient devices can be attributed to two factors. First, the required electrical properties of the ZnS layer are strongly dependent on the degree of crystallinity and the structural properties of the film. Second, the incorporation of high concentrations of Mn without serious disruption of the film must be achieved.

The brightness, efficiency, and ageing characteristics of the ZnS devices all appear to be related to the successful incorporation of Mn without film disruption. The present films improved in these characteristics as the Mn content in the source material was increased from 0.04 to 2.0 w/o. There is every reason to believe that further improvements will be possible when more sophisticated deposition techniques are used.

## Acknowledgment

The authors would like to thank Mr. W. Carkner for his assistance in the fabrication of the ZnS devices and the Bowmar Instrument Corporation for permission to publish information contained in the First and Second Annual Research Reports on DIR Grant E54. The work was carried out as part of a research program jointly supported by Bowmar Canada Limited and the Defence Industrial Research Program operated by the Canadian Defence Research Board.

Manuscript received May 15, 1967; revised manuscript received June 12, 1967.

Any discussion of this paper will appear in a Discussion Section to be published in the June 1968 JOURNAL.

## REFERENCES

1. R. E. Halsted and L. R. Koller, *Phys. Rev.*, **93**, 349 (1954).
2. W. A. Thornton, *J. Appl. Phys*, **30**, 123 (1959)
3. W. A. Thornton, *Phys. Rev.*, **116**, 893 (1959).
4. N. A. Vlasenko and Iu. A. Popkov, *Optics & Spectros*, **8**, 39 (1960).
5. W. A. Thornton, *This Journal*, **108**, 636 (1961).
6. W. J. Harper, *ibid.*, **109**, 103 (1962).
7. V. L. Bakumenko, G. S. Kojina, and V. N. Favorin, *Optics & Spectros*, **15**, 262 (1963).

8. F. F. Kodzhespirov and S. A. Kostylev, *Optics & Spectros*, **12**, 144 (1964).
9. F.I. Kolomoitsev, F. F. Kodzhespirov, and S. A. Kostylev, *ibid.*, **12**, 497 (1964).
10. A. G. Gol'dman, G. A. Zholkevich, and N. P. Lazar, *Soviet Phys., Doklady*, **10**, 1148 (1966).
11. V. A. Vlasenko and S. A. Zyn'o, *Zn. Priklad. Spectrosk (USSR)*, **5**, 67 (1966).
12. R. J. Studer and D. A. Cusano, *J. Opt. Soc. Amer.*, **42**, 878 (1952).
13. C. Feldman and M. O'Hara, *ibid.*, **47**, 300 (1957).
14. L. R. Koller and H. D. Coghill, *This Journal*, **107**, 973 (1960).
15. G. A. Antcliffe, *Brit. J. Appl. Phys.*, **16**, 1467 (1965).
16. P. Goldberg and J. W. Nickerson, *J. Appl. Phys.*, **34**, 1601 (1963).
17. D. A. Cusano, Doctoral Dissertation, Rensselaer Polytech. Inst. (Jan. 1959).
18. K. L. Chopra, *J. Appl. Phys.*, **36**, 655 (1965).
19. P. Goldberg in "Luminescence of Inorganic Solids," P. Goldberg, Editor, p. 408, Academic Press, New York (1966).
20. R. C. Jaklevic, D. K. Donald, J. Lambe, and W. C. Vassell, *Appl. Phys. Letters*, **2**, 7, (1961).
21. D. A. Cusano in "Luminescence of Organic and Inorganic Materials," H. P. Kallman and G. M. Spruch, Editors, p. 494, John Wiley & Sons, Inc. New York (1962).
22. W. W. Piper and F. E. Williams in "Solid State Physics," Volume VI, p. 96, Academic Press, New York (1958).
23. K. W. Boër and U. Kümmel, *Ann. Phys.*, **16**, 181 (1955).
24. G. F. Alfrey and J. B. Taylor, *Proc. Phys. Soc.*, **68B**, 775 (1955).
25. M. J. Russ, Ph.D. Thesis, University of Birmingham (1962).
26. S. Kawashima, *This Journal*, **113**, 1083 (1966).
27. H. F. Ivey in "Electroluminescence and Related Effects," p. 65, Academic Press, New York (1963).
28. H. K. Henisch in "Electroluminescence," MacMillan, New York (1962).

# Technical Notes

## (Cd,Zn)S Photoconductive Sintered Layer

**Miyoshi Haradome and Hirokuni Kawashima**

*The Physical Science Laboratories, Nihon University at Narashino, Chiba-ken, Japan*

As is widely known, light-sensitive sintered layers of CdS show a remarkable fall-off of photoconductive sensitivity in the spectral region below 520 mμ, because of surface recombination of carriers. In order to remove such a fault, one of the authors (1) previously examined the preparation of (Cd,Zn)S solid solution layers in the way similar to that for usual CdS layers (2). It must be noted, however, that such a conventional method was unsuccessful in producing satisfactorily adherent and uniform layers of recrystallized (Cd, Zn)S, especially in the Zn-rich region.

In the present study, the authors have succeeded in developing a new sintering technique for the (Cd, Zn)S, layer by making use of a high-temperature, high-pressure argon atmosphere and of NaCl solvent flux. The resultant product exhibits high sensitivity even in the spectral region from 520 down to 400 mμ.

### Experimental

The sintering apparatus utilized in this work is shown schematically in Fig. 1. In a stainless steel tube an impurity protector and sample chamber both made of quartz are enclosed, and the whole system is put in a SiC resistance furnace for heat-treatment. The sample chamber is loosely sealed with a quartz cap. Fluorescent powder of (Cd, Zn)S solid solution activated with a small amount of Ag or Cu (product of the Dai-Nippon Paint Company, Ltd.) was used as starting material. A mixture of $3 \times 10^{-2}$ mole of the fluorescent powder and $9 \times 10^{-3}$ mole of high grade NaCl was blended with 3 cc of distilled water and was ground in a quartz mixer for 5 hr. This suspension was sprayed on the surface of high-purity alumina plates by a quartz spray-gun. The sprayed layer was dried for 2 hr at 80°C and was then enclosed in the stainless steel tube which was evacuated to $10^{-4}$ Torr. After introducing high-purity argon gas (oxygen content of 0.2 ppm) into the tube, the heat-treatment for sintering was started. It took about 20 min to raise the temperature to 1100°C, at which the sintering was most appropriately conducted.

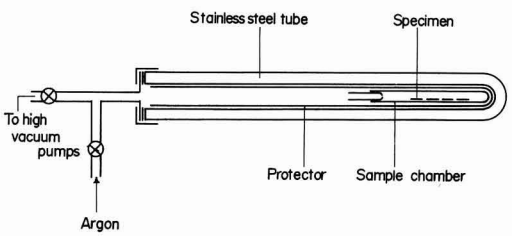


**Fig. 1. Schematic diagram of apparatus for sintering by the high-pressure sintering method.**

### Results and Discussions

From grain size observation with an optical microscope, the average grain size of the (Cd, Zn)S solid solution layers prepared in the pressure range above 30 atm has been found to indicate a monotonic increase with increasing sintering temperature (1000°-1150°C) and time (0-100 min). It must be noted that the evaporation of the specimen takes place under pressures below 30 atm. It may be emphasized, in addition, that x-ray diffraction data indicate no change in composition of (Cd, Zn)S solid solutions if the sintering is done at temperatures below 1150°C, under pressures exceeding 30 atm, and within times less than 100 min.

Figure 2 gives the sintering temperature dependence of the photocurrent and dark current produced in

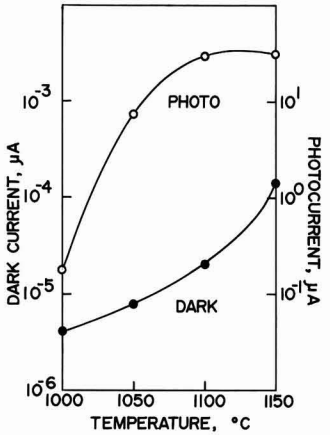


Fig. 2. Sintering temperature dependence of the photocurrent and dark current for the 30 m/o Zn, sintered for 60 min under 50 atm Ar.

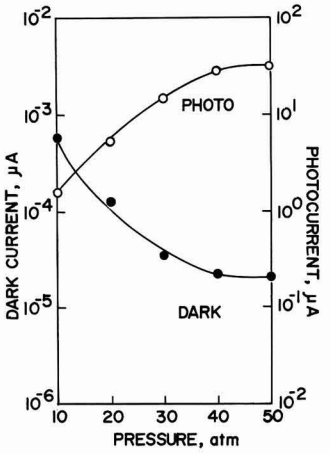


Fig. 3. Pressure dependence of the photocurrent and the dark current for the 30 m/o Zn, sintered for 60 min at 1100°C.

the specimens containing 30 m/o ZnS, while the sintering was done under a pressure of 50 atm for 60 min. A maximum of the photocurrent curve is found at 1100°C, making a sharp contrast to the monotonic increase of dark current. In Fig. 3 is presented the pressure dependence of the photocurrent and dark current for the specimen containing 30 m/o Zn when heat treated at 1100°C for 60 min. With increasing pressure, the photocurrent increases remarkably, while the dark current decreases, both showing leveling-off in the high-pressure range above 40 atm. The maximum position in the photoconductivity spectrum for a number of (Cd, Zn)S:Ag, Cl layers sintered at 1100°C for 60 min under 50 atm is shown schematically in Fig. 4. The shift of the photoconductivity peak with change in composition is almost parallel to that of the emission peak (3), which may suggest that composition of those (Cd, Zn)S layers has not changed during the heat-treatment. In Fig. 5, the decay time of the photocurrent when the same specimens were exposed to 100 Lx radiation is plotted against the composition. For the

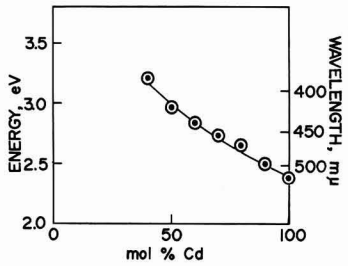


Fig. 4. Maximum of the photoconductivity spectrum of the (Cd,Zn)S:Ag, Cl solid solution sintered layers.

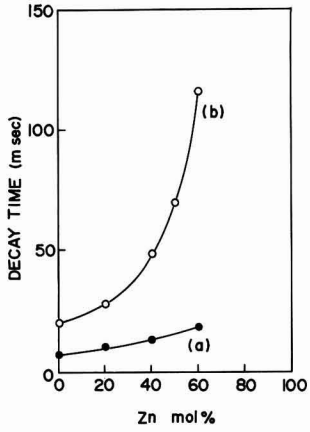


Fig. 5. Decay time of the photocurrent for the (Cd,Zn)S:Ag,Cl solid solution sintered layers. (a): high-pressure sintering method; (b) conventional sintering method.

sake of comparison, the behavior of specimens prepared by the conventional sintering method (1) is also shown in Fig 5. On the basis of these data, one can conclude that the much shorter decay times exhibited by the layers prepared at high pressures may be ascribed to the presence of fewer grain boundaries, causing less scattering of the photoconductivity carriers. On the other hand, the decay time is found to increase almost linearly with the content of Zn. Through a preliminary investigation of the behavior of thermally stimulated current and decayed thermally stimulated current, such an increase of the decay time has been concluded to arise from the increase of the density and depth of the electron traps.

Further studies, especially of electron and hole traps are being pushed forward and will be published in the not too far distant future.

Manuscript received June 12, 1967.

Any discussion of this paper will appear in a Discussion Section to be published in the June 1968 JOURNAL.

## REFERENCES

1. Ryuichi Hioki, Miyoshi Haradome, and Hiroshi Kukimoto, *Japan. J. Appl. Phys.*, **2**, (1963).
2. S. M. Thomsen and R. H. Bube, *Rev. Sci. Instr.*, **26**, 664 (1955).
3. R. E. Halsted, M. Aven, and H. D. Coghill, *This Journal*, **112**, 177 (1965).

# $Cd_4SiS_6$ and $Cd_4SiSe_6$, New Ternary Compounds

## Synthesis, Photoconductive and Fluorescent Properties

E. Kaldis,[1] L. Krausbauer, and R. Widmer

*Laboratories RCA Ltd., Zurich, Switzerland*

In the course of a program aimed at the synthesis of new photoconductors and phosphors attempts were made to synthesize ternary cadmium and zinc chalcogenides with silicon and germanium. Accordingly the following systems were examined: Cd-Si-S, Cd-Si-Se, Cd-Si-Te, Zn-Si-S, Zn-Si-Se, Zn-Si-Te, Zn-Ge-S, Zn-Ge-Se, Zn-Ge-Te. Ternary phases could be found only in the first two of these systems. The compounds $Zn_2GeS_4$ and $Zn_2GeSe_4$ which have been reported in the literature (1) could not be synthesized.

Since the compound $Cd_4GeS_6$ had been found to be a good photoconductor (2-5), it could be expected that metal silicon chalcogenides might also show photoconduction. Due to the lighter atomic weight of silicon the peak sensitivity was expected to be at shorter wavelengths than in the corresponding metal germanium chalcogenides (6).

This paper deals with the synthesis, crystal growth, and preliminary measurements of the photoconductivity and fluorescence properties of $Cd_4SiS_6$ and $Cd_4SiSe_6$.

$Cd_4SiS_6$ was synthesized by reacting stoichiometric quantities of cadmium sulfide, silicon, and sulfur (5*N* purity, Light, England) in evacuated quartz tubes. The tube with the well mixed starting materials was put in a furnace with a flat temperature profile and was slowly heated up to 850°C within 2 days. This slow heating rate was necessary to avoid explosions.

Guinier powder diagrams showed that the reaction product was isomorphous to the germanium compound which a new chemical analysis (3) showed to have the formula $Cd_4GeS_6$. The latter was found to crystallize in the $C_c$ space group with unit cell dimensions $a = 12.303$Å, $b = 7.056$Å, $c = 12.335$Å, and $\beta = 110°02'$ (4). The x-ray diagrams of $Cd_4SiS_6$ showed only the lines corresponding to those of $Cd_4GeS_6$. No additional lines could be detected. The angle $\beta$ for $Cd_4SiS_6$ was measured with the optical goniometer to $\beta = 110°30'$.

The $Cd_4SiS_6$ powder synthesized as described above looks very homogeneous but has a light olive green color, although the fundamental absorption edge of the compound lies at 4300Å (see below). Material synthesized in the presence of iodine or crystals grown by iodine transport have a lemon yellow color. Also, the powder synthesied in the presence of excess of sulfur is yellow. All these materials have the same x-ray diagram. The yellow color could not be restored by adding small amounts of excess cadmium sulfide, silicon, or a mixture of silicon and sulfur to the starting material. Yellow crystals of $Cd_4SiS_6$ heated at 1250°C in a small evacuated quartz ampoule become greenish. In the presence of a partial sulfur pressure of 1 atm the color of the crystals remains yellow.

It is possible that the green color is the result of a slight decomposition taking place only at the surface of the powder. At 1250°C this decomposition can obviously be suppressed by 1 atm of sulfur pressure. A partial sulfur pressure which is probably high enough to prevent decomposition is also built up during the iodine transport.

$Cd_4SiSe_6$ was synthesized from the elements in the presence of iodine at 800°C in an evacuated quartz ampoule.

Crystals of $Cd_4SiS_6$ with dimensions up to 10 x 5 x 6 $mm^3$ were grown by iodine transport at 800°C in a closed system. The iodine concentration in the ampoules was 4 $mg/cm^3$. Using values of undercooling (4) between 5° and 30°C and growth times of two to ten days crystals with varying dimensions and highly reflecting natural faces could be grown.

Doped crystals were grown by mixing the starting materials with the dopant in the form of the metal iodides.

Black crystals of $Cd_4SiSe_6$ with dimensions of a few millimeters were grown by iodine transport at 800°C.

The optical measurements were made with conventional apparatus. For photoconductivity and absorption measurements in the visible part of the spectrum a xenon high-pressure lamp was used as light source in connection with a Leiss single prism monochromator and a Zeiss double prism monochromator, respectively. In the near uv a hydrogen lamp was used. A high impedance Keithley micromicroammeter in connection with a Moseley X-Y-recorder was used to register photocurrent *vs.* wavelength and current-voltage curves.

Reflectivity measurements were carried out with a tungsten or hydrogen lamp, a Bausch and Lomb grating monochromator, and a RCA 1P28 phototube as detector.

For luminescence measurements the samples were irradiated with the 3660Å-Hg-line, the luminescent light was focussed onto the entrance slit of a single prism Leiss monochromator. An RCA 7265 photomultiplier was used as detector of the light at the exit slit of the monochromator. The output of the photomultiplier was fed into a Varian chart recorder, the speed of which was synchronized with the prism rotation of the monochromator. The curves so obtained were corrected for the multiplier sensitivity and the dispersion of the prism to give the true spectrum in arbitrary units.

It was found that as-grown crystals were covered with an insulating surface layer. To remove this surface layer the crystals were washed immediately after they had been taken out of the ampoule, first with hot hexane to dissolve silicon iodide and then with alcohol to dissolve cadmium iodide. In cases where this treatment was not successful the insulating layer could be removed mechanically by grinding and polishing the crystal surface. After these treatments evaporated contacts of silver, cadmium, indium, gallium, and aluminum were found to be ohmic and to give the same wavelength dependence of the photocurrent. Throughout this work indium electrodes were used unless otherwise stated. The electrodes were evaporated in a vacuum of $5 \cdot 10^{-5}$ Torr, the electrode separation $d$ being 0.3 to 0.8 mm.

Annealing experiments were made in air and hydrogen at different temperatures. For each experiment the crystals were kept at the annealing temperature for 30 min. All dark and photocurrent measurements were done at room temperature.

### Results

Undoped $Cd_4SiS_6$ crystals without any heat-treatment show good photoconductive properties. Measurements with a thermoelectric tester (7) showed n-type conductivity, both in the dark and under illumination. The crystals have a dark conductivity between $10^{-12}$ and $10^{-10}$ ohm-$cm^{-1}$. A typical wavelength dependence of the photoconduction is shown in Fig. 1. There

[1] Present address: Laboratorium für Festkörperphysik, ETH, Zürich, Switzerland.

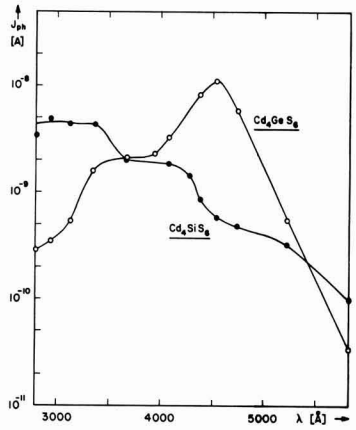


**Fig. 1. Wavelength dependence of the photocurrent for unannealed $Cd_4SiS_6$ and $Cd_4GeS_6$ crystals. The photocurrent is corrected for equal numbers of incident light quanta under the assumption that $J_{Ph} \alpha B$ ($B$ = light intensity).**

are three regions in the response curve: All $Cd_4SiS_6$ crystals show a photoconductivity shoulder around 5000Å, another one at about 4200Å, and a third one around 3300Å. Typical values for the photoconductivity of $Cd_4SiS_6$ crystals at 4200Å with a light intensity of $N = 10^{12}$ quanta/cm$^2$ sec lie between $10^{-6}$ ohm-cm$^{-1}$ and $10^{-7}$ ohm-cm$^{-1}$. At 3000Å and for the same light intensity the photoconductivity values vary between $10^{-7}$ and $10^{-5}$ ohm-cm$^{-1}$. The ratio of the photoconductivity to the dark conductivity lies between $10^3$ and $10^4$. The sensitivity defined by Bube (8) as $S = \Sigma_{Ph} \cdot d^2$/absorbed power ($\Sigma_{Ph} = I_{Ph}/U$, $U$ = applied voltage) reaches values of $10^{-2}$ mho cm$^2$/w, which is of the same order of magnitude as the values for cadmium sulfide and $Cd_4GeS_6$. The $Cd_4SiS_6$ crystals show a gain of several hundreds for a field strength of $10^3$ v/cm. The response time of these crytals is of the order of a few seconds for a light intensity of $N = 10^{12}$ quanta/cm$^2$ sec. It increases with decreasing light intensity.

Absorption measurements on $Cd_4SiS_6$ crystals showed the fundamental optical absorption edge to lie at about 4300Å. The absorption coefficient shows an exponential increase for wavelengths shorter than 4550Å and reaches a value of $k = 5 \cdot 10^3$ cm$^{-1}$ for $\lambda$ = 4360Å. We conclude therefore that the photoconductivity shoulder around 4200Å corresponds to the fundamental optical absorption edge and the shoulder around 5000Å is due to impurity photoconduction.

The question arises as to the origin of the third shoulder in the photoconductivity response around 3200Å. To our knowledge so far an increase in photoconductivity for energies higher than the fundamental absorption edge has only been observed for GaP (9). CdS and especially $Cd_4GeS_6$ do not show such an effect. (The fundamental absorption edge of $Cd_4GeS_6$ lies at about 4700Å). The increase in photoconductivity in the uv for $Cd_4SiS_6$ could be due to a change in the physical properties of $Cd_4SiS_6$ (absorption coefficient, mobility, carrier lifetime a.s.o.) as a function of light frequency or intensity, as is invoked to explain the anomalous photoresponse in GaP (9), or it could be due to a surface effect caused either by surface states, or by a surface of different chemical composition on top of the $Cd_4SiS_6$ crystals.

Reflectivity measurements have been made on a $Cd_4SiS_6$ and a $Cd_4GeS_6$ crystal from $\lambda$ = 5000Å to 2200Å (Fig. 2). Both curves show a maximum at the fundamental optical absorption edge and a weak peak around 3400Å in the case of $Cd_4SiS_6$ and around 3300Å in the case of $Cd_4GeS_6$. Similar results are known for GaP (10). Therefore the uv photoresponse in $Cd_4SiS_6$ could be due to strong direct optical transitions similar to the explanation presented by Nelson *et al.* for GaP (9).

It might be worthwhile mentioning that the photoconductivity response for $Cd_4GeS_6$ also shows a shoulder for energies higher than the fundamental absorption edge (Fig. 1). Therefore similar transitions might occur in $Cd_4GeS_6$, but different surface states in this material might cause a decrease in the carrier lifetime and by this a decrease in photoconductivity.

It is generally known that silicon-sulfur compounds hydrolyze easily (11-13). A colorless insulating layer has been found on the surface of the as-grown crystals. Although the greater part of this layer is removed by chemical or mechanical means, in order to get ohmic contacts on the crystal, it is probable that a thin layer still exists on the surface of the crystals. However, this layer must inhibit further hydrolysis because the photoconductive properties of as-grown and ground $Cd_4SiS_6$ crystals do not change after a treatment with hot water (100°C, for 30 min). An amorphous, hydrolyzed surface layer on the $Cd_4SiS_6$ crystals could be responsible, either alone or in conjunction with the $Cd_4SiS_6$ lattice, for the observed high uv-sensitivity if one assumes a high absorption coefficient of this surface layer for wavelengths between 3000 and 4000Å. Bradford *et al.* (14) have found a fairly high absorption coefficient for $SiO_{2-x}$ layers depending on the amount of oxygen and the degree of disorder of the layers. The higher the silicon to oxygen ratio or degree of disorder the higher the absorption coefficient around 3000Å was found to be.

Some indication for such an explanation of the uv photoconductivity can be found in annealing experiments in air and hydrogen. Annealing $Cd_4SiS_6$ crystals at 300°C in air, *e.g.*, decreases the uv sensitivity considerably whereas it is unchanged or increased for crystals annealed in hydrogen. In the first case the decrease of the uv sensitivity could be the result of a decrease of the silicon to oxygen ratio due to a partial surface oxidation which in its turn might lead to a decrease of the absorption coefficient. On the other hand annealing in hydrogen is not expected to decrease the silicon to oxygen ratio.

So far no final decision can be made about the origin of the uv photosensitivity of untreated $Cd_4SiS_6$ crystals. Further experiments are necessary to show if the uv photoresponse in $Cd_4SiS_6$ has a similar origin to that in GaP or to give direct evidence for the ex-

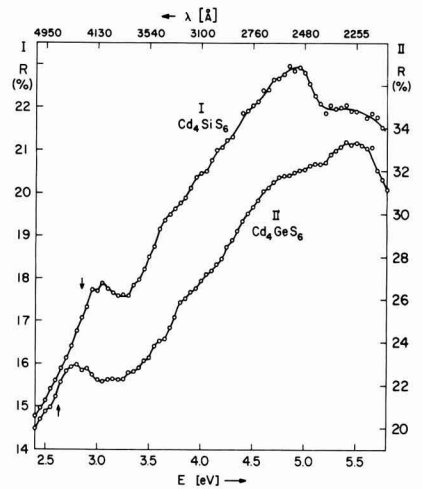


**Fig. 2. Reflectivity curve for $Cd_4SiS_6$ and $Cd_4GeS_6$. The arrows indicate the approximate positions of the fundamental optical absorption edge.**

**Table I. Peak wavelengths and intensities of various $Cd_4SiS_6$ phosphors in comparison with the commercial RCA CdZnS : Ag phosphor**

| Sample No. | Composition | $T$ = 300° $\lambda_{max}$ | $T$ = 300° $I_{rel}$, % | $T$ = 77°K $\lambda_{max}$ | $T$ = 77°K $I_{rel}$, % |
|---|---|---|---|---|---|
| 51 | CdZnS : Ag | 6800 | 100 | 6800 | 120 |
| 227 | $Cd_4SiS_6$ | 7100 | 1.0 | 6500 | 30 |
| 125 | + Cu | 7100 | 30 | 6900 | 36 |
| 127 | + Ag | 7000 | 4 | 6600 | 11 |
| 231 | + Hg | 7100 | 7 | 6700 | 37 |
| 131 | + Mn | — | — | 6650 | 48 |
| 133 | + Ga | 7100 | 1.5 | 6600 | 45 |
| 234 | + In | 7100 | 1 | 6650 | 30 |
| 132 | + Tl | 7300 | 1.2 | 6600 | 45 |
| 233 | + Nb | 7000 | 2 | 6600 | 28 |
| 129 | + Nernst filament* | — | — | 6600 | 60 |
| 232 | + Eu | 6900 | 0.6 | 6600 | 27 |
| 126 | + U | — | — | 6650 | 25 |
| 130 | + As | — | — | 6600 | 46 |

* Consisting of 85% $ZrO_2$ and 15% $Y_2O_3$.

istence and eventually the composition of a surface layer.

$Cd_4SiS_6$ crystals annealed in cuprous sulfide for 3 and 6 hr show a broad photoconductivity response in the wavelength region from 4400 to 6200Å with a maximum photoconductivity of $\sigma_{Ph} = 4 \cdot 10^{-4}$ and $4 \cdot 10^{-5}$ ohm-cm$^{-1}$, respectively, but no uv sensitivity. No further annealing experiments have been made with these crystals.

Preliminary measurements on $Cd_4SiSe_6$ crystals showed that this material is a good photoconductor. The dark conductivity is similar to that of $Cd_4SiS_6$. The photoconduction *vs.* wavelength curve shows a broad region of photosensitivity from about 4000 to 7000Å. The photoconductivity reaches values of $\sigma_{Ph} = 3 \cdot 10^{-5}$ ohm-cm$^{-1}$, and the sensitivity is $S = 10^{-2}$ mho cm$^2$/w. No photoconductivity was observed for wavelengths shorter than 4000Å.

Undoped $Cd_4SiS_6$ crystals and those doped with copper, silver, mercury, gallium, indium, thallium, europium, arsenic, niobium, manganese, uranium, and mixed with a powdered Nernst filament (consisting of 85% zirconia and 15% yttrium oxide) were examined for their luminescence properties.

At room temperature, only copper-doped material showed a considerable red luminescence with a broad maximum peaking at 7200Å, the intensity of the peak wavelengths being about one-third of the red commercial RCA ZnCdS : Ag phosphor (33-Z-639*D*) at its peak wavelength (see Table I).

At liquid nitrogen temperature we found the results listed in Table I. All luminescence peaks are shifted to shorter wavelengths in comparison with the peaks at room temperature. Undoped material shows a broad luminescence peak at 6600Å with an intensity about one-third of the mentioned red RCA phosphor. In general the dopant material has only little influence on the luminescence properties of $Cd_4SiS_6$ at 77°K. Only mercury and copper shift the peak to longer wavelengths, by 200 and 400Å, respectively. The highest intensity is achieved by $Cd_4SiS_6$ doped with a powdered Nernst filament; the intensity is twice as high as that of the undoped material. Silver, on the other hand, decreases the luminescence intensity to about one-third.

*Acknowledgment*

The authors wish to thank Dr. G. Harbeke, Dr. H. Kiess, and Dr. R. Nitsche for stimulating discussions, and Mr. E. Meier for taking the reflectivity measurements.

Manuscript received June 22, 1967.

Any discussion of this paper will appear in a Discussion Section to be published in the June 1968 JOURNAL.

## REFERENCES

1. H. Hahn, Paper given at the XVIIth IUPAC Congress, Munich, Germany, September 1959.
2. L. Krausbauer, F. Lappe, W. J. Merz, and R. Nitsche, *Physik. Verhandl.*, 366 (1962).
3. E. Kaldis and R. Widmer, *J. Phys. Chem. Solids*, **26**, 1697 (1965).
4. R. Nitsche, *Z. Krist.*, **120**, 1 (1964).
5. H. Kiess, *Helv. Phys. Acta*, **37**, 638 (1964). H. Kiess, To be published in *J. Phys. Chem. Solids*.
6. W. J. Merz, *Helv. Phys. Acta*, **35**, 274 (1962).
7. A. G. Fischer, J. N. Carides, and J. Dresner, *Solid State Comm.*, **2**, 157 (1964).
8. R. H. Bube, "Photoconductivity of Solids," p. 59, John Wiley & Sons, Inc., New York (1960).
9. D. F. Nelson, L. F. Johnson, and M. Gershenzon, *Phys. Rev.*, **135**, A1399 (1964).
10. R. Zallen and W. Paul, *ibid.*, **134**, A1628 (1964); E. F. Gross *et al.*, *Sov. Phys. - Dokl.*, **8**, 1103 (1964).
11. Gmelin's Handbuch der Anorganischen Chemie, Volume Silicon.
12. E. Zintl and K. Loosen, *Z. Phys. Chem.*, **A174**, 301 (1935).
13. A. Haas, *Z. angew. Chem.*, **77**, 1066 (1965).
14. A. P. Bradford, G. Hass, M. McFarland, and E. Ritter, *Appl. Optics*, **4**, 971 (1965).

# Temperature Oscillations in Czochralski Crystal Growth

J. R. Carruthers[1]

*Department of Metallurgy and Materials Science, University of Toronto, Toronto, Canada*

Temperature fluctuations resulting from thermal convection during crystal growth are known to cause growth rate fluctuations and impurity microsegregation. These fluctuations are normally random in otherwise stationary liquids, although Hurle (1) reports regular periodicities near the surface of liquid gallium at low-temperature gradients. When a liquid with such temperature oscillations is spun about a vertical axis or subjected to a magnetic field (if conducting), additional stabilizing forces are provided which eliminate the oscillations and allow steady flow. With spin, this additional force is the Coriolis force which acts on particles having a horizontal velocity component.

Spin may have a second important effect in addition to the stabilization of flow. When instability does arise under spin, the consequent motion might be oscillatory rather than unidirectional. This type of instability has been termed "overstability" and occurs only in fluids with a low Prandtl number, $N_{Pr}$, where

$$N_{Pr} = \nu/K < 0.68 \text{ for overstability}$$

where $\nu$ is the kinematic viscosity and $K$ the thermal diffusivity. This note reports the existence of overstable oscillations in rotating liquid silicon ($N_{Pr} \approx 0.088$) as observed from a fine set of growth striations appearing on the outer surface of nonrotated silicon crystals.

Chandrasekhar and Elbert (2) define a nondimensional frequency, $\sigma$, for overstable oscillations as

$$\sigma = \left[\frac{2}{1 + 2N_{Pr}}\right]^{1/2}\left[\frac{1 + N_{Pr}}{N_{Pr}}\right]^{1/3}\left[\frac{\pi^2}{2}\right]^{1/3} N_{Ta}{}^{1/3}$$

where $N_{Ta}$ is the dimensionless rotation rate given by

$$N_{Ta} = \frac{4\Omega^2 h^4}{\mu^2}$$

where $\Omega$ is the crucible rotation rate and $h$ is the liquid depth. Substitution of $N_{Pr}$ for liquid silicon gives

$$\sigma = 5.15\, N_{Ta}{}^{1/3}$$

Chandrasekhar and Elbert (2) write the oscillation period; $\tau$, as

$$\tau = \frac{2\pi}{\Omega}\frac{N_{Ta}{}^{1/2}}{2\sigma}$$

Substituting for $\sigma$ and using the crucible rotation rate, $\omega$, in revolutions per minute gives

$$\tau = 5.82\,\frac{N_{Ta}{}^{1/6}}{\omega} \text{ sec}$$

[1] Present address: Bell Telephone Laboratories, Inc., Murray Hill, New Jersey.

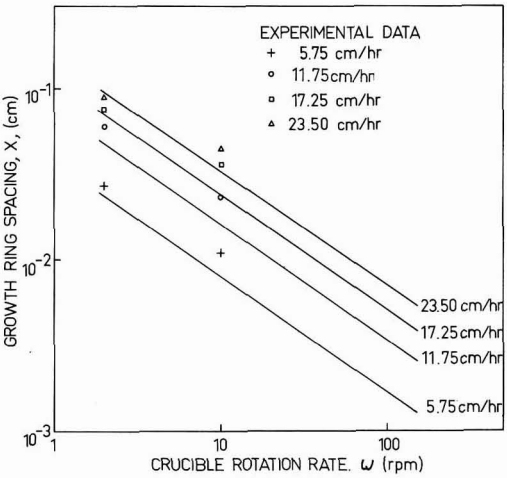


**Fig. 1. Variations of growth rate fluctuation spacing caused by overstable oscillations in rotating liquid silicon.**

The corresponding spacing period, $x$, (in growing crystals) of perturbations associated with overstable oscillations for a growth rate, $R$, will be

$$x = R\tau$$

This relation does not, of course, apply at very low crucible rotation rates. The spacing, $x$, is plotted as a function of $\omega$ for various growth rates, $R$, in Fig. 1 using $\nu = 0.0125$ cm²/sec and $h = 4.1$ cm. Experimentally observed points for crystals grown with no crystal rotation are shown for the different growth rates. These crystals were supplied to the author by K. E. Benson of the Bell Telephone Laboratories Inc., The observed spacings were obtained by counting the number of outer growth rings contained in a 1-in. length of the crystal surface. The agreement between theory and experiment is reasonably close, although the slope appears to be somewhat in error. This discrepancy undoubtedly arises because the analysis ignores the additional fluid circulation generated by horizontal temperature gradients and the resultant damping of temperature oscillations.

Manuscript received May 19, 1967; revised manuscript received June 30, 1967.

Any discussion of this paper will appear in a Discussion Section to be published in the June 1968 JOURNAL.

## REFERENCES

1. D. T. J. Hurle, *Phil. Mag.*, **13**, 305 (1966).
2. S. Chandrasekhar, and D. Elbert, *Proc. Roy. Soc. (London)*, **A231**, 198 (1955).

# Epitaxial InAs on InAs Substrates

G. R. Cronin and S. R. Borrello

*Texas Instruments Incorporated, Dallas, Texas*

Halogen transport and vapor growth of InAs were first reported by Effer *et al.* (1, 2). Epitaxial deposition of pure InAs as well as GaAs-InAs mixed crystals on low resistivity GaAs substrates has also been described by Minden (3), but the net carrier concentration and mobility of the deposits were not reported. By depositing InAs on chromium doped semi-insulating GaAs substrates, electrical measurements on pure epitaxial InAs deposits have been made (4, 5). While these deposits compared favorably with melt grown material in terms of net carrier concentration and mobility at 77°K, electron mobilities at 300°K were on the average somewhat lower than those observed for melt-grown material.

Since defect free deposits were not generally obtained on GaAs substrates, the influence of these defects on electrical properties cannot be ignored. Furthermore, strains in the deposited layer arising from differences in lattice spacing and thermal expansion coefficients may also influence the electrical characteristics of these deposits (6).

In order to avoid these effects as much as possible in the present series of experiments, epitaxial InAs was deposited on undoped InAs substrates. In order to make electrical measurements on the epitaxial layers alone, the deposits were made thick enough (75-100$\mu$) so that the substrates could be removed leaving the deposited layer intact.

The reactor and flow systems are the same as those described previously (4) using elemental indium and arsenic, 99.9999% pure.

InAs substrates were prepared from undoped pulled crystals cut on the (100) orientation. These crystals showed typical excess electron concentrations of 4-5 x $10^{16}$/cm$^3$ at 300°K with dislocation densities ranging from high $10^3$ to low $10^4$/cm$^2$. Wafers cut 30 mils thick were chemically polished on a paper pad soaked with a solution of bromine in methanol, 0.5% by volume (7).

Under the operating conditions shown in Table I approximately 6 hr of deposition time are required for a layer of sufficient thickness for substrate removal. The surfaces of these deposits were quite smooth, shiny, and, in general, free of visible defects. In instances where surface imperfections were observed they were identical in appearance with those described previously for deposits on GaAs substrates (4).

Unlike deposition on GaAs where the interface between deposit and substrate is clearly visible due to a slight color difference, epitaxial layers on InAs substrates are virtually impossible to distinguish on a cleaved edge. Growth rates were therefore obtained by using partially masked substrates. Masking is achieved with an $SiO_2$ film deposited on a portion of the substrate using standard photolithographic techniques. Since no deposit is generally observed on the masked portion of the substrate, deposit thickness is conveniently measured by observing the "step height" revealed on the cleaved edge of the sample (Fig. 1).

Hall measurements were made by the van der Pauw (8) technique on cloverleaf shaped samples 6 mm in diameter. The substrate portion of the specimen was almost totally removed by wet lapping with 5$\mu$ alumina abrasive. When the total thickness of the sample (deposit plus substrate residue) measured 125-150$\mu$, the remaining portion of the substrate was removed by etching the sample in a 5% bromine-methanol solution. Approximately 5 min etching time are required to remove 30-50$\mu$ of material.

**Table I. Temperature and flow conditions for epitaxial InAs deposition**

| Item | Temperature, °C | Flow rate cc/min |
|---|---|---|
| Arsenic | 400 | 15 |
| Indium | 870 | 100 |
| Substrate | 720 | — |
| Excess hydrogen flush | — | 5 |
| As $Cl_3$ reduction furnace | 880 | — |

**Table II. Mobility and carrier concentration at 300° and 77° K of InAs crystals grown epitaxially to InAs**

| Crystal No. | Thickness, $\mu$ | Carrier concentration, $\times 10^{15}$/cm$^3$ 300°K | Carrier concentration, $\times 10^{15}$/cm$^3$ 77°K | Hall mobility, $\times 10^3$ cm$^2$/v-sec 300°K | Hall mobility, $\times 10^3$ cm$^2$/v-sec 77°K |
|---|---|---|---|---|---|
| 474 | 100 | 15 | 12 | 30 | 69 |
| 475 | 70 | 6.2 | 5.3 | 31 | 98 |
| 476 | 125 | 9.5 | 8.6 | 30 | 73 |
| 477 | 95 | 12 | 10 | 29 | 71 |
| 485 | 110 | 15 | 14 | 28 | 65 |
| 489 | 80 | 16 | 15 | 28 | 65 |
| 491 | 94 | 26 | 22 | 25 | 53.2 |
| 492 | 85 | 14 | 11 | 28 | 67 |
| 493 | 90 | 33 | 31 | 27.5 | 47.5 |
| 494 | 95 | 34 | 31 | 26 | 44.6 |
| 505 | 75 | 17 | 15 | 30 | 61 |
| 507 | 75 | 17 | 14 | 28 | 61 |
| 513 | 100 | 4.9 | 3.7 | 30 | 112 |

The final thickness of the sample on which Hall measurements were made was usually about 75-100$\mu$ which corresponded to the minimum deposit thickness.

The electron mobility at 300°K for most of the epitaxial InAs crystals measured varies little from approximately 30,000 cm$^2$/volt-sec. Since the net carrier concentration varies as much as an order of magnitude, the results (see Table II) imply that the mobility at 300°K is probably limited by optical phonon scattering. At 77°K, however, the electron mobility is explicitly related to the carrier concentration (see Fig. 2) for both vapor deposited and melt grown InAs (9). The shift in data points in Fig. 2 represented by the GaAs substrates may be an indirect result of the 7% lattice mismatch between these two materials. The point which noticeably deviates from the best fit curves, we believe, represents rather closely compensated material.

The temperature variation of the electron mobility was determined for two epitaxial crystals and is shown in Fig. 3. These data can be fitted to a fair degree

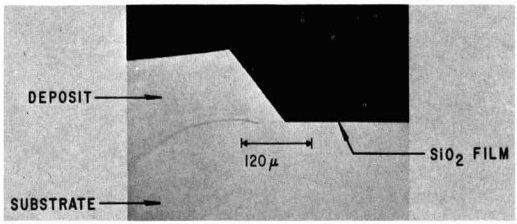


**Fig. 1. Cross section of InAs epitaxial deposit on partially masked ($SiO_2$) substrate. Height of "step" corresponds to deposit thickness. Note also a small amount (approximately 45 $\mu$) of overgrowth. The angle of growth between the surfaces of the masked substrate (100), and the epitaxial deposit corresponds closely to a (111) plane.**

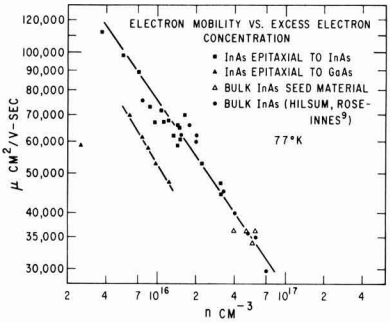


**Fig. 2. Electron mobility *vs.* excess electron concentration for vapor grown and melt grown InAs.**

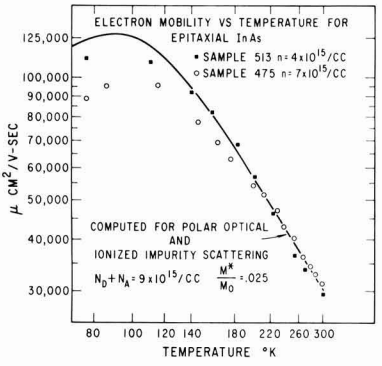


**Fig. 3. Electron mobility *vs.* temperature for InAs epitaxial to InAs.**

by a combination of polar optical (10) and ionized impurity (11) scattering and agree well with the results of Chasmar (12). An effective mass ratio of 0.025 and a donor plus acceptor concentration of 9 x $10^{15}$/cm$^3$ were used to obtain the computed curve. The computed curve and the data are in close agreement from 300° to 130°K below which the deviations are less than 30%. Since the assumed value of 9 x $10^{15}$/cm$^3$ for the total ionized impurity concentration produces a good fit for the temperature variation of the mobility and the net carrier concentration is measured at 3.7 x $10^{15}$/cm$^3$, the donor concentration becomes approximately 6.5 x $10^{15}$/cm$^3$ and the acceptor concentration 2.5 x $10^{15}$/cm$^3$. The functional dependence of mobility on net carrier concentration as shown in Fig. 2 is consistent with the ionized impurity scattering model (11) implying that the excess electron concentration is large compared with the acceptor concentration.

The vapor-grown samples shown in Fig. 2 represent an improvement in properties over InAs deposited on GaAs substrates as well as melt grown material. In the former case, it seems reasonable to attribute the increase in mobility to a decrease in the defect density and strains in the deposited layer. In the latter case, it is possible that the impurity segregation coefficients are smaller in this particular vapor-solid growth mechanism than in the liquid-solid. The possibility also exists that the higher excess carrier concentrations normally observed in melt grown InAs are a result of a defect structure introduced at the solidification temperature. We have tried several etchants to reveal differences in the structure of the vapor-grown layer and the InAs substrate but, as yet, without result.

## Acknowledgments

The authors acknowledge support of the Air Force Avionics Laboratory under Contract No. AF 33(615)-2913 for this work. They also thank W. L. Kriss for preparation of the samples, and H. Strack for helpful suggestions.

Manuscript received March 29, 1967; revised manuscript received June 22, 1967. This paper was presented at the Philadelphia Meeting. Oct. 9-14, 1967.

Any discussion of this paper will appear in a Discussion Section to be published in the June 1968 JOURNAL.

## REFERENCES

1. D. Effer, *This Journal*, **112**, 1020 (1965).
2. G. R. Antell and D. Effer, *ibid.*, **106**, 509 (1959).
3. H. T. Minden, *ibid.*, **112**, 300 (1965).
4. G. R. Cronin, R. W. Conrad, and S. R. Borrello, *ibid.*, **113**, 1336 (1966).
5. J. P. McCarthy, Paper presented at Institute of Physics and Physical Society Conference on "The Physics of Semiconducting Compounds," Swansea, Sept., 1966.
6. R. W. Conrad, P. L. Hoyt, and D. D Martin, *This Journal*, **114**, 164 (1967).
7. C. S. Fuller and H. W. Allison, *ibid.*, **109**, 880 (1962).
8. L. J. van der Pauw, *Philips Research Repts.*, **13**, 109 (1958).
9. C. Hilsum and A. C. Rose-Innes, "Semiconducting III-V Compounds," Pergamon Press, New York (1961).
10. H. Ehrenreich, *J. Phys. Chem. Solids*, **12**, 97 (1959).
11. H. Brooks, *Advances in Electronics and Electron Physics*, **7**, 85 (1955).
12. R. R. Chasmar, *J. Phys. Chem. Solids*, **20**, 164 (1961).

Brief Communication

# A Chemical Notation for Defect Solid State Chemistry

J. N. Ong, Jr.

*College of Applied Science and Engineering and Laboratory for Surface Studies, University of Wisconsin-Milwaukee, Milwaukee, Wisconsin*

Communication has been hindered among and between electrochemists, metallurgists, ceramists, and solid-state chemists and physicists, for lack of a consistent or standardized notation to describe chemical reactions in the solid state. This note demonstrates that normal chemical notation is adequate for most purposes and that existing notations are needlessly complicated.

Two familiar reactions are discussed, F-center formation and metal deficit nonstoichiometric oxide formation, (*a*) to illustrate the diversity of symbolism encountered in existing notations to describe vacancies (Schottky-Wagner defects) and charge carriers, (*b*) to suggest an alternate notation, (*c*) to demonstrate that one common adjustment to the existing notations renders their symbols for vacancies equivalent to each other and to normal chemical notation, and (*d*) to recommend alternate symbols for holes when used in chemical equations.

### *F-Center Formation*

Some of the ways in which the reaction of sodium vapor with rock salt to produce F-centers has been symbolized are shown in Table I, reactions (B)-(E). Not shown are another building unit system of notation due to Schottky (2, 8) and a notation of Schmalzried's (9), typographically similar to that of Schottky (1) but considered a structure element system (10). The proponents of both the building unit system and structure element system have discussed their notations elsewhere at length (1, 3). For present purposes it is sufficient to remark that Kröger, Stieltjies, and Vink (3) point out that Schottky's F-center symbol |Cl| in reaction (B) has the operational meaning "take away a chlorine atom" and is in the material balance sense a "negative mass" particle. Schottky (1) objects to the atomic notation because only virtual potentials, $\xi(Na_{Na})$ and $\xi(V_{Cl})$[1] may be assigned to the symbols $Na_{Na}$ (sodium atom at a sodium site) and $V_{Cl}$ (vacancy at a chlorine site).

On the other hand Anderson (11, 12) persists in the use of Rees' notation, reaction (D), even though it is less convenient for writing mass action expressions.

The ionic notation, reaction (E), presupposes purely ionic bonding in rock salt. However, the resulting symbol for F-center, $V^{-}{}_{Cl}-$ along with that of Rees, $e|\square-$ represents a more accurate physical picture of the location of the electron than that of Kröger and Vink (2), whose symbol, $V_{Cl}$, carries zero charge. For future reference and by comparison with Schottky's symbol, observe that the three F-center-symbols in reactions (C), (D), and (E) are essentially "zero mass" particles.

We may view reaction (A) in a more conventional sense and by so doing return to a simple notation, discover one point of difference between the notations, and indicate the procedure by which they may be reconciled on this point. Let us view the F-center as arising from the solution of sodium in NaCl and express the material balance as reaction (F), Table I. Since we know that a sodium atom in solution occupies a lattice site in NaCl normally occupied by sodium and that a chlorine atom is absent from its normal site we may, for purposes of convenience, convey such structural information within the symbol (6) as shown in reaction (G). [The subscripts identify the lattice sites and V denotes absence of matter (2)]. It is frequently desirable to convey polarization information within a symbol. In our example we know that the electron from the sodium atom is localized in the vicinity of the vacancy (6). We may then write the symbol in the form shown in reaction (H). These symbols, Na (identity), $(Na_{Na}V_{Cl})$ (structure) and $(Na^{+}{}_{Na}V^{-}{}_{Cl})$ (polarization) are directly comparable to conventional chemical symbols, for example $H_2O$,

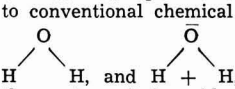

H, respectively. To complete the analogy, it is evident that we may solvate the solute atom to any convenient degree, reaction (I), and by incorporating the structure, polarization and solvation refinements to the basic symbol, Na (in solution), we finally arrive at the familiar schematic representation of the F-center (7) shown in reaction (J). In the chemical notation the F-center symbols are

**Table I. Comparisons of various notations used to describe dilute solution formation in an ionic crystal**

| | Reaction | System of notation | Ref. |
|---|---|---|---|
| A. | Sodium vapor + rock salt = rock salt + F-centers | Verbal | |
| B. | $Na(g) = NaCl + \|Cl\|$ | Building unit | (1) |
| C. | $Na(g) = Na_{Na} + V_{Cl}$ | Structure element, atomic | (2-4) |
| D. | $Na(g) = Na^{+} \|\square\|_{+} + e \|\square\|_{-}$ | Structure element, Rees | (2,5) |
| E. | $Na(g) = Na^{+}{}_{Na} + V^{-}{}_{Cl}$ | Structure element ionic | (2) |
| F. | $Na(g) = Na$ (in solution) | Chemical | |
| G. | $Na(g) = (Na_{Na}\ V_{Cl})$ | Chemical, with structure | (6) |
| H. | $Na(g) = (Na^{+}{}_{Na}\ V^{-}{}_{Cl})$ | Chemical, with polarization | (6) |
| I. | $nNaCl + Na(g) = Na(NaCl)_n$ | Chemical, with solvation | (6) |
| J. | $nNaCl + Na(g) = \begin{matrix} Cl^{-}\ Na^{+} - Na^{+} \\ Na^{+}\ Cl^{-}\ Na^{+}\ Cl^{-} \end{matrix}$ | Chemical, with structure polarization and solvation | (6,7) |

[1] We usually distinguish between chemical potentials (13) of neutral species, $\mu(i)$, whose values are normally experimentally accessible, and electrochemical potentials (13) of charged species (ions), $\mu_+(i)$ or $\mu_-(i)$, whose values are experimentally accessible only provided that their sum $\sum_j \nu_j \mu_{+} + \sum_k \nu_k \mu_{-}$ in any equilibrium equation is subject to the restriction of electrical neutrality, $\sum_j \nu_j z_j = 0$, where $\nu$ is the stoichiometric coefficient and $z$ is the charge number of the appropriate species. Kröger's (3) virtual thermodynamic potentials (virtual potentials), $\xi(i)$, are analogous to electrochemical potentials. The condition that they be experimentally accessible is, however, subject not to electrical neutrality but to a constant ratio between different types of lattice sites. We will write all potentials as $\mu(i)$, $\xi(i)$, etc., instead of $\mu_i$, $\xi_i$, etc. to avoid typesetting difficulties.

all "positive-mass" particles in contrast to the building unit and structure element symbols.

Mass action expressions relating defect concentrations to vapor pressure present another source of difficulty which is simplified by use of the conventional chemical notation. Experiment shows that the equilibrium number of F-centers formed is directly proportional to the sodium vapor pressure (6). We can obtain this relation by the usual procedure of equating chemical potentials. From reaction (G) for example we have

$$\mu(\mathrm{Na[g]}) = \mu(\mathrm{Na_{Na}V_{Cl}}) \quad [1]$$

from which we get the mass action expression (13)

$$K_G P_{Na} = a(\mathrm{Na_{Na}V_{Cl}}) \simeq [(\mathrm{Na_{Na}V_{Cl}})] \quad [2]$$

where $K_G$ is the equilibrium constant, $P_{Na}$ is the sodium vapor pressure, $a(\mathrm{Na_{Na}V_{Cl}})$ and $[(\mathrm{Na_{Na}V_{Cl}})]$ are the relative activity [ref. (13), p. 226] and concentration, respectively, of the F-center. The concentration is a good approximation to the relative activity when the solution is dilute.

If the same procedure is strictly followed with any of reactions (C), (D), and (E), (C) say, we may equate the chemical and virtual potentials according to

$$\mu(\mathrm{Na[g]}) = \xi(\mathrm{Na_{Na}}) + \xi(\mathrm{V_{Cl}}) \quad [3]$$

from which follows the relation

$$K_C P_{Na} = a(\mathrm{Na_{Na}})\,a(\mathrm{V_{Cl}}) \simeq [\mathrm{Na_{Na}}][\mathrm{V_{Cl}}] \quad [4]$$

relative activities $a(\mathrm{Na_{Na}})$ and $a(\mathrm{V_{Cl}})$ having been approximated by concentrations in the last term. Since there are equal numbers of excess[2] sodium atoms and vacancies, we have the additional restriction on Eq. [4] of

$$[\mathrm{Na_{Na}}] = [\mathrm{V_{Cl}}] \quad [5]$$

When Eq. [5] is substituted into Eq. [4], we obtain the result

$$(K_C P_{Na})^{1/2} = [\mathrm{V_{Cl}}] \quad [6]$$

which does not agree with experiment.

This conclusion may be avoided by arbitrarily assigning a value of unity to $a(\mathrm{Na_{Na}})$ in Eq. [4]. We may just as readily, and in many respects less arbitrarily, assign unit value to $a(\mathrm{V_{Cl}})$ and regard the changed properties of the crystal as arising from the activity of the excess sodium. A more satisfactory procedure is to regard the excess atom-vacancy pair as inseparable and its symbol accordingly associated, for example (NaCl+|Cl|) reaction (B),[3] ($\mathrm{Na_{Na}}+\mathrm{V_{Cl}}$) reaction (C), *etc.* It is clear from Table I that if the pairs of symbols on the right hand side of reactions (B) to (E) are combined as indicated above, they become equivalent in all but one respect to each other and to the symbols of reactions (F), (G), and (H), *i.e.*

$$(\mathrm{NaCl} + |\mathrm{Cl}|) \equiv (\mathrm{Na_{Na}} + \mathrm{V_{Cl}}) \equiv (\mathrm{Na^+}|\square_+ + \mathrm{e}|\square_-) \equiv (\mathrm{Na^+}_{\mathrm{Na}+} + \mathrm{V^-}_{\mathrm{Cl}-}) \equiv \mathrm{Na\,(in\ solution)} \equiv (\mathrm{Na_{Na}V_{Cl}}) \equiv (\mathrm{Na^+}_{\mathrm{Na}}\mathrm{V^-}_{\mathrm{Cl}}) \quad [7]$$

With this one change, all the symbols become "positive mass" particles, all can be assigned normal chemical potentials and all the reactions will lead to the correct equilibrium relationship between vapor pressure and concentration, Eq. [2].

The only difference between symbols lies in the degree of polarization which is implied or assumed. Rather than assign virtual potentials to the separate symbols $\mathrm{Na_{Na}}$ and $\mathrm{V_{Cl}}$ with their respective effective charges, we may assign a chemical potential to the combined symbol ($\mathrm{Na_{Na}V_{Cl}}$) and account for polarization by including an appropriate term in the chemical potential which reflects the contribution to it, due to the presence of the sodium atom in an electric field [ref. (13), p. 415]

$$\xi(\mathrm{Na_{Na}}) + \xi(\mathrm{V_{Cl}}) = \mu(\mathrm{Na_{Na}V_{Cl}}) = \mu^\circ(\mathrm{Na_{Na}V_{Cl}}) - \mu^E(\mathrm{Na_{Na}V_{Cl}}) \quad [8]$$

where $\mu^\circ(\mathrm{Na_{Na}V_{Cl}})$ denotes the value of $\mu(\mathrm{Na_{Na}V_{Cl}})$ at zero field strength and where $\mu^E(\mathrm{Na_{Na}V_{Cl}})$ is a function of electric field strength, molecular polarizability, electric moment, and temperature.

Regardless of the merits of the structure element notations for symbolizing polarization, for all other chemical purposes conventional chemical notation is preferable. These purposes include the performance of material balances and thermodynamic and kinetic analyses. The chemical notation can be used for solution, solvation, and ionization reactions, phase transformations or ordering phenomena, and half-cell, electrochemical, and oxidation-reduction reactions.

Table II summarizes the symbols, masses, and thermodynamic potentials associated with the most common defects in solid crystals; interstitial (Frenkel), substitutional, and Schottky-Wagner defects in the building unit, atomic, ionic, and chemical notations. Discussion of Table II is deferred until later.

### *Metal Deficit Nonstoichiometric Oxide Formation*

Both vacancies and positive charge carriers form in some solids. An example, which has been symbolized in Table III in the various notations, is the reaction between cobaltous oxide and oxygen which produces a metal deficit nonstoichiometric p-conducting oxide containing cobalt vacancies. First, I show that the symbols for the vacancies should be modified in a way similar to the F-center example. Second, I point out the differences in and discuss the relative merits of the symbols for charge carriers in the building unit, atomic and Rees notations (holes) and in the ionic, and chemical notations (ions).

Let us reconsider the question of symbolism for vacancies. By arguments similar to those of the preceding section, it is clear that the expected one sixth power oxygen pressure dependency upon equilibrium vacancy concentration (14, 15) cannot be obtained from the structure element notations unless either unit activity is arbitrarily assigned to $a(\mathrm{O^=_O})$ (15), reaction (N) for example, or unless the excess oxygen ion-vacancy pair can be considered associated, $(\mathrm{V_{Co}} + \mathrm{O^=_O})$.

We obtain the proper equilibrium pressure dependency on excess oxygen ion concentration (vacancy concentration) by the normal procedure of equating the appropriate potentials, using reaction (O), say

$$2\mu_+(\mathrm{Co^{++}}) + (\tfrac{1}{2})\mu(\mathrm{O_2,(g)}) = 2\mu_+(\mathrm{Co^{+++}}) + \mu_-(\mathrm{O^=}) \quad [9]$$

From Eq. [9] we may write for the equilibrium constant, $K_O$, the expression

$$K_O = a_+^2(\mathrm{Co^{+++}})\,a_-(\mathrm{O^=})/a_+^2(\mathrm{Co^{++}})P^{1/2}_{O_2} \quad [10]$$

where $a_+$ and $a_-$ are ion activities.

If we make the usual simplifying assumptions of $a_+(\mathrm{Co^{++}}) = 1$ and for the mean ion activity coefficient $\gamma_+^2(\mathrm{Co^{+++}})\gamma_-(\mathrm{O^=}) \simeq 1$, for the limiting condition of a dilute solution, [ref. (13), Chap. 8], Eq. [10] reduces to

$$P_{O_2}^{1/2} K_O = [\mathrm{Co^{+++}}]^2[\mathrm{O^=}] \quad [11]$$

Finally, by noting that $[\mathrm{Co^{+++}}] = 2[\mathrm{O^=}]$, we obtain the correct pressure dependence on either excess

[2] This is clearly a consequence of the precise statement of reactions (C), (D), and (E). If we rewrite reaction (C), say, to include the rock salt: $(m)$ NaCl + Na(g) = $(m)$ NaCl + $\mathrm{Na_{Na}}$ + $\mathrm{V_{Cl}}$ where usually $m >> 1$, common amounts of NaCl cancel on both sides of the equation leaving only the excess Na on the right-hand side present in equal numbers to vacancies. Alternatively, the activity of the original crystal cancels in the corresponding mass action expression

$$K_C = a^m(\mathrm{NaCl})\,a(\mathrm{Na_{Na}})\,a(\mathrm{V_{Cl}})/a^m(\mathrm{NaCl})P_{Na}$$

[3] In the building unit notation, this operation should be regarded as purely formal. It is not to be construed that the notation is inconsistent.

**Table II. Symbols, masses, and thermodynamic potentials of typical defects in solids in various notations**

| Type of defect and example | | Notation: Building Unit | Atomic | Ionic | Chemical |
|---|---|---|---|---|---|
| Frenkel (Interstitial Zn in ZnO) | Symbol | $Zn^x$ | $Zn_i$ | $Zn_i$ | $Zn_i$ |
| | Mass | + | + | + | + |
| | Potential | $\mu(Zn^x)$ | $\mu(Zn_i)$ | $\mu(Zn_i)$ | $\mu(Zn_i)$ |
| Substitutional (Be in Ge) | Symbol | $B\|Ge\|$ | $B_{Ge}$ | $B_{Ge}$ | $B_{Ge}$ |
| | Mass | $-$ [a] | + | + | + |
| | Potential | $\mu(B) - \mu(Ge)$ | $\mu(B_{Ge})$ | $\mu(B_{Ge})$ | $\mu(B_{Ge})$ |
| Schottky-Wagner (F-center in NaCl) | Symbol | $\|Cl\|$ | $V_{Cl}$ | $V^-{}_{Cl}$ | Na or $(Na^+{}_{Na}\ V^-{}_{Cl})$ |
| | Mass | $-$ | 0 | $O^{(b)}$ | + |
| | Potential | $-\mu(\|Cl\|)$ | $\xi(V_{Cl})$ | $\xi(V^-{}_{Cl})$ | $\mu(Na)$ |
| Schottky-Wagner (Co vacancy in non-stoichiometric CoO) | Symbol | $\|Co\|''$ | $V''_{Co}$ | $V_{Co}{}^{++}$ | $O^=$ or $(V_{Co}\ O_O)^=$ |
| | Mass | $-$ | $O^{(b)}$ | O | + |
| | Potential | $2\mu_-(e) - \mu(Co)$ | $\xi(V''_{Cl})$ | $\xi(V_{Co}{}^{++})$ | $\mu_-(O^=)$ |
| Immobile charge carrier ($Co^{+++}$ ion in non-stoichiometric CoO) | Symbol | $\|e\|^\bullet$ | h | $Co^{+++}{}_{Co}{}^{++}$ | $Co^{+++}$ or $Co^{+++}{}_{Co}$ |
| | Mass | $-$ | $-$ | + | + |
| | Potential | $\mu_+(Co^{+++}) - \mu_+(Co^{++})$ | $\mu_+(Co^{+++}) - \mu_+(Co^{++})$ | $\mu_+(Co^{+++}{}_{Co}{}^{++})$ | $\mu_+(Co^{+++})$ |
| Mobile charge carrier (Intrinsic conductivity in Si) | Symbol | $\|e\|^\bullet$ | h | $Si^+$ | $Si^+$ or $Si^+{}_{Si}$ |
| | Mass | $-$ | $-$ | + | + |
| | Potential | $\mu_+(Si^+) - \mu(Si)$ | $\mu_+(Si^+) - \mu(Si)$ | $\mu_+(Si^+)$ | $\mu_+(Si^+)$ |

Notes: (a) Mass can also be positive, *e.g.*, Ge|B|.
(b) Mass of electron or effective negative charge excluded.

oxygen ion (metal vacancy) concentration or $Co^{+++}$ ion concentration

$$P^{1/2}{}_{O_2}K_O = 4[O^=]^3 = (1/2)[Co^{+++}]^3 \quad [12]$$

The notation and the thermodynamic formulation employed here is nothing more than that which is normal for strong electrolytes (12). For example, when the reaction is expressed in the form of reaction (Q), we see that the product can be considered a dilute solution of dissociated $Co_2O_3$ in a CoO solvent. To the extent that association tends to occur with increasing $Co_2O_3$ concentration, we may represent this by the sum of the association reactions $2(CoO)^+ + O^= = (CoO)^+ + (CoO_2)^-$, and $(CoO)^+ + (CoO_2)^- = Co_2O_3$ and the solvation reaction $Co_2O_3 + CoO = Co_3O_4$.

Because of the associating and solvating tendencies of solutions of this type of reaction, any attempt to relate a definite number of vacancies to the number of excess oxygen ions in solution at high concentrations appears at present to be problematical (12, 16). As before, this difference between the three structure element notations in Table III disappears when the excess ion-vacancy pairs are associated; $(V_{Co} + O_O)''$ (atomic), $(V_{Co}{}^{++} + O_O{}^=)^=$ (ionic) *etc.*, provided, first, that the effective negative charge in the modified atomic notation is interpreted to be a real negative charge and equivalent to the real negative charge associated with the modified ionic and Rees symbols, and, second, that there is a direct correspondence between excess oxygen ions added and metal vacancies created in the crystal.

We now consider the charge carrier symbols. Recalling the equivalence of the vacancy symbols

$$(CoO + |Co|'') \equiv (O_O + V_{Co}'') \equiv (O^=|\square_- + \square_+) \equiv (O^={}_{O^=} + V_{Co}{}^{++}) \equiv O^= \equiv (V_{Co}O_O)^= \quad [13]$$

we may subtract reactions (K), (L), or (M) from (N), (O), or (P) to determine that the hole symbols, $|e|^\bullet$ and h, represent a difference of two chemical symbols

$$|e|^\bullet \equiv h \equiv (Co^{+++}{}_{Co} - Co^{++}{}_{Co}) \quad [14]$$

Furthermore, since the mass of $Co^{++}$ is greater by one electron than $Co^{+++}$, holes in both the building unit and atomic notations are "negative mass" particles, and when used in chemical equations, have the operational meaning: "take away an electron" (3). When the thermodynamic potentials of holes are to be considered, Eq. [14] serves to stress that such potentials from a chemical point of view must be regarded as the difference of two potentials, Table II

$$\mu_+(|e|^\bullet) \equiv \xi(h) = \mu_+(Co^{+++}) - \mu_+(Co^{++}) \quad [15]$$

The chemical origin of the hole is frequently of incidental importance for many electrical purposes, and from the electrical viewpoint we can appreciate the practice of representing the charge carrier by a single symbol. Nevertheless distinctions are often made between intrinsic and extrinsic and mobile and immobile holes. In addition to the reactions of Table III which give rise to extrinsic immobile p-conduction due to nonstoichiometry we have, using the chemical notation, extrinsic immobile p-conduction due to impurities, *e.g.*, Fe in MgO

$$(1/2)O_2(g) + 2Fe^{++}{}_{Mg} = (V_{Mg}O_O)^= + 2Fe^{+++}{}_{Mg} \quad [16]$$

intrinsic mobile p-conduction, *e.g.*, Si ionization

$$Si_{Si} = e + Si^+{}_{Si} \quad [17]$$

and extrinsic mobile p-conduction, *e.g.*, B-doped Ge

$$B_{Ge} + Ge_{Ge} = B^-{}_{Ge} + Ge^+{}_{Ge} \quad [18]$$

The last term on the right of the above equations clearly identifies the chemically different charge carriers. On the other hand a single electrical symbol for a hole can represent at least four chemically different conditions

$$|e|^\bullet \text{ or } h = (Co^{+++}{}_{Co} - Co^{++}{}_{Co}) = (Fe^{+++}{}_{Mg} - Fe^{++}{}_{Mg}) = (Si^+{}_{Si} - Si_{Si}) = (Ge^+{}_{Ge} - G_{Ge}) \quad [19]$$

Equation [19] will permit more precise distinctions to be made in the character of the holes where necessary.

Listed in Table II for the various notations are the symbols, masses, and thermodynamic potentials of the defects discussed in this section.

**Table III. Comparisons of various notations used to describe metal deficit nonstoichiometric oxide formation**

| | Reaction | System of Notation |
|---|---|---|
| K. | $(1/2)O_2(g) = CoO + \|Co\|'' + 2\|e\|^\bullet$ | Building unit |
| L. | $(1/2)O_2(g) = O_O + V''_{Co} + 2h$ | Structure element, atomic |
| M. | $(1/2)O_2(g) = O^=\|\square_- + \square_+ + 2h$ | Structure element, Rees |
| N. | $2Co^{++}{}_{Co}{}^{++} + (1/2)O_2(g) = O^={}_{O^=} + V_{Co}{}^{++} + 2Co^{+++}{}_{Co}{}^{++}$ | Structure element, ionic |
| O. | $2Co^{++} + (1/2)O_2(g) = O^= + 2Co^{+++}$ | Chemical |
| P. | $2Co^{++}{}_{Co}{}^{++} + (1/2)O_2(g) = (V_{Co}O_O)^= + 2Co^{+++}{}_{Co}$ | Chemical; with structure |
| Q. | $2CoO + (1/2)O_2(g) = O^= + 2(CoO)^+$ | Chemical; solution and dissociation of $Co_2O_3$ |

## *Discussion*

Two common solid-state reactions have been formulated using a variety of notations. The two reactions discussed were a simple solution of a polarizable sub-

stance (F-center formation, Table I), and an oxidation-reduction reaction (metal deficit p-conducting cobaltous oxide formation, Table III). One simplification of the notations results when properties of nonstoichiometric compounds usually attributed to the presence of vacancies in the lattice are attributed instead to the presence of the excess constituent giving rise to the vacancy. It is shown that structure element notations must be modified to produce correct thermodynamic relationships between the equilibrium concentrations of excess constituents in solution and their vapor pressures. When both building unit and structure element notations are modified in the same way, *e.g.*, Eq. [7] and [18], they become equivalent to each other and to conventional chemical notation in this respect. In the ionic and chemical notations, the identity of the positive charge carrier can be determined, whereas in the building unit, atomic, and Rees notations, which employ the hole symbol, this may not always be done.

Comparing notations in Table II it is important to note that in the chemical notation we may associate not only a positive mass with every symbol but also a single normal thermodynamic potential, a chemical potential for a neutral species and an electrochemical potential for a charged species. In these two crucial respects this notation is identical in form with all chemical notation. The building unit notation although formally correct has both positive and negative masses associated with the symbols and positive, negative, and differences of, thermodynamic potentials associated therewith. Unless one possesses an intimate knowledge of this notation, it is difficult to read and awkward to use (3). The ionic notation has positive and zero masses associated with its symbols. With only one modification, for the vacancy, it becomes equivalent to conventional notation. The symbols in the atomic notation have positive, zero and negative masses associated with them and consequently the gamut of normal, virtual, and differences of, thermodynamic potentials.

*Recommendations.*—Use the chemical notation to describe reactions in the solid state. No conceptual difficulties will be encountered by its use, and no thermodynamic or chemical confusion can result from its use from the symbols themselves.

If a selection among symbols is to be made, pick the simplest one that will fit your needs. In the F-center example, if the solubility of sodium in rock salt is under consideration, it is unnecessary to use a symbol more detailed than Na(in solution). On the other hand, if defect structure and polarization are under consideration, then use the symbol ($Na^{+}_{Na}V^{-}_{Cl}$). In the cobaltous oxide example the description of cation mobility, diffusivity and oxidation phenomena may require the use of the symbol $(V_{Co}O_O)^{=}$, in reaction (P). However, if the description of the positive charge carrier, $Co^{+++}$ is under consideration, the description of the counter ion, $O^{=}$, need not necessarily convey any structural information.

The use of h (and $|e|^{\bullet}$) as a symbol for positive charge carriers is widespread and a change in usage is unlikely. However, when this symbol is used in chemical equations it is important to keep in mind that it is not a chemical symbol. It describes the operation "take away an electron" and should be represented chemically as a difference of two chemical symbols and thermochemically as a difference of two thermodynamic potentials. When in doubt it is recommended that the use of the symbol h in chemical equations be replaced by an appropriate difference in chemical symbols, Eq. [19].

*Acknowledgment*

This work was supported in part by the Independent Research Program of Lockheed Missiles & Space Co., Palo Alto, California.

Manuscript received May 5, 1967; revised manuscript received June 27, 1967.

Any discussion of this paper will appear in a Discussion Section to be published in the June 1968 JOURNAL.

REFERENCES

1. W. Schottky, in "Halbleiterprobleme, Band IV," p. 235, W. Schottky, Editor, F. Vieweg u. Sohn, Braunschweig (1958).
2. F. A. Kröger and H. J. Vink in "Solid State Physics," Vol. 3, F. Seitz and D. Turnbull, Editors, p. 307, Academic Press, Inc., New York (1956).
3. F. A. Kröger, F. H. Stieltjies, and H. J. Vink, *Philips Res. Repts*, **14**, 557 (1959).
4. F. A. Kröger, "The Chemistry of Imperfect Crystals," North Holland Publishing Co., Amsterdam (1964).
5. A. L. G. Rees, "Chemistry of the Defect Solid State," John Wiley & Sons, Inc., New York (1954).
6. N. F. Mott and R. W. Gurney in "Electronic Processes in Ionic Crystals," 2nd ed., Chap. 4, Oxford (1948).
7. C. Kittel, in "Introduction to Solid State Physics," p. 493, McGraw-Hill, New York (1956).
8. W. Schottky and F. Stockmann, in "Halbleiterprobleme, Band I," p. 80, W. Schottky, Editor, F. Vieweg u. Sohn (1954).
9. H. Schmalzried, in "Progress in Solid State Chemistry" Vol. 2, p. 265, Pergamon Press, New York (1965).
10. H. Schmalzried, Private communication.
11. J. S. Anderson in "High Temperature Technology," p. 285, Butterworths, Washington, (1964).
12. J. S. Anderson, in "Non-Stoichiometric Compounds," p. 1, Adv. in Chem. Series No. 391, Am. Chem. Soc., Washington, D. C. (1963).
13. E. A. Guggenheim, "Thermodynamics," p. 301, 304, North-Holland Publishing Co. Amsterdam (1959).
14. B. Fisher and O. S. Tannhauser, *This Journal*, **111**, 1194, (1964).
15. S. P. Mitoff, *J. Chem. Phys.*, **35**, 882 (1961).
16. W. L. Roth, *Acta Cryst.*, **13**, 140, (1960).

# Electrochemical Books in Print

### John Wiley Publications In-Print

The following are books developed and sponsored by The Electrochemical Society and published by John Wiley & Sons Inc., 605 Third Ave., New York, N. Y., 10016. Members of the Society can receive a 33 1/3% discount by ordering from Society Headquarters. Book and invoice mailed by the publisher. Nonmembers (including subscribers) must order direct from the publisher.

**Corrosion Handbook.** Edited by Herbert H. Uhlig. Published 1948, 1188 pages, **$21.00.**

**Modern Electroplating,** Second Edition. Edited by Frederick A. Lowenheim. Published 1963, 769 pages, **$16.00.**

**Electrochemistry in Biology and Medicine.** Edited by Theodore Shedlovsky. Published 1955, 369 pages, **$12.50.**

**High-Temperature Technology** (Materials, Methods, and Measurements). Edited by I. E. Campbell. Published 1956, 526 pages, **$15.00.** (Out of print; new edition in press to be published 1967).

**Arcs in Inert Atmospheres and Vacuum.** Edited by W. E. Kuhn. Published 1956, 188 pages, **$7.50.** A 1956 Spring Symposium.

**The Structure of Electrolytic Solutions.** Edited by Walter J. Hamer. Published 1959, 441 pages, **$19.50.** A 1957 Spring Symposium.

**Ultrafine Particles,** Editor-in-Chief—William E. Kuhn. Published 1963, 561 pages, **$15.00.**

**First International Conference on Electron and Ion Beam Science and Technology.** Edited by R. Bakish. Published 1965, 945 pages, **$24.50.** (Sponsored by the Electrothermics and Metallurgy Division of The Electrochemical Society and the Metallurgy Society of AIME.)

**The Electron Microprobe.** Edited by T. D. McKinley, K. F. J. Heinrich, and D. B. Wittry. Published 1966, 1035 pages, **$27.50.** A 1964 Fall Symposium.

**Chemical Physics of Ionic Solutions.** Edited by B. E. Conway and R. G. Barradas. Published 1966, 622 pages. **$25.00.** A 1964 Spring Symposium.

**Vapor Deposition.** Edited by C. F. Powell, J. H. Oxley, and J. M. Blocher, Jr. Published 1966, 725 pages, **$19.95.**

**The Stress Corrosion of Metals** by Hugh I. Logan. Published 1966, 306 pages; **$13.95.**

**High Temperature Oxidation of Metals** by Per Kofstad. Published 1966, 340 pages; **$13.50.**

**The Corrosion of Light Metals,** by H. P. Godard, W. B. Jepson, M. R. Bothwell, and R. L. Kane. Published 1967, 360 pages; **$13.95.**

---

### Other ECS Publications

The following books are available through The Electrochemical Society and various other publishers. Consult each listing for ordering instructions.

**Vacuum Metallurgy,** third printing, 1958, Edited by J. M. Blocher, Jr.; 216 pages; **$5.00,** less a 20% discount to ECS members only. Available from Electrochemical Society Headquarters, 30 East 42 St., New York, N. Y. 10017. A 1954 Fall Symposium.

**Rhenium.** Edited by B. W. Gonser. Published by Elsevier Publishing Co., 1962; 225 pages; **$12.50.** A 1960 Spring Symposium. ECS Members can obtain a 30% discount by sending their orders directly to Society Headquarters, 30 East 42 St., New York, N. Y. 10017. Remittance, made payable to American Elsevier Publishing Co., 52 Vanderbilt Ave., New York, N. Y. 10017 should accompany the order. Nonmembers must order direct from the publisher.

**Iron Ore Reduction.** Edited by R. R. Rogers. Published by Pergamon Press Ltd., New York and London, 1962; 359 pages; **$12.50** A 1960 Spring Symposium. Send all orders to The Macmillan Co., 60 Fifth Ave., New York, N. Y.

**Stress Corrosion Cracking and Embrittlement.** Edited by W. D. Robertson. Published 1956 by John Wiley & Sons Inc., New York. 202 pages **$2.50** (Hard cover book originally priced at $7.50.) Distributed by Dover Publications, Inc., 180 Varick St., New York. Send all orders to Dover Publications, Inc.

**Electrode Processes.** Published by The Electrochemical Society, 1966. c. 160 pages; **$5.00.** Edited from invited papers and full discussion presented by the Theoretical Electrochemistry Division, and supported by the United States Air Force Office of Scientific Research, at the Spring Meeting held May 1-5, 1966 in Cleveland, Ohio. Order direct from Society Headquarters.

**Measurement Techniques for Thin Films.** Published by The Electrochemical Society, 1967. Edited by B. Schwartz and N. Schwartz. c. 380 pages; **$9.00.** Edited from selected papers presented by the Dielectrics and Insulation Division and by the Electronics Division at the 128th and 130th National Meeting, held October 1965 and October 1966. Order direct from Society Headquarters.

**Electrolytic Rectification and Conduction Mechanisms in Anodic Oxide Films.** Published by The Electrochemical Society, 1967. Edited by P. F. Schmidt and D. M. Smyth. c. 230 pages; **$7.00.** Papers presented at the Dielectrics and Insulation Division. Symposium on Anodic Oxides at the 131st Spring Meeting held in Dallas, Texas. Order direct from Society Headquarters.

ELECTROCHEMICAL SOCIETY NEWS

October 1967

# 1967 F. M. BECKET AWARD REPORT

As winner of the 1967 F. M. Becket Award, I would like to thank the committee for allowing me the richest and most invigorating ten weeks of my entire educational career. To Dr. Rogers, I express special thanks for his many helpful letters. I would also like to express my appreciation to Professor Carl Wagner for arranging my visit to Germany. He arranged with Professor Hermann Schmalzried of the Technical University at Clausthal to have me spend a month at his laboratory. The remaining six weeks were spent with Professor Wagner at the Max-Planck-Institute for Physical Chemistry at Göttingen.

Professor Schmalzried is director of the Institute for Theoretical Metallurgy at Clausthal. His present research interests include the phase relationships, structure, and defect structure of ternary oxides (spinels), and diffusion and solubility studies in metals and oxides. He has succeeded in using galvanic cells in many of these research problems.

During my visit there, I worked closely with a research assistant, Mr. H. G. Sockel, who is studying the Fe-Co-O system. As an aid to understanding his work, I studied previous work in this area by Professor Schmalzried (1, 2) and his co-workers. (3, 4) Diffusion studies, x-ray measurements, EMF measurements and coulometric titrations have been used to understand the structure of several spinels. A model for the defect structure considering vacant cation sites, either octahedral or tetrahedral, has been proposed which satisfactorily predicts many of the experimental results.

As the next step in the study, Mr. Sockel is using an oxygen concentration cell for EMF measurements and titrations on $Co_xFe_{3-x}O_{4-\Delta}$. The sample is placed in a gas-tight quartz tube with a zirconia pellet as electrolyte. The over-all goal is the study of the homogeneity range ($\Delta$) as a function of the cobalt-to-iron ratio and the study of the EMF or oxygen partial pressure as a function of the metal deficit within the homogeneity range of the single phase. These measurements can be compared with the calculations for the defect model.

While I worked with Mr. Sockel, we changed the experimental procedure and were able to eliminate some erroneous measurements. Previously, the powdered sample was placed in a small platinum crucible. Since iron is slightly soluble in platinum and since the activity of the components changes during a titration experiment, the amount of iron in the sample varies across the single phase region and therefore effects the measured EMF. The measurements were made more consistent by pressing the powder into a small disk and supporting it on the points of small pieces of dense alumina (very little contact area) which had already been equilibrated with another sample.

Another interesting observation which was made while studying the narrow homogeneity range was the need of excess oxygen, i.e., an extra driving force, to form the wüstite phase out of the cobalt ferrite lattice. This phenomenon does not occur in the reverse direction because no new lattice (phase) is formed.

I noticed immediately that although I had studied a semester of electrochemistry and had had several semesters of thermodynamics, I did not really begin to understand the principles until I studied and worked with Professor Schmalzried and Mr. Sockel.

At the Max-Planck-Institute I was directed in my studies by Professor Wagner. At present he is interested in phase relationships and thermodynamics in ternary systems, defect studies, and the kinetics of diffusion and solubility of gases in metals and nonmetals (sulfides, oxides, selenides, etc.). Working with Professor Wagner on the Ag-Cu-Se system is Dr. N. Valverde from the Rocasolano Physical Chemistry Institute in Madrid, Spain. Professor Wagner and Dr. Valverde introduced me to their studies of this system in a very interesting manner. First, I studied the original research proposal; after which I was instructed in the experimental techniques and shown the initial results and allowed also to make calculations from the data. Since the initial investigations introduced new research problems, I studied other proposals, methods, and theory corresponding to the total solution of the original problem. In other words, without doing the actual work, I felt as though I had participated in the research which originally covered a period of six months.

Beginning with rather limited information about the Ag-Cu-Se system, they first used x-ray techniques to put together a rough phase diagram at 300°C, the temperature at which the study was to be made. Diffusion studies were then used to find the exact location of a miscibility gap in the $Ag_2Se$-$Cu_2Se$ pseudobinary system. Coulometric titration was used in order to obtain the activity of copper in cuprous selenide and the activity of silver in $Ag_2Se$-$Cu_2Se$ solid solutions as a function of the metal-to-selenium ratio. However, before making EMF measurements, each electrolyte which was to be used was tested to make certain that reactions between electrolyte and sample were negligible. Thus, I became acquainted with several cell types and several electrolytes.

Several diffusion and solubility studies are being conducted using a simple but precise apparatus in which the volume of absorbed gas can be measured directly as a function of time and at the temperature of interest. One such investigation involves the diffusion of water vapor into yttria doped zirconia. The equations for the solution of this problem have already been derived by Professor Wagner. (7)

An auxiliary problem involving the copper-silver-selenide system is now being studied. Having some knowledge of the defect structure, Professor Wagner has theorized as to the absorption of hydrogen into the lattice. If hydrogen occupies the vacant cation sites as a proton ($H^{1+}$), the amount of soluble hydrogen will be a function of the metal-to-selenium ratio. If hydrogen is absorbed as an atom, the amount will be independent of the metal to selenium ratio.

Each day was filled with study and with discussion of what I had learned or principles which I did not understand. Almost daily Professor Wagner presented me with something new to study; either reprints, lecture notes or memoranda. (A memorandum from Professor Wagner can be a research proposal, a progress report, a twenty-page discussion about electron degeneracy and quantum mechanical resonance, or a chapter on the use of dimensional analysis to solve Fick's second law for different boundary conditions.)

I hope that this report can convey some of my enthusiasm. I have had opportunity to learn things that will greatly further my career as a scientist. I am very grateful to all those who gave me so much of their time and especially to Professor Wagner for demonstrating methods, explaining theory, and indicating how to attack an electrochemical research problem.

Included with this report is a list of a few of the more important papers that were studied during my visit to Germany.

Harvey Kent Bowen
Cambridge, Mass.

### References


1. H. Schmalzried, "Point Defects in Ternary Ionic Crystals," Prog. in Solid State Chemistry, Pergamon Press, New York (1965) pp. 265-303.
2. H. Schmalzried, "The EMF Method in Studying Thermodynamic and Kinetic Properties of Compounds at Elevated Temperatures," Thermodynamics I, Intern. Atomic Energy Agency, Vienna, (1966) p. 97-109.
3. H. Schmalzried and J. D. Tretjakow, "Fehlordnung in Ferriten," Ber. Bunsenges., 70 (2), 180-189 (1964).
4. W. Müller and H. Schmalzried, "Fehlordnung in Kobaltferrit," Ibid., 68 (3), 270-276 (1964).
5. A. Werner, "Untersuchungen am System Cu-Ag-S," Z. phys. Chem. N. F., 47 (5/6), pp. 267-285 (1965).
6. S. Stotz and C. Wagner, "Die Löslichkeit von Wasserdampf und Wasserstoff in festen Oxiden," Ber Bunsenges., 70 (6), 781-788 (1966).
7. H. Dünwald and C. Wagner, Z. phys. Chem., B 34, 53 (1934).
8. C. Wagner, Memoranda.


# SECTION NEWS

## Boston Section

The following officers of the Boston Section elected to serve the 1967-1968 term are:

Chairman—Mario D. Banus, MIT Lincoln Laboratory, 244 Wood St., Lexington, Mass. 02173

Vice-Chairman—Martin S. Frant, Orion Research, Inc., 11 Blackstone St., Cambridge, Mass. 02139

Secretary—Raymond G. Donald, Laboratory for Physical Science, P. R. Mallory & Co., Inc., Third Avenue-Northwest Industrial Park, Burlington, Mass. 01803

Treasurer—Edward Goon, Metals Division, National Research Corp., 45 Industrial Place, Newton, Mass. 02192

Raymond G. Donald,
Secretary

## Southern California-Nevada Section

The following officers of the Southern California-Nevada Section elected to serve the 1967-1968 term are:

Chairman—Theodore J. LaChapelle, Autonetics Division of North American Aviation, 3370 E. Anaheim Rd., Anaheim, Calif. 92805

Vice-Chairman—Irving M. Pearson, Electronics Division, National Cash Register Co., 2815 W. El Segundo, Hawthorne, Calif. 90250

Secretary—Howard L. Recht, Atomics International Division of North American Aviation, P.O. Box 309, Canega Park, Calif. 91304

Treasurer—Douglas N. Bennion, Department of Engineering, University of California, Los Angeles, Calif. 90024

Councilors—Ken Nobe, Department of Engineering, University of California, Los Angeles, Calif. 90024 and William M. Hetherington, Hughes Space Systems Division, El Segundo, Calif. 90245

Howard L. Recht,
Secretary

# Three $800 Electrochemical Society Summer Fellowships to be Awarded

The Board of Directors of The Electrochemical Society recently appropriated funds to support three 1968 Summer Fellowships for qualified graduate students. Each fellowship has a stipend of $800 and the purpose of the fellowship is to assist a student to continue his graduate work during the summer months in a "field of interest to The Electrochemical Society." These fellowships are to be known as the Edward Weston Fellowship, the Colin Garfield Fink Fellowship, and the ECS Fellowship Award.

Candidates' Qualifications: "The award shall be made without regard to sex, citizenship or race, or financial need. It shall be made to a graduate student pursuing work between the degree of B.S. and Ph.D. who has received a nine months' grant preceding the summer period and who will continue his studies after the summer period. A previous holder of the award is eligible for reappointment."

Qualified graduate students are invited to apply for these summer fellowships and should submit the following items:

1. a brief statement of educational objectives.
2. a brief statement of thesis research problems including objectives, work already accomplished, and work planned for the summer of 1968.
3. a transcript of undergraduate and graduate academic work.
4. two letters of recommendation.

The applicant should request his research advisor and one additional faculty member familiar with his work to write letters of recommendation.

Applications must be received by March 1, 1968 and award winners will be announced on May 1, 1968.

# NEW MEMBERS

It is a pleasure to announce the following new members of The Electrochemical Society as recommended by the Admissions Committee and approved of by the Board of Directors in August 1967.

### Active Members

Bassous, Ernest, Yorktown Heights, N. Y.
Brown, R. A., Lancaster, Pa.
Cialdella, Cataldo, Olean, N. Y.
Deiss, W. J., Voreppe, France
Fitz, R. A., Plaistow, N. H.
Fleming, R. H., Raleigh, N. C.
Hammond, M. L., Mountain View, Calif.
Henri, Richaud, Voreppe, France
Hillman, D. K., Manchester, Mo.
Martin, H. L., Richardson, Texas
Nelson, R. D., Hickory Hill, Ill.
Oei, D.-G., Dearborn, Mich.
Russell, L. K., Livermore, Calif.
Shaw, R. R., Jeannette, Pa.
Terner, Edward, Boston, Mass.
Treat, D. W. Richardson, Texas
Valenta, George, Berwyn, Ill.
Watson, J. F., Sherman, Texas
Weinberg, N. L., Stamford, Conn.

### Associate Members

Norton, W. A., Natick, Mass.
Wilson, J. D., Tempe, Ariz.

### Student Members

Dell'Oca, C. J., Vancouver, B. C., Canada
Foulkes, F. R., Toronto, Ont., Canada
Gagnon, E. G., Raleigh, N. C.
Marcantonio, Joseph, Denver, Colo.

### Reinstatement to Active Membership

Hoffman, A. O., Indianapolis, Ind.

# OBITUARY

## Garrett W. Thiessen

Garrett W. Thiessen, former chairman of the Monmouth College Chemistry Department, died suddenly in July. He was 65.

Dr. Thiessen, an active member and Past-Chairman of the Electro-Organic Division of The Electrochemical Society and a member of the Monmouth College Faculty for 37 years, had received numerous awards, including the coveted Manufacturing Chemists Association Award as one of the outstanding teachers in the field of undergraduate chemistry. He was chosen from a field of 158 nominees for the national honor in 1957.

Born in Stanwood, Iowa, on January 9, 1902, Dr. Thiessen received his B.A. degree from Cornell College in 1924, the M.S. and Ph.D. degrees from State University of Iowa in 1925 and 1927 respectively.

From 1927-1930 he was assistant professor of chemistry and mathematics at Geneva College in Pennsylvania. He joined Monmouth in 1930, beginning

his service as an instructor. He was promoted through the ranks to full professorship, and at the time of his death he was the Pressly Professor of Chemistry. From 1952 to 1962 he was chairman of the Department of Chemistry.

Dr. Thiessen's teaching was oriented toward the laboratory and research. He made maximum use of demonstrations during his lectures and viewed the laboratory as a place for solving chemistry problems. He saw the chemical library as an integral part of the laboratory experience.

He published numerous articles in scholarly journals throughout his career and was coauthor of a textbook, "How to Solve Problems in Physical Chemistry," in 1944.

He was the first chemistry professor to receive an appointment to the faculty at Argonne National Laboratory in conjunction with the Argonne Semester Program sponsored by the Associated Colleges of the Midwest. He spent 15 months in 1960-1961 at Argonne doing research and teaching.

In 1961 he was named a Fellow of the American Association for the Advancement of Science. In 1966, Dr. Thiessen was elected an honorary member of the Midwestern Association of Chemistry Teachers in Liberal Arts Colleges (MACTLAC). The association, founded at Monmouth in 1952, honored him for "extraordinary service and active leadership to the association through its history."

He was a member of the American Chemical Society, the American Association for the Advancement of Science, Sigma Xi, Phi Beta Kappa, Phi Lambda Upsilon, Illinois Academy of Science, the Kresge-Hooker Library Association, the American Institute of Chemists, and the National Rifle Association.

He was past chairman of the Illinois-Iowa Section of the American Chemical Society and was president of the Illinois Academy of Science.

## NEWS ITEMS

### Materials Research Symposium

In conjunction with the dedication of its new Graduate Center for Materials Research of the University of Missouri Space Science Research Center, the University of Missouri at Rolla will host an invited paper symposium on "Materials Research—Problems and Prospects" to be held October 30-31, 1967. The symposium will emphasize the present state of the science in selected fields and the more promising new analytical techniques available for its exploration.

Five technical sessions scheduled for the afternoon of October 30 and the next day will deal with the

following topics and feature the following distinguished participants.

"Applications of the Powder Method in X-ray Crystallography to Solid State Research." Chairman: L. V. Azaroff, University of Connecticut. Participants: Ben Post, Brooklyn Polytechnic; M. E. Straumanis, University of Missouri at Rolla; R. Young, Georgia Institute of Technology.

"Electrochemistry." Chairman: H. H. Uhlig, MIT. Participants: Sherlock Swann, Jr., University of Illinois; Jerome Kruger, NBS; H. A. Liebhafsky, G. E. and Texas A. & M.

"High Temperature Chemistry." Chairman: Paul Gilles, University of Kansas. Participants: Robert J. Thorn, Argonne National Laboratory; LeRoy Eyring, Arizona State University; G. M. Rosenblatt, Pennsylvania State University.

"Point Defects in Non-Stoichiometric Compounds." Chairman: George Libowitz, Ledgemont Laboratory, Kennecott Copper Corp. Participants: R. F. Brebrick, MIT Lincoln Laboratory; M. J. Sienko, Cornell; Gordon Lewis, University of Missouri at Rolla.

"High Temperature Polymers." Chairman: T. G. Fox, Mellon Institute. Participants: J. K. Stille, University of Iowa; Guy C. Berry, Mellon Institute; W. E. Gibbs, AFML, Wright-Patterson AFB.

Further information on the symposium and its published proceedings may be obtained from Dr. William J. James, Director of the Graduate Center for Materials Research, University of Missouri at Rolla, Rolla, Mo. 65401.

### Metal Finishing Conference

On behalf of the International Council for Electrodeposition and Metal Finishing, the Deutsche Gesellschaft fur Galvanotechnik e.V., Dusseldorf, will hold, during and after the Hanover Fair in 1968, the 7th International Metal Finishing Conference in Hanover, from May 5-9, 1968. Correspondence should be addressed to: Deutsche Messe- und Ausstellungs-AG, Abt. Vb/Tagungsburo, D-3000 Hanover, Messegelande.

## Acheson Medal Award

The Acheson Medal Award can be made no oftener than every two years. The next opportunity for the Society so to honor someone is at the Montreal, Canada Meeting in the Fall of 1968.

The Honors and Awards Committee is charged by the Bylaws to recommend a selection to the Board. The Rules adopted by the Society, amended as of March 3, 1949, require that the Award shall be made without distinction on account of sex, citizenship, race, or residence.

In addition to the above, with regard to the selection, the Rules have the following provisos:

1. Nominations shall be accepted, also, from the membership at large. Announcement to this effect shall be made by the Secretary through the Journal of The Electrochemical Society as promptly as possible after the appointment of the Committee.

2. All nominations, whether made by a member of the Nominating Committee or by another member of the Society, must be accompanied by a full record of qualifications of the nominee for the Award. Such supporting documents from friends of the candidate or from his organization shall be in order.

3. The nominator must assume the responsibility for providing the Chairman of the Honors and Awards Committee with nine copies of the supporting documents, one for each member.

It is desired that such suggestions be in the hands of the Committee not later than February 1, 1968.

Following is a list of Acheson Medalists since the Award was founded:

Edward G. Acheson*—1929
Edwin F. Northrup*—1931
Colin Garfield Fink*—1933
Frank J. Tone*—1935
Frederick M. Becket*—1937
Francis C. Frary—1939
Charles F. Burgess*—1942
William Blum—1944
H. Jermain Creighton—1946
Duncan A. MacInnes*—1948
George W. Vinal—1951
J. W. Marden—1953
George W. Heise—1954
Robert M. Burns—1956
William J. Kroll—1958
Henry B. Linford—1960
C. L. Faust—1962
Earl A. Gulbransen—1964
Warren C. Vosburgh—1966

Please address all nominations to the Chairman of the Honors and Awards Committee, Dr. Walter J. Hamer, Electrochemistry Section, National Bureau of Standards, Washington, D. C. 20234.

* Deceased

## NEW BOOKS

**"Composite Materials,"** A. Kelly, G. C. Smith, P. J. E. Forsyth, and A. J. Kennedy. Published for the Institution of Metallurgists, London, by American Elsevier Publishing Co., Inc., New York, 1967. 154 pages; $7.50.

The contents of this book are derived from four lectures delivered at the 21st Refresher Course of the Institute of Metallurgists is 1965 by the above authors. The topics covered are (1) Theory of Strengthening of Materials (2) Dispersion Strengthened Materials, (3) Fibre Strengthened Materials, and (4) The Potential of Composite Materials.

**"Glass Electrodes for Hydrogen and Other Cations,"** Edited by George Eisenman. Published by Marcel Dekker, Inc., New York, 1967. 582 pages; $24.75.

The subtitle, "Principles and Practice" describes the division of the book. There are seven chapters on theory of pH and cation measurement, glass-electrode composition properties, glass-electrode potential, diffusion potentials, ionic specificity and ion-exchange theory of the glass electrode. Twelve chapters are devoted to the construction and specific uses in biological and analytical chemistry for testing and determination of specific ion concentration.

**"Handbook of Epoxy Resins,"** Henry Lee and Kris Neville. Published by the McGraw-Hill Book Co., New York, 1967. 882 pages; $32.50.

This volume contains detailed and specific information on all types of epoxy resin systems, their chemistry, forming properties, uses, etc. It is extremely well referenced and up to date.

**"Silver-Economics, Metallurgy, and Use,"** Edited by Allison Butts with the Collaboration of Charles D. Coxe. Published by Van Nostrand Co., Inc., New York, 1967. 488 pages; $13.50.

The title describes the contents. It covers the properties of silver and its alloys, application, and uses.

**"Modern Aspects of Electrochemistry,"** No. 4. Edited by J. O'M. Bockris. Published by Plenum Publishing Corp., New York, 1967. 316 pages; $12.50.

The fourth volume of this series contains four monographs as follows: "Some Aspects of the Thermodynamic Structure of Electrochemistry," by P. Van Rysselbergh, "The Mechanism of Oxidation of Organic Fuels," by E. Gileadi, "Anodic and Electronic Currents at High Fields in Oxide Films" by L. Young, W. S. Goruk, and F. G. R. Zobel, and "An Economic Study of Electrochemical Industry in the United States," by G. Wenglowski.

## POSITIONS AVAILABLE

Please address replies to the box number shown c/o The Electrochemical Society, Inc., 30 East 42 St., New York, N. Y. 10017.

Research Specialist — experimental projects and laboratory studies on thin film materials and processes with emphasis on dielectrics, magnetics, and stability. Manufacturing Manager—be responsible to plant manager for manufacturing engineering, processing, shop operations, and QC involved in the manufacture of semiconductor power devices. Senior R&D Engineer—for semiconductor infrared detector and laser work. Crystal growing experience and interest desirable. Reply Box B-20.

Electrochemist wanted by small but well-financed private company. Someone with engineering bent preferred. Essential situation will be to develop new experimental electrochemical ideas for commercial exploitation. Reply Box B-21.

Electrochemists — experimental research in such areas as fuel cell development, industrial electrochemistry, electrode development, and electro-organic synthesis. Reply Box B-22.

## Electrochemical Technology

### July-Aug. 1967

**The following technical papers and technical notes appear in the July-Aug. 1967 issue of ELECTROCHEMICAL TECHNOLOGY, Vol. 5, No. 7-8. To receive a subscription to ELECTROCHEMICAL TECHNOLOGY, complete the coupon below and return with remittance to the address shown.**

### TECHNICAL PAPERS



### TECHNICAL NOTES



Fill out and return to

**The Electrochemical Society, Inc.,**
**30 East 42 St., New York, N. Y. 10017**

Please enter my subscription to ELECTROCHEMICAL TECHNOLOGY (bimonthly) for which I enclose my remittance.

☐ 1967 Subscription to ELECTROCHEMICAL TECHNOLOGY to Members only $6.00

☐ 1967 Subscription to ELECTROCHEMICAL TECHNOLOGY to Nonmembers $15.00
Overseas postage to Nonmembers (outside of U.S. and Canada) $1.50

All Payments must be in U.S. funds

Name _____ Title _____

Business affiliation _____

Address _____

City _____ State _____

Zip Code _____ Country _____

# The Electrochemical Society

## INSTRUCTIONS TO AUTHORS OF PAPERS

(Revised as of 6/1/67)

***Journal of the Electrochemical Society*** is the fundamental research journal serving the interdisciplinary interests of chemistry, physics, electronics, biology, medicine, and engineering as they pertain to electrochemistry and to electrochemical phenomena. Written for the research scientist in industry, government, the independent laboratory and the university, it publishes contributed Technical Papers, Technical Notes and Brief Communications describing current basic research of original character, and is edited in two sections: 1) ***Electrochemical Science*** including such areas as batteries, fuel cells, corrosion and corrosion mechanisms, electrothermics and metallurgy, electrodeposition, electroorganic reactions and phenomena, and allied work of theoretical electrochemical nature. 2) ***Solid State Science*** including such areas as dielectrics and insulation, electrothermics and metallurgy, semiconductors, luminescence and related solid state investigations.

***Electrochemical Technology*** is the journal of applied electrochemistry written for the application-oriented researcher, consultant, R & D engineer, product designer and production engineer whose responsibility lies in such areas as: batteries and fuel cells, corrosion and its control, dielectrics and insulation, electrodeposition and plating, electrothermics and metallurgy, electroorganic synthesis, industrial electrolysis and the process aspects of semiconductors and related solid state products. It publishes original contributed Technical Papers, Technical Notes and Brief Communications describing current application of electrochemistry and electrochemical phenomena to products and systems. Its Feature Section also publishes original contributed reviews pertinent to electrochemical interests.

## GENERAL

**Manuscripts** must be submitted in triplicate to expedite review. They should be typewritten, double-spaced, with 2½-4 cm (1½ in.) margins.

**Titles** should be brief, followed by the author's name and professional connection. Authors should be as brief as is consistent with clarity and should omit introductory or explanatory material which may be regarded as familiar to specialists in the particular field. Proprietary and trade names should be generally avoided; if used with discretion, they should be capitalized to protect the owners' rights.

Authors are encouraged to suggest qualified reviewers for their manuscripts, the Editor reserving the right of final choice. It is helpful if the author tells which ECS **Division** would be most interested in his paper.

Present Society policy permits manuscript review in several weeks. Manuscripts returned to the author for revision should be resubmitted promptly to allow publication in five months or less from date of original receipt.

## TYPES OF ARTICLES

**Fundamental Technical Articles** must describe original research of basic nature and must have adequate scientific depth. **Applied Technical Articles** may deal with any practical aspect of the fields of interest to the Society, **e.g.**, plant design or operation, production and control methods, economics. Articles of wide diversity of interest are acceptable, but subjects primarily covered in other specialized journals (**e.g.**, analytical or nuclear chemistry) are not considered appropriate. An **Abstract** should state the scope of the paper and summarize fully its results and contents. Suitable headings and subheadings should be included, but sections should not be numbered. Articles in recent issues should be consulted for current style.

**Technical Notes** are used for reporting briefer research, developmental work, process technology, new or improved devices, materials, techniques, or processes which do not involve more extensive basic scientific study. No abstract is required.

**Brief Communications** are used only to report new information of scientific or technological importance which warrants rapid dissemination. They need not necessarily reflect a complete research project; interim reports are acceptable. Length should be a nominal 700 words, with up to two illustrations. No abstract is required. Publishing time is normally less than three months.

## EQUATIONS

**Mathematical Equations** should be written on a single line if possible, and parentheses, brackets, the solidus (/), negative exponents, etc., may be used freely for this purpose. Authors are urged to consult Chapter VI of the "Style Manual" of the American Institute of Physics (available for $1.00 at American Institute of Physics, 335 East 45 Street, New York, N. Y. 10017) and to follow the patterns described there.

## SYMBOLS

Authors are encouraged to use symbols extensively. These should be defined in a list at the end of the paper, with units given. For example:

$a, b \ldots$ = empirical constants of Brown equation
$f_i$ = fugacity of pure $i$th component, atm
$D_v$ = volume diffusion coefficient, cm²/sec

## KEY WORDS

Authors are responsible for supplying a list of key words, to facilitate information retrieval. Generic terms generally are to be avoided. Key words acceptable to **Chemical Abstracts** are also generally acceptable in Society publications. List key words in the margin of the first page of the manuscript.

## ABBREVIATIONS UNITS

The AIP "Style Manual" referred to here gives a suitable list of common **Abbreviations.** Units usually will be abbreviated without periods throughout the text, as sec, min, hr, cm, mm, etc. **Metric Units** should be used throughout, unless English units are clearly more appropriate in the area of discussion.

## POTENTIAL SIGNS

**Electrode Potentials:** Authors are urged to state and make use of the polarity of test electrodes with respect to the reference electrode used, **i.e.,** Zn is normally negative, Cu normally positive with respect to the standard hydrogen electrode. The sign for the emf of a cell should conform to the free energy change of the chemical reaction as written or implied, in accordance with the definition $\Delta G = nFE$. These suggestions agree with the IUPAC conventions adopted in 1953.

## REFERENCES

**Literature References** should be listed on a separate sheet at the end of the paper in the order in which they are cited in the text. Authors' initials must be given, and the style and abbreviations adopted by **Chemical Abstracts** should be used. Any recent issue of Society journals may be consulted. Literature cited should be readily available; consequently personal communications, Department of Defense (DOD), and Office of Technical Services (OTS) citations should be minimized. When references are not readily accessible, **Chemical Abstracts** citation numbers must be supplied.

## PUBLICATION CHARGE

A charge of $40 per printed page is made for publication of technical material in Society journals. A 10% reduction is allowed if at least one author of an article is an ECS member or an employee of a Patron or Sustaining Member firm. However, acceptance of a manuscript is in no way dependent on such payment, and the charge may be waived in individual cases.

## ILLUSTRATIONS

**Photographs** should be used sparingly, must be glossy prints, and should be mailed with protection against folding. **Micrographs** should have a labeled length unit drawn or pasted on the picture. On both, label "top" where any uncertainty might arise. **Captions** for figures (including photographs) must be included on a separate sheet. Figure numbers must **not** appear in the body of the figure; they will be removed if they do. **Numerical Data** should not be duplicated in tables and figures.

**Drawings** and **Graphs** ordinarily will be reduced to 8.3 cm (3¼ in.) column width, and after such reduction should have lettering no less than 0.15 cm high. Lettering must be of letter-guide quality. India ink on tracing cloth or paper is preferred, but India ink on coordinate paper with blue ruling is acceptable. Line weight 2 is used for borders and zero lines. When several curves are shown, each may be numbered and described in the caption. Lettering shown is approximately ⅛ in. In plotting current or potential as ordinate, increasing negative values should go down. The sample graph shown conforms to suggestions of the United States of America Standards Institute (USA Report Y15.1-1959).

SAMPLE CURVE DRAWING FOR REDUCTION TO $\frac{1}{2}$ SIZE

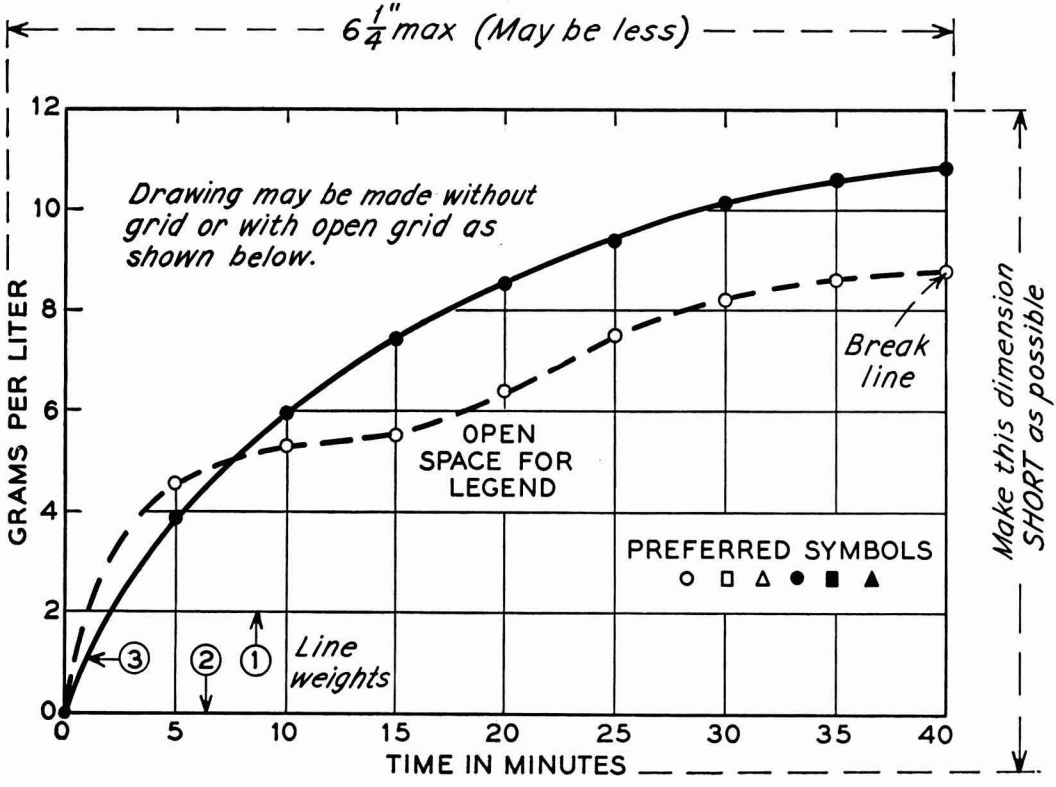

# Call for Papers
# 133rd National Meeting, Boston, Mass., May 5-9, 1968

Divisions which have scheduled sessions are listed overleaf, along with symposium topics.

## 1. Symposium Papers.

Authors desiring to contribute papers to a symposium listed overleaf should check first with the symposium chairman to ascertain appropriateness of the topic.

## 2. General Session Papers.

Each of the several Society Divisions which meets in Boston can plan a general session. If your paper does not fit readily into a planned symposium, you should specify "General Session."

## 3. To Submit a Meeting Paper.

Each author who submits a paper for presentation at a Society National Meeting should do four things:

A—Submit three copies on the form printed overleaf, of a 75-word abstract of the paper to be delivered. These are required for publication in the printed program of the meeting. You may use a facsimile of the abstact form if necessary.

B—Simultaneously submit three copies of an extended abstract. See below for details.

C—Determine whether the meeting paper is to be submitted for publication in a Society journal. If so, see below for details.

D—Send the 75-word abstract and the extended abstract to The Electrochemical Society, Inc., 30 East 42 St., New York, N. Y. 10017, not later than December 15, 1967. Your full manuscript for publication may accompany your abstracts.

## 4. Meeting Paper Acceptance.

Notification of acceptance for meeting presentation, along with scheduled time, will be mailed to authors with general instructions no earlier than two months before the meeting. Those authors who require more prompt notification are requested to submit with their abstracts a self-addressed postal card with full author-title listing on the reverse.

## 5. Extended Abstract Book Publication.

Each Division program will be the subject of an extended abstract volume in a manner prescribed by the Society Board of Directors. These volumes are published by photo offset directly from typewritten copy submitted by the author. Special care should therefore be given to the following typing instructions, to insure legibility.

A—Abstracts are to be from 500-1000 words in length (two pages single-spaced) and are to contain to whatever extent practical all significant experimental data to be presented during oral delivery.

B—Please send original and two copies of the abstract typed single-spaced. Use white bond paper, size 8½ x 11 inches, with 1¼ margins on all sides. Typing guide forms are available from Symposium Session Chairman and from National Headquarters.

C—Title of paper should be in capital letters. Author(s) name and affiliation should be typed immediately below. It is not necessary in the heading or body to designate paper as "Extended Abstract" or to quote the divisional symposium involved.

D—Submit all copy, including figures, symbols and corrections, in black ink. No handwritten corrections, please. Submit graphs on onion skin without grids, or on graph paper specifically designed for offset reproduction; strip-on tape is acceptable.

E—Paste figures within typing dimensions indicated, with lettering no smaller than ⅛ inch. Submit only the important illustrations. Avoid use of half-tones except where absolutely necessary. Type captions no wider than figure dimensions and paste in proper place in the abstract. Place figure caption at bottom of figure. Place table title at top of table.

F—Mail to The Electrochemical Society. Inc., unfolded.

G—Please note that the extraordinarily low price, per volume, of extended abstract volumes is made possible only through your strict adherence to these instructions. Any deviation threatens this low cost.

## 6. Manuscript Publication in a Society Journal.

Presentation of a paper at a Society National Meeting incurs no obligation to publish. However, all meeting papers upon presentation become the property of The Electrochemical Society, Inc., and should be submitted as promptly as possible in full manuscript form in order to be considered for publication in a Society publication. The Society "Instructions to Authors," are available from National Headquarters, set forth manuscript style and format.

# Boston Meeting Symposia Plans–Spring 1968

**Triplicate copies of the usual 75-word abstract, as well as of an extended abstract 500-1000 words are due at The Electrochemical Society, Inc., 30 East 42 St., New York, N. Y. 10017, not later than December 15, 1967.**

## Dielectrics and Insulation Division Symposia Plans

The Dielectrics and Insulation Division has planned two symposia and general sessions for the Boston Meeting of the Society, May 5-9, 1968. Also planned is a joint symposium with the Electronics Division.

### Optical Properties of Dielectric Films

A symposium on Optical Properties of Dielectric Films is scheduled. Dr. N. N. Axelrod, Bell Telephone Laboratories, Inc., Murray Hill, N. J., 07971, is Chairman

There will be a number of invited papers; contributed papers are also being solicited.

Categories of subject matter being actively considered for the sessions include:

(a) Optical studies from the infrared to the ultraviolet associated with electronic and vibrational transitions in solid dielectric thin films.

(b) Field related optical phenomena such as the photoelectric, photovoltaic and magneto-optical effects.

(c) Optical techniques for study of the growth of thin dielectric films.

(d) Properties of multilayer films and films with gradients in the index of refraction.

(e) Applications to optical components and electrical devices.

Suggestions and questions are welcome, and should be directed to the Chairman, Norman N. Axelrod.

### Theory of Dielectric Behavior (Tutorial)

Dr. L. Mandelcorn, Westinghouse Research Center, Pittsburgh, Pa., is Chairman for the symposium on Theory of Dielectric Behavior.

### Photoresist Technology and Applications

Dr. J. A. Offenbach, IBM Components Division Laboratories, East Fishkill Facility, Hopewell Junction, N. Y., is Chairman of the symposium on Photoresist Technology and Applications, jointly sponsored by the Electronics Division.

## Electronics Division Symposia Plans

The program for the 1968 Spring Meeting in Boston, Mass., May 5-9, 1968, will include general sessions and symposia in several areas of electronic materials.

### Luminescent and Laser Materials

Sessions on Luminescent and Laser Materials are being organized by the Luminescence group of the Electronics Division. Papers are solicited from those active in research and development of luminescent and laser materials. The program will include contributions ranging from fundamental phenomenological investigations to applications. A special session relating to color TV is also planned. Questions concerning the program should be addressed to the Program Chairman, Frank C. Palilla, General Telephone and Electronics Laboratories, Bayside, N. Y. 11360. Recent News Papers are also scheduled.

Triplicate copies of a 75-word abstract of Recent News Papers are to be sent to Mr. Frank C. Palilla at the above address not later than March 29, 1968.

### Preparation and Properties of Single Crystals for Acoustic, Optical, and Microwave Applications

This symposium will emphasize the relationship between the chemical and preparative parameters of single-crystal materials and their use or potential use in acoustic, optic, and microwave solid state electronics components. Papers describing new methods of synthesis, crystal growth, and physical phenomena or applications of general interest will also be welcomed. Questions concerning this symposium should be addressed to the Chairman, Roger Newman, Manager, Solid State Science Department, Sperry Rand Research Center, North Road, Sudbury, Mass. 01772.

### Semiconductor Symposium Plans

The program for the 1968 Spring Meeting in Boston, Mass., May 5-9, 1968 will include, but not be restricted to, contributions in the areas relating to elemental, compound, and alloy semiconductors:

Materials Synthesis and Characterization: crystal growth; epitaxy—homogeneous and heterogeneous; polycrystalline materials' properties; diffusion; and heterojunction formation and properties.

Device Technology: ion implantation techniques; electron beam processing; diffusion and alloying; contact preparation and properties; surface and oxides, photomasking materials' processes and techniques; and isolation techniques.

Questions concerning this symposium should be addressed to the Chairman, Dr. Alan Strauss, MIT Lincoln Laboratory, P. O. Box 73, Lexington, Mass. 02173.

A full day for presentation of Recent News Papers has also been planned.

Triplicate copies of a 75-word abstract of Recent News Papers are to be sent to Dr. Alan Strauss, MIT Lincoln Laboratory, P. O. Box 73, Lexington, Mass. 02173, not later than March 29, 1968.

## Electro-Organic and Theoretical Electrochemistry Division Joint Symposium

### The Electrochemical Reactions of Organic Molecules in Nonaqueous Solvents

A joint symposium by the Electro-Organic and Theoretical Electrochemistry Division is planned on the topic The Electrochemical Reactions of Organic Molecules in Nonaqueous Solvents for the 1968 Spring Meeting in Boston, Mass., May 5-9, 1968.

Invited papers will survey the oxidation and reduction of aromatic and olefinic hydrocarbons in nonaqueous solvents. Although reductions will be considered, the emphasis will be placed on the oxidation of organic molecules in these solvents. The electrochemical processes of simple heterocyclic hydrocarbons will also be discussed. Contributed papers in these areas will be considered for inclusion in this symposium.

Inquiries and suggestions should be addressed to either of the symposium Chairmen: Robert Visco, Bell Telephone Laboratories, Inc., Murray Hill, N. J., 07971, or A. C. Makrides, Tyco Laboratories, Inc., Bear Hill, Waltham, Mass. 02154.

Authors desiring to contribute papers are urged to check first with the Symposium Chairmen to ascertain appropriateness of their topic.

## Electrothermics and Metallurgy Division Symposia Plans

### Conference on Electron and Ion Beams in Science and Technology

The Electrothermics and Metallurgy Division wishes to announce that the Third International Conference on Electron and Ion Beams in Science and Technology will be held in Boston, Mass., May 5-9, 1968 as part of the Society's 133rd National Meeting.

The conference will include sessions on advances in the physics of electron and ion beams, electron beams in materials processing, including welding, melting, zone refining, evaporation, ion

propulsion, electron and ion beams in microelectronics and electron and ion beams in recording and information storage.

Many of the sessions will be followed by round table discussions.

All session chairmen have been selected and all administrative details have been completed.

Additional information relating to the conference can be obtained from Dr. Robert Bakish, 171 Sherwood Place, Englewood, N. J. 07631.

Authors desiring to contribute papers are urged to check first with the Symposium Chairman to ascertain appropriateness of their topic. Symposium plans are well advanced, and authors must anticipate submitting abstracts before November 1, 1967.

## Industrial Electrolytic Division Symposium Plans

### Chlorates and Perchlorates

The Industrial Electrolytic Division plans a symposium on the formation and manufacture of chlorates and perchlorates at the 1968 Spring Meeting in Boston, Mass., May 5-9, 1968.

Papers for this symposium can range from fundamental studies to descriptions of industrial installations. Related electrolytic oxidations such as the formation of bromates, iodates, and periodates will also be considered. Papers are solicited on reaction mechanism, electrode kinetics, electrode materials, electrolytic cell designs, analytical techniques, properties, economics, safety and industrial processes.

Inquiries and suggestions should be addressed to either of the symposium Chairmen: J. C. Schumacher, American Potash & Chemical Corp., 3000 W. Sixth St., Los Angeles, Calif. 90054, or D. N. Goens, American Potash & Chemical Corp., 12519 E. Washington Blvd., Whittier, Calif. 90602.

### Electrodialysis

The program of the Industrial Electrolytic Division will include a symposium on Electrodialysis.

Invited papers will be original contributions or reviews of theory, engineering and/or applications of electrodialysis or related processes such as electrosorption–desorption, electro-osmosis, electrochemical demineralization with ion absorbing electrodes or transport depletion electrodialysis: of theory, preparation and/or applications of natural or synthetic, organic or inorganic ion-selective or ion exchange membranes; of properties of natural or synthetic ion selective or ion exchange membranes.

Contributed papers are also solicited. Inquiries and suggestions should be addressed to either of the Symposium Chairmen: W. A. McRae or E. J. Parsi, Ionics, Inc., 65 Grove St., Watertown, Mass. 02172.

Authors desiring to contribute papers are urged to check first with the Symposium Chairmen to ascertain appropriateness of their topics.

## Theoretical Electrochemistry Division Symposium Plans

### Adsorption Phenomena on Solids

The Theoretical Electrochemistry Division plans a symposium on Adsorption Phenomena on Solids for the 1968 Spring Meeting to be held in Boston, Mass., May 5-9, 1968. There will be a number of invited papers on adsorption in the gas phase and adsorption from electrolytic solutions. Contributed papers are also solicited. Inquiries and suggestions should be sent to Dr. Manfred Breiter, Research and Development Center, General Electric Co., P. O. Box 8, Schenectady, N. Y. 12301.

## Future Meetings of The Electrochemical Society

**May 5-9, 1968**
Boston, Mass.
Statler Hilton Hotel

**October 6-11, 1968**
Montreal, Canada
Queen Elizabeth Hotel

**May 4-9, 1969**
New York City
Commodore Hotel

**October 5-10, 1969**
Detroit, Mich.
Statler Hilton Hotel
(also Sheraton Cadillac)

**May 10-15, 1970**
Los Angeles, Calif.
Statler Hotel (also Biltmore Hotel)

**October 4-9, 1970**
Pittsburgh, Pa.
Penn Sheraton Hotel

**May 9-14, 1971**
Washington, D. C.
Sheraton Park Hotel

**October 3-8, 1971**
Cleveland, Ohio
Sheraton Cleveland Hotel

**May 7-12, 1972**
Houston, Texas
Shamrock Hilton

**October 8-13, 1972**
Atlantic City, N. J.
Chalfonte Haddon Hall

**May 12-18, 1973**
Chicago, Ill.
Sheraton Chicago

**October 7-12, 1973**
Boston, Mass.
Sheraton Boston

**May 5-10, 1974**
San Francisco, Calif.
Sheraton Palace

**October 13-18, 1974**
New York City
Commodore Hotel

**May 11-16, 1975**
Toronto, Canada
The Roval York

**October 5-10, 1975**
Dallas, Texas
Sheraton Dallas

# 75-WORD ABSTRACT FORM

## BOSTON MEETING, MAY 5-9, 1968

Abstract No. .....
(do not write in this space)

.....
(Title of paper)

.....

.....
(Author)

.....
(Business Affiliation)

.....
(Address)

(Type your abstract in this space—double space with two carbon copies on plain white paper.)

**Division and Symposium** .....

**Is a full length paper on this work to be submitted for Society publication?** ☐ Yes ☐ No

Papers presented before a national technical meeting become the property of the Society and may not be published elsewhere without written permission of the Society.

For Office Use

Extended Abstract rec'd: ..... requested: .....

Sent to: .....

75-word Abstract sent to: ..... date: .....

# THE ELECTROCHEMICAL SOCIETY PATRON MEMBERS

**Aluminum Co. of Canada, Ltd.**, Montreal, Que., Canada

**Dow Chemical Co.**
Chemicals Dept., Midland, Mich.
Metals Dept., Midland, Mich.

**General Electric Co.**
Capacitor Dept., Hudson Falls, N. Y.
Chemical Laboratory, Knolls Atomic Power Laboratory, Schenectady, N. Y.
Chemical Systems and Processes Laboratory, Research and Development Center, Schenectady, N. Y. (3 memberships)
Direct Energy Conversion Operation, West Lynn, Mass.
Lamp Div., Cleveland, Ohio
Materials & Processes Laboratory, Large Steam Turbine-Generator Dept., Schenectady, N. Y.

**The International Nickel Co., Inc.**, New Yok, N. Y.

**Olin Mathieson Chemical Corp.**
Chemicals Div., Research Dept., New Haven, Conn.

**Union Carbide Corp.**
Divisions:
Carbon Products Div., New York, N. Y.
Consumer Products Div., New York, N. Y.

**Westinghouse Electric Corp.**
Electronic Tube Div., Elmira, N. Y.
Lamp Div., Bloomfield, N. J.
Molecular Electronics Div., Elkridge, Md.
Semiconductor Div., Youngwood, Pa.
Research Laboratories, Pittsburgh, Pa.

# THE ELECTROCHEMICAL SOCIETY SUSTAINING MEMBERS

**Air Reduction Co., Inc.,**
New York, N. Y.

**Allen-Bradley Co.,**
Milwaukee, Wis.

**Allied Chemical Corp.,**
General Chemical Div.,
Morristown, N. J.

**Aluminum Co. of America,**
New Kensington, Pa.

**American Metal Climax, Inc.,**
New York, N. Y.

**American Potash & Chemical Corp.,**
Los Angeles, Calif.

**American Smelting and Refining Co.,**
South Plainfield, N. J.

**American Zinc Co. of Illinois,**
East St. Louis, Ill.

**American Zinc, Lead & Smelting Co.,**
St. Louis, Mo.

**The M. Ames Chemical Works, Inc.,**
Glens Falls, N. Y.

**Ampex Corp.,**
Redwood City, Calif.

**Armco Steel Corp.,**
Middletown, Ohio

**Basic Inc.,**
Bettsville, Ohio

**Bell Telephone Laboratories, Inc.,**
New York, N. Y. (2 memberships)

**Bethlehem Steel Corp.,**
Bethlehem, Pa. (2 memberships)

**Boeing Co.,**
Seattle, Wash.

**Burgess Battery Co.,**
Freeport, Ill. (2 memberships)

**Burndy Corp.,**
Norwalk, Conn.

**Canadian Industries Ltd.,**
Montreal, Que., Canada

**Carborundum Co.,**
Niagara Falls, N. Y.

**Chrysler Corp.,**
Detroit, Mich.

**Cominco Ltd.,**
Trail, B. C., Canada (2 memberships)

**Corning Glass Works,**
Corning, N. Y.

**Cyclops Corp.,**
Universal-Cyclops Specialty Steel Div.,
Bridgeville, Pa.

**Diamond Alkali Co.,**
Painesville, Ohio

**Wilbur B. Driver Co.,**
Newark, N. J.

**E. I. du Pont de Nemours & Co., Inc.,**
Wilmington, Del.

**Eagle-Picher Industries, Inc.,**
Electronics Div.,
Joplin, Mo.

**Eastman Kodak Co.,**
Rochester, N. Y.

**Eltra Corp.**
Prestolite Div., Toledo, Ohio
C&D Batteries, Conshohocken, Pa.

**Engelhard Industries, Inc.,**
Newark, N. J.

**The Eppley Laboratory, Inc.,**
Newport, R. I.

**ESB Corp.,**
Philadelphia, Pa. (2 memberships)

**Esso Research and Engineering Co.,**
Engineering Technology Div.,
Florham Park, N. J.

**Exmet Corp.,**
Bridgeport, Conn.

# SUSTAINING MEMBERS (CONTINUED)

**Fairchild Semiconductor Corp.,**
Palo Alto, Calif.

**FMC Corp.,**
Inorganic Chemicals Div.,
Buffalo, N. Y.
Inorganic Chemicals Div.,
South Charleston, W. Va.

**Foote Mineral Co.,**
Exton, Pa.

**Ford Motor Co.,**
Dearborn, Mich.

**General Motors Corp.,**
Allison Div., Indianapolis, Ind.
Delco-Remy Div., Anderson, Ind.
Research Laboratories Div., Warren, Mich.

**General Telephone & Electronics Laboratories, Inc.,** Bayside, N. Y.

**Globe-Union, Inc.,**
Milwaukee, Wis.

**B. F. Goodrich Chemical Co.,**
Cleveland, Ohio

**Gould-National Batteries, Inc.,**
Minneapolis, Minn.

**Great Lakes Carbon Corp.,**
New York, N. Y.

**Harshaw Chemical Co.,**
Cleveland, Ohio (2 memberships)

**Hercules Inc.,**
Hercules Research Center,
Technical Information Div.,
Wilmington, Del.

**Hill Cross Co., Inc.,**
West New York, N. J.

**Hoffman Electronics Corp.,**
Semiconductor Div.,
El Monte, Calif.

**Honam Electric Industrial Co.,**
Kwangju City, Korea

**Honeywell, Inc.,**
Minneapolis, Minn.

**Hooker Chemical Corp.,**
Niagara Falls, N. Y. (2 memberships)

**HP Associates,**
Palo Alto, Calif.

**Hughes Research Laboratories, Div. of Hughes Aircraft Co.,** Malibu, Calif.

**International Business Machines Corp.,**
New York, N. Y.

**International Minerals & Chemical Corp.,**
Skokie, Ill.

**International Resistance Co.,**
Philadelphia, Pa.

**ITT Federal Laboratories, Div. of International Telephone & Telegraph Corp.,**
Nutley, N. J.

**Jones & Laughlin Steel Corp.,**
Pittsburgh, Pa.

**K. W. Battery Co.,**
Skokie, Ill.

**Kaiser Aluminum & Chemical Corp.,**
Metals Div. Research,
Permanente, Calif.
Div. of Metallurgical Research,
Spokane, Wash.

**Kawecki Chemical Co.,**
Boyertown, Pa.

**Kennecott Copper Corp.,**
New York, N. Y.

**Leesona Moos Laboratories, Div. of Leesona Corp.,** Great Neck, N. Y.

**Arthur D. Little, Inc.,**
Cambridge, Mass.

**Lockheed Aircraft Corp.,**
Missiles & Space Div.,
Sunnyvale, Calif.

**Mallinckrodt Chemical Works,**
St. Louis, Mo.

**P. R. Mallory & Co.,**
Indianapolis, Ind.

**Melpar, Inc.,**
Falls Church, Va.

**Miles Chemical Co., Div. of Miles Laboratories, Inc.,** Elkhart, Ind.

**Mobil Oil Corp.,**
Dallas, Texas

**Monsanto Chemical Co.,**
St. Louis, Mo.

**M&T Chemicals Inc.,**
Detroit, Mich.

**Nalco Chemical Co.,**
Chicago, Ill.

**National Cash Register Co.,**
Dayton, Ohio

**National Lead Co.,**
New York, N. Y.

**National Steel Corp.,**
Weirton, W. Va.

**North American Aviation, Inc.,**
El Segundo, Calif.

**Northern Electric Co.,**
Montreal, Que., Canada

**Norton Co.,**
Worcester, Mass.

**Owens-Illinois Glass Co.,**
Toledo, Ohio

**Pennsalt Chemicals Corp.,**
Philadelphia, Pa.

**Phelps Dodge Refining Corp.,**
Maspeth, N. Y.

**Philips Laboratories, Inc.,**
Briarcliff Manor, N. Y.

**Pittsburgh Plate Glass Co.,**
Chemical Div.,
Pittsburgh, Pa.

**Potash Co. of America,**
Carlsbad, N. Mex.

**Radio Corp. of America**
Electronic Components and Devices,
Lancaster, Pa.
RCA Victor Record Div.
Indianapolis, Ind.

**Republic Foil Inc.,**
Danbury, Conn.

**Reynolds Metals Co.,**
Richmond, Va.

**Shawinigan Chemicals Ltd.,**
Montreal, Que., Canada

**Sonotone Corp.,**
Elmsford, N. Y.

**Speer Carbon Co.,**
International Graphite & Electrode
Div., St. Marys, Pa.

**Sprague Electric Co.,**
North Adams, Mass.

**Stackpole Carbon Co.,**
St. Marys, Pa.

**The Standard Oil Company of Ohio,**
Cleveland, Ohio

**Stauffer Chemical Co.,**
Dobbs Ferry, N. Y.

**Texas Instruments, Inc.,**
Dallas, Texas
**Metals and Controls Corp.,**
Attleboro, Mass.

**3M Company,**
St. Paul, Minn.

**Titanium Metals Corp. of America,**
Henderson, Nev.

**Tyco Laboratories, Inc.,**
Waltham, Mass.

**Udylite Corp.,**
Detroit, Mich. (4 memberships)

**United States Steel Corp.,**
Pittsburgh, Pa.

**Univac, Div. of Sperry Rand Corp.,**
New York, N. Y.

**Upjohn Co.,**
Kalamazoo, Mich.

**Varian Associates,**
Palo Alto, Calif.

**Western Electric Co., Inc.,**
Chicago, Ill.

**Wyandotte Chemicals Corp.,**
Wyandotte, Mich.

**Yardney Electric Corp.,**
New York, N. Y.